

Acid Hydrolysis of Cellulose
and the Anomeric Effect:
A Computational Study

Inaugural-Dissertation

zur

Erlangung des Doktorgrades der
Mathematisch-Naturwissenschaftlichen Fakultät
der Heinrich-Heine-Universität Düsseldorf

vorgelegt von

Claudia Loerbroks

aus Wilhelmshaven

Mülheim an der Ruhr, Düsseldorf 2014

Gedruckt mit der Genehmigung der Mathematisch-Naturwissenschaftlichen
Fakultät der Heinrich-Heine-Universität Düsseldorf

Referent: Herr Prof. Dr. Walter Thiel

Korreferentin: Frau Prof. Dr. Christel Marian

Tag der mündlichen Prüfung:

Hiermit versichere ich, die hier vorgelegte Arbeit eigenständig und ohne unerlaubte Hilfe angefertigt zu haben. Die Dissertation wurde in der vorgelegten oder in ähnlicher Form noch bei keiner Institution eingereicht. Ich habe keine erfolglosen Promotionsversuche unternommen.

Mülheim an der Ruhr, den 5. Dezember 2014

(Claudia Loerbroks)

Abstract

This thesis presents a computational analysis of cellulose hydrolysis. Density functional theory (DFT), hybrid quantum mechanics/ molecular mechanics methods (QM/MM), and molecular dynamics (MD) were used to unravel the mechanism of this reaction and of down-stream processes like glucose-fructose isomerization. The main goal was to relate electronic and structural properties to energy barriers and to recommend improvements for the experimental work.

We first studied cellulose hydrolysis in water using a cellobiose model described by density functional theory with implicit solvation (DFT/CPCM). The calculated reaction mechanism involved protonation, conformational change, breaking of the glycosidic linkage, and addition of water to the anomeric carbon atom. This four-step mechanism was found to be preferred over an alternative three-step mechanism by 7 kcal mol⁻¹ due to entropic contributions. The total activation energy and the reaction free energy amounted to 31 and -3 kcal mol⁻¹, respectively. The low basicity of the glycosidic oxygen and the exo-anomeric effect were identified as the main impediments to hydrolysis.

Next we treated the solvent molecules explicitly (QM/MM) to obtain a more realistic picture. We chose cellobiose and a 40-unit glucose chain as cellulose models. While we found the same mechanisms as before, the ability of the explicit solvent molecules to undergo hydrogen bonding with the solute led to differences. Protonated cellulose structures and non-chair conformers were found not to be stable intermediates in most cases. Additionally, the anomeric effect that affects the barriers was influenced by intermolecular hydrogen bonding with water molecules.

After realizing the importance of solvation, we went one step further and investigated the impact of different solvents on cellulose hydrolysis. Considering the major role of conformational changes in the computed mechanisms, we applied MD simulations to the QM/MM models. As solvents we chose water and the ionic liquid 1-ethyl-3-methylimidazolium acetate (EmimAc). According to the simulations, EmimAc is capable of breaking structural and electronic barriers to hydrolysis, because the solvent-solute interactions are stronger than in water. The cellulose chain ends are predicted to be hydrolyzed before the center of the chain because they are better accessible by solvent.

There are many molecules other than glycosides that exhibit the anomeric effect. Spiroaminals are one example. Even though the ring opening reaction of spiroaminals is similar to cellulose hydrolysis, steric effects dominate over the anomeric effect in this case.

The product of cellulose hydrolysis is glucose, which can be converted to fructose. We investigated the glucose-fructose isomerization with different metal catalysts in water using DFT with implicit solvation (CPCM). The following criteria for efficient metal-based catalysts were identified: moderate Brønsted and Lewis acidity ($\text{pK}_a = 4\text{--}6$), coordination of glucose and either water or weaker σ donors as ligands, and energetically low-lying unoccupied orbitals.

Zusammenfassung

Diese Arbeit befasst sich mit der theoretischen Untersuchung der Hydrolyse von Cellulose. Dichtefunktionaltheorie (DFT), kombinierte quantenmechanische / molekularmechanische (QM/MM) Methoden und molekulardynamische (MD) Simulationen wurden verwendet, um den Mechanismus und Folgereaktionen aufzuklären. Ziel ist es, elektronische und strukturelle Eigenschaften mit den Energiebarrieren zu korrelieren und Verbesserungsmöglichkeiten für Experimente aufzuzeigen.

Als erstes untersucht wurde die Hydrolyse von Cellulose durch DFT-Rechnungen mit implizitem Lösungsmittel (Wasser) an einem Cellobiose-Modell. Der Reaktionsmechanismus besteht aus folgenden Schritten: Protonierung, Konformationsänderung, Bruch der glykosidischen Bindung und Addition von Wasser an das anomere Kohlenstoffatom. Ein vierstufiger Mechanismus ist aus entropischen Gründen um 7 kcal mol^{-1} energetisch günstiger als ein dreistufiger Mechanismus. Die Gesamtaktivierungsbarriere beträgt 31 kcal mol^{-1} und die freie Reaktionsenergie -3 kcal mol^{-1} . Die geringe Basizität des glykosidischen Sauerstoffatoms und der exo-anomere Effekt sind der Hauptgrund für die Höhe der Barriere.

Um einen realistischeren Einblick in die Rolle des Lösungsmittels zu gewinnen, haben wir QM/MM Methoden verwendet. Neben dem Cellobiose-Modell wurde eine Cellulosekette mit 40 Glukoseeinheiten in Wasser untersucht. Zwar wurde der gleiche Mechanismus wie in der DFT-Studie gefunden, doch die Wasserstoffbrückenbindungen mit dem Lösungsmittel führten zu Unterschieden. Protonierte und nicht-Sessel-Konformere sind in den meisten Fällen keine stabilen Intermediate. Darüber hinaus wird die Stärke des anomeren Effekts durch intermolekulare Wasserstoffbrücken beeinflusst.

Auf Grund der Wichtigkeit des Lösungsmittels für den Reaktionspfad haben wir für die Modelle aus der QM/MM Studie zwei verschiedene Lösungsmittel mittels MD Simulationen untersucht: Wasser und das ionische Lösungsmittel 1-Ethyl-3-methylimidazoliumacetat. Unseren Ergebnissen zu Folge interagiert das ionische Lösungsmittel stärker mit Cellulose und bricht dadurch die elektronischen und strukturellen Barrieren der Reaktion. Da die Enden einer Cellulosekette leichter für das Lösungsmittel zugänglich sind, sollte die Hydrolyse immer am Ende einer Kette beginnen.

Neben Glykosiden weisen auch andere Moleküle den anomeren Effekt auf; zum Beispiel Spiroaminale. Obwohl der Ringöffnungsmechanismus der Spiroaminale analog zur Hydrolyse von Cellobiose verläuft, dominieren in diesem Fall sterische Faktoren gegenüber dem anomeren Effekt.

Das Produkt der Hydrolyse von Cellulose ist Glukose, welche industriell oft zu Fruktose umgesetzt wird. Wir haben die Glukose-Fruktose-Isomerisierung mittels DFT und implizitem Lösungsmittel für verschiedene Metallkatalysatoren untersucht. Folgende Kriterien wurden für einen effizienten Katalysator gefunden: moderate Brønsted und Lewis Acidität ($\text{pK}_a = 4-6$); die Fähigkeit, Glukose, Wasser oder andere schwache Elektronendonoren als Liganden zu binden; und tiefliegende unbesetzte Orbitale.

List of papers included in this thesis

Paper I

The Electronic Nature of the 1, 4- β -Glycosidic Bond and Its Chemical Environment: DFT Insights into Cellulose Chemistry

Claudia Loerbroks, Roberto Rinaldi, and Walter Thiel, *Chemistry - A European Journal*, **2013**, 19, 16282 – 16294.

Carried out all calculations, analysed the results, and wrote parts of the manuscript

Paper II

Solvent Influence on Cellulose 1, 4- β -Glycosidic Bond Cleavage: A Molecular Dynamic and Metadynamic Study

Claudia Loerbroks, Eliot Boulanger, and Walter Thiel, *Chemistry - A European Journal*, **2014**, submitted.

Carried out all calculations, analysed the results, and wrote the draft of the manuscript

Paper III

Spiroaminals – Crystal Structure and Computational Investigation of Conformational Preferences and Tautomerization Reactions

Claudia Loerbroks, Birte Böker, Jens Cordes, Anthony G. M. Barrett, and Walter Thiel, *European Journal of Organic Chemistry*, **2014**, 25, 5476 – 5486.

Carried out all calculations, analysed the results, and wrote the major part of the manuscript

Paper IV

Reactivity of Metal Catalysts in Glucose–Fructose Conversion

Claudia Loerbroks, Jeaphianne van Rijn, Marc-Philipp Ruby, Qiong Tong, Ferdi Schüth, and Walter Thiel, *Chemistry - A European Journal*, **2014**, 38, 12298 – 12309.

Carried out the majority of the calculations, analysed the results, and wrote the draft of the manuscript

Contents

1	Introduction	1
1.1	Acid Hydrolysis of Cellulose	1
1.2	Anomeric Effect	5
1.3	Down-Stream Processes: Glucose-Fructose Isomerization	6
2	Theoretical Methods	9
2.1	Density Functional Theory	9
2.1.1	Basis Functions	11
2.2	Solvation: PCM and QM/MM	12
2.3	Geometry Optimizations and Dynamics	16
2.4	Natural Bonding Orbitals	19
3	Results and Discussion	21
3.1	Mechanism of Cellulose Hydrolysis	21
3.2	Influence of Solvent on Cellulose Hydrolysis	26
3.2.1	Comparison of Solvent Models	26
3.2.2	Comparison of Solvents: Water and EmimAc	38
3.3	Anomeric Effect in Tautomerism of Spiroaminals	43
3.4	Glucose-Fructose Isomerization	48
3.5	Conclusion	56
4	Bibliography	57
A	Paper I	73

B Paper II	119
C Paper III	133
D Paper IV	157

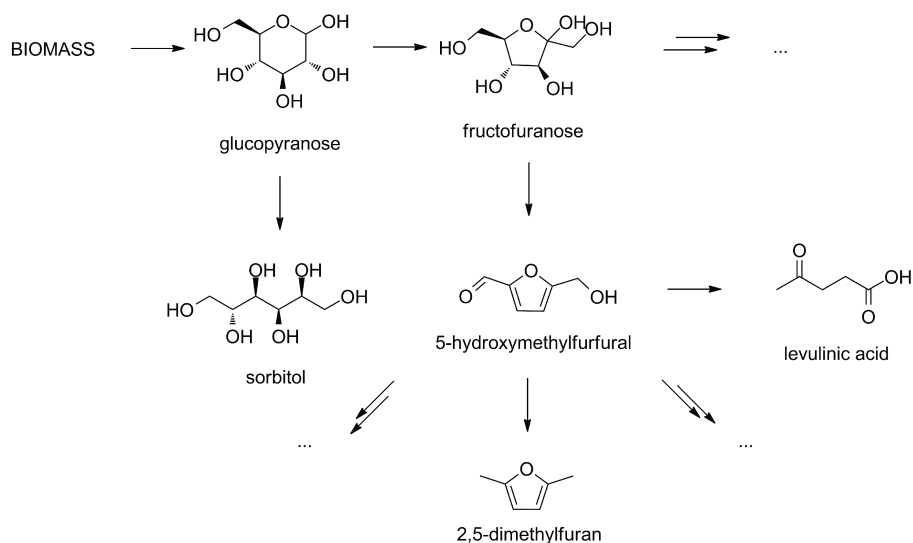
Chapter 1

Introduction

This thesis covers a mechanistic analysis of reactions related to biomass usage. The focus is on the relation between electronic and structural properties and the barrier heights of the mechanisms. An introduction to biomass usage is given, including background information on the relevant reactions and on the results from previous studies. The next chapter describes the theoretical methods applied in this thesis, including density functional theory, implicit and explicit treatments of solvents, natural bonding orbital analysis, and molecular dynamics simulations. Thereafter the computational results are presented and discussed, starting with the mechanism of cellulose hydrolysis, followed by the influence of solvent and the anomeric effect, as well as an investigation of catalysts for glucose-fructose isomerization. The last section contains the publications resulting from this thesis.

1.1 Acid Hydrolysis of Cellulose

Cellulose is like CO₂ an alternative carbon source, which might substitute the world's dwindling coal and oil resources in the future. It can be obtained from biomass, after separation from ligno- and hemicellulose, and transformed to valuable platform molecules used in industry like 2,5-dimethylfuran (Scheme 1.1). In comparison to classical energy sources, cellulose has the advantage of being renewable and of storing CO₂ during its growth. Taken from sources other than crops, like wood or straw, it does not inhibit worldwide food supply.¹ Processes to convert cellulose include acid hydrolysis, enzymatic reactions^{2,3} and pyrolysis.^{4,5} Acid hydrolysis is the process least employed in industry and needs more research to become attractive.⁶ In this thesis acid hydrolysis and



Scheme 1.1: Possible pathways for the formation of platform molecules from biomass.

one down-stream process are investigated computationally in order to get one step closer to industrial usage.

First, we must discuss why acid hydrolysis is not a widely used process. To hydrolyze cellulose in water, high temperatures (> 413 K) and strong acids ($\text{p}K_a < -3$) have to be applied.⁷⁻¹² The overall reaction from cellulose to glucose is exothermic (-3 kcal mol^{-1} in water at 286 to 316 K),¹³ but has high energy barriers (30 to 40 kcal mol^{-1}).¹⁴⁻¹⁶ Several improvements of reaction conditions were made, e.g., the change of solvent from water to ionic liquids,¹⁷⁻¹⁹ the change of catalyst from strong acids like sulfuric acids to solid phase and metal catalysts,^{9,20} and the introduction of up-stream processes like ball milling.²¹

One of the goals of this study is to find the reasons why the barriers to hydrolysis are so high and why the changes mentioned above make the reaction more feasible. For this we have to take a closer look at the structural and electronic properties of cellulose. The structure of cellulose is generally considered to be the main obstacle to hydrolysis.^{6,20,22-29} The most widespread form in nature is cellulose I_β (Figure 1.1). It consists of glucose units in the chair conformation, which are connected by 1,4- β -glycosidic linkages C(1)–O(1) that form long chains.³⁰ Within the chains intramolecular hydrogen bonds (O(3')H \cdots O(5), O(2) \cdots O(6')) exist, while intermolecular hydrogen bonds O(6')H \cdots O(3'') connect the chains.³¹⁻³⁴ In this way large sheets of cellulose chains are created, which are stacked upon each other and connected by van der Waals forces.³¹⁻³⁴

This polymer is not only special due to its three-dimensional network but also

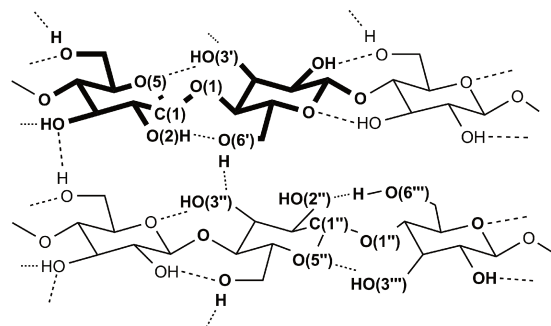


Figure 1.1: Part of the cellulose I_{β} structure. One cellobiose unit marked in bold.

because of its electronic properties, especially the anomeric effect. Generally speaking, the anomeric effect describes the delocalisation of electronic density from a lone pair orbital n of atom X to an anti-bonding orbital σ^* of bond $Y-Z$ ($n(X) \rightarrow \sigma^*(Y-Z)$). The $Y-Z$ bond is aligned in an anti-periplanar arrangement to the lone pair. In cellulose the atoms $O(1)-C(1)-O(5)$ form an acetal moiety and hence there can be two anomeric interactions (Figure 1.2). The first one is the exo-anomeric effect, which describes donation from the $O(1)$ lone pair into the anti-bonding $C(1)-O(5)$ orbital ($n(O(1)) \rightarrow \sigma^*(C(1)-O(5))$). Due to the anti-periplanar alignment this effect exists only in glucose conformations with an equatorial $C(1)-O(1)$ bond, e.g., β -glucose in the 4C_1 conformation; the result is a shortened $C(1)-O(1)$ bond.^{35,36} The second one is the endo-anomeric effect, which involves donation from the $O(5)$ lone pair into the anti-bonding $C(1)-O(1)$ orbital ($n(O(5)) \rightarrow \sigma^*(C(1)-O(1))$) and lengthens the $C(1)-O(1)$ bond. Glucose conformers with an axial $C(1)-O(1)$ bond feature the endo-anomeric effect. Such axial bonds appear after a conformational change from chair to non-chair conformers, like boat (B) or half-boat (H).³⁰ The anomeric effects are not only regulated by ring conformations, but also by the hydrogen bonding situation, as $H \cdots O(Y)-C(1)$ interactions can increase the acceptor strength of $\sigma^*(O(Y)-C(1))$ and $O \cdots O(X)$ interactions can increase the donor strength of $n(O(X))$.

Different mechanisms have been proposed to break the rigid cellulose structure (Scheme 1.2),⁶ all of which include the following steps: protonation of cellulose, cleavage of the glycosidic linkage, and addition of water to $C(1)$. We can distinguish between stepwise (A1), concerted (A2) and barrierless pathways (B). In A1, the $C(1)-O(1)$ bond is first cleaved to form a carbocation intermediate, followed by the addition of water in the next step. In A2, the cleavage of the glycosidic linkage and the addition of water to $C(1)$ occur concomitantly in the same step, without any carbocation intermediate. For A1 there are pathways via cyclic

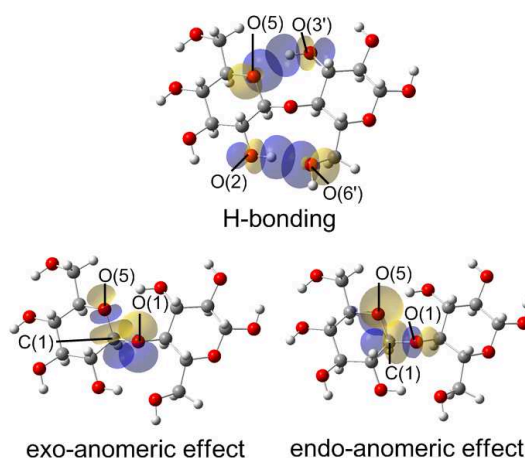


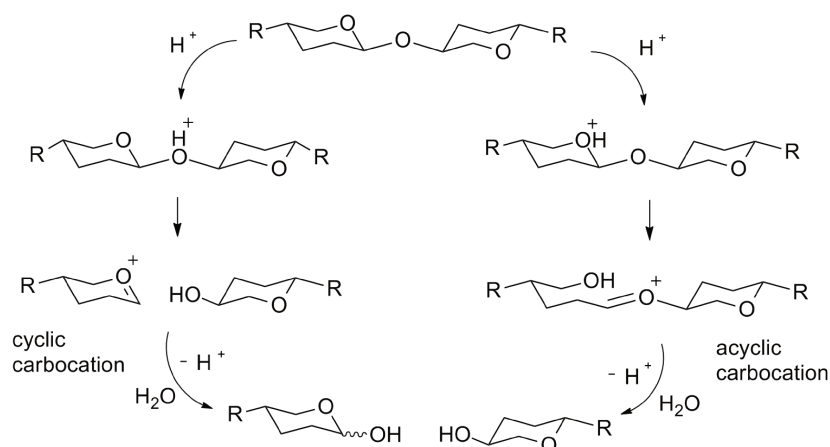
Figure 1.2: Important orbital interactions in cellobiose: hydrogen bonding, exo- and endo-anomeric effect.

carbocations (protonation of O(1) and C(1)–O(1) cleavage) and acyclic carbocations (protonation of O(5), C(1)–O(5) cleavage and then C(1)–O(1) cleavage). Which pathway is taken is decided by the leaving group,^{37,38} the solvent,^{39,40} and the life time of the cations.⁴¹ Earlier experimental studies favor the A1 pathway^{42,43} via a cyclic carbocation^{44–47} for cellulose hydrolysis. Protonation of the glycosidic oxygen O(1), a rapid, equilibrium-controlled process,^{26,48,49} and the formation of the carbocation by cleavage of the glycosidic linkage⁵⁰ have both been suggested as rate-determining steps.

Since cellulose hydrolysis is an important reaction for biomass processing, it has been investigated computationally before. Different computational methods (ab initio,^{51–55} density functional theory,^{39,40} molecular dynamics^{16,19,56–59}), models (dimethoxymethane,⁵⁰ 2-methoxy-tetrahydropyran,⁵² 2-oxanol,⁵⁴ 2-methoxyoxane,⁵⁵ and cellobiose¹⁶) and solvents (water, alcohols, and ionic liquids^{39,57,60,61}) were applied. The proton transfer and the C(1)–O(1) cleavage were identified as critical steps, and a barrier of about 33 kcal mol⁻¹ was reported, consistent with experimental results.^{14,15}

The impact of different solvents was studied focusing mostly on the dissolution of cellulose^{62–66} and less often on the impact of the solvent on the cleavage of the C(1)–O(1) glycosidic linkage.⁶⁷ In ionic liquids, the interaction of anions with hydroxyl groups was proposed to be of importance for stabilizing the reaction products.⁶⁰

Regardless of the chosen model system and solvent, the previous studies addressed a large number of factors that may influence the utilization of cellulose including: the puckering of the non-reducing glucose ring attached to the C(1)–O(1) bond,

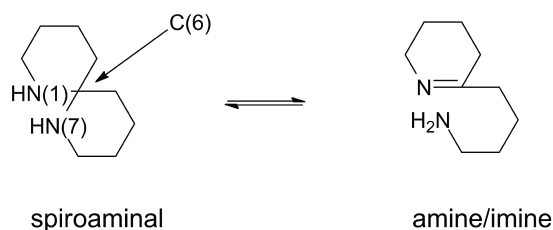


Scheme 1.2: A1 mechanism for cellobiose hydrolysis with cyclic and acyclic carbocation intermediates.

the charge on the C(1) atom, the axial or equatorial position of the C(1)–O(1) bond in the non-reducing ring, intermolecular or intramolecular hydrogen bonds, and the anomeric effect.^{16,64,68–71} However, none of them provided a detailed analysis of the relation between electronic effects (such as the anomeric effect) and the barriers to cellulose hydrolysis.

1.2 Influence of the Anomeric Effect on Other Reactions

Delocalisation of electronic density due to the anomeric effect is found not only in O–C–O systems, but also in the presence of other electronegative donor atoms like nitrogen, for example in spiroaminals (Scheme 1.3). Spiroaminals are the nitrogen analogues of spiroketals, which have often been the subject of experimental and computational investigations.^{72–75} Even though spiroaminals are studied less frequently, their synthesis and reactivity towards electrophiles has been reported recently.⁷⁶ In our study, the focus was on the mechanism of the ring opening reaction that connects spiroaminals with their open-ring tautomers, in which one nitrogen atom is of amine-type and the other one is of imine-type (Scheme 1.3). The C(6)–N(7) bond, which is cleaved in this reaction, is analogous to the O(1)–C(1) glycosidic linkage in cellulose. In spiroaminals the N(1)–C(6)–N(7) group exhibits two anomeric effects with either N(1) or N(7) contributing the donor lone pair: $n(N) \rightarrow \sigma^*(C-N)$. In contrast to oxygen donors, nitrogen atoms are less electronegative and donate into less electron drawing groups than oxygen lone pairs. This leads to three types of hyperconjugation



Scheme 1.3: Tautomerism between aminal and amine/imine.

(different from those considered in cellulose): $n(\text{N}) \rightarrow \sigma^*(\text{C-N})$, $n(\text{N}) \rightarrow \sigma^*(\text{C-C})$, and $n(\text{N}) \rightarrow \sigma^*(\text{C-H})$.

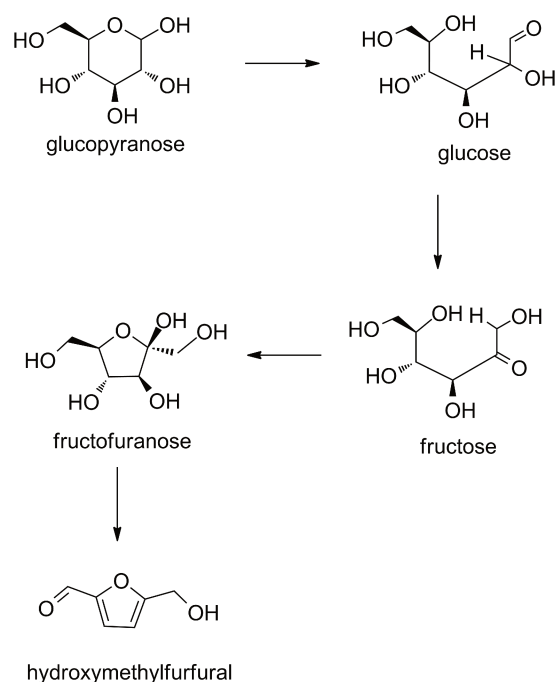
In the literature, the influence of the anomeric effect on spiroaminals has not yet been discussed. We explore its impact on the tautomerism mechanism and provide a comparison with cellulose.

1.3 Down-Stream Processes: Glucose-Fructose Isomerization

The product of cellulose hydrolysis, glucose, is a starting material for the synthesis of many platform molecules like sorbitol and hydroxymethylfurfural, and therefore transformations of glucose are a growing research topic (Scheme 1.1).^{6,22,62-65,77} One reaction of interest in these down-stream processes is glucose-fructose isomerization.⁷⁸ Experimentally the isomerization can be carried out in different solvents (ionic liquids,⁷⁹⁻⁸² organic solvents,⁸³ water⁸⁴⁻⁸⁶) with various catalysts (acids,⁷⁹ metal salts^{79-82,84}). Chromium(III) salts in ionic liquids gave so far the best results.

Two types of mechanisms have been proposed for this isomerization, namely proton (Brønsted acid) catalysis⁸⁵⁻⁸⁹ and Lewis acid catalysis in water.⁹⁰ The mechanism of the isomerization has been studied for different Lewis acids in ionic liquids. Density functional theory was applied using CrCl_2 ,^{91,92} CrCl_3 ,^{92,93} FeCl_2 ,⁹² FeCl_3 ,⁹³ CuCl_2 ,⁹² WCl_3 ,⁹³ MoCl_3 ,⁹³ and SnCl_4 ⁹⁴ as catalysts. Some of these studies concluded that a dimeric complex catalyzes the reaction better than a monomeric catalyst and that chloride and hydroxyl ligands facilitate proton transfers during the reaction. The rate-determining step and its barrier height was found to depend on the chosen metal: For CrCl_3 a hydrogen shift with a barrier of about 16 kcal mol^{-1} was identified.⁹² Other metal catalysts, FeCl_2 and CuCl_2 ,⁹² were considered inactive, because of unfavorable glucose catalyst coordination. Moreover, a kinetic study suggested that the isomerization

1.3. DOWN-STREAM PROCESSES: GLUCOSE-FRUCTOSE ISOMERIZATION⁷



Scheme 1.4: Mechanism of the glucose-fructose isomerization.

is catalyzed not only by the Lewis acidity of CrCl_3 , but also by the Brønsted acidity of its metal-water complex.⁹⁵

Computationally the mechanism of the isomerization has only been studied in ionic liquids so far. Nevertheless, water is a more abundant and economic solvent. Therefore our goal was to explain the different activity of metal salt catalysts in water and to predict possible improvements.

So far a lot of experimental research has been done on reactions related to biomass usage. Our computational study aims at complementing the available experimental knowledge and at providing insights that may guide future experimental work. In the following section the applied computational tools are described.

Chapter 2

Theoretical Methods

In this chapter we introduce the different theoretical methods that have been used to study the main topics of this thesis, reaction mechanisms and conformational changes. We explored the utilization of biomass with many different methods to obtain a comprehensive picture. An efficient method to investigate reaction mechanisms for small molecules (50–100 atoms) is density functional theory (DFT, Section 2.1) with implicit solvent (Polarizable Continuum Model, PCM, Section 2.2). For larger systems and an explicit treatment of solvent effects, a combination of quantum mechanics with molecular mechanics (QM/MM, Section 2.2) was applied. Molecular dynamics (MD) simulations (Section 2.3) were performed to inspect conformational preferences and changes. To characterize the electronic structure of intermediates, the bonding situation was analyzed using natural bonding orbitals (NBO, Section 2.4).

The basic features of all these methods will be described below. For more detailed information we refer to standard textbooks on theoretical chemistry.^{96–101}

2.1 Density Functional Theory

In density functional theory, one aims at directly computing the one-electron density of the system, rather than the wave function as in *ab initio* methods. This reduces the number of relevant coordinates in an n -electron system from $4n$ to 3 and thus simplifies the computation significantly.

Hohenberg and Kohn¹⁰² proved (a) that every ground-state density results in a different potential $\nu(r)$ and a different wave function and (b) that there exists one universal functional, which will provide the lowest (exact) ground-state

energy for all systems. Because of this mapping between the wave function and the density, the total energy of the ground state can in principle be calculated exactly from the density. The total electronic energy is composed of the potential energy due to the external potential $\nu(r)$, which can be calculated classically, and the sum $F[\rho]$ of the kinetic energy of the electrons and electron-electron interactions (2.1.2). However, the universal functional is yet unknown. In general, functionals contain three terms that account for kinetic energy $T[\rho]$, nuclei-electron attractions $E_{ne}[\rho]$, and electron-electron repulsions $E_{ee}[\rho]$.

$$E[\rho] = \int \rho(r)\nu(r)dr + F[\rho] \quad (2.1.1)$$

$$F[\rho] = T[\rho] + E_{ee}[\rho] \quad (2.1.2)$$

The first term $T[\rho]$ is difficult to approximate and is not directly accessible so far. The second term $E_{ee}[\rho]$ is made up of Coulomb, exchange, and correlation contributions. The Coulomb part $J[\rho]$ can be computed classically, unlike the latter two contributions. The search for approximate functionals connecting density and energy is a topic of intense ongoing research.

A pragmatic approximation for the kinetic energy was introduced by Kohn and Sham.¹⁰³ $T[\rho]$ can be calculated exactly (as in wave function theory), if one assumes a reference system with non-interacting electrons that has the same density as the real (interacting) system, for the same external potential. This new term $T_S[\rho]$ is expected to be close to the exact kinetic energy of interacting electrons. The (small) difference from the exact kinetic energy is incorporated into the exchange-correlation term E_{XC} , which represents the non-classical part of the electron-electron interactions (exchange and correlation); the main contribution to E_{XC} comes from the exchange interactions. Hence, the whole energy functional can be written as:

$$E[\rho] = \int \rho(r)\nu(r)dr + T_S[\rho] + J[\rho] + E_{XC}[\rho] \quad (2.1.3)$$

$$\text{with } E_{XC} = T[\rho] - T_S[\rho] + E_{ee} - J[\rho]. \quad (2.1.4)$$

The electronic energy $E_{DFT}[\rho]$ can be calculated variationally for a Kohn-Sham determinant built from orthogonal orbitals, by introducing a Lagrange operator and optimizing the orbitals iteratively. One thus obtains canonical Kohn-Sham orbitals from the pseudo-eigenvalue Equation 2.1.5:

$$[-\frac{1}{2}\nabla^2 + \nu_{\text{eff}}(r_i)]\phi_i = \epsilon_i\phi_i \quad (2.1.5)$$

The remaining unknown is the exchange-correlation term $E_{XC}[\rho]$. The local

density approximation (LDA) is the simplest way to handle $E_{XC}[\rho]$. It approximates the electron density as a homogenous electron gas of the density ρ . An extension is the local spin density approximation. It takes different spin states into consideration and sums up the individual spin densities.

In order to improve LDA one considers a non-homogenous electron gas by introducing reduced density derivatives. Many different GGA functionals have been developed. Popular examples include the exchange functionals of Perdew and Wang¹⁰⁴ and of Becke¹⁰⁵ and the correlation functional of Lee, Yang and Parr (LYP).^{106,107} A further generalization are meta-generalized gradient approximations (MGGA). Such MGGA functionals also include second derivative terms of the electron density.

Another approach to improve the exchange-correlation treatment is pursued by the hybrid methods. They provide a link between Hartree-Fock theory and DFT, by including some fraction of the exactly computed exchange term from wave function theory in the exchange-correlation functional $E_{XC}[\rho]$. An example is the Becke-3-parameter-functional B3LYP,¹⁰⁸ in which the coefficients α , β and γ are fitted to experimental data:

$$E_{XC}^{B3} = (1 - \alpha)E_X^{LSDA} + \alpha E_X^{\text{exact}} + \beta E_X^{B88} + E_C^{LSDA} + \gamma E_C^{GGA}. \quad (2.1.6)$$

In our work we mainly used hybrid functionals: the BB1K functional¹⁰⁹ for the study of cellobiose (Appendix A), the PBE0 functional¹¹⁰ for the calculation of down-stream processes (Appendix D), and the M06-2X functional¹¹¹ for the investigation of spiroaminals (Appendix C). In each case, the functional was chosen on the basis of relevant benchmark studies,^{110,112–119} and the results were compared to those from other functionals for further validation (see respective papers and the associated Supporting Information in the appendices). In some cases, dispersion corrections were added to the Kohn-Sham energy.¹¹¹

2.1.1 Basis Functions

Traditionally, two types of basis functions are used: Slater-type orbitals (STO)¹²⁰ and Gaussian-type orbitals (GTO),¹²¹ in spherical or cartesian coordinates. STOs have a realistic shape resembling hydrogen-like orbitals, whereas GTOs exhibit an incorrect shape close to and far away from the nucleus. However, many-center integrals can be calculated analytically for GTOs and normally only numerically for STOs. To combine the advantages of both choices, several GTOs (primitive GTOs) can be fused into one STO-like basis function (contracted GTOs) by a proper linear combination.

A collection of basis functions is called a basis set. The simplest version is the minimal basis set, with one basis function per atomic orbital, in which the core and valence regions are commonly represented by the same number (n) of primitive GTOs (STO- n G).¹²² The split-valence basis sets are an obvious improvement: here the valence electrons are described by more basis functions (double- ζ , triple- ζ , ...). Polarization functions can be added to improve flexibility and to capture anisotropy.^{123,124} Multiple families of basis sets are commonly used in practice, including Pople basis sets of the form x-yzG (number of primitive GTOs for core (x) and for valence electrons (y, z)), Ahlrichs basis sets (SVP, TZVP, QZVP, ...),^{125,126} and Dunning basis sets (cc-pVnZ, correlation-consistent polarized valence n- ζ basis).^{127,128}

In our study we used several Pople basis sets (Appendix A and D) and Ahlrichs basis sets (Appendix C). Basis sets with diffuse functions were employed whenever needed for the proper description of intramolecular hydrogen bonds.¹¹²

2.2 Solvation: PCM and QM/MM

Solvent effects are of importance for most chemical reactions. A pure QM description of all solvent molecules would be prohibitively expensive. Two types of approximations for simulating solvent effects are affordable: implicit solvation using dielectric continuum theory, and explicit solvation using QM/MM methods with a force field treatment for the bulk solvent molecules. Both types are discussed in the following.

Polarizable Continuum Model

One of the computationally least demanding methods is implicit solvation by a polarizable continuum model (PCM) or a conductor-like polarizable continuum model (CPCM).^{129,130} In these models the solute is placed in a cavity with a dielectricity constant of 1, which is surrounded by a dielectric continuum with the permittivity ϵ . The definition of the cavity may be different for different models. In most cases it consists of spheres centered on atoms or groups of atoms. In general, the free solvation energy in the CPCM model can be written as:

$$\Delta G_{solv} = \Delta G_{el} + \Delta G_{cav} + \Delta G_{dis} + \Delta G_{rep} \quad (2.2.1)$$

The terms describe the free energy contributions arising from electrostatic interactions ΔG_{el} , the generation of non-spherical cavities ΔG_{cav} , dispersion ΔG_{dis} , and repulsion ΔG_{rep} . Other terms accounting for volume changes or

different partition functions are in most cases so small that they do not influence the results and are therefore neglected in most PCM and CPCM methods. The generation of the cavities may employ radii optimized for a given approach (e.g. united-atom topology model optimized for HF/6-31G(d)) or taken from standard van der Waals values (e.g. PAULING, van der Waals values from Pauling atomic radii). These models have the drawback that they do not account for specific solute-solvent interactions such as hydrogen bonds and that they neglect entropic effects.

In our work we used the CPCM model with united force field radii, which is established as one of the best models for treating cationic and neutral species,¹³⁰ and the solvation density model (SMD) for the calculation of ΔG_{solv} in thermodynamic cycles.¹³¹ More detailed information on the chosen solvation models can be found in the Supporting Information of Appendix A and D.

Hybrid Quantum Mechanics / Molecular Mechanics Method

The drawbacks of continuum models may be overcome by hybrid quantum mechanics / molecular mechanics approaches (QM/MM). QM methods were already outlined in Section 2.1. Here we will first focus on MM methods and then address the QM/MM combination.

Force Fields

Force fields use classical mechanics to treat particle-particle interactions in order to calculate the potential energy of a system. In general, force fields are employed in molecular dynamics (MD, see Section 2.3) or Monte-Carlo simulations to explore conformational changes in large chemical or biological systems.¹⁰¹ By themselves force fields are not able to describe reaction mechanisms, since they usually do not allow for bond breaking.

They can be classified into three kinds: all-atom force fields, united-atom force fields, and coarse-grained models. All-atom force fields treat each atom individually and thus require parameters for every atom type. United-atom force fields combine certain heavy atoms with the connected hydrogen atoms into single interaction centers (e.g., for CH₂ groups), thus reducing the number of degrees of freedom for simulations. Coarse-grained models go even further in this regard, by condensing even larger moieties into a single bead (e.g., four water molecules). For a given application, one has to weigh computational efficiency against the required level of detail and accuracy when choosing the force field.

Typical force field potentials include terms for bonded (bonds, angles, dihedrals)

and for non-bonded interactions (electrostatic, van der Waals forces). As an example, Equation 2.2.2 gives the energy expression for the all-atom AMBER force field,¹³² which includes the following terms: harmonic potentials for bond lengths r and bond angles θ , a periodic term for dihedral angles χ , the standard Lennard-Jones potential for van der Waals interactions, and the Coulomb potential for the electrostatic interactions. Variables k denote force constants, subscripts 0 refer to equilibrium, i and j are labels for atoms, n specifies the order of the rotational barrier for dihedrals, and δ denotes the phase shift.

$$V_{\text{pot}} = \sum_{\text{bonds}} k_b(r - r_0)^2 + \sum_{\text{angles}} k_\theta(\theta - \theta_0)^2 + \sum_{\text{dihedrals}} \frac{1}{2}k_\chi[1 + \cos(n\chi - \delta)] \\ + \sum_{i=1}^{N-1} \sum_{j>i}^N \left(\epsilon_{ij} \left[\left(\frac{r_{\text{min},ij}}{r_{ij}} \right)^{12} - 2 \left(\frac{r_{\text{min},ij}}{r_{ij}} \right)^6 \right] + \frac{q_i q_j}{4\pi\epsilon_0 r_{ij}} \right) \quad (2.2.2)$$

Force field parameters are commonly generated either from theoretical data (e.g., using ab initio results for geometries $(r_0, \theta_0, \chi, r_{\text{min},ij})$, vibrational frequencies (k_b, k_θ) , and partial charges (q_i, q_j)) or from experimental data (e.g., spectroscopy and crystal structures). Additionally, force fields can include special terms and/or special parameters to take into account specific electronic effects: for example, the anomeric effect is very important in carbohydrates, and therefore it is included in the GLYCAM force field via adapted charges.^{133,134}

As hydrogen bonding is important in biomass, we used all-atom force fields throughout. Glycosides were described by the GLYCAM06 force field, which has been demonstrated to give good results in comparison with other force fields and which also takes the anomeric effect into account.¹³⁵ Water was represented by the TIP3P model, and the general Amber force field (GAFF) was used for the ionic liquid EmimAc, in view of its thorough validation in previous studies.^{57,133,136} As GLYCAM06 and GAFF are Amber-type force fields they are compatible.

Combining QM and MM Methods

Hybrid Quantum Mechanics / Molecular Mechanics (QM/MM) methods allow the detailed study of reaction mechanisms with explicit solvent in a reasonable time frame.^{137–139} This approach takes advantage of the accuracy of QM methods for calculating reactions in the active site (QM region) and of the efficiency of MM methods for providing a realistic treatment of the environment (MM region).

There are two main approaches to calculate the QM/MM energy: In the sub-

tractive model, the MM energy is calculated for the whole system and the MM energy for the QM region is then replaced by the corresponding QM energy; the accuracy of this approach depends on the quality of the (non-standard) MM parameters for the QM region. In the additive model, the energy of the QM and MM regions are calculated by QM and MM theory, respectively, and the QM-MM interaction energies are evaluated explicitly using one of the available embedding schemes (see below); the sum of the three terms is the QM/MM energy. The additive model is more flexible and generally considered to be more accurate.

The choice of an optimal QM region is crucial for the quality of QM/MM calculations. The QM region should include all atoms relevant to the reaction, but still be small enough to keep the computation time reasonably low. Ideally, no covalent bonds should be cut when defining the QM and MM regions. If this is unavoidable, one should try to cut unpolar bonds, preferably such that the charge groups in the MM region are kept intact to preserve the overall MM charge distribution.

Cuts through covalent bonds at the QM-MM boundary require special measures for compensation both at the QM and MM level. To satisfy the valency in the QM treatment of the QM region, one may use frozen orbitals to represent the bond being cut or one may add a link atom, for example a hydrogen atom or a specially parametrized atom.¹⁴⁰ In addition, to avoid electrostatic artifacts, one normally also modifies the MM charges close to the QM-MM boundary. Several approaches are available for this purpose (e.g., deleting nearby MM charges, removing certain one-electron integrals involving the link atom, representing MM charges as a Gaussian distribution, etc.). We adopted the charge shift scheme, where the charge of the MM atom next to the link atom is set to zero and re-distributed to the surrounding MM atoms so that the net charge is conserved; the resulting change in the bond dipoles is compensated by adding two extra charges at the corresponding MM atoms.^{141,142}

The non-bonded interactions between the QM and MM regions can be treated by mechanical, electrostatic, or polarized embedding. In mechanical embedding, the QM region is treated as in vacuum and the non-bonded terms are evaluated at the MM level. In electrostatic embedding, the van der Waals interactions are still handled by MM, but the MM charges are included in the QM Hamiltonian so that the QM wave function can respond to the polar environment. In polarized embedding, the back-polarization of the MM environment is taken into account.¹⁴³

In our work we used the additive model, the hydrogen link atom approach com-

bined with the charge shift scheme, and electrostatic embedding as implemented in ChemShell.^{144,145}

In this subsection, we have discussed the advantages and drawbacks of implicit and explicit solvation treatments in general terms. A direct comparison between DFT/CPCM results (section 3.1) and DFT/MM results (section 3.2) has been performed in the case of cellulose hydrolysis (see Results and Discussion, pages 21 and 26).

2.3 Geometry Optimizations and Dynamics

The methods discussed so far can be applied to generate potential energy surfaces (PES). The energy of stationary points on the PES can be approximated as a Taylor series around the point R_0 .

$$E_{\text{tot}}(R) = E_{\text{tot}}(R_0) + \mathbf{g}^T(R - R_0) + \frac{1}{2}(R - R_0)^T \mathbf{H}(R - R_0) + \dots \quad (2.3.1)$$

where \mathbf{g} and \mathbf{H} are the gradient and the Hessian matrix at point R_0 , respectively.

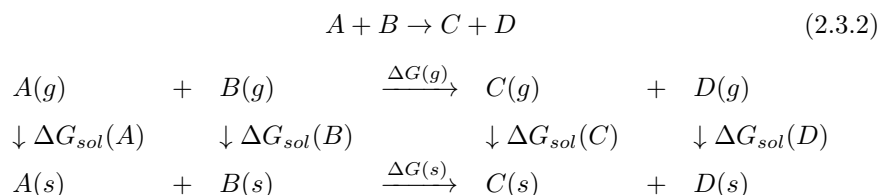
In geometry optimizations using the Newton-Raphson method, the expansions are truncated after the quadratic term. In the case of harmonic potentials, the nearest exact stationary point is reached by one single Newton-Raphson step. The QM calculation of the Hessian matrix is expensive. Therefore one normally makes a guess for \mathbf{H} that is recursively improved in every iteration (pseudo-Newton-Raphson method). The convergence of the geometry optimization is influenced not only by the approximation used for the Hessian matrix, but also by a number of other factors (initial geometry, choice of coordinates, etc.).

The character of optimized stationary points can be verified by diagonalizing their Hessian matrix. For a minimum, all eigenvalues are positive, while there is exactly one negative eigenvalue for a transition state. The connection between a transition state and the associated minima can be established by intrinsic reaction coordinates (IRC) calculations. They follow the steepest-descent path of lowest energy in mass-weighted Cartesian coordinates.^{146,147}

In the commonly applied IRC algorithm, the Hessian matrix is only calculated at the transition state, and the following IRC steps are made using only gradient information (using an appropriate update of the Hessian).¹⁴⁶ Such IRC calculations do not capture tunneling and the influence of excited vibrational modes. If there are very weak imaginary modes ($< 100i \text{ cm}^{-1}$), the IRC algorithm often fails to follow such modes downhill. In such cases one may modify the IRC step manually or carry out a simple PES scan.

The electronic energy of optimized minima and transition states cannot be compared directly with experiment. To account for zero-point vibrational energies, one has to add the zero point correction (ZPC) which is commonly evaluated in harmonic approximation. To model the actual temperatures and pressures in the experimental work, one has to include the appropriate thermal and entropic contributions to compute the Gibbs free energy, which is again normally done with the rigid-rotor harmonic-oscillator approximation.

For condensed-phase reactions it is sometimes not possible to calculate accurate free energy differences $\Delta G(s)$ in this manner, e.g. for protonation reactions or when bringing reactants together from infinity. In such cases, thermodynamic cycles involving the relevant reaction may be used instead (Equation 2.3.2).^{148,149} The required solvation energies ΔG_{sol} of the reactants and products as well as their gas-phase energies may be determined by experimental or computational means (see Section 2.2).



If two reactions compete with each other, kinetic control will yield the product reached via the lower transition state (at low temperatures), while thermodynamic control will lead to the more stable product (at high temperatures). The product ratio depends on the energy difference between the two relevant points and can be determined from the Boltzmann distribution:

$$\frac{N_i}{N_j} = e^{-\frac{\Delta E_{(j-i)}}{kT}} \quad (2.3.3)$$

More detailed information on IRC calculations and thermodynamic cycles can be found in the Supporting Information of Appendix A.

Molecular Dynamics and Metadynamics Simulations

For complex potential energy landscapes (e.g., in condensed-phase reactions with many degrees of freedom), properties such as free energy differences can often no longer be obtained accurately with static approaches such as geometry optimizations. In such cases a sampling method has to be used. The most popular approach in the force field community is molecular dynamics (MD). In MD simulations the atomic coordinates are propagated in time using Newton's

equations of motions. The system is first equilibrated (e.g., to a given temperature or pressure) and then subjected to a production run, in which the properties of the system are calculated and averaged over time. For condensed-phase systems, MD simulations are often done with periodic boundary conditions. In this approach the system is duplicated in all directions to infinity so that there are long-range interactions with all other particles from the original and the duplicated systems. To avoid excessive computational costs, one usually introduces a truncation so that two-particle interactions are calculated only up to a certain cut-off distance r . In MD simulations the potentials are generally not only truncated but also shifted such that the potential becomes zero at distance r (to avoid discontinuities that would require even more complicated corrections).

A problem in the investigation of conformational changes in MD simulations is that the available simulation time is shorter than the real (natural) time of the investigated process. This can be due to high free energy barriers or to a large number of conformational arrangements that cannot be visited often enough for a proper statistical evaluation. This drawback may be overcome in metadynamics simulations.¹⁵⁰ This is a technique that can be applied together with MD simulations to calculate free energy surfaces as a function of well-chosen parameters. These parameters are called collective variables (CV) and can for example be reaction coordinates or dihedral angles. Mathematically one can define a set of CVs:

$$S(R) = (S_1(R); \dots, S_d(R)) \quad (2.3.4)$$

The basic idea of metadynamics is to add a Gaussian bias potential to the actual potential during the MD simulation in order to decrease the likelihood of visiting previous points again. The bias potential V_G at time t is given by:

$$V_G(S, t) = \int_0^t dt' \omega \exp \left(- \sum_{i=1}^d \frac{(S_i(R) - S_i(R(t')))^2}{2\sigma_i^2} \right) \quad (2.3.5)$$

In this equation ω is the energy rate, which describes the height of the Gaussian potential and the distance between the Gaussian potentials. The term σ_i is the width of the Gaussian, and i is the label of the collective variable S . Accordingly, Gaussians will be first added to the parts of the potential surface where the free energy ($A'(S) = A(S) + V_G(S, t)$) is lowest. In metadynamics simulation, conformations that have been explored before, are artificially destabilized and will thus less likely be visited again. When the full free energy landscape is filled with Gaussians, $-V_G(S, t)$ is a good approximation for the free energy. Variables like ω can be set by the user; their choice involves a compromise between the

accuracy of the resulting free energy landscape and the computational effort. Apart from accelerated sampling, one major advantage of metadynamics is that it requires no knowledge about the potential before the simulation. However, it may be complicated to find the optimum CV(s) for a given application and the right moment to stop the calculations. Metadynamics simulations should in general be stopped when the desired saddle point is found or when all relevant conformations are explored.

We performed metadynamics simulations in addition to molecular dynamics in our work on solvent effects, since it is known that ionic liquids may stabilize certain conformers over nanoseconds.¹⁵¹ We used the NAMD code¹⁵² for molecular dynamics and metadynamics simulations, both of which led to similar conclusions (Appendix B). Non-bonded interactions were truncated at a cut-off distance of 12 Å. The collective variables (dihedrals) were chosen in analogy to previous work.¹⁵³

2.4 Natural Bonding Orbitals

We used natural bonding orbitals (NBOs) to analyze the electron density distribution.^{154–156} Natural orbitals can help to visualize bonding concepts such as atomic charges, polarity of bonds, Lewis structures, bond types, hybridization or charge transfer. Compared with conventional canonical molecular orbitals (MOs) NBOs are non-degenerate, localized, and cannot be subjected to arbitrary unitary transformations. Moreover, they are known to be rather insensitive to the chosen basis set or method (e.g., functional).

Two types of natural orbitals can be distinguished: (a) Lewis-types (L-types) including electron donors like 1-center lone pairs n_A , core orbitals c_A , and 2- or 3-center bond pairs (Ω_{AB} , τ_{ABC}); and (b) non-Lewis types (nL-types) including electron acceptors like delocalized pairs (Rydberg orbitals r_A , anti-bonding bond pairs (Ω^*_{AB} , τ^*_{ABC})). A high occupancy is a sign for an L-type orbital, while a population close to zero is characteristic of nL-types; the occupations can adopt values between 0 and 2 according to the Pauli exclusion principle.

The more electron density is covered by the L-type orbitals and the less is covered by the nL-types, the better is the description by a Lewis structure. In well-behaved systems, less than 1% of total density is found in nL-type orbitals, and a single Lewis structure is dominant. If the percentage is larger, donor-acceptor interactions can be assumed, which can be qualitatively investigated by second-order perturbation theory and the associated energy terms $\Delta E_{i \rightarrow j}^{(2)}$. These interactions can also be visualized as possible resonance structures. The

term $\Delta E_{i \rightarrow j^*}^{(2)}$ indicates the energy gained from the interaction between donor orbital (energy ϵ_i) and acceptor orbital (energy ϵ_{j^*}). Mathematically, it can be derived from perturbation theory by writing the Hamiltonian operator as a sum of perturbed one-electron Fock operators $F^{(\text{pert.})}$. The resulting interaction energy is given by:

$$\Delta E_{i \rightarrow j^*}^{(2)} = -2 \frac{\langle \Theta_i^{(0)} | \mathbf{F} | \Theta_j^{(0)} \rangle^2}{\epsilon_i^{(0)} - \epsilon_{j^*}^{(0)}} \quad (2.4.1)$$

The prefactor stems from the orbital occupation number, which is two in the case of a donation from an L-type to an nL-type orbital.

After this survey over the wide range of computational methods used, we now move to the Results and Discussion section, which also includes comparisons between the applied methods and evaluations of their performance with respect to the available experimental data.

Chapter 3

Results and Discussion

The objective of this thesis is to answer the following questions about biomass conversion:

1. Why is the barrier for cellulose hydrolysis so high?
2. What is the effect of solvents on the hydrolysis mechanism?
3. Which role does the anomeric effect play for hydrolysis and other mechanisms?
4. Why do some Lewis acids catalyze one of the down-stream processes of hydrolysis, glucose–fructose isomerization, better than others?

To answer these questions we studied cellulose hydrolysis with DFT, MD simulations, and QM/MM methods. We considered different cellulose models (cellobiose, cellulose chain with 40-glucose units) and solvents (water and the ionic liquid 1-ethyl-3-methylimidazolium acetate (EmimAc)). The anomeric effect was explored for acetal (O–C–O) and aминаl (N–C–N) systems. The glucose–fructose isomerization was investigated with different metal salts in water. The main results of the study are summarized here, while the complete results and discussion can be found in the publications (Appendix A to D).

3.1 Mechanism of Cellulose Hydrolysis

In order to identify the main obstacles to cellulose hydrolysis, we study the mechanism for the cellulose model cellobiose (Figure 3.1) in water using DFT (BB1K/6-31++G(d,p)) and an implicit solvation model (CPCM) (see Appendix A). In

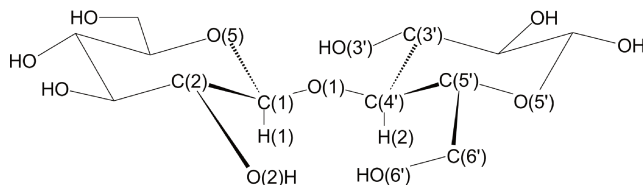


Figure 3.1: Atom numbering used in cellobiose structures.

this endeavor we first scrutinized the factors that might influence hydrolysis prior to the actual C(1)–O(1) bond cleavage, in particular the different conformations and the possible protonation processes in cellobiose. Afterwards the mechanism itself was explored.

Conformers were analyzed with regard to their anomeric effects ($n(\text{O}(1)) \rightarrow \sigma^*(\text{C}(1)\text{--O}(5))$, $n(\text{O}(5)) \rightarrow \sigma^*(\text{C}(1)\text{--O}(1))$), the dihedral angle ϕ ($\text{O}(5)\text{--C}(1)\text{--O}(1)\text{--C}(4')$), the bond lengths C(1)–O(1) and C(1)–O(5), as well as hydrogen bonding ($\text{O}(2) \cdots \text{O}(6')$, $\text{O}(3)\text{H} \cdots \text{O}(5')$). We chose conformers that are expected to be present in crystalline (**1–4**) and amorphous cellulose units (**5,6**) (see Figure 3.2). Conformations **1–4** differ with regard to $\text{O}(2) \cdots \text{O}(6')$ hydrogen bonding, while in **5** and **6** the glucose units are twisted against each other. Amorphous cellulose units are known to hydrolyze more easily than crystalline units.⁶ Also, to investigate the influence of hydrogen bonding, the hydroxyl groups O(3') and O(6') were substituted with methyl groups in structure **1** (**7–9**).

The differences between the two types of cellulose units are evident in Table 3.1. Crystalline conformers (**1–4**) are close in relative free energy and more stable than their amorphous counterparts by 8 to 9 kcal mol⁻¹ (**5,6**). We find that the exo-anomeric effect is reduced to one third going from crystalline (18 kcal mol⁻¹) to amorphous regions (6 kcal mol⁻¹), but is never fully suppressed. When the intramolecular hydrogen bonds are broken by methyl substitution (**7–9**) the crystalline conformation is retained (no rotation around the glycosidic linkage, see ϕ values), and the exo-anomeric effect remains strong (18 kcal mol⁻¹). As will be shown later, this is due to the use of an implicit solvent model that does not capture the influence of intermolecular solute-solvent hydrogen bonds (see Section 3.2.1). A reduced exo-anomeric effect is connected with an elongated glycosidic linkage: for example, when the exo-anomeric effect is reduced by two thirds (**1** versus **5**), the C(1)–O(1) bond is elongated by about 1 % (0.02 Å).

The protonation at O(1) is also important for the activation of the glycosidic linkage. However, cellulose has many oxygen sites close to O(1), which compete for the proton: O(2), O(3'), O(5) and O(6'). We calculated the energies needed to protonate the conformers mentioned above (**1–6**) at different proto-

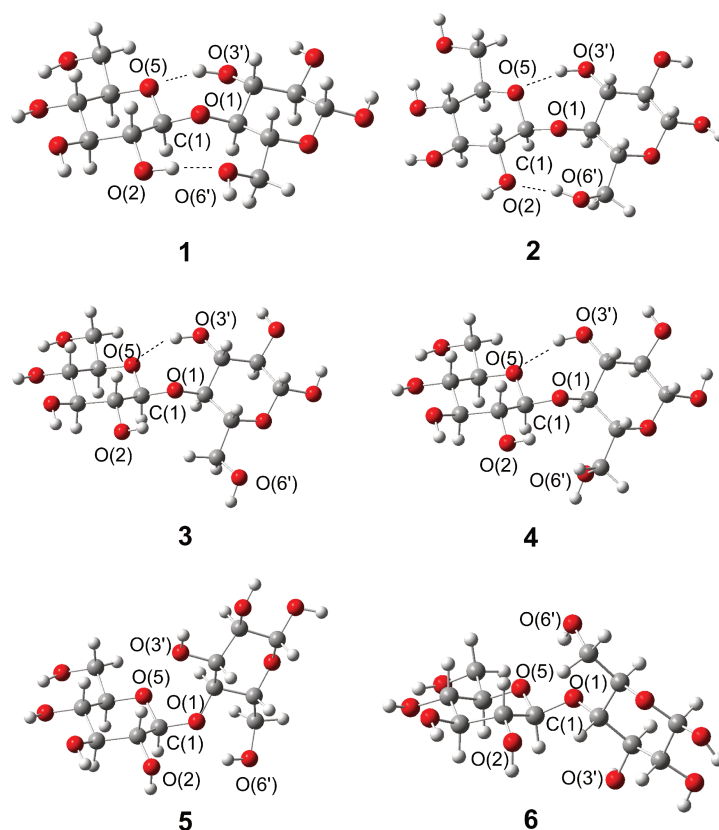


Figure 3.2: Cellulose structures found in crystalline (**1–4**) and amorphous (**5,6**) regions of cellulose.

nation sites (Table 3.2). For O(1) and O(5) two possibilities exist in principle: protonation at the axial or equatorial lone pair. However, protonation of the equatorial position does not yield stable species, and hence we consider only the axial position. It turns out that O(1) is the least favorable protonation site in all conformers, while O(3') and O(6') are the most favorable due to hydrogen bonding with other hydroxyl groups. O(6'), the most basic hydroxyl group, can abstract an added proton from O(1) in a barrierless process, making protonation of O(1) unlikely in the presence of an O(2)···O(6') hydrogen bond. Only for amorphous structures (**5,6**), the protonation energy of O(1) is in the same range as that of O(5).

In addition, the protonation of O(1) affects the structures of the conformers more than the protonation of other oxygen sites, by elongating the C(1)–O(1) bond and reducing the exo-anomeric effect. For example, in structure **10** (Table 3.1, O(1) protonated) the C(1)–O(1) bond is elongated by 0.09 Å and the exo-anomeric effect is reduced by 12 kcal mol⁻¹ compared to **16**, in which O(6') is protonated.

Table 3.1: Gibbs free energies $\Delta\Delta G$ in kcal mol⁻¹ relative to structure **1**, selected geometric parameters and NBO energies E(2) in kcal mol⁻¹ for structures **1–10** and **16–19** (BB1K/6-31++G**, CPCM(water)).

type	Structure	$\Delta\Delta G$	$\phi/^\circ$	Bond length / Å		E(2)	
				C(1)–O(1)	C(1)–O(5)	exo	endo
crystalline	1	0.0	-92	1.38	1.41	18	4
	2	-1.1	-90	1.37	1.41	18	4
	3	0.3	-78	1.37	1.41	18	4
	4	-0.4	-74	1.38	1.41	17	4
amorphous	5	7.5	0	1.40	1.39	7	5
	6	9.1	180	1.40	1.40	6	5
substituted OH-groups	7	–	89	1.37	1.41	18	5
	8	–	-76	1.37	1.41	18	4
	9	–	-75	1.37	1.41	18	4
protonated	10	–	-105	1.47	1.37	5	8
	16	–	-94	1.38	1.40	17	2
non-chair structures	17	–	–	1.50	1.35	7	29
	18	–	–	1.58	1.33	3	40
	19	–	–	1.55	1.34	6	37

The free energy barrier for protonation of O(1) (**1**→**10**), which is the first step of the hydrolysis mechanism, was calculated using a thermodynamic cycle, which gave a free energy difference of 28 kcal mol⁻¹.

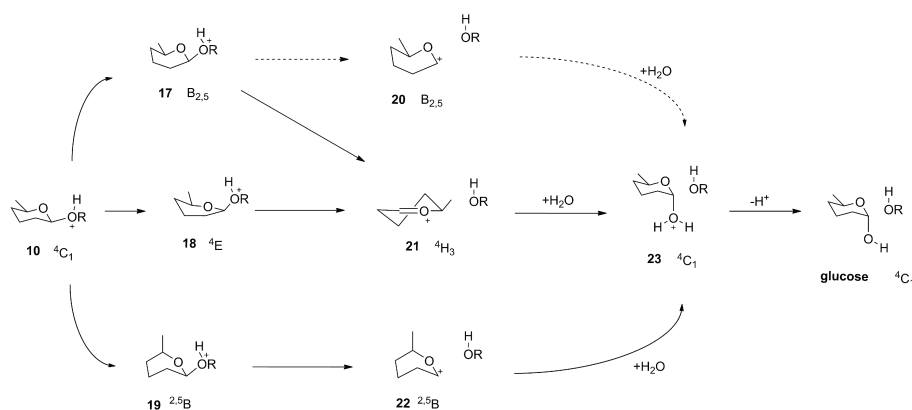
With this background knowledge, we calculated the A1 and A2 mechanisms via a cyclic carbocation for the crystalline cellobiose conformer **1** protonated at O(1) (**10**). These mechanisms were also explored for acyclic carbocations, but the barriers were higher in energy, so we do not discuss them here (see Appendix A). We found three A1 pathways, which differ by the conformation of the non-chair intermediate (B_{2,5} (**17**), ⁴E (**18**), or ^{2,5}B (**19**)). Otherwise the steps are similar (Scheme 3.1): activation of the glycosidic bond upon conformational changes from chair to non-chair conformations (**10**→**17**, **18**, or **19**), heterolytic cleavage of the C(1)–O(1) bond (**17**→**20**, **18**→**21**, **19**→**22**), and nucleophilic attack of water at the anomeric carbon atom (**20**→**23**, **21**→**23**, **22**→**23**). In the A2 mechanism the non-chair structures are directly connected to the product (**17**, **18** or **19**→**23**).

The conformational change is an important step for the activation of the glycosidic bond. In the non-chair structures (**17**, **18**, **19**) the exo-anomeric effect is diminished and instead the endo-anomeric effect is prominent (**10**→**18**: $\Delta E(2)$ endo = 32 kcal mol⁻¹) (Table 3.1). In contrast to the exo-anomeric effect, it

Table 3.2: Relative Gibbs free energy of protonation (in kcal mol⁻¹) for the oxygen sites in structures **1**–**6** (BB1K/6-31++G**, CPCM(water), 298.15 K). The values are given relative to the O(1) protonation site of each structure.

Structure	O(1)	O(2)	O(3')	O(5)	O(6')
1	0.0	-13.2	-16.0	-3.4	-17.9
2	0.0	-1.8	-15.6	-3.5	-19.5
3	0.0	-8.4	-19.8	-7.6	-13.0
4	0.0	-6.1	-18.8	-3.8	-18.4
5	0.0	-3.9	-5.9	1.6	-5.1
6	0.0	-1.7	-5.1	-0.6	-16.4

increases the bond length of the C(1)–O(1) bond (e.g. 4 kcal mol⁻¹, 1.38 Å (**1**) → 8 kcal mol⁻¹, 1.47 Å (**10**) → 40 kcal mol⁻¹, 1.58 Å (**18**)). All steps in the A1 mechanism have small barriers (3 to 7 kcal mol⁻¹) and the addition of water to C(1) is barrierless. The A2 pathway is 7 kcal mol⁻¹ higher in energy than the lowest A1 pathway and therefore less likely (Figure 3.3).



Scheme 3.1: Structures involved in the stepwise A1 mechanism via cyclic carbocations. The concerted A2 mechanism assumes that structures **17**, **18**, and **19** are directly converted to structure **23** (not indicated in the scheme).

Adding the free energy difference of 28 kcal mol⁻¹ for the protonation of O(1) to the lowest energy barrier (3 kcal mol⁻¹, B_{2,5}) of the A1 mechanism, we obtain a total barrier of 31 kcal mol⁻¹. The reaction free energy from cellobiose to glucose was calculated using a thermodynamic cycle, which gave a reaction energy of -3 kcal mol⁻¹, in agreement with experimental data.^{14,15,49} With 28 kcal mol⁻¹ the protonation is the most energy demanding step of the reaction.

We conclude that the most critical step of the hydrolysis reaction is the activation of the glycosidic bond by protonation and conformational change. Both are impeded by the neighboring hydroxyl groups and their hydrogen bonding

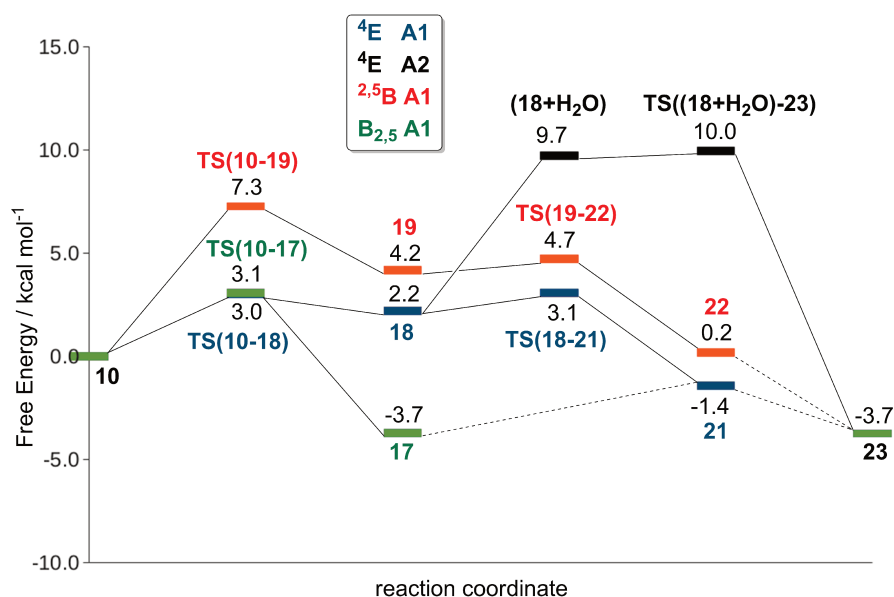


Figure 3.3: Reaction pathways for the hydrolysis of cellobiose through the stepwise A1 mechanism and the concerted A2 mechanism (BB1K/6-31++G**, CPCM(water)). Blue = ⁴E A1, black = ⁴E A2, red = ^{2,5}B A1, and green = B_{2,5} A1.

as well as by the exo-anomeric effect. These results explain why amorphous regions hydrolyze better, why strong acids are necessary for hydrolysis, and why techniques like ball milling may make the reaction more feasible by introducing conformational changes. However, other experimental findings such as the improved hydrolysis in solvents like ionic liquids cannot be explained in this manner. For this we need an explicit treatment of solvation.

3.2 Influence of Solvent on Cellulose Hydrolysis

We are interested in the influence of explicit solvation in general and in the comparison of different solvents (water versus EmimAc). QM/MM methods (QM=BB1K/TZVP, MM=GLYCAM, TIP3P) as well as classical molecular dynamics and metadynamics simulations (MM=GLYCAM, AMBER, TIP3P) were applied to explore these issues.

3.2.1 Comparison of Solvent Models

In the following we focus on the hydrolysis mechanism with explicit solvation in water (QM/MM). We chose two models, namely cellobiose and a cellulose

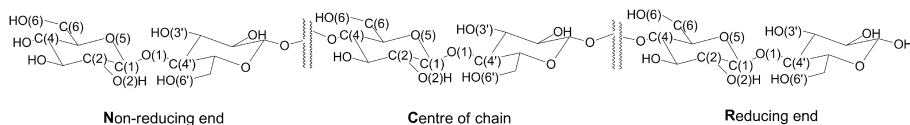


Figure 3.4: Simplified representation of the cellulose chain model and the nomenclature of the different regions.

chain with 40-glucose units that resembles dissolved cellulose in solution and enables us to study regional reactivity differences. Three regions of the chain were analyzed: region N (non-reducing end), region R (reducing end), and region C (center of the chain) (Figure 3.4). For each model or region six snapshots were taken (named **a** to **f**) to compare the impact of different starting structures. Additionally, two QM regions of different size (see Figure 3.5) were investigated: a small one (microsolvated cellobiose with 2 H_2O and H_3O^+) and a large one (microsolvated cellobiose with a second local solvent layer, in total 10 H_2O and H_3O^+). As the computed energy values and conformations scatter in the small sample of only six starting structures for each region and each QM size, we can only draw qualitative conclusions.

In order to find a common energy reference, we took single point energies for all QM regions of the educts and products. The lowest single point energy of all educts was chosen as a reference point and for all snapshots the relative energy was calculated once relative to this educt and once relative to its product. With this procedure we obtained two energy profiles for each snapshot. All pathways are relative to the reference and can be averaged, resulting in energy profiles, which are comparable, even though the active region around the QM region is different in energy due to hydrogen bonding and glucose conformations.¹⁵⁷ We also note that the computed QM/MM energies cannot be compared directly with the free energies from the preceding DFT study on cellobiose.

We first analyze the geometries and pathways and then the energies in relation to structural properties. To get an impression of the general effect of using explicit solvent, we compare the DFT mechanism from Section 3.1 with the QM/MM mechanism for cellobiose. The similarities and differences are displayed in Table 3.3 and in Figure 3.6. We find for all solvation models the same types of mechanisms (A1 and A2). However, with explicit solvation there are less intermediates: protonated cellobiose (DFT structure **10**) is rare and the non-chair conformers without a broken C(1)–O(1) bond (DFT structures **17**, **18**, **19**) are no longer stable. The carbocation INT2 is the only surviving intermediate in explicit solvent, with non-chair conformers that are also found in DFT (^{2,5}B) and new ones like E_3 .³⁰

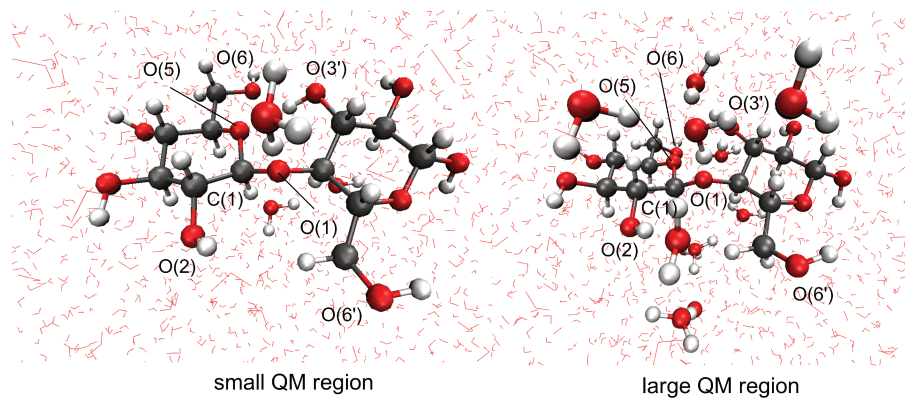


Figure 3.5: Small (left) and large (right) QM region for a model cellobiose snapshot **b** in water.

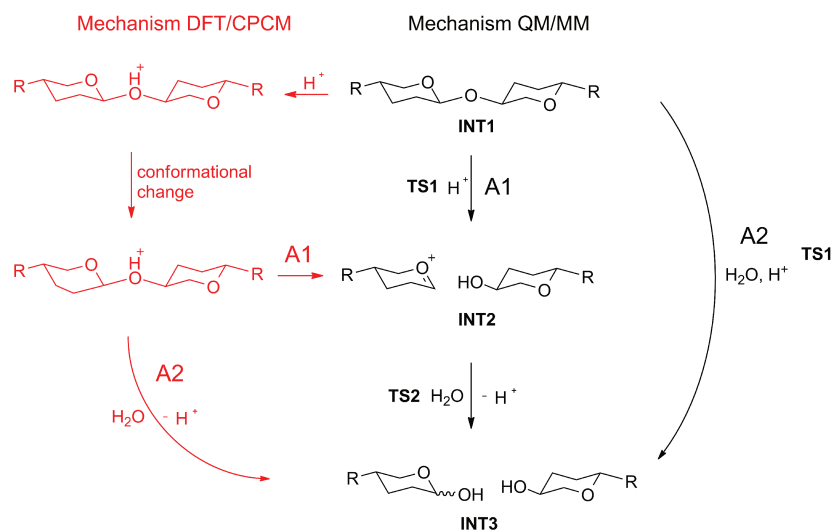


Figure 3.6: Schematic reaction mechanism for hydrolysis of cellulose as found in implicit solvent (DFT/CPCM) and explicit solvent (QM/MM).

Table 3.3: Differences and similarities for the hydrolysis of cellobiose in water (implicit and explicit solvent). Average energies are shown (energy range in brackets).

	DFT/CPCM	QM/MM		experiment
		small	large	
pathways				
intermediates	carbocation protponated O(1) non chair conf.	carbocation protponated O(1)		carbocation ^{42,43}
types	A1, A2	A1, A2		A1 ^{42,43}
conformations	⁴ H ₃ , ^{2,5} B, B _{2,5}	^{2,5} B, E ₃	^{2,5} B, E ₃	–
geometries				
C(1)–O(1) (INT1) / Å	1.38	1.38–1.50	1.39–1.44	1.40 ^{158,159}
E(2) exo (INT1) / kcal/mo	18	6–17	7–14	–
ϕ (INT1) / °	-92	-59 – -134	-58 – -107	-73 – -80 ^{34,57,68,70,71}
C(1)–O(1) (TS1) / Å	1.87–1.96	1.74–2.60	1.9–2.6	–
O _{water} –C(1) (TS1) / Å	2.99	1.99–4.02	1.9–3.1	–
hydrogen bonds		O(3')H···O(5) and O(2)···O(6')		
energies				
TS1 / kcal mol ⁻¹	34 (31–38)	24 (14–31)	21 (15–26)	30–40 ^{14,15}
reaction energy / kcal mol ⁻¹	-3	10 (3–14)	2.1 (-4 – 6)	-3 ¹³

The geometries of the various species are similar for all solvent models. While QM/MM distances and dihedrals cover a greater range of values (larger distances, more flexible dihedrals and anomeric effects), the DFT values are always within this range. The same hydrogen bonds are found in DFT and QM/MM, although in the larger QM region intramolecular hydrogen bonds are likely to be replaced by intermolecular hydrogen bonds with water. For example, in Figure 3.5 the $O(3')H \cdots O(5)$ and $H_3O \cdots O(1)$ hydrogen bonds are broken when increasing the number of QM water molecules in the QM region.

These findings for cellobiose agree with the results for the cellulose chain in explicit solvent (Table 3.6, Table 3.7). However, new mechanistic features can be seen occasionally in calculations with the large QM region: A barrierless transition (B) from cellobiose to two glucose units can occur, if there is a large endo-anomeric effect (e.g. C-d, R-c). No reaction (N) is observed, if the proton is located at O(5) or too far away from O(1) for protonation (e.g. R-d, R-b-large, R-d-large). In summary, the main impact of explicit solvation concerns the intermediates and the higher flexibility of the conformers.

In order to find the origin of these features, we investigated hydrogen bonds and specific interactions with the explicit solvent (Table 3.6, Table 3.7). Protonated cellulose (DFT structure **10**) is in most cases not a stable minimum at the QM/MM level, since the QM water molecules surrounding O(1) are more basic than O(1) and abstract the proton without a barrier. With implicit solvent this process cannot occur, because there are no explicit (basic) water molecules that could accept a proton. In the QM/MM calculations, protonated O(1) can be present, if no water molecule is close enough to abstract it (cellobiose-d, cellobiose-e, C-d, cellobiose-a-large, N-b-large). In addition, a stationary point of the flipped non-reducing glucose unit with an unbroken C(1)-O(1) bond (DFT structures **17**, **18**, or **19**) is not stable in explicit solvent. We note that already with CPCM the non-chair minima are very shallow, since the energy differences to the nearest transition state are below 1 kcal mol^{-1} .

We also examined the conformational freedom in the starting structures. We found that intra- and intermolecular hydrogen bonds affect different distances and dihedrals in the educt and thus lead to larger variations than in implicit solvent. According to our data the $O(3')H \cdots O(5)$ hydrogen bond is the most important of all intramolecular hydrogen bonds. If it is present (Table 3.6, Table 3.7, HBB intra=1), C(1)-O(1) can be shorter and E(2) exo larger than usual, and ϕ is restricted to values between -100° to -80° (e.g. N-e-large, R-a-large). Additionally, these parameters are also influenced by the presence of a hydrogen bond to O(1). If the proton is close to O(1) (Table 3.6, Table 3.7, HBB O(1)/O(5) = 3 or 4), the C(1)-O(1) bond distance is significantly increased and

the exo-anomeric effect reduced (e.g. N-e, R-a). Hence, the hydrogen bonds in the large QM region exert an influence on the starting structures that is too large to be ignored in mechanistic investigations (albeit missing in our DFT/CPCM study (section 3.1)).

Turning to the energetics, the QM/MM barriers and reaction energies for the different pathways were computed without including entropic contributions (Table 3.5). All barriers range between 20 to 40 kcal mol⁻¹, which is close to the experimental values of 30 to 40 kcal mol⁻¹. Table 3.4 summarizes the computed QM/MM barriers for the different models and mechanisms (average values over the snapshots considered). There are no striking differences in these barriers with regard to the size of the QM region, type of mechanism or model.

Table 3.4: Averaged QM/MM barriers in kcal mol⁻¹ for different models and mechanisms.

average barrier	$\Delta E(\text{TS1})$	
	small	large
all	27.8	32.3
A1	28.6	27.2
A2	27.5	30.1
cellobiose	25.5	23.4
region N	28.1	32.4
region C	30.2	28.9
region R	27.3	31.3

Unlike the experiment and the DFT results, we find no clear preference for the A1 mechanism at the QM/MM level. Nevertheless, we analyzed structural factors that may favor the A1 or A2 mechanism in individual snapshots. Whether an A1 or an A2 pathway is taken is mostly determined by the position of the water molecules in the starting structures. If water molecules are positioned within 3.8 Å under C(1) an A2 mechanism is more likely than an A1 mechanism (Table 3.6, Table 3.7). In the literature, structures with water molecules under the rings, and therefore close to C(1), are considered less likely, as the ring is hydrophobic and the water molecules are instead attracted by the hydrophilic hydroxyl groups.⁶ This explains why experimentally the A1 mechanism was found to be preferred for cellulose hydrolysis, even though the computed QM/MM barriers are similar.

Table 3.5: QM/MM energies relative to QM single-point calculations for INT1 and INT3. Empty entries indicate that no results are available.

		small					large				
		INT1	TS1	INT2	TS2	INT3	INT1	TS1	INT2	TS2	INT3
cellobiose	a	15.8			14.0	6.2	1.7			14.8	3.6
	b	13.1	28.6	28.5		13.9	6.3	25.5	20.4		
	c	-3.3	22.6			3.3	-4.2	22.8			
	d	15.3	30.5			13.9					
	e	18.0	25.3	24.1	22.9	9.6					
	f	6.7	20.8	19.8		12.9	-6.4	21.8			-3.8
region N	a	5.4									
	b	16.0	21.7			18.9	19.0	25.1			9.2
	c	12.8	31.4			18.1	-1.8	33.9			10.4
	d	12.7	31.1			18.2	8.2	39.0			25.5
	e	12.1	29.4			14.3	-3.1	30.1			4.5
	f	9.6	26.7			4.2	4.6	34.1			14.0
region C	a	19.8	30.0	24.8		7.3					
	b	25.4	33.1			19.8	0.7				
	c	13.4	38.5	28.1		17.0					
	d	44.0		42.9		22.1					
	e	15.8	29.1			23.3	4.3	28.9			13.7
	f	15.9	20.2			9.2	5.9				
region R	a	13.3	29.2			16.3	-1.4	24.8			9.0
	b	11.0	22.4			9.9	1.4	28.9	22.9		
	c	17.1				33.8					
	d	10.3					12.6				
	e	2.3	26.9			18.7					
	f	10.0	30.4			7.7	4.5	40.2			11.2

Having discussed the general effects of explicit solvents on geometries and energies, we now focus on the barriers to hydrolysis and solvent effects on these barriers. Our DFT study (see Section 3.1) identified several obstacles to hydrolysis: the exo-anomeric effect E(2) exo, hydrogen bonds, protonation, and conformational changes. In the following we will examine whether and to which extent these obstacles remain valid at the QM/MM level, by checking their correlation with the computed QM/MM barriers (energy differences between TS1 and INT1).

In Figure 3.7 we plot the QM/MM barriers energy versus the second-order perturbation energies E(2) exo indicative of the exo-anomeric effect. In general, a larger exo-anomeric effect seems to lead to a higher barrier, especially in the case of the cellobiose model (small and large) shown in blue. However, the data points are widely scattered, and the trend is not seen for all models (e.g. region R). Some of these irregularities can be explained by the presence of unusual conformations that increase or reduce the barrier for reasons unrelated to the anomeric effect. For example, flipped conformers (cellobiose-f, cellobiose-f-large, C-a) have higher barriers than expected from the strength of their anomeric effects.

In our DFT study, we found that a value of ϕ around -90° leads to the highest possible exo-anomeric effect. This is generally confirmed by the QM/MM calculations with explicit solvent (Figure 3.8), but there are exceptions. Dihedrals ϕ around -90° can have the highest E(2) exo values, but hydrogen bonds can influence the exo-anomeric effect even more. For example, R-d has a high exo-anomeric effect at a dihedral of -117° due to a strong O(3')H...O(5) hydrogen bond, whereas C-d ($\phi = -85^\circ$) has a low exo-anomeric effect because O(1) is protonated in INT1. This importance of hydrogen bonding was not visible in implicit solvent.

In Figure 3.9 we address the connection between $\Delta E(\text{TS1-INT1})$ and the type of intramolecular hydrogen bond present in INT1. Most structures do not possess intramolecular hydrogen bonds and ΔE varies between 5 and 40 kcal mol⁻¹. Among all structures with hydrogen bonds, slightly higher barriers are found for those with O(3')H...O(5) hydrogen bonds, probably because they enhance the exo-anomeric effect. The effect is stronger for the large QM region: For example, in N-e and R-a we find for the small QM region $\Delta E(\text{TS1-INT1}) = 18$ or 25 kcal mol⁻¹ and E(2) exo = 7 or 8 kcal mol⁻¹, respectively, while for the large region both the barrier and the exo-anomeric effect increase ($\Delta E(\text{TS1-INT1}) = 31$ or 32 kcal mol⁻¹ and E(2) exo = 14 or 16 kcal mol⁻¹, respectively). The O(2)...O(6') intramolecular hydrogen bond, proposed to be important in our DFT study due to the high basicity of O(6'), does not lead to high QM/MM barriers; hence a hindrance of protonation in the presence of the O(2)...O(6')

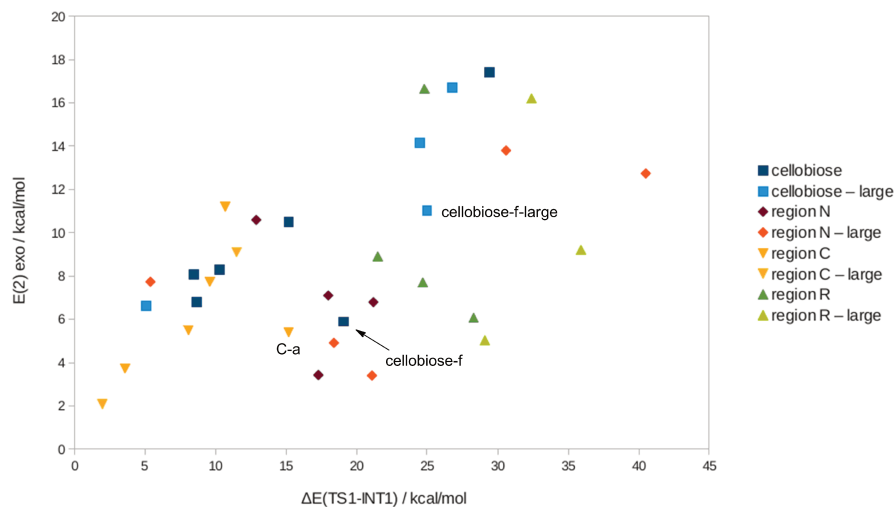


Figure 3.7: Plot of the energy difference between TS1 and INT1 versus the second-order perturbation energy $E(2)$ exo indicative of the exo-anomeric effect in INT1.

hydrogen bond cannot be confirmed at the QM/MM level.

In summary, the QM/MM calculations with explicit water confirm all qualitatively important features identified in the preceding DFT study with implicit solvent (with regard to pathways, conformations, and energies). They give a more diverse and presumably more realistic picture (stationary points, conformational freedom, and A1 versus A2) because the water molecules and their interactions with the solute by hydrogen bonds are treated explicitly. The anomeric effect and hydrogen bonding are confirmed to be important obstacles to cellulose hydrolysis.

The QM/MM work outlined above will be continued in various directions. QM/MM calculations are underway (or planned) to study more snapshots in water, to extend the investigation to the ionic liquid EmimAc, and to determine free energy profiles. However, the present QM/MM results in aqueous solution already show that (and to what extent) solvents can influence cellulose hydrolysis.

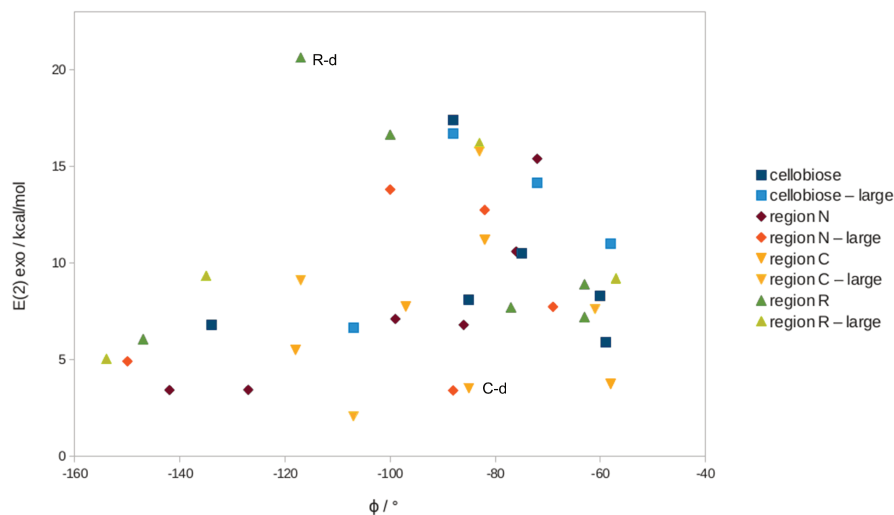


Figure 3.8: Plot of $E(2)$ exo indicative of the exo-anomeric effect in INT1 versus the dihedral ϕ ($O(5)-C(1)-O(1)-C(4')$).

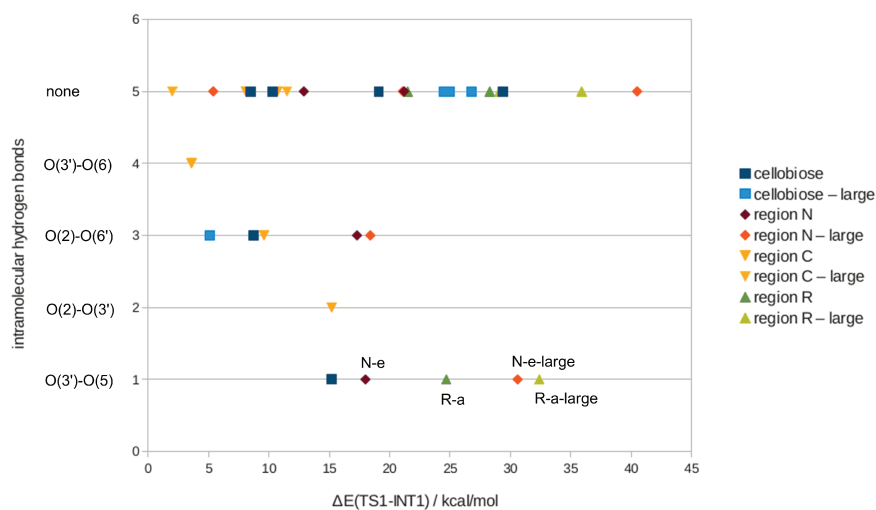


Figure 3.9: Correlation of the QM/MM energy difference between TS1 and INT1 with the intramolecular hydrogen bonds in INT1. Number code: 1 = $O(3')H \cdots O(5)$, 2 = $O(2) \cdots O(3')$, 3 = $O(2) \cdots O(6')$, 4 = $O(3') \cdots O(6)$, 5 = none.

Table 3.6: Geometries, energies in kcal mol⁻¹, and hydrogen bonding situation for all QM/MM models (small QM region). Number codes: hydrogen bonds (HBB): intramolecular (intra) 1=O(3')H...O(5), 2=O(2)...O(3'), 3=O(2)...O(6'), 4=O(3')...O(6), 5=none; HBB to O(1) or O(5): 1=O(1)...H₂O, 2=none, 3=O(1)...H₃O, 4 = O(1)...H, 5 = O(5)...H; Mechanism (mech): 1=A1, 2=A2, 3=B, 4=N.

		ΔE	E(2)		d(TS1) /Å		d(INT1) /Å		ϕ °	HBB		mech	conf. TS1
		TS-INT1	exo	endo	C(1)-O(1)	O-(C1)	C(1)-O(1)	O-(C1)		intra	O(1)/O(5)		
cellobiose	a	8.7	7	4	2.60	1.99	1.41	3.62	-134	3	3	2	^{2,5} B (TS2)
	b	15.2	11	4	1.79	3.27	1.41	3.80	-75	1	3	1	E ₃
	c	29.4	17	2	1.88	2.72	1.38	3.37	-88	5	5	2	E ₃
	d	10.3	8	4	1.74	2.98	1.45	3.53	-60	5	4	2	E ₃
	e	8.5	8	30	2.00	4.02	1.50	4.49	-85	5	4	1	^{2,5} B
	f	19.1	6	4	1.93	3.29	1.41	4.12	-59	5	3	1	flip, E ₃
region N	a	–	15	3	–	–	1.38	4.57	-72	5	2	4	^O S ₂ (INT1)
	b	12.9	11	4	1.81	3.15	1.42	3.75	-76	5	3	2	E ₃
	c	17.3	3	4	1.94	2.97	1.43	3.33	-127	3	3	2	⁴ C ₁
	d	17.3	3	4	1.93	2.91	1.43	3.33	-142	3	3	2	E ₃
	e	18.0	7	4	1.95	3.11	1.42	3.51	-99	1	3	2	E ₃
	f	21.2	9	4	1.98	2.79	1.42	3.84	-86	5	3	2	E ₃
region C	a	15.2	5	4	1.93	3.71	1.43	4.20	154	2	3	1	flip, E ₃
	b	10.7	11	4	1.71	2.83	1.43	3.11	-82	5	3	2	⁴ E
	c	9.6	8	5	1.91	4.32	1.48	4.55	-97	3	3	1	E ₃
	d	–	4	48	–	–	1.46	4.30	-85	5	4	3	E ₃ (INT1)
	e	8.1	6	4	2.02	2.83	1.41	3.33	-118	5	3	2	E ₃
	f	3.6	6	5	1.89	3.29	1.43	3.54	-58	4	3	2	E ₃
region R	a	24.7	8	3	2.18	2.47	1.41	3.27	-77	1	3	2	E ₃
	b	28.3	6	2	2.67	2.04	1.39	3.51	-147	5	5	2	E ₃
	c	–	7	31	–	–	1.51	3.32	-63	5	5	3	^{2,5} B (INT1)
	d	–	21	1	–	–	1.35	4.94	-117	3	5	4	⁴ C ₁ (INT1)
	e	24.8	17	2	1.97	2.66	1.39	3.12	-100	5	5	2	E ₃
	f	21.5	9	4	2.03	2.58	1.41	3.42	-63	5	3	2	E ₃

Table 3.7: Geometries, energies in kcal mol⁻¹, and hydrogen bonding situation for all QM/MM models (large QM region). Number codes: hydrogen bonds (HBB): intramolecular (intra) 1=O(3')H...O(5), 2=O(2)...O(3'), 3=O(2)...O(6'), 4=O(3')...O(6), 5=none; HBB to O(1) or O(5) 1=O(1)...H₂O, 2=none, 3=O(1)...H₂O, 4 = O(1)...H, 5 = O(5)...H; Mechanism (mech) 1=A1, 2=A2, 3=B, 4=N. Empty entries indicate that no results are available yet.

		ΔE TS1-INT1	E(2)		d(TS1) /Å		d(INT1) /Å		ϕ °	HBB		mech	conf. TS1
			exo	endo	C(1)-O(1)	O-(C1)	C(1)-O(1)	O-(C1)		intra	O(1)/O(5)		
cellobiose	a	5.1	7	16	2.57	1.90	1.44	3.73	-107	3	4	2	^{2,5} B
	b	24.5	14	3	2.05	3.11	1.40	4.25	-72	5	1	1	E ₃
	c	26.8	17	2	1.88	2.73	1.39	3.35	-88	5	2	2	⁴ C ₁
	d												
	e												
	f	25.0	9	4	1.96	2.72	1.40	3.40	-58	5	3	2	flip, E ₃
region N	a												
	b	5.4	8	5	1.82	3.24	1.46	3.24	-69	5	4	2	E ₃
	c	40.5	13	4	1.83	2.55	1.41	3.40	-82	5	3	2	E ₃
	d	18.4	5	3	1.97	3.07	1.41	3.54	-150	3	1	2	E ₃
	e	30.6	14	3	1.93	3.36	1.39	3.59	-100	1	1	2	^o C ₃
	f	21.1	3	4	1.92	3.17	1.41	1.39	-88	5	3	2	E ₃
region C	a												
	b	–	16	3	–	–	1.38	1.40	-83	1	2	4	² C ₅ (INT1)
	c												
	d	2.0		6									
	e	11.5	9	4	2.02	2.83	1.41	3.62	-117	5	3	2	E ₃
	f	–	8	5	–	–	1.41	3.72	-61	4	3	3	⁴ C ₁ (INT1)
region R	a	32.4	16	3	2.14	2.66	1.38	3.47	-83	1	2	2	E ₃
	b	29.1	5	4	2.01	2.80	1.41	3.56	-154	5	3	1	E ₃
	c												
	d	–	9	3	–	–	1.39	4.94	-135	3	5	4	⁴ C ₁ (INT1)
	e												
	f	35.9	9	3	2.18	2.77	1.40	3.43	-57	5	1	2	E ₃

3.2.2 Comparison of Solvents: Water and EmimAc

In the previous chapters we found that hydrogen bonding, chair conformations, and the exo-anomeric effect impede hydrolysis, while conformational changes yielding non-chair conformers and the resulting endo-anomeric effect facilitate hydrolysis. Therefore we were interested how different solvents (water and EmimAc) influence these factors and investigated the conformational flexibility in both solvents using classical molecular dynamics and metadynamics simulations.

Guided by our previous DFT results, we focused in our analysis of the simulations on the following geometrical variables: (a) the O(5)–C(1)–O(1)–C(4') dihedral angle (ϕ) as an indicator for the strength of the exo-anomeric effect ($n(\text{O}(1)) \rightarrow \sigma^*(\text{C}(1)\text{--O}(5))$) and for the existence of intramolecular hydrogen bonds; and (b) the ring flip dihedral angle C(1)–O(5)–C(2)–C(4) (α_1) along with the angles describing the orientation of the C(1)–O(1) bond relative to the ring (β_1 C(5)–O(5)–C(1)–O(1), β_2 C(3)–C(2)–C(1)–O(1)) as the key criteria that decide about the presence of the exo- or the endo-anomeric effect. We will first analyze the results for cellobiose and then compare with those for the cellulose chain.

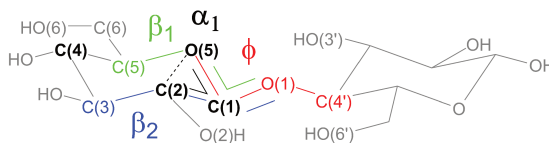


Figure 3.10: Dihedral angles β_1 , β_2 , ϕ , and α_1 for cellobiose.

Concerning the strength of the exo-anomeric effect in relation to ϕ and the related hydrogen bonds O(3')H \cdots O(5) and O(2) \cdots O(6'), the following is known from the literature: The dihedral angle ϕ ranges from -73° to -89° in water and assumes values around -125° in EmimAc.^{34,57,68,70,71} The angle is influenced by hydrogen bonds as shown in Section 3.2.1.

In our dynamics study three maxima were found for ϕ in water, M1 around -150° (3%), M2 around -78° (96%), and M3 around 64° (1%), compared with only two in EmimAc, M1 (-165° , 12%) and M2 (-66° , 88%) (Figure 3.11 top, Figure 3.12). Regarding the strength of the exo-anomeric effect and the hydrogen bonding, M1 and M2 can be connected with the following properties: In water M2 has the maximum exo-anomeric effect and features the O(3')H \cdots O(5) (80%)^{57,68,70,71} hydrogen bond; M1 has a reduced exo-anomeric effect and 36% of the structures contain a O(2) \cdots O(6') hydrogen bond. In EmimAc, both the exo-anomeric effect and the probability of hydrogen bonds are reduced for M1 and M2: M2 13% O(3')H \cdots O(5) and M1 5% O(2) \cdots O(6').

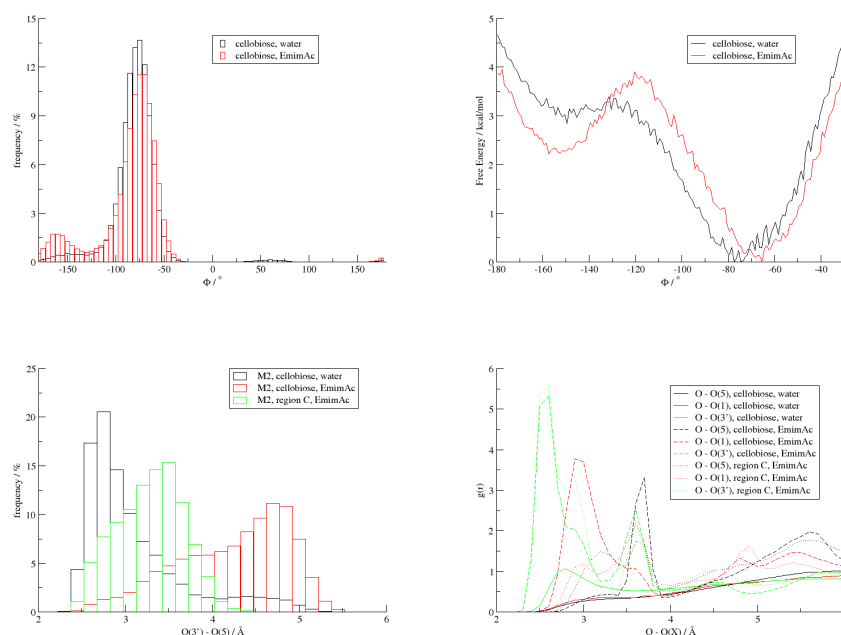


Figure 3.11: Top: Distributions and free energy profiles for the rotation of ϕ . Bottom: Distributions of the $O(3')H \cdots O(5)$ hydrogen bond and radial distributions of selected $O \cdots O(X)$ distances. Both in water and EmimAc for cellobiose and region C.

The reason for the reduced exo-anomeric effect and the broken hydrogen bonds are the different maximum dihedrals for ϕ (M2 water -78° , EmimAc -66°) and the substitution of intra- by intermolecular hydrogen bonds (Figure 3.11, bottom).^{62,65,160–164} Consequently, in water cellulose hydrolysis is most hindered in M2 by the maximum exo-anomeric effect and intramolecular hydrogen bonds, while EmimAc facilitates hydrolysis by a reduced exo-anomeric effect and broken hydrogen bonds caused by stronger-solvent solute interactions.

Next we check whether an exo- or endo-anomeric effect is present in a given conformer by investigating the dihedral angles α_1 , β_1 , and β_2 . For α_1 a global minimum (-150° , e.g. 4C_1 , 3,0B , and 2,5B conformers) and two higher-lying minima (-180° , e.g. skew conformers 3S_5 , 5S_3 ; -230° e.g. $B_{0,3}$, $B_{2,5}$, 1,4B , 1S_3 , and 1S_5 conformers) have been reported.¹⁵³ Compared to water, ionic liquids increase the population around -230° .^{19,61,62,66} However, a conformational change described by α_1 is not the only prerequisite for replacing the exo-anomeric effect by the endo-anomeric effect, which facilitates hydrolysis. In addition, the $C(1)-O(1)$ bond must be axial, which requires the dihedral angles β_1 and β_2 to be axial (90° or -270° , respectively). To check the connection between the three

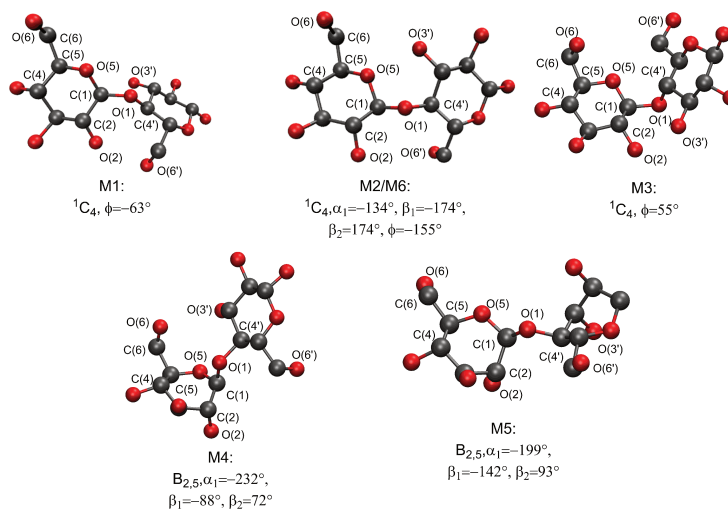


Figure 3.12: Exemplary structures for M1 to M6 and selected values of important dihedral angles. Hydrogen atoms are omitted for clarity.

dihedrals and to find the best criterion for the endo-anomeric effect, we analyzed the correlations between the dihedrals. We found that β_1 is most representative for the distinction between the exo-anomeric effect (with an equatorial C(1)–O(1) bond) and the endo-anomeric effect (with an axial C(1)–O(1) bond) (see Appendix B).

In our simulations we found three main conformers with regard to α_1 (Figure 3.13 top, Figure 3.12): M4 (-230°), M5 (-190°), and M6 (-150° , water 93% and EmimAc 83%). With regard to the dihedral β_1 there are two conformers (Figure 3.13 middle, Figure 3.12): axial (ax, 270°) and equatorial (eq, 180° , water 92% and EmimAc 83%).

Next we address the hydrogen bonding situation in the axial and equatorial conformers. In water a stabilizing O(3')H \cdots O(6) hydrogen bond is formed in the axial conformers. In EmimAc we find no such intramolecular interaction due to the stronger intermolecular solute-solvent hydrogen bonds (see Figure 3.11); in addition, there is also a stronger O \cdots C(1) interaction (Figure 3.13, bottom), which stabilizes non-chair conformers (like in M4) with an increased positive charge at C(1) (see Section 3.1).

In summary, we find the following solvent-dependent features for ϕ , α_1 , and β_1 : In water conformers are preferentially populated that hinder hydrolysis, because of a stable glycosidic linkage (M2), intramolecular hydrogen bonds (O(3')H \cdots O(5), O(2) \cdots O(6')), and chair structures (M6) with a strong exo-anomeric effect (eq). The same conformers are still present in EmimAc, but

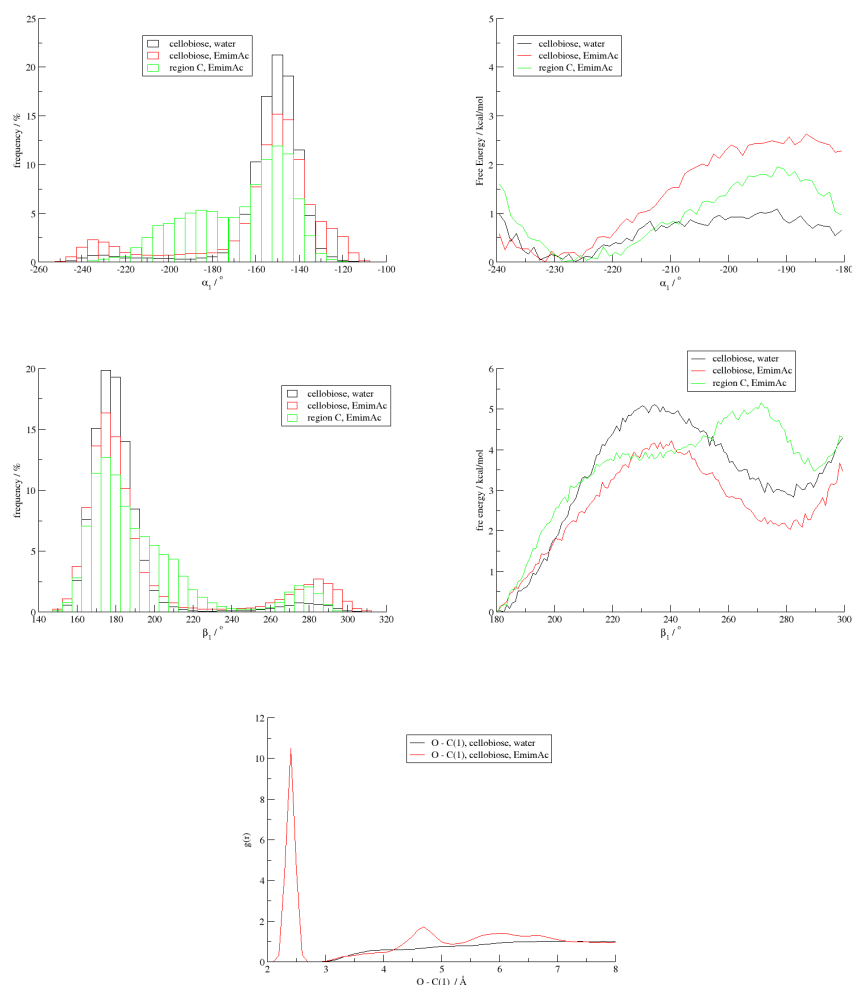


Figure 3.13: Distributions and free energy profiles for α_1 (top) and β_1 (middle). Bottom: Radial distributions of selected O \cdots C(1) distances. Both in water and EmimAc for cellobiose and region C.

the population of minima (M1, M4, M5, ax) with a reduced exo-anomeric effect or an endo-anomeric effect is increased. Additionally, intramolecular hydrogen bonds are substituted in EmimAc by intermolecular interactions with the anions.

We now turn to the simulations performed for a 40-glucose chain. To validate the cellobiose model we examined the distributions of ϕ and β_1 for the chain. In addition, we checked whether the solvent effects differ between the two ends and the center of the chain (Figure 3.4). Accordingly, the populations of all conformations found for both models and solvents are listed in Table 3.8. We decided to take the presence of M4 and of an axial C(1)–O(1) bond (β_1) as

Table 3.8: Conformer populations taken from 100 ns molecular dynamics simulations at 420 K in water and EmimAc: results for cellobiose and the regions N, C, and R of the cellulose chain.

		water				EmimAc			
		cellobiose	cellulose chain			cellobiose	cellulose chain		
			N	C	R		N	C	R
ϕ	M1	3	3	7	4	12	57	32	0
	M2	96	96	92	95	88	43	68	100
	M3	1	1	1	1	0	0	0	0
α_1	M4	4	4	6	6	11	15	6	13
	M5	3	3	4	6	6	6	32	20
	M6	93	93	90	88	83	79	62	67
β_1	eq	92	91	89	87	83	78	68	69
	eqax	4	4	5	7	7	6	22	18
	ax	4	5	6	6	10	16	10	14

the main criteria for a feasible hydrolysis. In water, comparing all models and regions, we find hardly any differences in the population of M4 and the axial conformers, which is consistent with our QM/MM results in aqueous solution (see Section 3.2.1). The situation is different in EmimAc: regions N and R reach populations of 13 to 15% for M4 and 14 to 16% for ax, whereas region C shows slightly lower populations (M4 6%, ax 10%).

To further examine these deviations we correlated the dihedrals and the hydrogen bonding situation of region C and compared with the corresponding results for cellobiose in EmimAc. There are differences in two aspects: First, the axial conformers of region C are more rare and are correlated with M5 rather than M4 (Figure 3.13, top left, green). Second, the hydrogen bond O(3')H \cdots O(5) is found more often for region C (Figure 3.11, bottom left, green). The underlying reason is that the interaction with the acetate anions of EmimAc is weaker for region C than for cellobiose, as can be seen from the computed radial distribution functions (Figure 3.11, bottom right).

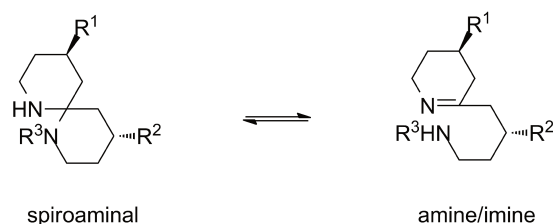
Our simulations thus show that different regions in a cellulose chain may behave differently from each other and from cellobiose in the solvent EmimAc. The end regions N and R seem easier to hydrolyze than the central region C, which has less axial C(1)–O(1) bonds and more intramolecular hydrogen bonds because of less pronounced solute-solvent interactions in region C.

To summarize, our QM/MM and molecular dynamics studies reveal that the solvent may affect cellulose hydrolysis mainly by specific hydrogen bonds and that it is therefore important to use explicit solvent models. In our mechanistic

study the calculations with explicit solvent give more realistic intermediates and explain the preference for A1 and A2 mechanisms. In water, conformers are stabilized that hinder hydrolysis mainly through intramolecular hydrogen bonds and the exo-anomeric effect. By contrast, in EmimAc the population of hydrolysis-facilitating conformers with axial C(1)–O(1) bonds and non-chair structures is higher, and hence this solvent is better suited for hydrolysis. In EmimAc, the ends of a cellulose chain are predicted to hydrolyze more easily than the center of the chain, as the ionic liquid interacts more strongly with the ends of the chain.

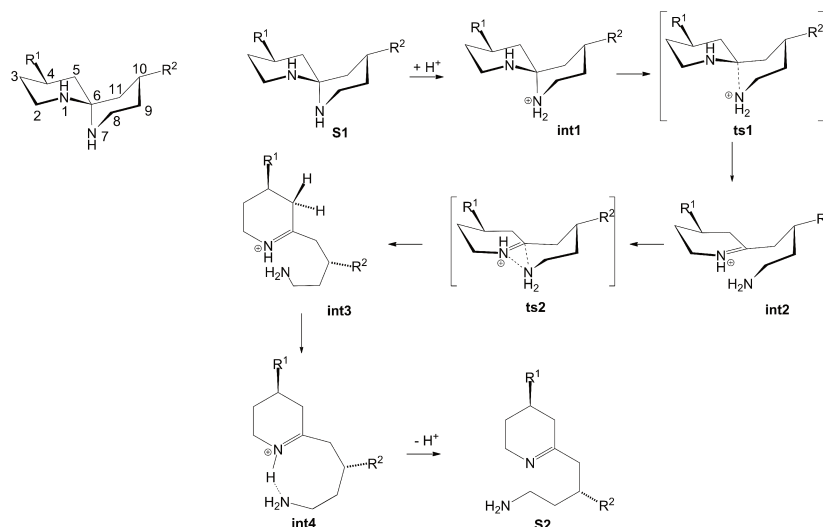
3.3 Influence of the Anomeric Effect on Other Reactions: Tautomerism in Spiroaminals

Hyperconjugative interactions like the anomeric effect influence not only cellulose hydrolysis but also other reactions (Appendix C). One of these is the tautomerism of spiroaminals from the closed-ring to the open-ring tautomer (Scheme 3.2). We have explored the influence of the anomeric effect on this equilibrium computationally (M06-2X-D3/TZVP,CPCM(water)) for 1,7-diazaspiro[5.5]-undecane (**S1**), 1-allyl-1,7-diazaspiro[5.5]-undecane (**S3**), (4R)-4-isopropyl-1,7-diazaspiro[5.5]undecane (**S5**) and (4R,10R)-4,10-diisopropyl-1,7-diazaspiro[5.5]undecane (**S7**). Experimentally, the equilibrium lies at the closed-ring form for **S1** and at the open ring-structure for **S3**. There are no experimental data for **S5** and **S7**.



Scheme 3.2: Tautomerism between aminal and amine/imine. $R^1 = R^2 = R^3 = \text{H}$ (**S1**, **S2**); $R^1 = R^2 = \text{H}$, $R^3 = \text{allyl}$ (**S3**, **S4**); $R^1 = \text{isopropyl}$, $R^2 = R^3 = \text{H}$ (**S5**, **S6**); $R^1 = R^2 = \text{isopropyl}$, $R^3 = \text{H}$ (**S7**, **S8**).

The pathway (Scheme 3.3) for the ring opening mechanism in spiroaminals is governed by two factors, which we have already encountered in cellulose hydrolysis: protonation and conformational change. The C(6)–N(7) bond, which has to be cleaved, is activated by protonation (**S1**→**int1**) and is subsequently broken, which involves a conformational change from a chair to a non-chair conformation

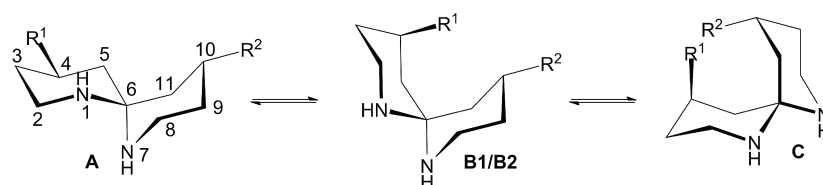


Scheme 3.3: Proposed mechanism of the amination to amine/imine conversion for the reaction from **S1** to **S2**. $R^1/R^2 = H$.

(**int1**→**int2**). Thereafter the molecule undergoes other conformational changes to prevent the back-reaction to **int1** and to adopt a more stable low-lying structure (**int2**→**int3**→**int4**). The last step is reprotonation (**int4**→**S2**).

We investigated the geometries and energies of the starting conformers (Table 3.9), the reaction energy and the barriers for the pathways of the four spiroaminals (Table 3.10). Like glycosides spiroaminals can have different conformations.³⁰ We will refer to the investigated conformers as follows: The number denotes the molecule (**S1**, **S3**, **S5**, **S7**), the small letter specifies the position of the H atoms on N(1) and N(7) (**a** both equatorial; **b** one equatorial, one axial; **c** both axial), and the capital letter defines the conformation according to Scheme 3.4.

Considering the energetics of the spiroaminals steric effects overrule electronic factors (Table 3.9). For example, in **S1** there is no steric hindrance in any conformer, and hence **S1a-A** is the global minimum due to the strong anomeric effect, whereas for **S3** the sterically unhindered conformer **S3a-C** is lowest in



Scheme 3.4: Different chair conformers of spiroaminals. B1 = ring flip of the unsubstituted ring. B2 = ring flip of the substituted ring.

Table 3.9: Selected free energies ΔG in kcal mol⁻¹, magnitudes of the anomeric effect E(2)-1 (n(N(1)) \rightarrow σ^* (C(6)-N(7))) and E(2)-2 (n(N(1)) \rightarrow σ^* (C(6)-N(1))) in kcal mol⁻¹, and C-N bond lengths [\AA] of different conformers of the spiroaminals **S1**, **S3**, **S5**, and **S7** [M06-2X-D3/TZVP,CPCM(water)]. B1 = ring flip of the unsubstituted ring. B2 = ring flip of the substituted ring.

structure	$\Delta\Delta G$	Anomeric effect		Bond length		D_a / %
		E(2)-1	E(2)-2	C(6)-N(1)	C(6)-N(7)	
S1a-A	0.0	16	16	1.47	1.47	35.9
S1c-A	0.5	-	-	1.47	1.47	21.7
S1a-B	0.8	-	14	1.46	1.48	15.5
S1c-B	1.2	-	-	1.47	1.47	10.4
S1a-C	1.3	-	-	1.47	1.47	9.8
S1c-C	1.8	-	-	1.47	1.47	6.1
S3a-A	0.0	17	15	1.47	1.49	1.0
S3c-A	-2.6	-	-	1.47	1.48	12.5
S3a-B1	-2.9	13	-	1.48	1.48	17.7
S3c-B1	0.3	-	-	1.47	1.49	0.7
S3a-B2	0.7	-	14	1.46	1.50	0.5
S3c-B2	-2.7	-	-	1.47	1.48	15.1
S3a-C	-3.9	-	-	1.47	1.48	49.7
S3c-C	-1.0	-	-	1.47	1.49	2.8
S5a-A	0.0	16	16	1.48	1.47	41.3
S5c-A	0.6	-	-	1.47	1.47	22.7
S5a-B1	0.7	14	-	1.48	1.46	20.2
S5c-B1	1.0	-	-	1.47	1.47	15.2
S5a-B2	5.1	-	13	1.47	1.48	0.3
S5c-B2	5.5	-	-	1.47	1.47	0.2
S5a-C	5.7	-	-	1.47	1.47	0.1
S5c-C	7.9	-	-	1.47	1.48	0.0
S7a-A	0.0	16	16	1.47	1.47	58.3
S7c-A	0.4	-	-	1.47	1.47	40.6
S7a-B	4.5	-	13	1.46	1.48	0.6
S7c-B	5.0	-	-	1.47	1.47	0.4
S7a-C	11.5	-	-	1.47	1.47	0.0
S7c-C	12.5	-	-	1.48	1.48	0.0

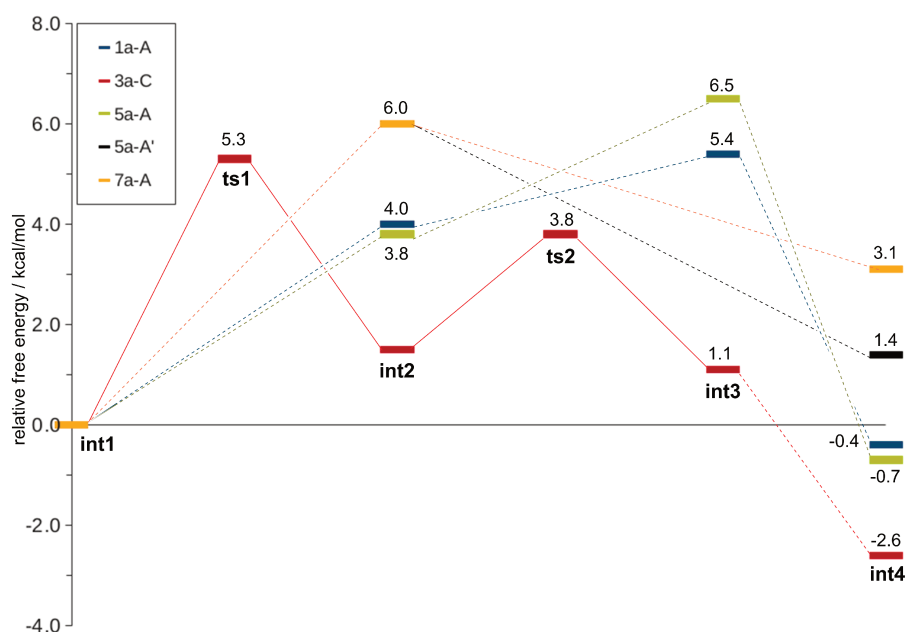


Figure 3.14: Free energy profiles for the reaction from **int1** to **int4** for the lowest conformer of each protonated spiroaminal. The energies are given relative to **int1**. They were computed at the M06-2X-D3/TZVP,CPCM(water) level; the ' indicates that the substituted ring is protonated and opened.

energy even though no anomeric effect is present. Steric hindrance introduces larger energy differences between conformers of the same spiroaminal: Going from **S1a-A** to **S1a-C** causes only the anomeric effect to vanish, which increases the energy by merely $1.3 \text{ kcal mol}^{-1}$, while going from **S7a-A** to **S7a-C** diminishes the anomeric effect and also introduces an axial propyl group, which leads to a destabilization by $11.5 \text{ kcal mol}^{-1}$. For **S1**, **S5**, and **S7** the main conformer always shows the largest anomeric effect (**a-A**), while for **S3** the anomeric effect is negligible in the highest populated conformer **S3a-C**.

Another topic in our study was the influence of the anomeric effects on the reaction energy. We looked at the reaction on the unprotonated (aminal→amine) and on the protonated (**int1**→**int4**) energy surface (Table 3.10). In all unprotonated cases this reaction is endothermic by 4 to 10 kcal mol^{-1} for the lowest-energy conformers. **S3** is the only spiroaminal with reasonably populated conformers (**S3a-A**, **S3a-B1**) that have a slightly exothermic reaction energy (-2 to -3 kcal mol^{-1}). Next we explored the reaction energy for the corresponding protonated spiroaminals (Table 3.10). Here we found the reaction to be endothermic for **S5a-A'** and **S7**, almost thermoneutral for **S1** and **S5a-A**, and exothermic for **S3**.

Table 3.10: Selected free reaction energies ΔG in kcal mol⁻¹ of different conformers of the spiroaminals **S1**, **S3**, **S5**, and **S7** [M06-2X-D3/TZVP,CPCM(water)]. B1 = ring flip of the unsubstituted ring; B2 = ring flip of the substituted ring; the ' indicates that the substituted ring is protonated and opened.

		$\Delta\Delta G$ / kcal mol ⁻¹	
		aminal→amine	int1→int4
S1 → S2	a-A	5.0	-0.4
	a-B	4.2	–
	a-C	3.7	–
S3 → S4	a-A	-0.6	–
	a-B1	2.3	–
	a-B2	-1.5	–
	a-C	3.3	-3.6
S5 → S6	a-A	4.8	1.4
	a-A'	10.0	–
S7 → S8	a-A	9.5	3.1

Furthermore, reaction barriers for unprotonated and protonated pathways were calculated (Figure 3.14). The reaction barriers from the open-ring to the closed-ring structure for unprotonated spiroaminals are unfeasibly high (over 50 kcal mol⁻¹) for **S1** and **S3** (see Appendix C). After protonation the barriers to tautomerization are much lower (between 5 and 7 kcal mol⁻¹) so that the reaction should be very facile at room temperature. Spiroaminals conformers with an anomeric effect (**S1a-A**, **S5a-A**, **S7a-A**) have barrierless transitions and higher-lying intermediates than spiroaminal **S3**. For **S3a-C**, which has a negligible anomeric effect, the intermediates are lower in energy by 3 to 5 kcal mol⁻¹ and the reaction is not barrierless.

To summarize: The tautomerism is only possible, if the reaction is proton catalyzed. **S3** prefers an open-ring structure, while **S1** favors the spiroaminal tautomer, consistent with the experimental findings. According to our calculations, **S5** and **S7** behave more like **S1** than like **S3**. Therefore we expect them to prefer the spiroaminal tautomer. Regarding the influence of steric and electronic effects, the tautomerism of spiroaminals is clearly more driven by steric rather than electronic effects. We conclude that the anomeric effect has a lesser impact on C–N bonds and spiro-molecules than on the acetate C–O bond in glycosidic linkages.

3.4 Down-Stream Process of Cellulose Hydrolysis: Glucose-Fructose Isomerization

The product of cellulose hydrolysis, glucose, is the starting point for further conversions that yield valuable platform molecules for chemical industry (Scheme 1.1). One such reaction is the transformation of glucose to fructose (Appendix D). Experimentally, this reaction can be catalyzed by different metal complexes that give different conversions and product yields, even though they all classify as Lewis acids (Table 3.11). The goal of our computational study was to explain the observed differences and to establish criteria for good metal catalysts in water.

Table 3.11: Experimental results for the reaction of glucose (413 K, 60 bar) with the given catalyst in water.¹⁶⁵

Catalyst	Conv. /%	HPLC yield/%			pK _a
		Fructose	HMF	LA	
CrCl ₃ ·6 H ₂ O	99	0	13	13	4.1
AlCl ₃ ·6 H ₂ O	88	11	19	6	5.5
CuCl ₂ ·2 H ₂ O	23	1	6	2	8.0
FeCl ₃ ·6 H ₂ O	12	0	3	0	2.2
MgCl ₂	2	0.8	0.6	0	11.4
uncatalysed	0	0	0	0	15.7
FeCl ₃ ·6 H ₂ O in 2M H ₂ SO ₄	85	0	0	51	–
Ferroin	4	3	1	0	–
ScCl ₃	67	8	8	2	2.2
FeCl ₃ @Poly-VIm-DVB	4	2	2	0	–

We divided the catalysts used experimentally into three groups. Group one: high conversion (Al³⁺, Cr³⁺); group two: medium conversion (Fe³⁺, Cu²⁺); and group three: no conversion (Mg²⁺, no catalyst). In general, the conversion is higher for catalysts with lower pK_a values (Table 3.11). However, iron(III) deviates from this trend and yields only moderate conversion despite the low pK_a value of 2.2.

In order to find the reason for this abnormal behavior, we investigated the glucose-fructose isomerization mechanism for the catalysts listed above using DFT (PBE0/6-31+G**) and implicit solvation (CPCM). Since the overall mechanism does not change drastically with the chosen metal cation, we will first discuss the complexes and the mechanism in general and then focus on the most important differences between catalysts.

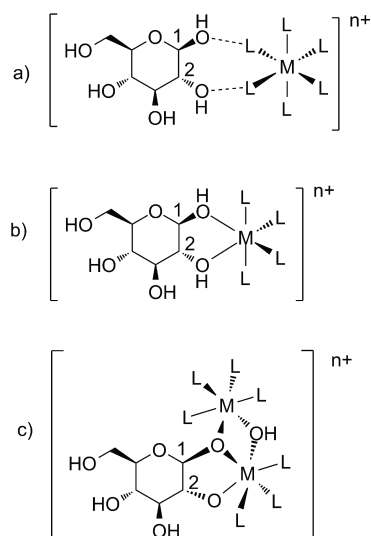


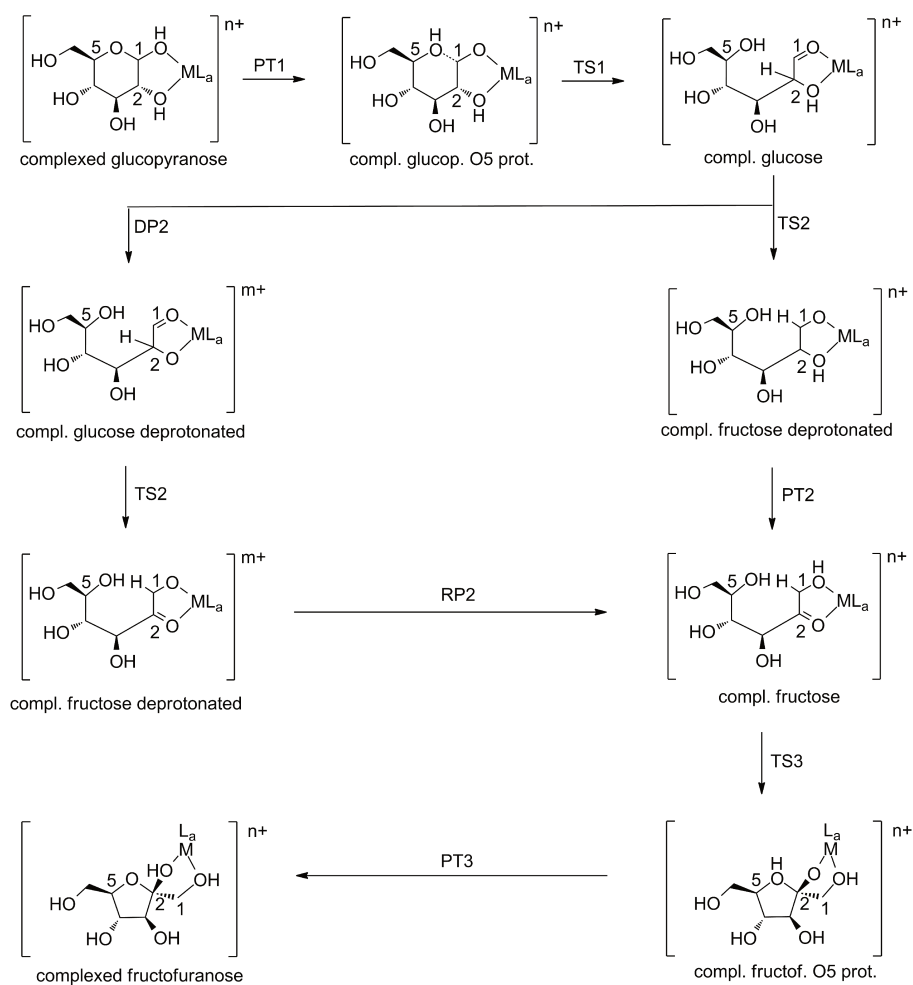
Figure 3.15: Glucose complexes of different metal cations with an octahedral ligand sphere: a) Hydrogen-bonding coordination, b) direct complexation of glucopyranose, and c) bonding of a dimeric catalyst.

In water at 413 K and 60 bar (the standard experimental conditions) a large variety of metal complexes can be formed (Figure 3.15). Possible ligands in the reaction mixture are H_2O , Cl^- , and OH^- . The ligand sphere around the metal center can be octahedral, tetrahedral or square-planar. The catalyst can have a single $[\text{M}(\text{H}_2\text{O})_6]^{n+}$ or dimeric metal core $[\text{M}_2(\text{H}_2\text{O})_8(\text{OH})_2]^{n+}$. Additionally, it can be attached to glucose by hydrogen bonds $[\text{M}(\text{H}_2\text{O})_6]^{n+}$ or by substitution of two ligands by two hydroxyl groups of glucose $[\text{MO}(1)\text{O}(2)(\text{H}_2\text{O})_4]^{n+}$. Due to this large variety, we chose our catalytic species according to published experimental findings.^{166–174} All investigated metal complexes have most likely an octahedral ligand sphere. Aluminum(III), copper(II) and magnesium(II) prefer water ligands. Chromium(III) and iron(III) complexes are common with water and one to three chloride ligands. Deprotonated and dimeric complexes are possible for chromium(III) and expected for iron(III). Magnesium(II) is the only catalyst that prefers a hydrogen bonding complex with glucose instead of a direct coordination to hydroxyl groups.

After selecting the most likely catalyst species for each metal cation under the given reaction conditions, we focus on the mechanism (Scheme 3.5). Glucose and $[\text{M}(\text{H}_2\text{O})_6]^{n+}$ serve as energy reference of the reaction pathways for each metal M. The quoted barriers always refer to the lowest intermediate of the whole reaction pathway (see Appendix D).

The starting point of the mechanism is a catalyst-glucopyranose complex, which

needs to be transformed to an open-chain glucose-catalyst complex. First, a proton is transferred from O(1) to O(5) (PT1) followed by C(1)–O(5) bond cleavage (TS1). PT1 consists of two steps: deprotonation of O(1) and protonation of O(5); in some cases (uncatalyzed, magnesium(II)- and copper(II)-catalyzed pathways) the protonation of O(5) leads to a direct opening of the C(1)–O(5) bond, often in a barrierless process. The catalyst influences the C(1)–O(1) and C(1)–O(5) bond lengths and thereby the free energy needed for the protonation and deprotonation reactions (PT1).



Scheme 3.5: Proposed mechanism for glucose-to-fructose isomerization. Shown is an example with α -glucose and a metal cation M with a ligands L.

In the next step fructose is formed from glucose. This requires a hydrogen atom transfer from C(2) to C(1) (TS2) and a proton transfer from O(2) to O(1) (PT2). An alternative route can be taken: deprotonation of O(2) (DP2), hydrogen atom transfer (TS2), and reprotonation of O(1) (RP2) (uncatalyzed reaction, some

$[\text{MO}(1)\text{O}(2)(\text{H}_2\text{O})_4]^{n+}$ complexes, and dimeric catalysts). The main role of the catalyst in TS2 is to stabilize the electron density, which is delocalized between the transferred hydrogen atom H, the $\sigma^*(\text{C}(1)-\text{O}(1))/\sigma^*(\text{C}(2)-\text{O}(2))$ orbitals, and the orbitals of the metal or the M–O(1)/O(2) bonds.

The last step is the formation of fructofuranose from fructose by the closing of the C(2)–O(5) bond (TS3) and subsequent proton transfer from O(5) to O(2) (PT3). Like PT1, PT3 proceeds by a deprotonation followed by a protonation, and like in TS1, the C(2)–O(5) bond formation is usually a barrierless process.

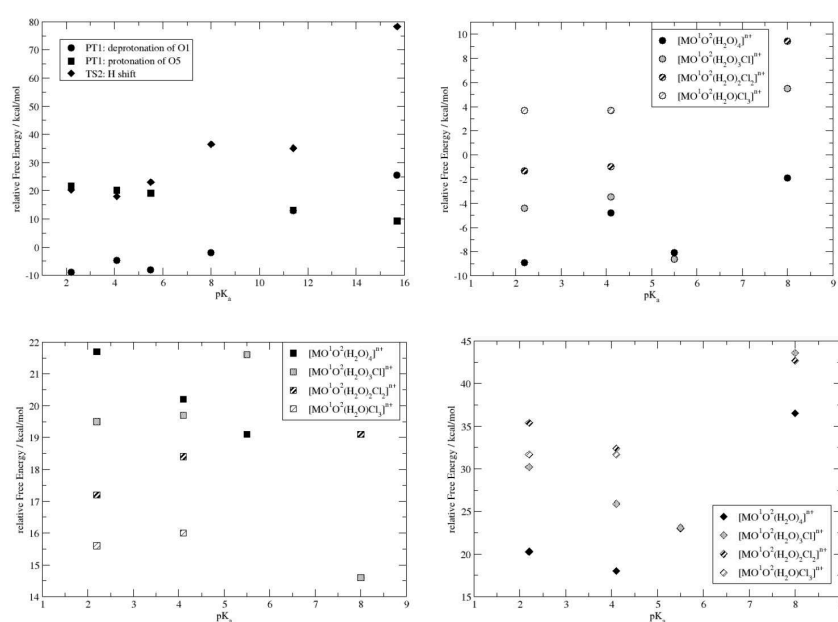


Figure 3.16: Relative free energy of the PT1 (O(1) deprotonation (●), O(5) protonation (■)) and TS2 steps (◆) for $[\text{MO}(1)\text{O}(2)(\text{H}_2\text{O})_4]^{n+}$ (top, left) and $[\text{MO}(1)\text{O}(2)(\text{H}_2\text{O})_{4-a}\text{Cl}_a]^{n+}$ $a = 0-3$ (top, right and bottom). pK_a of metal complex: Fe^{3+} 2.2, Cr^{3+} 4.1, Al^{3+} 5.5, Cu^{2+} 8.0, Mg^{2+} 11.4, water 15.7. PBE0/6-31+G**, CPCM (water).

Within this mechanism the following steps are critical (Table 3.12): PT1 (proton transfer with highest barrier), TS2 (in most cases rate determining), separation of catalyst and fructose (sep.) as well as the overall reaction energy (gluc.-fruc.). Barriers up to 36 kcal mol^{-1} are considered feasible at 413 K. Each of the catalysts was investigated with regard to the critical steps in the mechanism (PT1, TS2, sep., and gluc.-fruc.) and to their properties (Brønsted and Lewis acidity, ligand sphere, orbital occupations, transition state structures, ability to form a glucose complex).

The Brønsted acidity of the catalyst complex is one of the properties that may determine the conversion rates, as previously suggested. It was found that the lower the Brønsted acidity of the complex, the lower the barriers for PT1 and TS2 (Figure 3.16). However, if we separate the deprotonation (deprot) and the protonation (prot) steps of PT1, we find that the barrier reduction does not scale linearly with the pK_a difference. For example, comparison of iron(III) to aluminum(III) ($\Delta\text{pK}_a = 3.3$) shows that the deprotonation energy is only slightly lower for iron(III) ($\Delta\Delta\text{G}(\text{PT1-deprot}) = 0.7 \text{ kcal mol}^{-1}$). The corresponding energy gain from copper(II) to aluminum(III) ($\Delta\text{pK}_a = 2.5$) is distinctively larger ($\Delta\Delta\text{G}(\text{PT1-deprot}) = 6.2 \text{ kcal mol}^{-1}$).

Similar results are found for the transition state TS2: barriers are lower for lower pK_a values, but the improvement stagnates below a pK_a value of 6. For example, $13.5 \text{ kcal mol}^{-1}$ are gained from Cu^{2+} to Al^{3+} ($\Delta\text{pK}_a = 2.5$), and only $2.7 \text{ kcal mol}^{-1}$ from Al^{3+} and Fe^{3+} ($\Delta\text{pK}_a = 3.3$). We conclude that all complexes with a pK_a value below 6 should catalyze the glucose-fructose isomerization, while higher pK_a values produce barriers over 35 kcal mol^{-1} and little conversion (Table 3.12). This agrees with most of the experimental results (high conversion with aluminum(III) ($\text{pK}_a = 5.5$) and chromium(III) ($\text{pK}_a = 4.1$) and low conversion with copper(II) ($\text{pK}_a = 8.0$) and magnesium(II) ($\text{pK}_a = 11.4$), but not with the data for iron(III), which has the lowest pK_a value (2.2), but only medium conversion (12%). To resolve this problem we have to look into other properties of the catalysts.

In addition to the Brønsted acidity, we found that the ligand sphere influences the catalytic capabilities of the metal complex. Hydrogen-bonded catalysts $[\text{M}(\text{H}_2\text{O})_6]^{n+}$ catalyze the reaction not as well as directly coordinated catalysts. For example, the $[\text{MgO}(1)\text{O}(2)(\text{H}_2\text{O})_4]^{2+}$ catalyst leads to a barrier of 26 kcal mol^{-1} for $\Delta\Delta\text{G}(\text{PT1})$, while for $[\text{Mg}(\text{H}_2\text{O})_6]^{2+}$ the barrier amounts to 34 kcal mol^{-1} . Apparently, a directly coordinated metal complex is better in stabilizing the electron density being shifted during proton and hydrogen atom transfers.

Moreover, as soon as negatively charged ligands like OH^- and Cl^- are introduced, the transition state energies increase. An example is the TS2 barrier for chromium(III) with varying ligands: $18.0 \text{ kcal mol}^{-1}$ $[\text{CrO}(1)\text{O}(2)(\text{H}_2\text{O})_4]^{3+}$ $<$ $25.9 \text{ kcal mol}^{-1}$ $[\text{CrO}(1)\text{O}(2)(\text{H}_2\text{O})_3\text{Cl}]^{2+}$ $<$ $32.4 \text{ kcal mol}^{-1}$ $[\text{CrO}(1)\text{O}(2)-(\text{H}_2\text{O})_2\text{Cl}_2]^+$. This increase can be explained by the stronger σ - and π -electron donation from the negatively charged ligands to the metal center. This reduces the positive charge and the acidity on the metal center (natural charge on Cr^{3+} : $1.18e$ $[\text{CrO}(1)\text{O}(2)(\text{H}_2\text{O})_4]^{3+}$ $>$ $0.89e$ $[\text{CrO}(1)\text{O}(2)(\text{H}_2\text{O})_3\text{Cl}]^{2+}$ $>$ $0.59e$ $[\text{CrO}(1)\text{O}(2)(\text{H}_2\text{O})_2\text{Cl}_2]^+$).

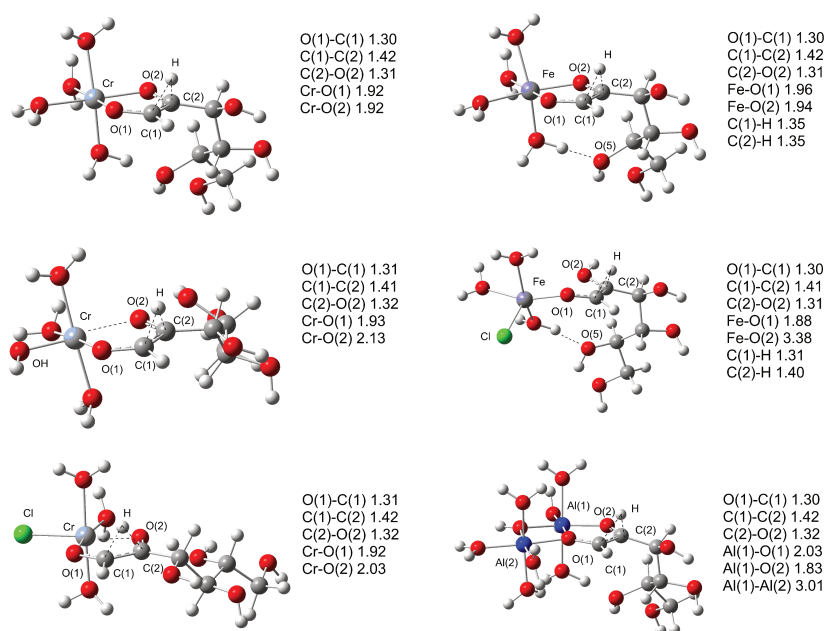


Figure 3.17: Transition states for hydrogen atom transfer (TS2) for different complexes ($[\text{CrO}(1)\text{O}(2)(\text{H}_2\text{O})_4]^{3+}$, $[\text{CrO}(1)\text{O}(2)(\text{H}_2\text{O})_3\text{OH}]^{2+}$, $[\text{CrO}(1)\text{O}(2)(\text{H}_2\text{O})_3\text{Cl}]^{2+}$, $[\text{FeO}(1)\text{O}(2)(\text{H}_2\text{O})_4]^{3+}$, $[\text{FeO}(1)\text{O}(2)(\text{H}_2\text{O})_3\text{Cl}]^{2+}$, $[\text{Al}_2\text{O}(1)\text{O}(2)(\text{H}_2\text{O})_7\text{OH}]^{5+}$) and selected bond lengths. PBE0/6-31+G**₂, CPCM (water).

Negatively charged ligands have a larger impact on structures and transition state energies for iron(II) and copper(II) than for chromium(III). TS2 barrier: $[\text{MO}(1)\text{O}(2)(\text{H}_2\text{O})_3\text{Cl}]^{2+}$: 25.9 (Cr^{3+}) versus 30.2 kcal mol⁻¹ (Fe^{3+}); $[\text{MO}(1)\text{O}(2)(\text{H}_2\text{O})_2\text{Cl}_2]^{+}$: 32.4 (Cr^{3+}) versus 35.4 kcal mol⁻¹ (Fe^{3+}). This can be attributed to the occupation of d-orbitals: Empty d-orbitals accept electron density and rise in energy (0.11e/-1.93 eV $[\text{CrO}(1)\text{O}(2)(\text{H}_2\text{O})_4]^{3+}$, 0.12e/-0.27 eV $[\text{CrO}(1)\text{O}(2)(\text{H}_2\text{O})_3\text{Cl}]^{2+}$, and 0.15e/0.49 eV $[\text{CrO}(1)\text{O}(2)(\text{H}_2\text{O})_2\text{Cl}_2]^{+}$), while higher lying and partly filled orbitals are less capable of stabilizing electron density in TS2. If there are no d-orbitals available in combination with weak acidity (magnesium(II)) or if all d-orbitals are occupied (iron(III) and copper(II)), negatively charged ligands have a stronger impact and raise the energy. This effect is also visible structurally. These ligands lead to an increase in the M...O(2) distance by 0.1 to 0.2 Å (aluminum(III), chromium(III)), and to bond cleavage in iron(III) (M-O(2) 3.38 Å, Figure 3.17). The resulting less compact transition states may be disadvantageous at the usual reaction conditions (60 bar).

Another modification of the catalyst is the formation of dimers. According to our calculations, the reaction with a dimer is feasible for iron(III) ($\Delta\text{TS2} =$

31 kcal mol⁻¹), but not for chromium(III) and aluminum(III) ($\Delta TS2 > 35$ kcal mol⁻¹). The difference between the metal catalysts arises from the formation energy of the dimer. Iron(III) complexes are easier to deprotonate due to their high acidity, and the energy needed to form dimers is therefore lower than in the case of chromium(III) and aluminum(III).^{95,175}

Consequently, metal cations must fulfill the following criteria to reach a high conversion in the glucose-fructose isomerization: moderate Lewis acidity and moderate Brønsted acidity ($pK_a = 4-6$), only water ligands or ligands further up the spectrochemical series which are weak σ donors and can accept π back donation (e.g. CN⁻ and CO), low-lying unoccupied orbitals that accept electron density, and coordination of glucose as a ligand. Iron(III) and copper(II) are therefore only moderate catalysts for the reaction, as they are high-spin complexes; iron(II) attracts Cl⁻ and OH⁻ ligands and copper(II) is not acidic enough. Magnesium(II) is an inefficient catalyst since it is too basic and does not coordinate directly to glucopyranose.

With the help of these guidelines new catalysts can be proposed: One option are low-spin iron(III) complexes¹⁶⁶ with ligands such as phenanthroline, 2,2'-bipyridine or CN⁻. Another possibility is to use so far unexplored catalytic species: for example, Sc³⁺, since it has a similar pK_a as aluminum(III). These suggestions were examined experimentally (Table 3.11): Iron(III) complexes with aromatic nitrogen ligands (ferroin and Fe@Poly-VIm-DVB) give a lower yield but show higher selectivity, while scandium(III) complexes produce high yield, but suffer from strong side reactions.¹⁶⁵ Hence, there are some improvements but the perfect catalyst still has to be found.

Table 3.12: Relative free energies in kcal mol⁻¹ at 298 K and 1 atm for critical steps (PT1, TS2, product/catalyst separation (sep.), and reaction energy for the complexed glucopyranose-fructofuranose (gluc.-fruc.) conversion) in the glucose-fructose isomerization with Al³⁺, Cr³⁺, Fe³⁺, Cu²⁺ and Mg²⁺ catalysts and uncatalyzed. PBE0/6-31+G**, CPCM (water).

Catalyst	$\Delta\Delta G(\text{PT1})$	$\Delta\Delta G(\text{TS2})$	$\Delta\Delta G(\text{sep.})$	$\Delta\Delta G(\text{gluc.-fruc.})$
[Al(H ₂ O) ₆] ³⁺	17.0	29.2	9.4	-3.1
[AlO(1)O(2)(H ₂ O) ₄] ³⁺	13.3	23.0	15.4	-16.2
[AlO(1)O(2)H ₂ O) ₃ OH] ²⁺	30.1	41.0	17.7	-14.1
[AlO(1)O(2)H ₂ O) ₃ Cl] ²⁺	13.2	23.1	13.0	-11.8
[Al ₂ O(1)O(2)H ₂ O) ₇ OH] ⁵⁺	–	40.1	–	–
[Cr(H ₂ O) ₆] ³⁺	13.9	26.9	13.0	-7.2
[CrO(1)O(2)H ₂ O) ₄] ³⁺	16.2	18.0	18.3	-17.5
[CrO(1)O(2)H ₂ O) ₃ OH] ²⁺	25.4	34.2	14.4	-10.9
[CrO(1)O(2)H ₂ O) ₃ Cl] ²⁺	16.2	25.9	17.0	-13.5
[CrO(1)O(2)H ₂ O) ₂ Cl ₂] ⁺	17.4	32.4	12.7	-8.0
[CrO(1)O(2)H ₂ O)Cl ₃]	19.7	31.7	6.8	-4.3
[Cr ₂ O(1)O(2)H ₂ O) ₇ OH] ⁵⁺	–	36.2	–	–
[Fe(H ₂ O) ₆] ³⁺	16.9	25.5	13.0	-7.1
[FeO(1)O(2)H ₂ O) ₄] ³⁺	14.9	20.3	17.2	-17.9
[FeO(1)O(2)H ₂ O) ₃ OH] ²⁺	18.0	32.3	13.1	-9.6
[FeO(1)O(2)H ₂ O) ₂ (OH) ₂] ⁺	44.8	53.9	13.1	-4.3
[FeO(1)O(2)H ₂ O) ₃ Cl] ²⁺	15.1	30.2	16.0	-10.7
[FeO(1)O(2)H ₂ O) ₂ (OH)Cl] ⁺	30.1	42.0	13.8	-4.9
[FeO(1)O(2)H ₂ O) ₂ Cl ₂] ⁺	15.9	35.4	11.5	-4.8
[FeO(1)O(2)H ₂ O)(OH)Cl ₂]	39.1	51.6	9.5	-1.4
[FeO(1)O(2)H ₂ O)Cl ₃]	19.3	31.7	3.0	0.0
[FeO(1)O(2)(HO)Cl ₃] ⁻	–	60.4	–	–
[Fe ₂ O(1)O(2)(H ₂ O) ₇ OH] ⁵⁺	–	31.1	–	–
[Cu(H ₂ O) ₆] ²⁺	–	36.4	4.5	-2.3
[CuO(1)O(2)H ₂ O) ₄] ²⁺	–	36.5	6.1	-2.1
[CuO(1)O(2)H ₂ O) ₂] ²⁺	20.1	38.2	10.5	-1.6
[CuO(1)O(2)H ₂ O)Cl] ⁺	20.2	43.3	6.6	0.1
[CuO(1)O(2)Cl ₂]	28.5	42.7	8.3	0.6
[Mg(H ₂ O) ₆] ²⁺	33.7	40.1	-0.4	-0.3
[MgO(1)O(2)H ₂ O) ₄] ²⁺	25.5	35.1	7.4	-5.2
uncatalyzed	38.1	78.2	1.5	1.5

3.5 Conclusion

This thesis has addressed reaction mechanisms related to cellulose usage. Structure-energy relations were investigated computationally with several methods, including DFT, QM/MM, and MD calculations, which allowed a systematic study of biomass conversion using different cellulose models and solvents.

The high barrier to cellulose hydrolysis was related to structural and electronic factors. Hydroxyl groups, hydrogen bonds, and the exo-anomeric effect present obstacles that prevent the required protonation and conformational changes in cellulose. These obstacles are not separate problems, but correlated to each other, which makes them particularly effective in hindering the depolymerization of cellulose.

One way of reducing the barrier to cellulose hydrolysis is the use of a proper solvent. While water is not effective in this regard, the anions of ionic liquids interact strongly with cellulose so that they can disrupt the stabilizing hydrogen bonds and the exo-anomeric effect. Since the central regions in a cellulose chain tend to be less accessible by solvent, hydrolysis should start preferentially at the end of the chains.

For cellulose hydrolysis the anomeric effect plays a key role for the mechanism. This effect seems particularly pronounced in O–C–O systems, since it is less important in similar systems with N–C–N moieties as in spiroaminals.

A down-stream process starting at the product of cellulose hydrolysis is the glucose-fructose isomerization. Structural and electronic effects also play a role in this reaction. The mechanism of this reaction was elucidated in a systematic computational study for a variety of metal complex catalysts, which identified guidelines for effective catalysts, for example with regard to ligand selection and optimum pK_a ranges.

At the beginning of this Section, we listed several open questions about cellulose hydrolysis. By answering them at least partially through our computational work, we hope to get one step closer to practical applications of cellulose hydrolysis in industry and therefore to the utilization of biomass as a renewable energy source.

Chapter 4

Bibliography

- [1] J. Hill, E. Nelson, D. Tilman, S. Polasky, D. Tiffany. Environmental, economic, and energetic costs and benefits of biodiesel and ethanol biofuels. *P. Natl. A. Sci.* **2006**, *103*, 11206–11210.
- [2] L. P. Walker, D. B. Wilson. Enzymatic hydrolysis of cellulose: An overview. *Bioresource Technol.* **1991**, *36*, 3–14.
- [3] R. R. Singhanian, A. K. Patel, R. K. Sukumaran, C. Larroche, A. Pandey. Role and significance of beta-glucosidases in the hydrolysis of cellulose for bioethanol production. *Bioresource Technol.* **2013**, *127*, 500–507.
- [4] V. Agarwal, P. J. Dauenhauer, G. W. Huber, S. M. Auerbach. Ab Initio Dynamics of Cellulose Pyrolysis: Nascent Decomposition Pathways at 327 and 600°C. *J. Am. Chem. Soc.* **2012**, *134*, 14958–14972.
- [5] D. Mohan, C. U. Pittman, P. H. Steele. Pyrolysis of Wood/Biomass for Bio-oil: A Critical Review. *Energy & Fuels* **2006**, *20*, 848–889.
- [6] R. Rinaldi, F. Schüth. Acid Hydrolysis of Cellulose as the Entry Point into Biorefinery Schemes. *ChemSusChem* **2009**, *2*, 1096–1107.
- [7] C. Li, Q. Wang, Z. K. Zhao. Acid in ionic liquid: An efficient system for hydrolysis of lignocellulose. *Green Chem.* **2008**, *10*, 177–182.
- [8] C. Li, Z. Zhao. Efficient Acid-Catalyzed Hydrolysis of Cellulose in Ionic Liquid. *Adv. Synth. Catal.* **2007**, *349*, 1847–1850.
- [9] R. Rinaldi, N. Meine, J. vom Stein, R. Palkovits, F. Schüth. Which Controls the Depolymerization of Cellulose in Ionic Liquids: The Solid Acid Catalyst or Cellulose? *ChemSusChem* **2010**, *3*, 266–276.

- [10] R. Rinaldi, R. Palkovits, F. Schüth. Depolymerization of Cellulose Using Solid Catalysts in Ionic Liquids. *Angew. Chem. Int. Ed.* **2008**, *47*, 8047–8050.
- [11] N. Meine, R. Rinaldi, F. Schüth. Solvent-Free Catalytic Depolymerization of Cellulose to Water-Soluble Oligosaccharides. *ChemSusChem* **2012**, *5*, 1449–1454.
- [12] L. Vanoye, M. Fanselow, J. D. Holbrey, M. P. Atkins, K. R. Seddon. Kinetic model for the hydrolysis of lignocellulosic biomass in the ionic liquid, 1-ethyl-3-methyl-imidazolium chloride. *Green Chem.* **2009**, *11*, 390–396.
- [13] Y. B. Tewari, R. N. Goldberg. Thermodynamics of hydrolysis of disaccharides. Cellobiose, gentiobiose, isomaltose, and maltose. *J. Biol. Chem.* **1989**, *264*, 3966–3971.
- [14] J.-H. Q. Pinto, S. Kaliaguine. A Monte Carlo analysis of acid hydrolysis of glycosidic bonds in polysaccharides. *AIChE J.* **1991**, *37*, 905–914.
- [15] Z.-E. Dadach, S. Kaliaguine. Acid hydrolysis of cellulose. Part i: Experimental kinetic analysis. *Can. J. Chem. Eng.* **1993**, *71*, 880–891.
- [16] X. Liang, A. Montoya, B. S. Haynes. Local Site Selectivity and Conformational Structures in the Glycosidic Bond Scission of Cellobiose. *J. Phys. Chem. B* **2011**, *115*, 10682–10691.
- [17] R. P. Swatloski, S. K. Spear, J. D. Holbrey, R. D. Rogers. Dissolution of Cellulose with Ionic Liquids. *J. Am. Chem. Soc.* **2002**, *124*, 4974–4975.
- [18] R. Rinaldi. Instantaneous dissolution of cellulose in organic electrolyte solutions. *Chem. Commun.* **2011**, *47*, 511–513.
- [19] H. Liu, K. L. Sale, B. A. Simmons, S. Singh. Molecular Dynamics Study of Polysaccharides in Binary Solvent Mixtures of an Ionic Liquid and Water. *J. Phys. Chem. B* **2011**, *115*, 10251–10258.
- [20] H. Kobayashi, T. Komanoya, S. K. Guha, K. Hara, A. Fukuoka. Conversion of cellulose into renewable chemicals by supported metal catalysis. *Appl. Catal. A-Gen.* **2011**, *409–410*, 13–20.
- [21] H. Zhao, J. H. Kwak, Y. Wang, J. A. Franz, J. M. White, J. E. Holladay. Effects of Crystallinity on Dilute Acid Hydrolysis of Cellulose by Cellulose Ball-Milling Study. *Energy Fuels* **2005**, *20*, 807–811.
- [22] R. Rinaldi, F. Schüth. Design of solid catalysts for the conversion of biomass. *Energy Environ. Sci.* **2009**, *2*, 610–626.

- [23] G. T. Beckham, J. F. Matthews, B. Peters, Y. J. Bomble, M. E. Himmel, M. F. Crowley. Molecular-Level Origins of Biomass Recalcitrance: Decrystallization Free Energies for Four Common Cellulose Polymorphs. *J. Phys. Chem. B* **2011**, *115*, 4118–4127.
- [24] C. M. Payne, M. E. Himmel, M. F. Crowley, G. T. Beckham. Decrystallization of Oligosaccharides from the Cellulose I_β Surface with Molecular Simulation. *J. Phys. Chem. Letters* **2011**, *2*, 1546–1550.
- [25] S. P. Chundawat, G. T. Beckham, M. E. Himmel, B. E. Dale. Deconstruction of Lignocellulosic Biomass to Fuels and Chemicals. *Annu. Rev. Chem. Biomol. Eng.* **2011**, *2*, 121–145.
- [26] P. Dhepe, A. Fukuoka. Cellulose Conversion under Heterogeneous Catalysis. *ChemSusChem* **2008**, *1*, 969–975.
- [27] L. R. Lynd, C. E. Wyman, T. U. Gerngross. Biocommodity Engineering. *Biotechnol. Progr.* **1999**, *15*, 777–793.
- [28] S. van de Vyver, J. Geboers, P. A. Jacobs, B. F. Sels. Recent Advances in the Catalytic Conversion of Cellulose. *ChemCatChem* **2011**, *3*, 82–94.
- [29] J. Veredel, T. Church, P. Andersson. Catalytic One-Pot Production of Small Organics from Polysaccharides. *Synthesis* **2011**, *2011*, 1649–1677.
- [30] The notations of conformers in this work follow the recommendations for sugar compounds: Conformational Nomenclature for Five- and Six-Membered Ring Forms of Monosaccharides and Their Derivatives, Recommendations, IUPAC-IUB Joint Commission on Biochemical Nomenclature (JCBN), 1980; *Arch. Biochem. Biophys.* **1981**, *207*, 469–472; *Eur. J. Biochem.* **1980**, *111*, 295–298; *Pure Appl. Chem.* **1981**, *53*, 1901–1905.
- [31] A. O’Sullivan. Cellulose: the structure slowly unravels. *Cellulose* **1997**, *4*, 173–207.
- [32] Y. Nishiyama, P. Langan, H. Chanzy. Crystal Structure and Hydrogen-Bonding System in Cellulose I_β from Synchrotron X-ray and Neutron Fiber Diffraction. *J. Am. Chem. Soc.* **2002**, *124*, 9074–9082.
- [33] Y. Nishiyama, J. Sugiyama, H. Chanzy, P. Langan. Crystal Structure and Hydrogen Bonding System in Cellulose I_α from Synchrotron X-ray and Neutron Fiber Diffraction. *J. Am. Chem. Soc.* **2003**, *125*, 14300–14306.
- [34] M. Jarvis. Chemistry: Cellulose stacks up. *Nature* **2003**, *426*, 611–612.

- [35] G. L. Strati, J. L. Willett, F. A. Momany. Ab initio computational study of β -cellobiose conformers using B3LYP/6-311++G**. *Carbohydr. Res.* **2002**, *337*, 1833–1849.
- [36] G. L. Strati, J. L. Willett, F. A. Momany. A DFT/ab initio study of hydrogen bonding and conformational preference in model cellobiose analogs using B3LYP/6-311++G**. *Carbohydr. Res.* **2002**, *337*, 1851–1859.
- [37] A. J. Kirby. Stereoelectronic effects on acetal hydrolysis. *Acc. Chem. Res.* **1984**, *17*, 305–311.
- [38] H. Satoh, S. Manabe, Y. Ito, H. P. Lüthi, T. Laino, J. Hutter. Endocyclic Cleavage in Glycosides with 2,3-trans Cyclic Protecting Groups. *J. Am. Chem. Soc.* **2011**, *133*, 5610–5619.
- [39] J. M. Beck, S. M. Miller, M. W. Pecuh, C. M. Hadad. C2 Hydroxyl Group Governs the Difference in Hydrolysis Rates of Methyl- α -d-glycero-d-guloseptanoside and Methyl- β -d-glycero-d-guloseptanoside. *J. Org. Chem.* **2012**, *77*, 4242–4251.
- [40] H. Satoh, H. S. Hansen, S. Manabe, W. F. van Gunsteren, P. H. Hünenberger. Theoretical Investigation of Solvent Effects on Glycosylation Reactions: Stereoselectivity Controlled by Preferential Conformations of the Intermediate Oxocarbenium-Counterion Complex. *J. Chem. Theory Comput.* **2010**, *6*, 1783–1797.
- [41] T. L. Amyes, W. P. Jencks. Lifetimes of oxocarbenium ions in aqueous solution from common ion inhibition of the solvolysis of α -azido ethers by added azide ion. *J. Am. Chem. Soc.* **1989**, *111*, 7888–7900.
- [42] T. E. Timell. The acid hydrolysis of glycosides: I. General Conditions and the effect of the nature of the aglycone. *Can. J. Chem.* **1964**, *42*, 1456–1472.
- [43] S. R. Wann, M. M. Kreevoy. Acetal hydrolysis: the A1 mechanism. *J. Org. Chem.* **1981**, *46*, 419–423.
- [44] R. B. Gupta, R. W. Franck. Direct experimental evidence for cleavage of both exo- and endo-cyclic carbon-oxygen bonds in the acid-catalyzed reaction of alkyl β -tetrahydropyranyl acetals. *J. Am. Chem. Soc.* **1987**, *109*, 6554–6556.
- [45] J. L. Liras, E. V. Anslyn. Exocyclic and Endocyclic Cleavage of Pyranosides in Both Methanol and Water Detected by a Novel Probe. *J. Am. Chem. Soc.* **1994**, *116*, 2645–2646.

- [46] J. L. Liras, V. M. Lynch, E. V. Anslyn. The Ratio between Endocyclic and Exocyclic Cleavage of Pyranoside Acetals Is Dependent upon the Anomer, the Temperature, the Aglycon Group, and the Solvent. *J. Am. Chem. Soc.* **1997**, *119*, 8191–8200.
- [47] D. R. McPhail, J. R. Lee, B. Fraser-Reid. Exo and endo activation in glycoside cleavage: acetolysis of methyl α - and β -glucopyranosides. *J. Am. Chem. Soc.* **1992**, *114*, 1905–1906.
- [48] P. L. Ragg, P. R. Fields, P. B. Tinker. The Development of a Process for the Hydrolysis of Lignocellulosic Waste [and Discussion]. *Philos. Trans. R. Soc. London Ser. A* **1987**, *321*, 537–547.
- [49] J. B. Binder, R. T. Raines. From the Cover: Fermentable sugars by chemical hydrolysis of biomass. *Proc. Natl. Acad. Sci. USA* **2010**, *107*, 4516–4521.
- [50] J. Bemiller, *Acid-Catalyzed Hydrolysis of Glycosides in Advances in Carbohydrate Chemistry, Vol. Volume 22*, Academic Press, **1967**, pp. 25–108.
- [51] C. W. Andrews, J. P. Bowen, B. Fraser-Reid. An ab initio study of dimethoxymethane protonation and its relevance to glycoside hydrolysis. *J. Chem. Soc., Chem. Commun.* **1989**, 1913–1916.
- [52] C. W. Andrews, B. Fraser-Reid, J. P. Bowen. An ab initio study (6-31G*) of transition states in glycoside hydrolysis based on axial and equatorial 2-methoxytetrahydropyrans. *J. Am. Chem. Soc.* **1991**, *113*, 8293–8298.
- [53] P. Deslongchamps, S. Li, Y. L. Dory. Hydrolysis of α - and β -Glycosides. New Experimental Data and Modeling of Reaction Pathways. *Org. Lett.* **2004**, *6*, 505–508.
- [54] B. J. Smith. A Conformational Study of 2-Oxanol: Insight into the Role of Ring Distortion on Enzyme-Catalyzed Glycosidic Bond Cleavage. *J. Am. Chem. Soc.* **1997**, *119*, 2699–2706.
- [55] B. J. Smith. Effect of Ring Distortion on the Acid Hydrolysis of 2-Methylsulfanyloxane. *J. Phys. Chem. A* **1998**, *102*, 4728–4733.
- [56] H. Dong, M. R. Nimlos, M. E. Himmel, D. K. Johnson, X. Qian. The Effects of Water on β -d-Xylose Condensation Reactions. *J. Phys. Chem. A* **2009**, *113*, 8577–8585.
- [57] H. Liu, K. L. Sale, B. M. Holmes, B. A. Simmons, S. Singh. Understanding the Interactions of Cellulose with Ionic Liquids: A Molecular Dynamics Study. *J. Phys. Chem. B* **2010**, *114*, 4293–4301.

- [58] F. Momany, U. Schnupf. DFTMD studies of β -cellobiose: conformational preference using implicit solvent. *Carbohydr. Res.* **2011**, *346*, 619–630.
- [59] W. Plazinski, M. Drach. The dynamics of the conformational changes in the hexopyranose ring: a transition path sampling approach. *RSC Adv.* **2014**, *4*, 25028–25039.
- [60] Y. Nishimura, D. Yokogawa, S. Irlé. Theoretical study of cellobiose hydrolysis to glucose in ionic liquids. *Chem. Phys. Lett.* **2014**, *603*, 7–12.
- [61] Z. Jarin, J. Pfaendtner. Ionic Liquids Can Selectively Change the Conformational Free-Energy Landscape of Sugar Rings. *J. Chem. Theory Comput.* **2014**, *10*, 507–510.
- [62] H. M. Cho, A. S. Gross, J.-W. Chu. Dissecting Force Interactions in Cellulose Deconstruction Reveals the Required Solvent Versatility for Overcoming Biomass Recalcitrance. *J. Am. Chem. Soc.* **2011**, *133*, 14033–14041.
- [63] K. Kulasinski, S. Keten, S. Churakov, D. Derome, J. Carmeliet. A comparative molecular dynamics study of crystalline, paracrystalline and amorphous states of cellulose. *Cellulose* **2014**, *21*, 1103–1116.
- [64] M. Bergenstråhle, E. Thormann, N. Nordgren, L. A. Berglund. Force Pulling of Single Cellulose Chains at the Crystalline Cellulose–Liquid Interface: A Molecular Dynamics Study. *Langmuir* **2009**, *25*, 4635–4642.
- [65] A. Pinkert, K. N. Marsh, S. Pang. Reflections on the Solubility of Cellulose. *Ind. Eng. Chem. Res.* **2010**, *49*, 11121–11130.
- [66] B. Mostofian, X. Cheng, J. C. Smith. Replica-Exchange Molecular Dynamics Simulations of Cellulose Solvated in Water and in the Ionic Liquid 1-Butyl-3-Methylimidazolium Chloride. *J. Phys. Chem. B* **2014**, *118*, 11037–11049.
- [67] K. L. Fleming, J. Pfaendtner. Characterizing the Catalyzed Hydrolysis of β -1,4 Glycosidic Bonds Using Density Functional Theory. *J. Phys. Chem. A* **2013**, *117*, 14200–14208.
- [68] L. Peric-Hassler, H. S. Hansen, R. Baron, P. H. Hünenberger. Conformational properties of glucose-based disaccharides investigated using molecular dynamics simulations with local elevation umbrella sampling. *Carbohydr. Res.* **2010**, *345*, 1781–1801.

- [69] H. B. Mayes, L. J. Broadbelt, G. T. Beckham. How Sugars Pucker: Electronic Structure Calculations Map the Kinetic Landscape of Five Biologically Paramount Monosaccharides and Their Implications for Enzymatic Catalysis. *J. Am. Chem. Soc.* **2013**, *136*, 1008–1022.
- [70] C. S. Pereira, D. Kony, R. Baron, M. Müller, W. F. van Gunsteren, P. H. Hünenberger. Conformational and Dynamical Properties of Disaccharides in Water: a Molecular Dynamics Study. *Biophys. J.* **2006**, *90*, 4337–4344.
- [71] A. D. French, G. P. Johnson. Quantum mechanics studies of cellobiose conformations. *Can. J. Chem.* **2006**, *84*, 603–612.
- [72] S. Favre, P. Vogel, S. Gerber-Lemaire. Recent Synthetic Approaches Toward Non-anomeric Spiroketal in Natural Products. *Molecules* **2008**, *13*, 2570–2600.
- [73] S. K. Ghosh, R. P. Hsung, J. Liu. An Anomeric Control on Remote Stereochemistry in the Synthesis of Spiroketal. *J. Am. Chem. Soc.* **2005**, *127*, 8260–8261.
- [74] K. Mead, B. Brewer. Strategies in Spiroketal Synthesis Revisited: Recent Applications and Advances. *Curr. Org. Chem.* **2003**, *7*, 227–256.
- [75] P. Deslongchamps, D. D. Rowan, N. Pothier, J. K. Saunders. 1,7-Dithia and 1-oxa-7-thiaspiro[5.5]undecanes. Excellent systems for the study of stereoelectronic effects (anomeric and exo-anomeric effects) in the monothio and the dithioacetal functions. *Can. J. Chem.* **1981**, *59*, 1122–1131.
- [76] J. Cordes, P. R. D. Murray, A. J. P. White, A. G. M. Barrett. 1,7-Diazaspiro[5.5]undecane: A Neglected Heterocycle. *Org. Lett.* **2013**, *15*, 4992–4995.
- [77] W.-H. Hsu, Y.-Y. Lee, W.-H. Peng, K. C.-W. Wu. Cellulosic conversion in ionic liquids (ILs): Effects of H₂O/cellulose molar ratios, temperatures, times, and different ILs on the production of monosaccharides and 5-hydroxymethylfurfural (HMF). *Catal. Today* **2011**, *174*, 65–69.
- [78] A. A. Rosatella, S. P. Simeonov, R. F. M. Frade, C. A. M. Afonso. 5-Hydroxymethylfurfural (HMF) as a building block platform: Biological properties, synthesis and synthetic applications. *Green Chem.* **2011**, *13*, 754–793.
- [79] T. Ståhlberg, W. Fu, J. M. Woodley, A. Riisager. Synthesis of 5-(Hydroxymethyl)furfural in Ionic Liquids: Paving the Way to Renewable Chemicals. *ChemSusChem* **2011**, *4*, 451–458.

- [80] G. Yong, Y. Zhang, J. Ying. Efficient Catalytic System for the Selective Production of 5-Hydroxymethylfurfural from Glucose and Fructose. *Angew. Chem. Int. Ed.* **2008**, *47*, 9345–9348.
- [81] S. Hu, Z. Zhang, J. Song, Y. Zhou, B. Han. Efficient conversion of glucose into 5-hydroxymethylfurfural catalyzed by a common Lewis acid SnCl₄ in an ionic liquid. *Green Chem.* **2009**, *11*, 1746–1749.
- [82] H. Zhao, J. E. Holladay, H. Brown, Z. C. Zhang. Metal Chlorides in Ionic Liquid Solvents Convert Sugars to 5-Hydroxymethylfurfural. *Science* **2007**, *316*, 1597–1600.
- [83] J. B. Binder, R. T. Raines. Simple Chemical Transformation of Lignocellulosic Biomass into Furans for Fuels and Chemicals. *J. Am. Chem. Soc.* **2009**, *131*, 1979–1985.
- [84] T. Wang, Y. J. Pagán-Torres, E. J. Combs, J. A. Dumesic, B. H. Shanks. Water-Compatible Lewis Acid-Catalyzed Conversion of Carbohydrates to 5-Hydroxymethylfurfural in a Biphasic Solvent System. *Top. Catal.* **2012**, *55*, 657–662.
- [85] X. Qian, M. R. Nimlos, M. Davis, D. K. Johnson, M. E. Himmel. Ab initio molecular dynamics simulations of β -d-glucose and β -d-xylose degradation mechanisms in acidic aqueous solution. *Carbohydr. Res.* **2005**, *340*, 2319–2327.
- [86] T. Ståhlberg, S. Rodriguez-Rodriguez, P. Fristrup, A. Riisager. Metal-Free Dehydration of Glucose to 5-(Hydroxymethyl)furfural in Ionic Liquids with Boric Acid as a Promoter. *Chem. Eur. J.* **2011**, *17*, 1456–1464.
- [87] R. S. Assary, P. C. Redfern, J. Greeley, L. A. Curtiss. Mechanistic Insights into the Decomposition of Fructose to Hydroxy Methyl Furfural in Neutral and Acidic Environments Using High-Level Quantum Chemical Methods. *J. Phys. Chem. B* **2011**, *115*, 4341–4349.
- [88] R. S. Assary, T. Kim, J. J. Low, J. Greeley, L. A. Curtiss. Glucose and fructose to platform chemicals: understanding the thermodynamic landscapes of acid-catalysed reactions using high-level ab initio methods. *Phys. Chem. Chem. Phys.* **2012**, *14*, 16603–16611.
- [89] G. Yang, E. A. Pidko, E. J. Hensen. Mechanism of Brønsted acid-catalyzed conversion of carbohydrates. *J. Catal.* **2012**, *295*, 122–132.
- [90] Y. Román-Leshkov, M. Moliner, J. A. Labinger, M. E. Davis. Mechanism of Glucose Isomerization Using a Solid Lewis Acid Catalyst in Water. *Angew. Chem. Int. Ed.* **2010**, *49*, 8954–8957.

- [91] E. A. Pidko, V. Degirmenci, R. A. van Santen, E. J. M. Hensen. Glucose Activation by Transient Cr^{2+} Dimers. *Angew. Chem. Int. Ed.* **2010**, *49*, 2530–2534.
- [92] E. A. Pidko, V. Degirmenci, E. J. M. Hensen. On the Mechanism of Lewis Acid Catalyzed Glucose Transformations in Ionic Liquids. *ChemCatChem* **2012**, *4*, 1263–1271.
- [93] J. Guan, Q. Cao, X. Guo, X. Mu. The mechanism of glucose conversion to 5-hydroxymethylfurfural catalyzed by metal chlorides in ionic liquid: A theoretical study. *Comput. Theor. Chem.* **2011**, *963*, 453–462.
- [94] G. Yang, E. A. Pidko, E. J. M. Hensen. The Mechanism of Glucose Isomerization to Fructose over Sn-BEA Zeolite: A Periodic Density Functional Theory Study. *ChemSusChem* **2013**, *6*, 1688–1696.
- [95] V. Choudhary, S. H. Mushrif, C. Ho, A. Anderko, V. Nikolakis, N. S. Marinkovic, A. I. Frenkel, S. I. Sandler, D. G. Vlachos. Insights into the Interplay of Lewis and Brønsted Acid Catalysts in Glucose and Fructose Conversion to 5-(Hydroxymethyl)furfural and Levulinic Acid in Aqueous Media. *J. Am. Chem. Soc.* **2013**, *135*, 3997–4006.
- [96] I. Levine, *Quantum Chemistry*, Prentice Hall, **2000**.
- [97] W. Kutzelnigg, *Einführung in die Theoretische Chemie*, Wiley-VCH, Weinheim, **1992**.
- [98] A. Szabo, N. S. Ostlund, *Modern Quantum Chemistry*, Dover, **1996**.
- [99] F. Jensen, *Introduction to Computational Chemistry*, Wiley-VCH, Weinheim, **2003**.
- [100] C. Cramer, *Essentials of Computational Chemistry: Theories and Models*, Wiley-VCH, Weinheim, **2004**.
- [101] D. Frenkel, B. Smit, *Understanding Molecular Simulation: from Algorithms to Applications 1st ed.*, Academic press: San Diego, **2001**.
- [102] P. Hohenberg, W. Kohn. Inhomogeneous Electron Gas. *Phys. Rev.* **1964**, *136*, 864–871.
- [103] W. Kohn, L. Sham. Self-Consistent Equations Including Exchange and Correlation Effects. *Phys. Rev. A* **1965**, *140*, 1133–1138.
- [104] J. Perdew. Density-functional approximation for the correlation energy of the inhomogeneous electron gas. *Phys. Rev. B* **1986**, *33*, 8822–8824.

- [105] A. D. Becke. Density-functional exchange-energy approximation with correct asymptotic behavior. *Phys. Rev. A* **1988**, *38*, 3098–3100.
- [106] S. Vosko, L. Wilk, M. Nusair. Accurate spin-dependent electron liquid correlation energies for local spin density calculations: a critical analysis. *Can. J. Phys.* **1980**, *58*, 1200–1211.
- [107] C. Lee, W. Yang, R. G. Parr. Development of the Colle-Salvetti correlation-energy formula into a functional of the electron density. *Phys. Rev. B* **1988**, *37*, 785–789.
- [108] A. D. Becke. Density-functional thermochemistry. III. The role of exact exchange. *J. Chem. Phys.* **1993**, *98*, 5648–5652.
- [109] Y. Zhao, B. J. Lynch, D. G. Truhlar. Development and Assessment of a New Hybrid Density Functional Model for Thermochemical Kinetics. *J. Phys. Chem. A* **2004**, *108*, 2715–2719.
- [110] C. Adamo, V. Barone. Toward reliable density functional methods without adjustable parameters: The PBE0 model. *J. Chem. Phys.* **1999**, *110*, 6158–6169.
- [111] Y. Zhao, N. E. Schultz, D. G. Truhlar. Design of Density Functionals by Combining the Method of Constraint Satisfaction with Parametrization for Thermochemistry, Thermochemical Kinetics, and Noncovalent Interactions. *J. Chem. Theory Comput.* **2006**, *2*, 364–382.
- [112] G. I. Csonka, A. D. French, G. P. Johnson, C. A. Stortz. Evaluation of Density Functionals and Basis Sets for Carbohydrates. *J. Chem. Theory Comput.* **2009**, *5*, 679–692.
- [113] S. F. Sousa, P. A. Fernandes, M. J. Ramos. General Performance of Density Functionals. *J. Phys. Chem. A* **2007**, *111*, 10439–10452.
- [114] N. F. Brás, S. A. Moura-Tamames, P. A. Fernandes, M. J. Ramos. Mechanistic studies on the formation of glycosidase-substrate and glycosidase-inhibitor covalent intermediates. *J. Comput. Chem.* **2008**, *29*, 2565–2574.
- [115] N. F. Brás, P. A. Fernandes, M. J. Ramos. QM/MM Studies on the β -Galactosidase Catalytic Mechanism: Hydrolysis and Transglycosylation Reactions. *J. Chem. Theory Comput.* **2010**, *6*, 421–433.
- [116] Y. Zhao, D. G. Truhlar. Benchmark Energetic Data in a Model System for Grubbs II Metathesis Catalysis and Their Use for the Development, Assessment, and Validation of Electronic Structure Methods. *J. Chem. Theory Comput.* **2009**, *5*, 324–333.

- [117] J. M. del Campo, J. L. Gázquez, S. B. Trickey, A. Vela. Non-empirical improvement of PBE and its hybrid PBE0 for general description of molecular properties. *J. Chem. Phys.* **2012**, *136*, 104108.
- [118] Y. Zhao, D. G. Truhlar. Density Functionals with Broad Applicability in Chemistry. *Acc. Chem. Res.* **2008**, *41*, 157–167.
- [119] E. A. Pidko, V. Degirmenci, R. A. van Santen, E. J. M. Hensen. Coordination Properties of Ionic Liquid-Mediated Chromium(II) and Copper(II) Chlorides and Their Complexes with Glucose. *Inorg. Chem.* **2010**, *49*, 10081–10091.
- [120] J. Slater. Atomic Shielding Constants. *Phys. Rev.* **1930**, *36*, 57–64.
- [121] S. Boys. Electronic Wave Functions. I. A General Method of Calculation for the Stationary States of Any Molecular System. *Proc. R. Soc. (London) A* **1950**, *200*, 542–554.
- [122] W. Hehre, R. Stewart, J. Pople. Self-Consistent Molecular-Orbital Methods. I. Use of Gaussian Expansions of Slater-Type Atomic Orbitals. *J. Chem. Phys.* **1969**, *51*, 2657–2664.
- [123] P. Hariharan, J. Pople. The influence of polarization functions on molecular orbital hydrogenation energies. *Theor. Chim. Acta* **1973**, *28*, 213–222.
- [124] F. Weigend, R. Ahlrichs. Balanced basis sets of split valence, triple zeta valence and quadruple zeta valence quality for H to Rn: Design and assessment of accuracy. *Phys. Chem. Chem. Phys.* **2005**, *7*, 3297–3305.
- [125] A. Schaefer, H. Horn, R. Ahlrichs. Fully optimized contracted Gaussian-basis sets for atoms Li to Kr. *J. Chem. Phys.* **1992**, *97*, 2571–2577.
- [126] A. Schaefer, C. Huber, R. Ahlrichs. Fully optimized contracted Gaussian-basis sets of triple zeta valence quality for atoms Li to Kr. *J. Chem. Phys.* **1994**, *100*, 5829–5835.
- [127] T. Dunning. Gaussian basis sets for use in correlated molecular calculations. I. The atoms boron through neon and hydrogen. *J. Chem. Phys.* **1989**, *90*, 1007–1023.
- [128] D. Woon, T. Dunning. Gaussian basis sets for use in correlated molecular calculations. III. The atoms aluminum through argon. *J. Chem. Phys.* **1993**, *98*, 1358–1371.
- [129] M. Cossi, N. Rega, G. Scalmani, V. Barone. Energies, structures, and electronic properties of molecules in solution with the C-PCM solvation model. *J. Comp. Chem.* **2003**, *24*, 669–681.

- [130] Y. Takano, K. N. Houk. Benchmarking the Conductor-like Polarizable Continuum Model (CPCM) for Aqueous Solvation Free Energies of Neutral and Ionic Organic Molecules. *J. Chem. Theory Comput.* **2005**, *1*, 70–77.
- [131] A. V. Marenich, C. J. Cramer, D. G. Truhlar. Performance of SM6, SM8, and SMD on the SAMPL1 Test Set for the Prediction of Small-Molecule Solvation Free Energies. *J. Phys. Chem. B* **2009**, *113*, 4538–4543.
- [132] W. D. Cornell, P. Cieplak, C. Bayly, I. Gould, K. Merzi, J. D. M. Ferguson, D. Spellmeyer, T. Fox, J. Caldwell, P. A. Kollman. A Second Generation Force Field for the Simulation of Proteins, Nucleic Acids, and Organic Molecules. *J. Am. Chem. Soc.* **1995**, *117*, 5179–5197.
- [133] B. L. Foley, M. B. Tessier, R. J. Woods. Carbohydrate force fields. *WIREs Comput. Mol. Sci.* **2012**, *2*, 652–697.
- [134] K. N. Kirschner, A. B. Yongye, S. M. Tschampel, J. González-Outeiriño, C. R. Daniels, B. L. Foley, R. J. Woods. GLYCAM06: A generalizable biomolecular force field. Carbohydrates. *J. Comput. Chem.* **2008**, *29*, 622–655.
- [135] V. Spiwok, B. Králová, I. Tvaroška. Modelling of β -d-glucopyranose ring distortion in different force fields: a metadynamics study. *Carbohydr. Res.* **2010**, *345*, 530–537.
- [136] C. A. Stortz, G. P. Johnson, A. D. French, G. I. Csonka. Comparison of different force fields for the study of disaccharides. *Carbohydr. Res.* **2009**, *344*, 2217–2228.
- [137] P. Sherwood, A. de Vries, M. F. Guest, G. Schreckenbach, C. A. Catlow, S. A. French, A. A. Sokol, S. T. Bromley, W. Thiel, A. J. Turner, S. Billeter, F. Terstegen, S. Thiel, J. Kendrick, S. C. Rogers, J. Casci, M. Watson, F. King, E. Karlsen, M. Sjøvoll, A. Fahmi, A. Schäfer, C. Lennartz. QUASI: A general purpose implementation of the QM/MM approach and its application to problems in catalysis. *J. Mol. Struct.* **2003**, *632*, 1–28.
- [138] H. M. Senn, W. Thiel. QM/MM Methods for Biological Systems. *Top. Curr. Chem.* **2007**, *268*, 173–290.
- [139] H. M. Senn, W. Thiel. QM/MM Methods for Biomolecular Systems. *Angew. Chem. Int. Ed.* **2009**, *48*, 1198–1229.
- [140] U. C. Singh, P. Kollmann. A combined ab initio quantum mechanical and molecular mechanical method for carrying out simulations on complex molecular systems: Applications to the $\text{CH}_3\text{Cl} + \text{Cl}^-$ exchange reaction

- and gas phase protonation of polyethers. *J. Comput. Chem.* **1986**, *7*, 718–730.
- [141] A. H. de Vries, P. Sherwood, S. J. Collins, A. M. Rigby, M. Rigutto, G. J. Kramer. Zeolite Structure and Reactivity by Combined Quantum-Chemical-Classical Calculations. *J. Phys. Chem. B* **1999**, *103*, 6133–6141.
- [142] P. Sherwood, A. H. de Vries, S. J. Collins, S. P. Greatbanks, N. A. Burton, I. H. Hillier. Computer simulation of zeolite structure and reactivity using embedded cluster methods. *Faraday Discuss.* **1997**, 79–92.
- [143] D. Bakowies, W. Thiel. Hybrid Models for Combined Quantum Mechanical and Molecular Mechanical Approaches. *Phys Chem.* **1996**, *100*, 10580–10594.
- [144] J. Kästner, J. M. Carr, T. W. Keal, W. Thiel, A. Wander, P. Sherwood. DL-FIND: An Open-Source Geometry Optimizer for Atomistic Simulations. *J. Phys. Chem. A* **2009**, *113*, 11856–11865.
- [145] ChemShell, a Computational Chemistry Shell, see: www.chemshell.org.
- [146] C. Gonzalez, H. B. Schlegel. An improved algorithm for reaction path following. *J. Chem. Phys.* **1989**, *90*, 2154–2161.
- [147] C. Gonzalez, H. B. Schlegel. Reaction path following in mass-weighted internal coordinates. *J. Phys. Chem.* **1990**, *94*, 5523–5527.
- [148] J. Ho, M. L. Coote. A universal approach for continuum solvent pK_a calculations: are we there yet? *Theo. Chem. Acc.* **2010**, *125*, 3–21.
- [149] V. S. Bryantsev, M. S. Diallo, W. A. G. III. Calculation of Solvation Free Energies of Charged Solutes Using Mixed Cluster/Continuum Models. *J. Phys. Chem. B* **2008**, *112*, 9709–9719.
- [150] A. Barducci, M. Bonomi, M. Parrinello. Metadynamics. *WIREs Comput. Mol. Sci.* **2011**, *1*, 826–843.
- [151] T. G. A. Youngs, C. Hardacre, J. D. Holbrey. Glucose Solvation by the Ionic Liquid 1,3-Dimethylimidazolium Chloride: A Simulation Study. *J. Phys. Chem. B* **2007**, *111*, 13765–13774.
- [152] J. C. Phillips, R. Braun, W. Wang, J. Gumbart, E. Tajkhorshid, E. Villa, C. Chipot, R. D. Skeel, L. Kalé, K. Schulten. Scalable molecular dynamics with NAMD. *J. Comput. Chem.* **2005**, *26*, 1781–1802.

- [153] H. S. Hansen, P. H. Hünenberger. Using the local elevation method to construct optimized umbrella sampling potentials: Calculation of the relative free energies and interconversion barriers of glucopyranose ring conformers in water. *J. Comput. Chem.* **2010**, *31*, 1–23.
- [154] F. Weinhold, C. R. Landis. Natural Bond Orbitals and Extensions of Localized Bonding Concepts. *Chem. Educ. Res. Pract. Eur.* **2001**, *2*, 91–104.
- [155] P.-O. Löwdin. Quantum Theory of Many-Particle Systems. I. Physical Interpretations by Means of Density Matrices, Natural Spin-Orbitals, and Convergence Problems in the Method of Configurational Interaction. *Phys. Rev.* **1955**, *97*, 1474–1489.
- [156] E. D. Glendenning, C. R. Landis, F. Weinhold. Natural bond orbital methods. *WIREs Comput. Mol. Sci.* **2012**, *2*, 1–42.
- [157] S. Metz, W. Thiel. A Combined QM/MM Study on the Reductive Half-Reaction of Xanthine Oxidase: Substrate Orientation and Mechanism. *J. Am. Chem. Soc.* **2009**, *131*, 14885–14902.
- [158] J. T. Ham, D. G. Williams. The crystal and molecular structure of methyl β -cellobioside methanol. *Acta Crystallogr. Sect. B* **1970**, *26*, 1373–1383.
- [159] A. Rencurosi, J. Röhring, J. Pauli, A. Potthast, C. Jäger, S. Pérez, P. Kosma, A. Imberty. Polymorphism in the Crystal Structure of the Cellulose Fragment Analogue Methyl 4-O-Methyl- β -D-Glucopyranosyl-(1-4)- β -D-Glucopyranoside. *Angew. Chem. Int. Ed.* **2002**, *41*, 4277–4281.
- [160] T. G. A. Youngs, J. D. Holbrey, C. L. Mullan, S. E. Norman, M. C. Lagunas, C. D’Agostino, M. D. Mantle, L. F. Gladden, D. T. Bowron, C. Hardacre. Neutron diffraction, NMR and molecular dynamics study of glucose dissolved in the ionic liquid 1-ethyl-3-methylimidazolium acetate. *Chem. Sci.* **2011**, *2*, 1594–1605.
- [161] Y. Zhao, X. Liu, J. Wang, S. Zhang. Effects of Cationic Structure on Cellulose Dissolution in Ionic Liquids: A Molecular Dynamics Study. *ChemPhysChem* **2012**, *13*, 3126–3133.
- [162] B. D. Rabideau, A. Agarwal, A. E. Ismail. Observed Mechanism for the Breakup of Small Bundles of Cellulose I_α and I_β in Ionic Liquids from Molecular Dynamics Simulations. *J. Phys. Chem. B* **2013**, *117*, 3469–3479.
- [163] Y. Zhao, X. Liu, J. Wang, S. Zhang. Effects of anionic structure on the dissolution of cellulose in ionic liquids revealed by molecular simulation. *Carbohydr. Polym.* **2013**, *94*, 723–730.

- [164] J. Zhang, H. Zhang, J. Wu, J. Zhang, J. He, J. Xiang. NMR spectroscopic studies of cellobiose solvation in EmimAc aimed to understand the dissolution mechanism of cellulose in ionic liquids. *Phys. Chem. Chem. Phys.* **2010**, *12*, 1941–1947.
- [165] Personal communication with Marc-Philipp Ruby.
- [166] A. F. Hollemann, N. Wiberg, *Lehrbuch der Anorganischen Chemie 101st ed.*, N. Wiberg (Ed.), Walter de Gruyter, Berlin/New York, **1995**.
- [167] Entry of Merck Millipore for CAS 10125–13–0, copper(II) chloride dihydrate.
- [168] L. Nagy, H. Ohtaki, T. Yamaguchi, M. Nomura. EXAFS study of iron(III) complexes of sugar-type ligands. *Inorg. Chim. Acta* **1989**, *159*, 201–207.
- [169] J. Briggs, P. Finch, M. C. Matulewicz, H. Weigel. Complexes of copper(II), calcium, and other metal ions with carbohydrates: Thin-layer ligand-exchange chromatography and determination of relative stabilities of complexes. *Carbohydr. Res.* **1981**, *97*, 181–188.
- [170] W. Grzybowski. Nature and Properties of Metal Cations in Aqueous Solutions. *Polish J. of Environ. Stud.* **2006**, *15*, 655–663.
- [171] G. Ottonello, M. V. Zuccolini. Ab-initio structure, energy and stable Fe isotope equilibrium fractionation of some geochemically relevant H–O–Fe complexes. *Geochim. Cosmochim. Ac.* **2009**, *73*, 6447–6469.
- [172] G. Ottonello, M. V. Zuccolini. Ab-initio structure, energy and stable Cr isotopes equilibrium fractionation of some geochemically relevant H–O–Cr–Cl complexes. *Geochim. Cosmochim. Ac.* **2005**, *69*, 851–874.
- [173] R. Martin. Fe³⁺ and Al³⁺ hydrolysis equilibria. Cooperativity in Al³⁺ hydrolysis reactions. *J. Inorg. Biochem.* **1991**, *44*, 141–147.
- [174] K. Geetha, M. S. Raghavan, S. K. Kulshreshtha, R. Sasikala, C. P. Rao. Transition-metal saccharide chemistry: synthesis, spectroscopy, electrochemistry and magnetic susceptibility studies of iron(III) complexes of mono- and disaccharides. *Carbohydr. Res.* **1995**, *271*, 163–175.
- [175] S. Bogatko, P. Geerlings. Factors influencing Al³⁺-dimer speciation and stability from density functional theory calculations. *Phys. Chem. Chem. Phys.* **2012**, *14*, 8058–8066.

Appendix A

The Electronic Nature of the 1, 4- β -Glycosidic Bond and Its Chemical Environment: DFT Insights into Cellulose Chemistry

Claudia Loerbroks, Roberto Rinaldi, and Walter Thiel

Chemistry - A European Journal, **2013**, 19, 16282 – 16294.

Carried out all calculations, analyzed the results, and wrote parts of the manuscript

The cartesian coordinates were deleted from the Supporting Information and can be found in the published version of the manuscript.

The Electronic Nature of the 1,4- β -Glycosidic Bond and Its Chemical Environment: DFT Insights into Cellulose Chemistry

Claudia Loerbroks, Roberto Rinaldi,* and Walter Thiel*[a]

Abstract: The molecular understanding of the chemistry of 1,4- β -glucans is essential for designing new approaches to the conversion of cellulose into platform chemicals and biofuels. In this endeavor, much attention has been paid to the role of hydrogen bonding occurring in the cellulose structure. So far, however, there has been little discussion about the implications of the electronic nature of the 1,4- β -glycosidic bond and its chemical environment for the activation of 1,4- β -glucans toward

acid-catalyzed hydrolysis. This report sheds light on these central issues and addresses their influence on the acid hydrolysis of cellobiose and, by analogy, cellulose. The electronic structure of cellobiose was explored by DFT at the BB1K/6-31++G(d,p) level. Natu-

ral bond orbital (NBO) analysis was performed to grasp the key bonding concepts. Conformations, protonation sites, and hydrolysis mechanisms were examined. The results for cellobiose indicate that cellulose is protected against hydrolysis not only by its supramolecular structure, as currently accepted, but also by its electronic structure, in which the anomeric effect plays a key role.

Keywords: cellobiose · cellulose hydrolysis · computational chemistry · density functional calculations · NBO analysis

Introduction

Enormous efforts have been made toward economically feasible and environmentally friendly processes for hydrolysis of cellulose.^[1,2] These efforts aim at the utilization of lignocellulose materials (e.g., crop residues, wood, and several others) for the production of fermentable sugars and, ultimately, biofuels that do not threaten food and feed supply. Despite the progress achieved in the last hundred years, several key aspects of the chemistry of cellulose hydrolysis are still unclear or rely too heavily upon qualitative judgment.^[1-10]

The anhydroglucose units (AGUs) are linked by 1,4- β -glycosidic bonds in cellulose. The glycosidic linkage is part of an acetal formed by the O(5)–C(1)–O(1) bonds. The orbital interactions within the acetal group give rise to the anomeric effect. Despite the fact that several structural and reactivity features of carbohydrates are manifestations of the anomeric effect, there has been almost no discussion of its influence on the reactivity of cellulose. Reportedly, the major implication of the anomeric effect for cellulose seems to be the shortening of the C(1)–O(1) bond, relative to the C(4')–O(1) bond, by about 0.04 Å.^[11-16]

The chemical environment of the 1,4- β -glycosidic linkage is defined by the pyranic O site and the vicinal hydroxyl groups. The intramolecular hydrogen bonding involving these groups constitutes an important part of the chemical environment. In the crystal form of cellulose I $_{\beta}$, which occurs in plants,^[17] the intra- and intermolecular hydrogen-bonding patterns were characterized by neutron diffraction.^[18-20] This technique revealed the occurrence of several intramolecular hydrogen bonds: O(5)···HO(3'), O(2)H···O(6'), and O(2)···HO(6'), in addition to the intermolecular hydrogen bond O(6')H···O(3''), as shown in Figure 1.^[18] Although the position of the hydrogen atom in O(5)···HO(3') was determined with good precision by neutron diffraction, the hydrogen atoms at the O(2) and O(6) atoms could not be located exactly.^[18] In this study, two hy-

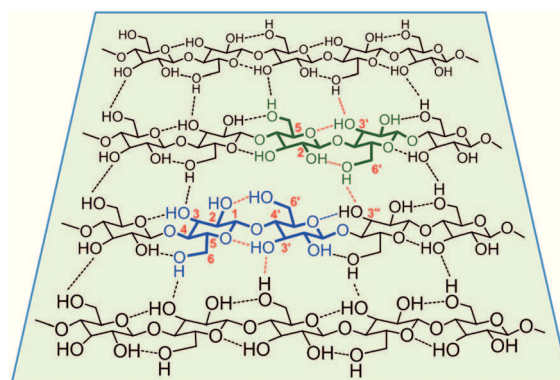


Figure 1. Fragment of a cellulose sheet depicting the hydrogen-bond patterns: network I (in green) and network II (in blue), as proposed by neutron diffraction studies.^[18]

[a] C. Loerbroks, Dr. R. Rinaldi, Prof. Dr. W. Thiel
Max-Planck-Institut für Kohlenforschung
Kaiser-Wilhelm-Platz 1
45470 Mülheim an der Ruhr (Germany)
Fax: (+49) 208-306-2996
E-mail: rinaldi@kofo.mpg.de
thiel@kofo.mpg.de

Supporting information for this article is available on the WWW under <http://dx.doi.org/10.1002/chem.201301366>.

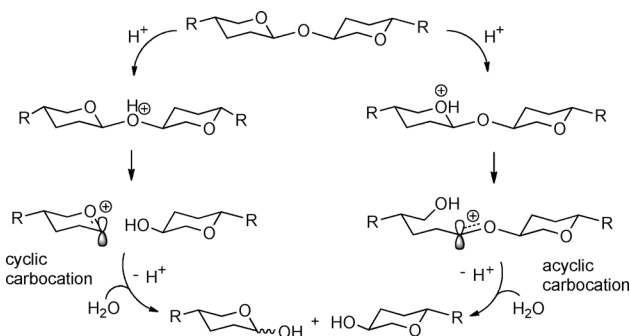
hydrogen-bonding networks were identified containing either O(2)H...O(6') (74 to 81 % hydrogen occupancy, forming the so-called "network I") or O(2)...HO(6') (19 to 26 % hydrogen occupancy, "network II").^[18] It was concluded that both O(2)H...O(6') and O(2)...HO(6') bonds may randomly occur in cellulose I_β and that they may even be dynamically interconverting, in addition to the possible occurrence of other hydrogen-bonding patterns.^[18]

The intermolecular hydrogen bond O(6')H...O(3'') is responsible for keeping the cellulose chains together within the sheets,^[18–20] through side-by-side packing of the chains (Figure 1). The sheets are stacked on top of each other, and held together by van der Waals forces and by weak intersheet hydrogen bonding between CH...O sites.^[18] These interactions build up the supramolecular structure of cellulose I_β in which solvents, reactants, acid catalysts, or enzymes can access only the polymeric chains at the surface of the cellulose microfibrils. Accordingly, the supramolecular structure is considered as one of the major hurdles to hydrolysis of cellulose.^[1]

Upon dissolving the biopolymer, for example, in ionic liquids (ILs),^[23–25] the supramolecular structure of cellulose is disassembled, and as a result, cellulose displays reactivity similar to cellobiose. In solution, both cellobiose and cellulose are prone to undergo hydrolysis in the presence of an acid at temperatures as low as 100 °C.^[26–29] Nonetheless, even in solution, the hydrolysis of 1,4-β-glucans needs a strong acid catalyst (pK_a < -3) to proceed at reasonable reaction rates.^[30–32] This fact suggests that there should be other factors contributing to the high resistance of 1,4-β-glucans to hydrolysis.

It is evident from studies of cellobiose hydrolysis that the protonation of the glycosidic O site is a rapid, equilibrium-controlled process.^[1–9,20–32] Earlier experimental studies propose a so-called "stepwise A1 mechanism."^[33,34] The formation of a (cyclic) carbocation, upon heterolytic cleavage of the C(1)–O(1) bond, is regarded as the rate-determining step.^[35]

Two mechanisms are commonly considered for the hydrolysis of glycosides, as depicted in Scheme 1.^[1] Substituents at the glycoside and the reaction solvent exert a decisive influence on the reaction pathway.^[36,37] A mechanism involving an acyclic carbocation is often proposed for the hydroly-



Scheme 1. Mechanisms proposed for the hydrolysis of glycosides. The hydroxyl groups are omitted for clarity.

sis of glycosides confronted with ring strain issues or containing a poor leaving group,^[38,39] whereas a mechanism through a cyclic carbocation is often assumed for cellulose.^[40–43] Both acyclic and cyclic carbocations should have a short life time in solution.^[44]

Computational studies applying *ab initio*,^[45–49] density functional theory (DFT),^[36,37] and molecular dynamics (MD) methods^[37,50–53] have been performed in order to uncover some mechanistic aspects of the hydrolysis of cellulose. Although cellobiose is an excellent model for cellulose, smaller molecules, such as dimethoxymethane,^[45] 2-methoxytetrahydropyran,^[46] 2-oxanol,^[48] and 2-methoxyoxane^[49] were chosen in the earlier computational studies because of limited computing power. These models lack the hydroxyl groups surrounding the glycosidic linkage. There is experimental evidence, however, that the activation of the O-glycosidic site could be hindered by the preferential protonation of the hydroxyl O sites in cellulose.^[30,54]

The acid hydrolysis of guloseptanosides in methanol was investigated by relaxed potential energy scans (M06-2X/6-311+G** with methanol represented by a polarizable continuum model).^[36] This study showed that the hydroxyl group on the C(2) atom affects the hydrolysis mechanism because of its proximity to the anomeric carbon atom. The calculations predicted that the reaction should be also affected by the hydrogen-bond interaction of the hydroxyl group with the departing methanol from the α anomer.

Recently, Car-Parrinello MD simulations combined with metadynamics were applied to study the acid-catalyzed hydrolysis of cellobiose in aqueous solution.^[51] It was found that a stepwise mechanism for the glycosidic-bond cleavage is not significantly favored over a concerted mechanism. A slow conformational change in the cyclic carbocation was also detected. Both the proton transfer from water to the glycosidic O site and the glycosidic-bond cleavage were identified as critical steps. For both processes, a barrier of about 33 kcal mol⁻¹ was reported. This value is consistent with experimental results.^[55,56]

This article sheds light on the electronic nature of the 1,4-β-glycosidic bond and its chemical environment. To understand the fundamental bonding concepts based on DFT computations, natural bond orbital (NBO) analysis was performed. In the light of our results, the importance of the anomeric effect and hydrogen bonding in the structural stabilization and reactivity of cellobiose are discussed. In addition, the roles of the chemical environment of the 1,4-β-glycosidic bond in the activation of cellobiose toward acid hydrolysis are addressed in detail. The implications of these findings for the resistance of cellulose against acid hydrolysis are also examined. The paper is organized as follows: after a brief description of the computational methodology, we address the influence of *endo*-, *exo*-anomeric effects, and hydrogen bonding on the stability of various cellobiose structures. Thereafter, we discuss the protonation of the different O sites in cellobiose. Finally, we report a DFT study on the hydrolysis mechanism of cellobiose, with consideration of stereoelectronic effects.

Computational Details

Because a bundle of several cellulose chains, comprising 30–40 AGUs each and interacting by intermolecular hydrogen bonding, is a very large system for DFT calculations, we chose cellobiose (Figure 2) as a model for the assessment of the electronic nature of the 1,4- β -glycosidic bond and its chemical environment.

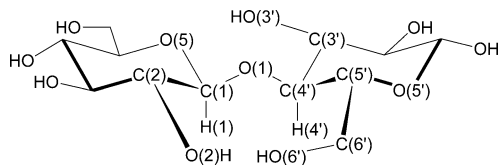


Figure 2. Atom numbering used in the cellobiose structures.

By using the BB1K density functional and the 6-31++G(d,p) basis set provided within the Gaussian 09 program suite, DFT calculations were performed on cellobiose structures.^[57] The chosen basis set contains diffuse functions that are required for the correct description of intramolecular hydrogen bonds.^[58] The BB1K functional is a hybrid functional with 42% Hartree–Fock exchange, designed for kinetic studies.^[59] This functional shows good performance in general for calculations on barrier heights (mean unsigned error (MUE) ≤ 1.58 kcal mol⁻¹) and transition-state structures (MUE = 0.02 Å) in benchmark studies both on hydrogen-transfer and non-hydrogen-transfer reactions with the MG3S and aug-cc-pVTZ basis sets.^[60] The BB1K functional was successfully used for hydrolysis studies of different methyl galactose systems (DFT and QM/MM) and yielded energies closer to QCISD(T)/6-31G(d) than the B3LYP functional.^[61,62] Furthermore, the B3LYP functional showed the worst performance, when compared with GGA, meta-GGA, and hybrid functionals, in calculations on saccharide conformations by various DFT functionals and MP2/aug-cc-pVTZ.^[58] These literature data prompted us to adopt the BB1K functional.

Unless stated otherwise, solvent effects were included in all calculations and treated by a polarizable continuum model (CPCM)^[63] with universal force field (UFF) cavities (water as solvent). For comparison and validation, different solvent models and cavities were investigated (see the Supporting Information). The calculation of solvation free energies through thermodynamic cycles was done with the SMD solvation model.^[64] Geometry optimizations were carried out without any constraints, unless noted otherwise. Local minima (no imaginary mode) and transition states (one imaginary mode) were characterized by harmonic force constant analysis. Gibbs free energies were obtained by adding thermal corrections. The connectivity of transition states and minima was verified by intrinsic reaction coordinate (IRC)^[65,66] calculations, unless mentioned otherwise. To estimate the energy of elusive transition states, scans of the potential energy surface (PES) were performed.

For comparison, selected stationary points (structures **1**, **3–6**, and **10–16**) were optimized completely with different DFT functionals (B3LYP,^[67–70] M06-2X^[71]). Furthermore, single-point calculations were carried out on the BB1K/6-31++G(d,p) geometries of structures **1**, **3–6**, and **10–16** by using BB1K and a larger basis set, 6-311++G(3df,3pd). Compared with the BB1K/6-31++G(d,p) results, the standard deviations of the B3LYP/6-31++G(d,p), M06-2X/6-31++G(d,p), and BB1K/6-311++G(3df,3pd) Gibbs free energies for structures **1**, **3–6**, and **10–16** (STD_{BB1K}) were 2.2, 1.0, and 2.3 kcal mol⁻¹, respectively (see the Supporting Information). In turn, structures **17–25** were also subjected to single-point energy evaluation employing B3LYP/6-31++G(d,p), M06-2X/6-31++G(d,p) and BB1K/6-311++G(3df,3pd). These calculations were performed on geometries previously predicted by BB1K/6-31++G(d,p). The corresponding standard deviations of the single-point energies for structures **17–25** were 4.2, 10.2, and 1.7 kcal mol⁻¹, respectively. Even though these deviations are large, the trend of the energy profiles is generally similar to BB1K/6-31++G(d,p) (see the Supporting Information).

A natural bonding orbital (NBO) analysis for selected structures was performed by using the NBO 3.1 package^[72] implemented in Gaussian 09. The interactions of localized orbitals, involved in hydrogen bonding and anomeric effects, were quantified by second-order perturbation theory analysis, which characterizes the strength of the interaction in terms of the second-order energy $E(2)$ and the charge transfer from a donor to an acceptor orbital.

The basicity of its O sites was investigated by adding one proton at each relevant site. The relative basicity of these sites was assessed by calculating the corresponding free energies of protonation. The differences in the pK_b values were also determined directly from a thermodynamic cycle (see the Supporting Information for detailed data).

The mechanism of cellobiose hydrolysis was explored starting with a protonated species. Two water molecules were added sequentially, one for the nucleophilic attack at the cyclic carbocation and another one for the final proton transfer. In the following, the results of these computations are reported in terms of Gibbs free energies.

Results and Discussion

NBO analysis of cellobiose conformers: The NBO method characterizes hydrogen bonds $O(x)\cdots HO(y)$ in terms of hyperconjugative donor–acceptor interactions $n_{O(x)} \rightarrow \sigma_{O(y)H}^*$. In turn, the *exo*- and *endo*-anomeric effects are described by $n_{O(1)} \rightarrow \sigma_{C(1)O(5)}^*$ and $n_{O(5)} \rightarrow \sigma_{C(1)O(1)}^*$ interactions, respectively. The *exo*- and *endo*-anomeric effects involve the lone pair $O(1)_2$ and $O(5)_1$ that are located at the equatorial and axial position, respectively. Albeit, depending on the conformation of the pyranic ring, the *endo*-anomeric effect may involve the lone pair $n_{O(5)_2}$ instead of $n_{O(5)_1}$. Figure 3 depicts the localized molecular orbitals describing the donor–acceptor interactions, as found by the NBO analysis of structure **1**.

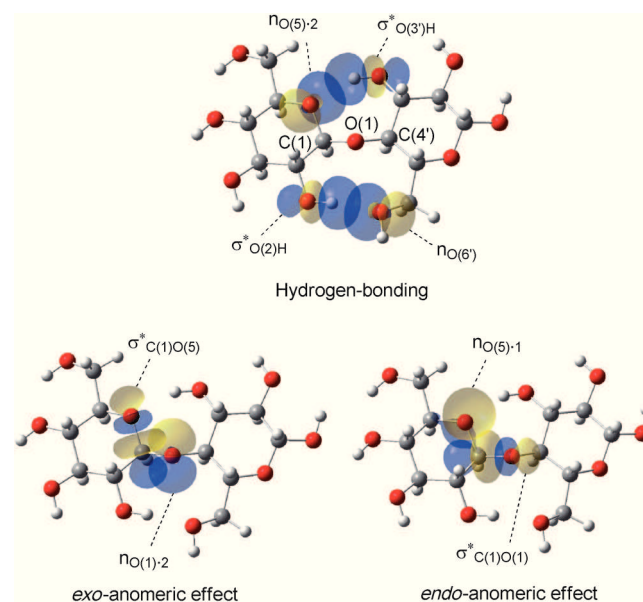


Figure 3. Interaction of the localized molecular orbitals involved in the hydrogen bonding and the *exo*- and *endo*-anomeric effects occurring in structure **1**. The labeling “-1” and “-2”, respectively, denote the axial and equatorial positions of the lone pairs on the O(1) and O(5) atoms.

In an endeavor to understand the significance of these secondary interactions for the structure and reactivity of cellulose, we performed calculations on the cellobiose structures **1–6** as models of subunits in cellulose (Figure 4). Structures **1** and **2** correspond to the subunits of cellulose occurring in crystalline domains, representing the intramolecular hydrogen bonds found in network I and network II, respectively.^[19] Structures **3** and **4** were generated to examine the effect of the rotation of the hydroxymethyl group involving the O(6') atom on the

Table 1. Gibbs free energies $\Delta\Delta G$ (in [kcal mol⁻¹]) relative to structure **1**, selected torsional angles and bond lengths for structures **1–6** (BB1K/6-31++G**, CPCM(water)).

Entry	Structure	$\Delta\Delta G$	Torsion angle [°]			Bond length [Å]	
			ϕ	ψ	χ	C(1)–O(1)	C(1)–O(5)
1	1	0.0	-91.9 (-88.7) ^[a]	-144.5 (-147.1) ^[a]	-76.9 (-83) ^[a]	1.375 (1.396) ^[a] (1.395) ^[b]	1.413 (1.438) ^[a] (1.445) ^[b]
2	2	-1.1	-89.5	-139.6	-82.9	1.373	1.410
3	3	0.3	-77.5	-150.9	-168.9	1.374	1.410
4	4	-0.4	-73.9	-121.3	53.2	1.376	1.410
5	5	7.5	0	-141.8	-79.4	1.400	1.392
6	6	9.1	180	-141.6	-80.2	1.397	1.396

[a] Experimental values for cellulose I_b taken from reference [19]. [b] Experimental values for methyl 4-O-methyl- β -cellobioside taken from references [76, 77].

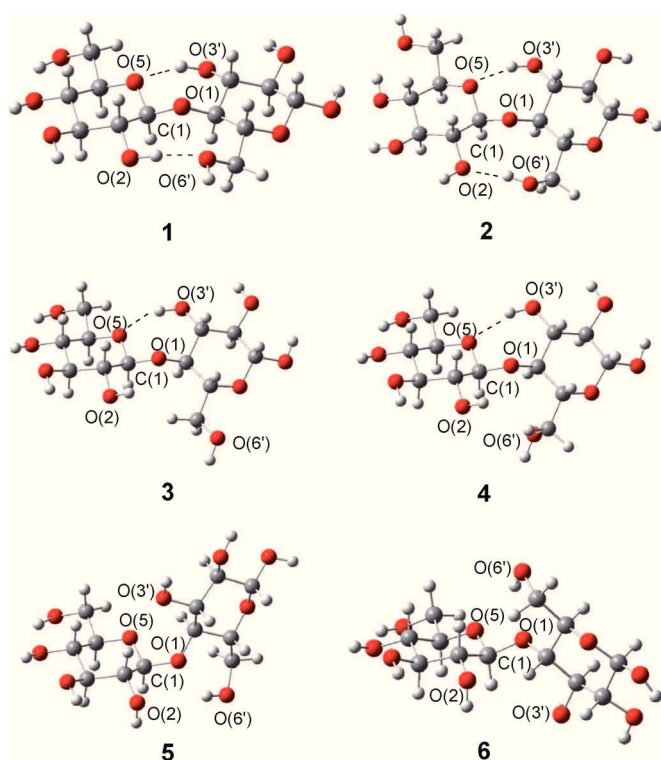


Figure 4. Optimized structures of the cellobiose conformers **1–6** (BB1K/6-31++G**, CPCM(water)). For a large-size version of this figure please see the Supporting Information.

1,4- β -glycosidic bond (compared with structure **1**). In these structures, the chemical environment of the 1,4- β -glycosidic bond is defined by the non-interacting hydroxyl groups O(2)H and O(6')H and by the hydrogen bond O(5)···HO(3'). As in structures **3** and **4**, the O(2)H···O(6') motif is also absent in several types of crystalline cellulose.^[1, 73, 74] Finally, structures **5** and **6** were chosen for the purpose of assessing the influence of the C(1)–O(1) bond rotation on the electronic nature of the 1,4- β -glycosidic bond (i.e., on the anomeric effect). These hypothetical structures characterize chemical environments without O(5)···HO(3') and O(2)H···O(6') or O(2)···HO(6') hydrogen bonds, which may be present in highly disordered subunits of cellulose in amorphous domains. Structures **1–6** are characterized by the torsional angles ϕ , that is, O(5)–C(1)–O(1)–C(4'), ψ , that is, C(1)–O(1)–C(4')–C(5'), and χ , that is, C(4')–C(5')–C(6')–O(6'), and by the bond lengths C(1)–O(1) and C(1)–O(5), as listed in Table 1.

Structure **1** contains the intramolecular hydrogen bonds O(5)···HO(3') and O(2)H···O(6'). It shows features similar to those found for cellulose I_b by X-ray and neutron diffraction studies (see Table 1, entry 1).^[19, 74] According to the NBO analysis (Table 2), the hydrogen bonds O(5)···HO(3') and O(2)H···O(6') stabilize structure **1** by 8.5 and 14.5 kcal mol⁻¹, respectively, with associated occupancies of $\sigma_{O(2)H}^*$ and $\sigma_{O(3')H}^*$ of 0.035 and 0.029 *e*. The dominant interaction comes from a $n_{O(1)} \rightarrow \sigma_{C(1)O(5)}^*$ charge transfer, which leads to a stabilization of 18.1 kcal mol⁻¹ and an occupancy of $\sigma_{C(1)O(5)}^*$ of 0.064 *e*.

Structure **2** has the intramolecular hydrogen bonds O(5)···HO(3') and O(2)···HO(6'). Despite this distinction

Table 2. Selected NBO results for structures **1–6** (BB1K/6-31++G**, CPCM(water)).

Entry	Structure	$E(2)$ donor–acceptor interactions [kcal mol ⁻¹]				Occupancy [<i>e</i>]			
		anomeric effect		hydrogen bonding					
		<i>exo</i>	<i>endo</i>			$\sigma_{C(1)O(5)}^*$	$\sigma_{C(1)O(1)}^*$	$\sigma_{O(3')H}^*$	$\sigma_{O(2)H}^*$
1	1	18.1	3.8	8.5	14.5	0.064	0.035	0.029	0.035
2	2	18.4	3.6	9.0	11.9 ($n_{O(2)} \rightarrow \sigma_{O(6')H}^*$)	0.064	0.035	0.030	0.031 ($\sigma_{O(6')H}^*$)
3	3	17.8	3.9	6.2	–	0.062	0.034	0.025	0.005
4	4	17.4	4.2	6.2	–	0.060	0.040	0.022	0.008
5	5	6.6	4.6	–	–	0.036	0.040	0.008	0.007
6	6	6.0	5.2	–	–	0.036	0.037	0.004	0.034

from structure **1**, structure **2** shows torsional angles and bond lengths as well as NBO properties similar to those predicted for structure **1** (Tables 1 and 2, entries 1 and 2). Even though structure **2** is computed to be the lowest-energy conformer (1.1 kcal mol⁻¹ below structure **1**), we will focus in the following discussion mostly on structure **1** because of its higher occurrence in cellulose I_β (network I).^[18–20] However, we will compare the results for structures **1** and **2** whenever addressing key aspects of cellobiose chemistry.

Structures **1**, **3**, and **4** are minimum-energy conformations that differ from one another by less than 1 kcal mol⁻¹. They are found as subunits in several different types of crystalline celluloses.^[1,74] The torsional angle χ is the feature distinguishing structures **3** and **4** from structure **1** (Table 1, entries 1, 3, and 4). In these structures, the hydroxymethyl group (C(6')O(6')) assumes the conformation *trans-gauche* (*tg*, structure **1**), *gauche-trans* (*gt*, structure **3**), or *gauche-gauche* (*gg*, structure **4**) relative to the O(5') and C(4') atoms. The barriers for the interconversions through TS(**1**→**3**), TS(**3**→**4**), and TS(**4**→**1**) are 3.0, 7.6, and 4.1 kcal mol⁻¹, respectively. In structures **3** and **4**, the intramolecular hydrogen bond O(2)H...O(6') is missing, which leads to an increase in the torsional angle ϕ from -91.9 (**1**) to -77.5 (**3**), and -73.9° (**4**). In spite of these changes, the *exo*-anomeric effect remains an important secondary interaction stabilizing structures **3** and **4** by 17.8 and 17.4 kcal mol⁻¹, respectively, according to NBO analysis (Table 2, entries 3 and 4). Again, the occupancy of $\sigma_{C(1)O(5)}^*$ is about 0.06 *e* for structures **3** and **4**. The C(1)–O(1) bond length remains at about 1.37 Å and is thus not affected by disrupting the hydrogen bond O(2)H...O(6').

To assess the structural changes occurring upon weakening the *exo*-anomeric interaction, the torsional angle ϕ was constrained at 0 and 180°, which yields the highly distorted conformers **5** and **6**. The *exo*-anomeric interaction is smaller by about 10 kcal mol⁻¹ both in structures **5** and **6** relative to structure **1**, and the C(1)–O(1) bond is elongated by 0.02–0.03 Å. It is important to point out, however, that even with the lone pairs of the glycosidic O site in an orientation unsuitable for an optimal overlapping with the localized orbital $\sigma_{C(1)O(5)}^*$, the *exo*-anomeric effect still contributes to the stabilization of structures **5** and **6** (by 6 kcal mol⁻¹), and there is still a low occupancy of $\sigma_{C(1)O(5)}^*$ (0.036 *e*).

Indeed, the presence of two lone pairs on the glycosidic O site makes it impossible to simultaneously position both of them perpendicular to the localized orbital $\sigma_{C(1)O(5)}^*$ (Figure 5). Consequently, the anomeric effect cannot be fully eliminated by merely rotating around the C(1)–O(1) bond. Even in the case of structure **6**, in which the lone pairs are directed toward a *syn*-coplanar configuration, there is still a weak *exo*-anomeric interaction.

Exo-anomeric effect versus hydrogen bonding: Further evidence for the importance of the *exo*-anomeric effect to the structural stabilization of the glycosidic linkage is found by

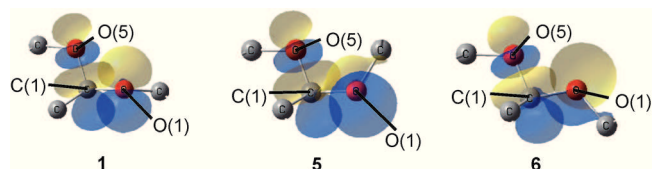


Figure 5. Orientation of the localized orbitals involved in the interaction $n_{O(1)} \rightarrow \sigma_{C(1)O(5)}^*$ occurring in structures **1**, **5**, and **6** (BB1K/6-31 + +G**, CPCM(water)).

DFT calculations on 3-deoxy-cellobiose (**7**), 6-deoxy-cellobiose (**8**), and 3,6-dideoxy-cellobiose (**9**). Structures **7–9** partially or fully lack the intramolecular hydrogen bonding occurring in structure **1** (Figure 6). Despite this, structures **7–9**

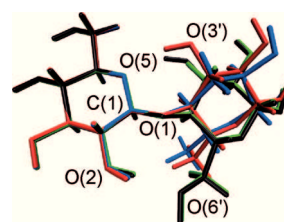


Figure 6. Superimposed structures **1** (black), **7** (green), **8** (red), and **9** (blue) optimized at the BB1K/6-31 + +G** level, CPCM(water).

Table 3. Selected geometric parameters and NBO results for structures **1** and **7–9** (BB1K/6-31 + +G**, CPCM(water)).

Entry	Structure	ϕ [°]	Bond length [Å]		$E(2)$ [kcal mol ⁻¹]		Occupancy [e] $\sigma_{C(1)O(5)}^*$
			C(1)–O(1)	C(1)–O(5)	$n_{O(1)} \rightarrow \sigma_{C(1)O(5)}^*$	$n_{O(5)} \rightarrow \sigma_{C(1)O(1)}^*$	
1	1	-91.9	1.375	1.413	18.1	3.8	0.064
2	7	-89.0	1.374	1.406	18.0	4.5	0.062
3	8	-76.1	1.374	1.410	17.8	4.0	0.062
4	9	-74.5	1.374	1.405	17.8	4.4	0.060

show only small changes in the torsional angle ϕ and in the C(1)–O(1) and C(1)–O(5) bond lengths (Table 3). Moreover, NBO analysis indicates that the *exo*-anomeric effect on structures **7–9** is as large as on structure **1** (18 kcal mol⁻¹, Table 3) and that there is no significant change in the occupancy of $\sigma_{C(1)O(5)}^*$ relative to structure **1**. Overall, these results predict that the *exo*-anomeric effect as an important interaction because it creates an optimal environment for the hydroxyl groups to establish the intramolecular hydrogen bonds in 1,4- β -glucans.

For the purpose of comparison, we also performed calculations on 4-*O*-methyl-cellobiose in conformations resembling those of structures **1** and **3–6**. The NBO analysis did not show any significant differences between the results found for structures **1** and **3–6** and for the corresponding conformers of 4-*O*-methyl-cellobiose (see the Supporting Information, Table SI8). Moreover, to estimate the influence of explicit water molecules and their hydrogen bonds on the anomeric effect,^[11] we added one to three water molecules

to the surroundings of the glycosidic linkage in structure **1** and performed NBO analyses, which gave only marginal changes of 1 kcal mol^{-1} in the $E(2)$ energy values (see the Supporting Information, Table SI9). These results clearly suggest that only conformational changes along the 1,4-β-glycosidic linkage should markedly affect the electronic properties of cellobiose, and by analogy, cellulose. However, changes in the conformation of the hydroxyl groups surrounding the 1,4-β-glycosidic linkage are expected to influence the basicity of cellobiose (see below).

Basicity of the O sites of cellobiose: The NBO analysis identified the *exo*-anomeric effect as one of the key interactions in the electronic structure of cellobiose. Obviously, this invites further questions: Does the *exo*-anomeric effect also influence the basicity of the glycosidic O(1) site? What is the role played by the hydroxyl groups (O(2), O(3'), O(5), and O(6')) in the protonation of the glycosidic O(1) site? And, which are the electronic effects involved in the activation of the C(1)–O(1) bond upon protonation of the O(1) site?

Energetics of protonated conformers: To address these questions, we examined the protonation of the O sites^[75] in structures **1–6**. Because the position of the atoms in the acetalic system of cellobiose is locked by the *exo*- and *endo*-anomeric effects, the axial and equatorial lone pairs of the pyranic O(5) and glycosidic O(1) sites are assumed to be nonequivalent in this analysis. They are henceforth indicated as O(1)•1, O(1)•2, O(5)•1, and O(5)•2, where “•1” and “•2” denote the axial and equatorial positions, respectively. In the case of the flexible hydroxyl O sites (O(2), O(3'), and O(6')), we only considered the energetically most favorable orientation. Moreover, the proton–oxygen distance $O(x)–H^+$ was frozen at 0.98 \AA at unstable protonation sites (spontaneous proton dissociation to another O site), which are marked with an asterisk in Table 4. In the calculations on structures **5** and **6**, the torsional angle ϕ was constrained at 0 and 180° , respectively. All these calculations were carried out just with cellobiose and a proton, because geometry optimizations in the presence of an explicit water molecule always led to the proton dissociating from cellobiose and binding to the water molecule. This result confirms that the

Table 4. Relative Gibbs free energy of protonation for the oxygen sites in structures **1–6** (BB1K/6-31++G**, CPCM(water), 298.15 K). The values are relative to the O(1)•1 protonation site of each structure.

Entry/ Structure	$\Delta\Delta G [\text{kcal mol}^{-1}]$						
	O(1)•1	O(1)•2	O(2)	O(3')	O(5)•1	O(5)•2	O(6')
1	0.0	-3.2*[a]	-13.2*	-16.0	-3.4	-14.8	-17.9
2	0.0	-6.4*	-1.8	-15.6	-3.5	-16.2	-19.5
3	0.0	1.2	-8.4	-19.8	-7.6	-19.3	-13.0
4	0.0	-1.1	-6.1	-18.8	-3.8	-18.4	-18.4
5	0.0	-4.8	-3.9	-5.9	1.6*	9.1*	-5.1
6	0.0*	-15.3*	-1.7	-5.1	-0.6	-6.8	-16.4

[a] * = $[O(x)–H]^+$ distance fixed at 0.98 \AA . In structures **5** and **6** the torsional angle ϕ is generally fixed at 0 and 180° , respectively.

proton affinity of water is intrinsically higher than that of cellobiose, as predicted in a previous study.^[51]

Table 4 summarizes the relative free energies of structures **1–6** protonated at different O sites. A consistent trend for the basicity of the O sites is seen in these data. In general, the protonation of the hydroxyl O-sites O(2), O(3'), and O(6') and of the pyranic O(5) site are significantly favored over the protonation of the glycosidic O(1) site (Table 4, entries 1–4). The comparison of the results for structures **1** and **2** indicates that the different hydrogen-bonding networks surrounding the 1,4-β-glycosidic linkage will only slightly affect the basicity of most of the indicated O sites, with one clear exception: the basicity of the hydroxyl O(2) site is markedly lower in structure **2** than in structure **1**, due to the replacement of the strong O(2)•HO(6') hydrogen bond in structure **2** by the weak O(1)•HO(6') hydrogen bond in structure **1** (see Figure SI5 in the Supporting Information). Only in structures **5** and **6** is the free energy of protonation of the glycosidic O(1)•2-site in the same range as that of the hydroxyl groups (Table 4, entries 5 and 6). The protonation of O(1)•1 ranks always among the energetically least favorable one.

We have applied a thermodynamic cycle to directly estimate the differences in the pK_b values among the O(1)•1, O(5)•1, O(2), O(3'), and O(6') sites in structure **1** (see the Supporting Information for details). The calculations that employ the SMD solvation model for solvation energies yield a pK_b difference of 9–11 pK_b units between the glycosidic oxygen atom and the hydroxyl groups (Table 5). A pre-

Table 5. Differences in the pK_b values (1 M, 298.15 K) for the oxygen sites in structure **1** (BB1K/6-31++G**, SMD(water)) relative to the O(1)•1 protonation site.

Entry	Structure	ΔpK_b				
		O(1)•1	O(2)	O(3')	O(5)•1	O(6')
1	1	0.0	-9.2*[a]	-10.1	-1.7	-10.7

[a] * = $[O(x)–H]^+$ distance fixed at 0.98 \AA .

vious estimate based on the experimental pK_b values of protonated acetal groups and alcohol groups gives the same trend, but predicts the hydroxyl O sites to be about 10–100 times more basic than the glycosidic O sites.^[30] The calculations thus appear to overestimate the pK_b value differences between the sites, possibly due to the limited accuracy of both the solvent corrections and the DFT gas-phase reaction energies (both may correspond to several kcal mol^{-1}).^[78,79] Despite this limitation, the predictions on the basicity of the O sites of cellobiose lead to a main conclusion: Because the hydrolysis of the glycosidic bond will require protonation of the O(1) site, any preferential protonation of the hydroxyl O sites is expected to protect the glycosidic linkage. As a matter of fact, strong acids are needed for the reaction to overcome the selective protonation of the hydroxyl O sites and to ensure that the glycosidic O site is also protonated, thus initiating the activation of the glycosidic bond toward hydrolysis.

Table 6. Selected geometric parameters and NBO results for structure **1** protonated at different sites (BB1K/6-31++G**, CPCM(water)).

Entry	Structure	protonated site	torsion angle [°]			bond length [Å]	<i>E</i> (2) donor–acceptor interactions [kcal mol ^{−1}]				
			ϕ	ψ	χ		hydrogen bonding		anomeric effect		<i>endo</i>
						C(1)–O(1)	C(1)–O(5)	$n_{O(5)} \rightarrow \sigma_{O(3')H}^*$	$n_{O(6')} \rightarrow \sigma_{O(2)H}^*$	$n_{O(1)} \rightarrow \sigma_{C(1)O(5)}^*$	$n_{O(5)} \rightarrow \sigma_{C(1)O(1)}^*$
1	1	–	–91.9	–144.5	–76.9	1.375	1.413	8.5	14.5	18.1	3.8
2	10	O(1)·1	–105.3	–148.3	–66.1	1.468	1.369	0.8	11.0	4.5	7.6
3	11 *[a]	O(1)·2	–107.9	–159.6	–58.4	1.458	1.373	1.4	44.0	7.7	7.2
4	12 *	O(2)	–98.4	–140.5	–74.1	1.369	1.401	4.4	50.9	18.0	4.3
5	13	O(3)	–83.2	–144.9	–73.1	1.370	1.432	64.4	9.2	19.6	2.5
6	14	O(5)·1	–104.9	–146.5	–71.4	1.334	1.535	–	18.2	32.8	0.5
7	15	O(5)·2	–88.6	–147.7	–70.6	1.348	1.487	75.0	9.6	27.2	1.3
8	16	O(6)	–94.0	–141.2	–76.3	1.375	1.401	4.4	82.7	17.4	2.3

[a] * = structures with [O–H]⁺ distance constrained at 0.98 Å.

Cooperativity of *exo*- and *endo*-anomeric effects: Table 6 summarizes the results obtained from the geometry optimization (Figure 7) and the NBO analysis of structure **1** protonated at O(1)·1 (**10**), O(1)·2 (**11**), O(2) (**12**), O(3') (**13**), O(5)·1 (**14**), O(5)·2 (**15**), and O(6') (**16**). It is clear from Table 6 that protonation at different O sites influences the C(1)–O(1) and C(1)–O(5) bond lengths. But only the protonation at the O(1) site is able to elongate the C(1)–O(1) bond and thus, supposedly, to activate the glycosidic linkage toward hydrolysis. Most strikingly, however, is the cooperativity of *exo*- and *endo*-anomeric effects upon protonation of O(1) or O(5). According to Table 6 (entries 2 and 3) the protonation of O(1) mitigates the *exo*-anomeric effect and, at the same time, enhances the *endo*-anomeric effect, by lowering the energy of $\sigma_{C(1)O(1)}^*$ from 0.014 eV (in structure **1**) to 0.007 and 0.008 eV (in structures **10** and **11**, respectively). Hence, the $n_{O(5)} \rightarrow \sigma_{C(1)O(1)}^*$ charge transfer is facilitated. As a result, the occupancy of $\sigma_{C(1)O(1)}^*$ increases from 0.035 *e* (in structure **1**) to 0.067 *e* (in structures **10** and **11**), and the C(1)–O(1) bond elongates by approximately 7% relative to structure **1**. By contrast, protonation of O(5) eliminates the *endo*-anomeric effect. The $n_{O(1)} \rightarrow \sigma_{C(1)O(5)}^*$ charge transfer increases by about 70%, as indicated by high *E*(2) values (Table 6, entries 6 and 7). In structures **14** and **15**, the occupancies of $\sigma_{C(1)O(5)}^*$ are 0.131 and 0.104 *e*, respectively, and thus about 100% higher than found in structure **1** (Table 2, entry 1). This gives rise to an elongation of the C(1)–O(5) bond by 10% in structure **14** and by 9% in structure **15**. Meanwhile, the C(1)–O(1) bond is shortened by about 3% in both structures **14** and **15** relative to structure **1**.

Other implications for the acid–base chemistry of cellobiose:

The differences between the free energies of protonation at different O sites cannot be explained only by the occupancy of the lone pairs. Due to the *exo*-anomeric effect, the O(1)·1 and O(1)·2 lone pairs are unevenly populated. In structure **1**, for example, the occupancy of $n_{O(1)·1}$ is 1.962 *e*, whereas that of $n_{O(1)·2}$ is only 1.898 *e*. For comparison, the occupancy of $n_{O(6')}$, the most basic site, is 1.977 *e*. Despite the fact that $n_{O(1)·1}$ and $n_{O(6')}$ possess very similar electron occupancies, the protonation of O(1)·1 is least favorable (Table 4, entry 1). The factor accounting for the less favorable protonation of O(1)·1 compared with O(1)·2 is the lack of hydro-

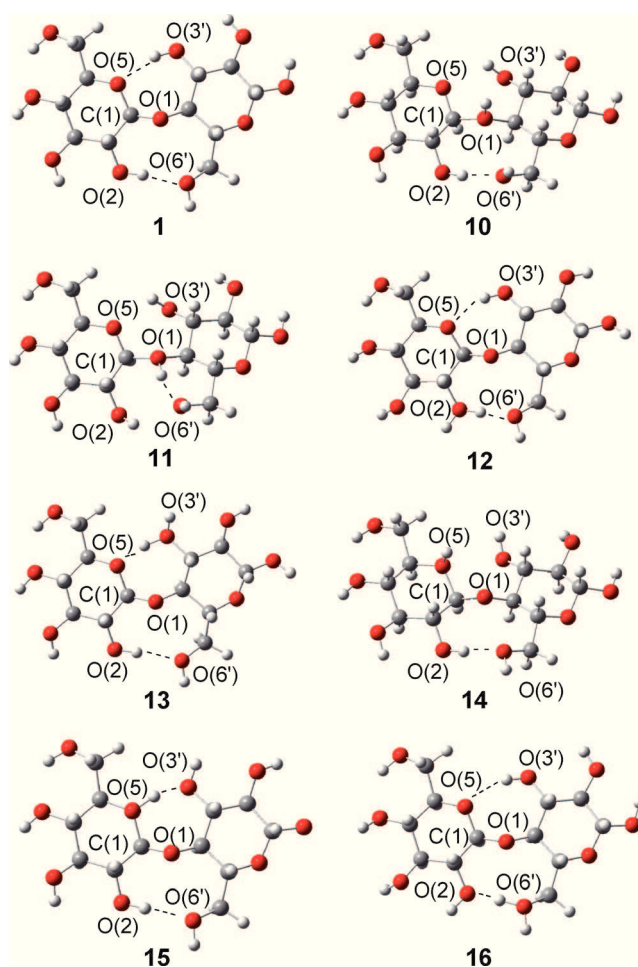
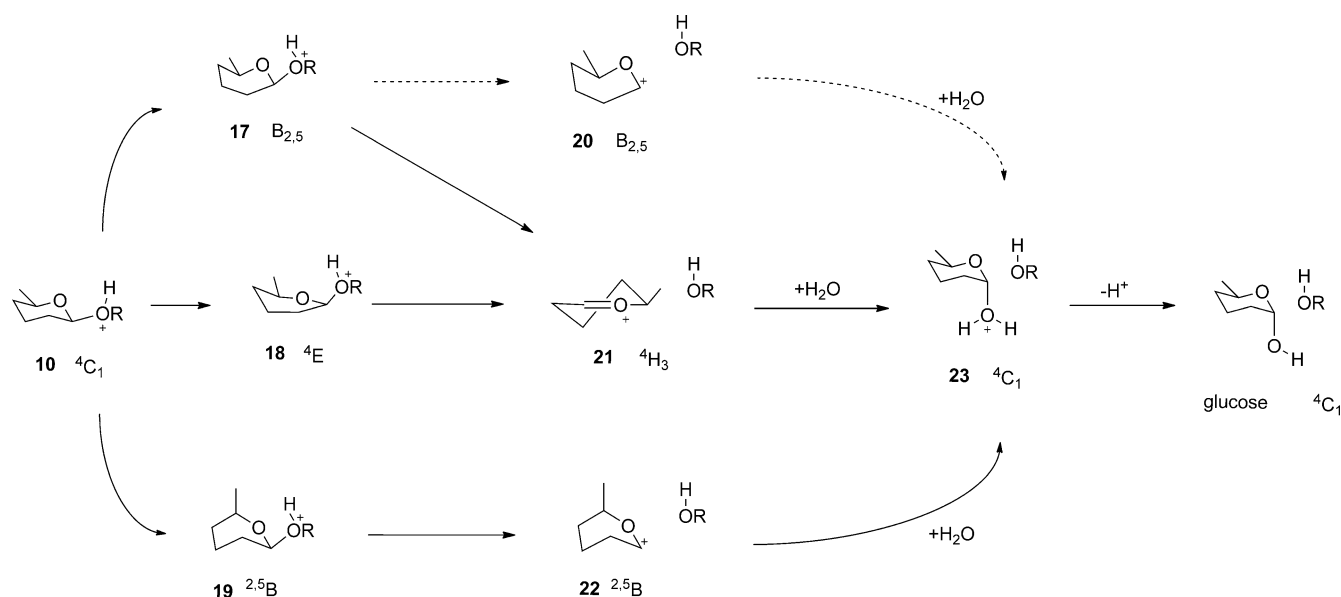


Figure 7. Optimized structures of **1** protonated at different sites (BB1K/6-31++G**, CPCM(water)). A larger version of this figure can be found in the Supporting Information.

gen bonding between the H⁺ species on O(1)·1 and the hydroxyl O(6') site, as depicted in Figure 7 (structures **10** and **11**). According to the NBO analysis, this interaction in structure **11** leads to a stabilization three times stronger compared with the hydrogen bond O(2)H...O(6') in structure **1** (Table 6, entries 1 and 3). In the case of the protonation of O(6'), the H⁺ species is located between hydroxyl O(2) and



Scheme 2. Structures involved in the stepwise A1 mechanism via cyclic carbocations. The concerted A2 mechanism assumes that structures **17**, **18**, or **19** are directly converted to structure **23** (not indicated in the scheme).

O(6') sites. In this case, the stabilization is almost six times stronger compared with the hydrogen bond O(2)H \cdots O(6') occurring in structure **1** (Table 6, entries 1 and 8).

The proximity of the glycosidic O site to the highly basic sites, O(2), O(3'), O(5)-2, and O(6'), should be taken into consideration in the acid–base chemistry of cellobiose and cellulose. Protonation of O(1)-2 will place O(1)-H $^+$ in a hydrogen-bonding distance (≈ 1.6 Å) to O(6'). This will allow the highly basic O(6') site to easily scavenge the proton from the glycosidic O site. This proton transfer from O(1)-2 to O(6') is indeed a barrierless process, leading to one of the lowest minima found. In the light of our results, the high basicity of the O sites surrounding the glycosidic linkage emerges as an elegant mechanism of chemical protection of the glycosidic linkage against acid-catalyzed hydrolysis.

Insights into the hydrolysis mechanism: In this section, we present the computed reaction pathways for the hydrolysis of cellobiose and a detailed analysis of the underlying electronic effects. We first discuss PES scans and evaluate the A1 and A2 mechanisms via cyclic carbocations starting from structure **10**. Because structure **11** is not a stationary one, we did not take this one as a starting structure. Scheme 2 de-

picts the reactions investigated. Figures 8–12 and Table 7 summarize the main results. Pathways through acyclic carbocations are not discussed here, because they are found to proceed through transition states that are significantly higher in energy (by more than 14 kcal mol $^{-1}$). The A1 and A2 mechanisms via cyclic cations were also calculated for 4-*O*-methyl-cellobiose and structure **2**. The corresponding energy profiles (see the Supporting Information, Table SI5, Figures SI2 and SI4) are very similar to those computed for the hydrolysis of cellobiose structure **1**, corroborating the prediction that it is only the conformational changes along the 1,4-β-glycosidic linkage, which will markedly affect the electronic properties of cellobiose, and hence the energy profile for hydrolysis of cellobiose. The computed free energies (Figure 12) are given relative to the protonated structure **10**.

The A1 mechanism: We consider the following steps in the A1 mechanism: activation of the glycosidic bond upon conformational changes in structure **10** (**10**→**17**, **18**, or **19**), heterolytic cleavage of the C(1)–O(1) bond (**17**→**20**, **18**→**21**, **19**→**22**), and nucleophilic attack of water onto the anomeric carbon atom (**20**→**23**, **21**→**23**, **22**→**23**). In the last step, re-

Table 7. Selected bond lengths and results from the NBO analysis for structures **1**, **10**, and **17–19** (BBIK/6-31++G**, CPCM(water)).

Entry	Structure	Bond length [Å]		$E(2)$ donor–acceptor interactions [kcal mol $^{-1}$]				Charge at C(1) [e]	Occupancy [e]	
		C(1)–O(1)	C(1)–O(5)	hydrogen bonding		anomeric effect			$\sigma_{C(1)O(1)}^*$	$\sigma_{C(1)O(5)}^*$
				$n_{O(5)} \rightarrow \sigma_{O(3')H}^*$	$n_{O(6')} \rightarrow \sigma_{O(2)H}^*$	<i>exo</i> $n_{O(1)} \rightarrow \sigma_{C(1)O(5)}^*$	<i>endo</i> $n_{O(5)} \rightarrow \sigma_{C(1)O(1)}^*$			
1	1	1.375	1.413	8.5	14.5	18.1	3.8	0.395	0.035	0.064
2	10	1.468	1.369	0.8	11.0	4.5	7.6	0.416	0.067	0.030
3	17	1.503	1.352	–	–	7.0	28.9	0.402	0.110	0.033
4	18	1.582	1.333	–	6.3	2.5	39.7	0.413	0.152	0.027
5	19	1.548	1.337	–	9.9	5.6	36.6	0.414	0.144	0.031

tention or inversion of the anomeric center is possible; we consider only the process with inversion, which is known to be stereoelectronically preferred.^[37] In both the A1 and A2 mechanism, the product (**23**) consists of two glucose units, one of which is still protonated. The reaction is completed by transferring this proton to water, leading to two glucose molecules.

The heterolytic cleavage of the C(1)–O(1) bond was first investigated in the non-protonated species with an open-shell unrelaxed scan (see the Supporting Information, Figure SI10), in which all internal coordinates were frozen. Elongation of the C(1)–O(1) bond in structure **1** leads to a prohibitively large increase of the energy upon bond cleavage (above 150 kcal mol⁻¹). Another open-shell unrelaxed scan (see the Supporting Information, Figure SI10) was carried out, starting from the protonated structure **10**. As discussed above, protonation of the O(1)•1 site mitigates the *exo*-anomeric effect and enhances, at the same time, the $n_{O(5)} \rightarrow \sigma_{C(1)O(1)}^*$ charge transfer, which results in an overall elongation of the C(1)–O(1) bond in structure **10** by about 7% relative to structure **1**. The scan shows that the dissociation energy of the C(1)–O(1) bond indeed decreases to 70 kcal mol⁻¹ in **10**. Nonetheless, this value is still much too high to allow the hydrolysis taking place under low-severity conditions. Finally, an open-shell unrelaxed scan was carried out with structure **16**, which is lowest in energy among all protonated structures of **1**. The energy for C(1)–O(1) bond cleavage is again prohibitive (above 150 kcal mol⁻¹, see the Supporting Information, Figure SI10).

Structure **10** may undergo conformational changes to further enhance the $n_{O(5)} \rightarrow \sigma_{C(1)O(1)}^*$ charge transfer, and thus fur-

ther activate the glycosidic bond toward dissociation. Accordingly, mechanisms involving three different conformations of the non-reducing AGU in structure **10** were investigated. In these conformers, the geometry of the first AGU was changed from ⁴C₁ (**10**) to B_{2,5} (**17**), ⁴E (**18**), or ^{2,5}B (**19**). Figure 8 displays the transition states found for the conformational conversions (**10** → **17**, **18**, or **19**). The transition states are 3.0–7.3 kcal mol⁻¹ higher in energy than structure **10**. Overall, these barriers are comparable to those reported for similar systems (2-methoxytetrahydropyran, HF/6-31G(d) level;^[46] 2-methyl-oxane, MP2/6-311+G(2df,p) level^[49]).

Figure 9 shows a plot of the C(1)–O(x) bond lengths against the occupancies of $\sigma_{C(1)O(x)}^*$. Obviously, both the C(1)–O(1) and the C(1)–O(5) bond lengths increase in an almost linear fashion with the occupancy of the respective anti-bonding localized orbital. According to Table 7, the conformational changes in structure **10** give rise to a larger $n_{O(5)} \rightarrow \sigma_{C(1)O(1)}^*$ charge transfer in structures **17**, **18**, and **19**, as indicated by the marked increase of *E*(2) to values up to approximately 40 kcal mol⁻¹, as found in structure **18**. In addition, the occupancy of $\sigma_{C(1)O(1)}^*$ increases from 0.067 *e* in structure **10** up to 0.152 *e* in structure **18**. Consequently, there is a marked elongation of the C(1)–O(1) bond to 1.503, 1.582, and 1.548 Å in structures **17**, **18**, and **19**, respectively (Table 7, entries 3–5), corresponding to changes by 10, 15, and 13% relative to structure **1**.

The conformational changes in structure **10** do not cause any significant change in the partial natural charge at the C(1) atom in structures **17**–**19**, which remains close to that found for **10** (+0.416 *e*, Table 7), indicating that the electro-

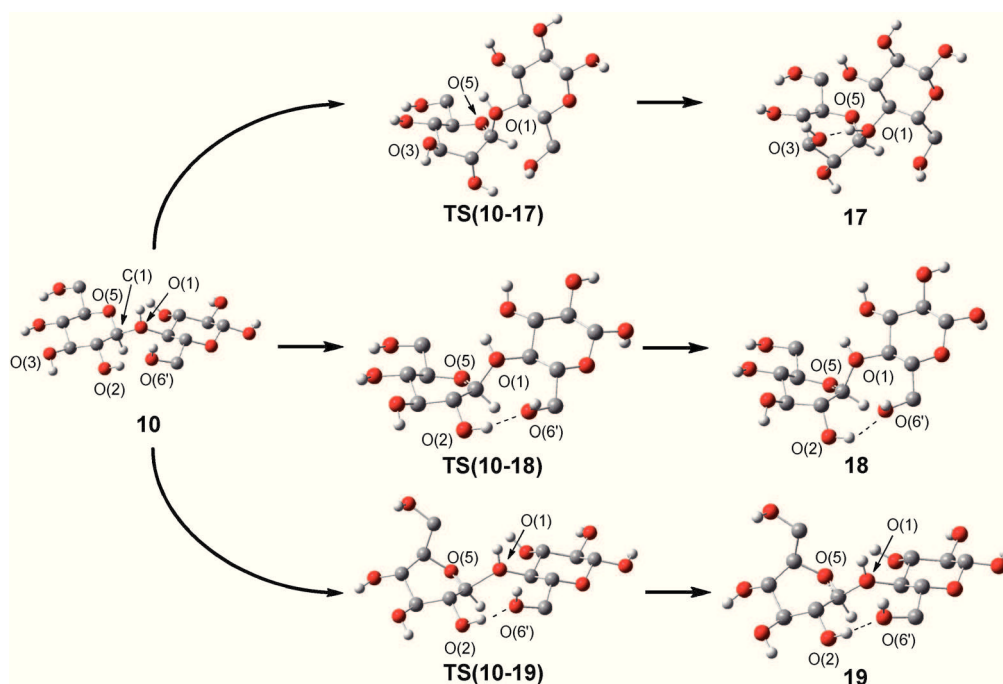


Figure 8. Transition states for the conformational conversion of structure **10** into structures **17**, **18**, or **19** (BB1K/6-31 + G**, CPCM(water)). Aliphatic hydrogen atoms are removed for clarity.

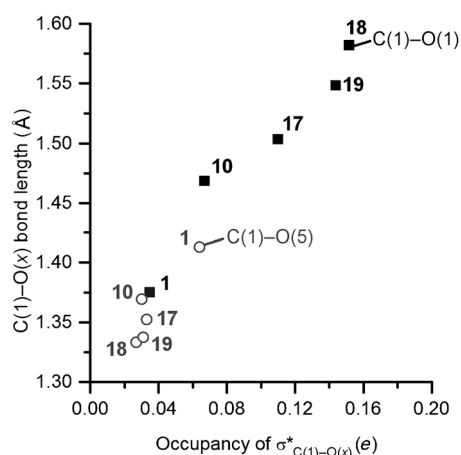


Figure 9. Correlation of the C(1)–O(x) bond length versus the occupancy of $\sigma^*_{C(1)-O(x)}$ in structures **1**, **10**, and **17–19**.

philicity at the C(1) site is not affected. Relative to structure **10**, the energies of the intermediates **17**, **18**, and **19** are -3.7 , 2.2 , and 4.2 kcal mol $^{-1}$, respectively. Structure **17** is strongly stabilized by a $n_{O(3)} \rightarrow \sigma^*_{[O(1)H]^+}$ charge transfer, as indicated by the $E(2)$ value of 59.8 kcal mol $^{-1}$. This interaction does not occur in structures **18** and **19**.

Cleavage of the C(1)–O(1) bond in structures **17**, **18**, and **19** leads to the carbocations **20**, **21**, and **22**, respectively. The transition states TS(**18**→**21**) and TS(**19**→**22**) are early transition states with C(1)–O(1) bond lengths in the range of 1.957 – 1.962 Å (Figure 10) and barriers of 0.9 and 0.5 kcal mol $^{-1}$, respectively. We did not find a transition state for the direct conversion of structure **17** to structure **20**. A relaxed scan with gradual elongation of the C(1)–O(1) bond length in structure **17** led to a continual increase of the energy up to a maximum that lies 15 kcal mol $^{-1}$ above **17** and 6 – 8 kcal mol $^{-1}$ above the transition states TS(**18**→**21**) and TS(**19**→**22**), followed by a conformational change giving rise to an

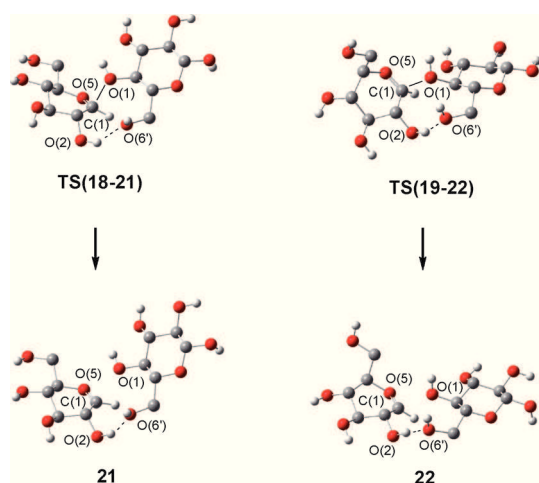


Figure 10. Structures of TS(**18**→**21**) and TS(**19**→**22**) involved in the stepwise A1 mechanism (BB1K/6-31++G**, CPCM(water)). Aliphatic hydrogen atoms are removed for clarity.

endo-sofa conformation, which resembles structure **21** more closely than structure **20** (see the Supporting Information for the energy profile, Figure SI12). The direct conversion of structure **17** into structure **20** requires breaking of the O(1)H $^+$...O(3) hydrogen bond, which will contribute to making this process unfavorable. We conclude that the cleavage of the C(1)–O(1) bond will proceed preferentially through TS(**18**→**21**) and TS(**19**→**22**).

In the next step, a water molecule attacks the C(1) (*si*-face) in structures **21** and **22**, forming α -glucose protonated at the O(1) site, that is, structure **23**. Scans of the potential surfaces between the carbocations (**20**–**22**) and structure **23** show a barrierless approach of the water molecule toward the C(1) atom. The proton transfer from structure **23** to a surrounding water molecule, generating α -glucose, is also a barrierless process.^[51,52]

The A2 mechanism: We consider the concerted A2 mechanism going directly from structures **17**, **18**, or **19** to structure **23**. The transition state TS((**18**+H $_2$ O)→**23**) could be located (Figure 11). Its energy is 10.0 kcal mol $^{-1}$ relative to structure

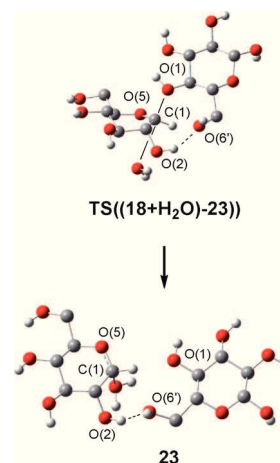


Figure 11. Structures of TS((**18**+H $_2$ O)→**23**) and **23** involved in the concerted A2 mechanism (BB1K/6-31++G**, CPCM(water)). Aliphatic hydrogen atoms are removed for clarity.

10, and the distances H $_2$ O...C(1) and C(1)–O(1) are computed to be 2.992 and 1.868 Å, respectively. The non-reducing AGU of cellobiose assumes a half-chair conformation. The concerted transition state TS((**18**+H $_2$ O)→**23**) is computed to lie 6.9 kcal mol $^{-1}$ above its counterpart TS(**18**→**21**) from the stepwise A1 mechanism (Figure 12). Clearly, high entropic cost disfavors TS((**18**+H $_2$ O)→**23**) and appears to be responsible for the higher free-energy barrier relative to TS(**18**→**21**).^[80] In fact, a concerted A2 mechanism is either not supported by experimental evidence.^[33,34]

Overall proposed mechanism: According to our calculations, the favored stepwise A1 mechanism proceeds from structure **10** through the transition states TS(**10**→**18**) and TS(**18**→**21**) that have Gibbs free energies of 3.0 and 3.1 kcal mol $^{-1}$, re-

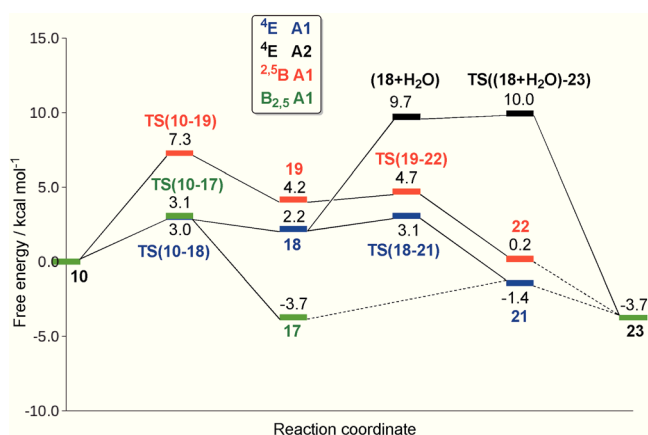


Figure 12. Reaction pathways for the hydrolysis of cellobiose through the stepwise A1 mechanism and the concerted A2 mechanism (BB1K/6-31 + +G**, CPCM(water)). Blue = ⁴E A1, black = ⁴E A2, red = ^{2,5}B A1, and green = ^{B_{2,5}} A1.

spectively, relative to **10**. At face value, these very small barriers would indicate a fast hydrolysis reaction. However, this view ignores the free energy cost of generating structure **10** by protonation of cellobiose **1** in aqueous solution. We have estimated this cost from a thermodynamic cycle as follows (see the Supporting Information for details): the gas-phase free energy of protonation is computed at the BB1K/6-31 + +G(d,p) level, the solvation free energies of cellobiose **1** and protonated cellobiose **10** are determined by applying BB1K/6-31 + +G(d,p) in combination with the SMD solvation model, and the solvation free energy of the proton is taken from experiment.

Combining these data as required by the thermodynamic cycle, places structure **10** far above the solvated reactants, by 27.6 kcal mol⁻¹. We note that similar considerations have recently been applied in the context of Car-Parrinello simulations,^[51] which gave a free energy of 28.8 kcal mol⁻¹ for protonated cellobiose (R4 in Ref. [51]) relative to the solvated reactants. Taking the free energy cost of generating structure **10** into account, we thus find that the overall barrier for the hydrolysis of cellobiose through the transition states TS(**10**→**18**) and TS(**18**→**21**) amounts to 30.6 and 30.7 kcal mol⁻¹, respectively. Experimental studies obtained similar results by kinetic analyses: 32.3 kcal mol⁻¹ (cellobiose, 90–135°, sulfuric acid 0.05–0.10 N)^[55] and 31.7 kcal mol⁻¹ (cellobiose, 117–165°, sulfuric acid 0.03 N).^[56]

We have also estimated, in an analogous manner, the reaction free energy of the hydrolysis of cellobiose in aqueous solution that yields α-glucose and β-glucose (see the Supporting Information for details). By using a suitable thermodynamic cycle in combination with BB1K/6-31 + +G(d,p) calculations and the SMD solvation model, the overall reaction is found to be exergonic by -2.7 kcal mol⁻¹. Calorimetric measurements gave a value of -3 kcal mol⁻¹ for this reaction in water at 286 to 316 K.^[81]

Conclusion

The cellobiose subunit **1** occurring in crystalline cellulose has a structure that allows for optimal intramolecular hydrogen bonding and a strong n_{O(1)}→σ*_{C(1)O(5)} charge transfer (*exo*-anomeric effect). In the light of our results from NBO analysis, the stabilization of the glycosidic bond in cellobiose and, by analogy, in cellulose is among other factors a manifestation of the *exo*-anomeric effect. The intramolecular hydrogen bonding O(5)⋯HO(3') and O(2)H⋯O(6') occurs in the structural environment created by the *exo*-anomeric effect.

The protonation of cellobiose is a complex process with clear implications for the acid–base chemistry of cellulose. In the solid state, the conformations of the polymeric chains are constrained. We find that the basicity of the glycosidic O site varies upon structural distortion of the “cellobiose subunits” in the polymeric chains. Accordingly, the crystallinity of the biopolymer is able to keep the basicity of the glycosidic O site lower than that of the hydroxyl O sites, which provides protection against hydrolysis by hindering the protonation of the glycosidic bond. In this context, it is important to emphasize that the activation of the C(1)–O(1) bond requires not only the protonation of the glycosidic O site but also conformational changes, which are considerably more cumbersome in the crystalline domains of cellulose.

For the hydrolysis of cellobiose, the stepwise A1 mechanism is computed to be favored over the concerted A2 mechanism. Starting from protonated cellobiose **10**, the reaction involves a conformational change followed by the dissociation of the C(1)–O(1) bond, with a calculated free energy barrier of about 3 kcal mol⁻¹ relative to structure **10**. By using an appropriate thermodynamic cycle, the free energy cost of generating **10** in aqueous solution is estimated to be around 28 kcal mol⁻¹, thus contributing by far the largest share to the computed overall free-energy barrier of about 31 kcal mol⁻¹ for the hydrolysis of cellobiose. This value agrees well with the available experimental data. This is also true for the calculated reaction free energy of about -3 kcal mol⁻¹.

These findings also shed light on the results recently reported for the solvent-free, mechanocatalytic depolymerization of cellulose, in which the biopolymer can be fully converted into water-soluble oligosaccharides in the presence of a strong acid.^[31,83] Apparently, mechanical forces are capable of driving the solid-state reaction by providing the energy for the conformational changes required for the activation of the C(1)–O(1) bond toward hydrolysis. Nonetheless, the reaction still requires a strong acid, which is conveniently provided by impregnation of cellulose with H₂SO₄ or HCl.^[31] Indeed, milling cellulose without additives leads mainly to the destruction of the crystalline domains. In this case, there is only little depolymerization, with very low yields of water-soluble products.^[31,82]

The present findings strongly suggest that experimental procedures for the amorphization of cellulose (e.g., conventional ball milling) should not only make the cellulosic

chains more accessible to added chemicals, as currently accepted, but also should relax the conformational restrictions, and thus should create reactive subunits with a concomitant marked increase in the basicity and reactivity of the glycosidic O site.

Concerning cellulose itself, it is clear that the accessibility to the cellulosic chains is not the only issue adversely affecting the hydrolytic process, because conformational changes are required for the activation of the glycosidic bond. The hydrogen-bond network in cellulose will hinder the necessary conformational changes occurring in the rate-determining step of the A1 mechanism. As a consequence of both effects, the apparent activation free energy for the hydrolysis of cellulosic fibers in heterogeneous reactions is higher than that determined here for the hydrolysis of cellobiose.^[1]

Acknowledgements

R.R. is grateful to the Alexander von Humboldt Foundation for the financial support provided in the framework of the Sofja Kovalevskaja Award 2010 endowed by the Federal Ministry of Education and Research. Financial support from the research cluster “Sustainable Chemical Synthesis—A Systems Approach (SusChemSys)” is also acknowledged. The project “Sustainable Chemical Synthesis (SusChemSys)” is co-financed by the European Regional Development Fund (ERDF) and the state of North Rhine-Westphalia, Germany, under the Operational Program “Regional Competitiveness and Employment” 2007–2013. This work is supported by the Cluster of Excellence RESOLV (EXC 1069) funded by the Deutsche Forschungsgemeinschaft.

- [1] R. Rinaldi, F. Schüth, *ChemSusChem* **2009**, *2*, 1096–1107.
- [2] R. Rinaldi, F. Schüth, *Energy Environ. Sci.* **2009**, *2*, 610–626.
- [3] S. P. S. Chundawat, G. T. Beckham, M. E. Himmel, B. E. Dale, *Annu. Rev. Chem. Biomol. Eng.* **2011**, *2*, 121–145.
- [4] P. Dhepe, A. Fukuoka, *ChemSusChem* **2008**, *1*, 969–975.
- [5] H. Kobayashi, T. Komanoya, S. K. Guha, K. Hara, A. Fukuoka, *Appl. Catal. A* **2011**, *409*, 13–20.
- [6] L. R. Lynd, C. E. Wyman, T. U. Gerngross, *Biotechnol. Prog.* **1999**, *15*, 777–793.
- [7] S. Van de Vyver, J. Geboers, P. A. Jacobs, B. F. Sels, *ChemCatChem* **2011**, *3*, 82–94.
- [8] J. Veredel, T. Church, P. Andersson, *Synthesis* **2011**, 1649–1677.
- [9] P. L. Ragg, P. R. Fields, P. B. Tinker, *Philos. Trans. R. Soc. London Ser. A* **1987**, *321*, 537–547.
- [10] V. Agarwal, P. J. Dauenhauer, G. W. Huber, S. M. Auerbach, *J. Am. Chem. Soc.* **2012**, *134*, 14958–14972.
- [11] J. P. Praly, R. U. Lemieux, *Can. J. Chem.* **1987**, *65*, 213–223.
- [12] M. K. Dowd, A. D. French, P. J. Reilly, *Carbohydr. Res.* **1992**, *233*, 15–34.
- [13] J. L. Asensio, F. J. Cañada, A. García-Herrero, M. T. Murillo, A. Fernández-Mayoralas, B. A. Johns, J. Kozak, Z. Zhu, C. R. Johnson, J. Jiménez-Barbero, *J. Am. Chem. Soc.* **1999**, *121*, 11318–11329.
- [14] G. A. Jeffrey, J. A. Pople, J. S. Binkley, S. Vishveshwara, *J. Am. Chem. Soc.* **1978**, *100*, 373–379.
- [15] G. A. Jeffrey, J. A. Pople, L. Radom, *Carbohydr. Res.* **1972**, *25*, 117–131.
- [16] a) G. L. Strati, J. L. Willett, F. A. Momany, *Carbohydr. Res.* **2002**, *337*, 1833–1849; b) G. L. Strati, J. L. Willett, F. A. Momany, *Carbohydr. Res.* **2002**, *337*, 1851–1859; c) U. Schnupf, F. A. Momany, *Cellulose* **2011**, *18*, 859–887.
- [17] A. O’Sullivan, *Cellulose* **1997**, *4*, 173–207.
- [18] Y. Nishiyama, P. Langan, H. Chanzy, *J. Am. Chem. Soc.* **2002**, *124*, 9074–9082.
- [19] M. Jarvis, *Nature* **2003**, *426*, 611–612.
- [20] Y. Nishiyama, J. Sugiyama, H. Chanzy, P. Langan, *J. Am. Chem. Soc.* **2003**, *125*, 14300–14306.
- [21] G. T. Beckham, J. F. Matthews, B. Peters, Y. J. Bomble, M. E. Himmel, M. F. Crowley, *J. Phys. Chem. B* **2011**, *115*, 4118–4127.
- [22] C. M. Payne, M. E. Himmel, M. F. Crowley, G. T. Beckham, *J. Phys. Chem. Lett.* **2011**, *2*, 1546.
- [23] R. P. Swatloski, S. K. Spear, J. D. Holbrey, R. D. Rogers, *J. Am. Chem. Soc.* **2002**, *124*, 4974–4975.
- [24] R. Rinaldi, *Chem. Commun.* **2011**, *47*, 511–513.
- [25] R. Rinaldi, *J. Chem. Eng. Data* **2012**, *57*, 1341–1343.
- [26] J. B. Binder, R. T. Raines, *Proc. Natl. Acad. Sci. USA* **2010**, *107*, 4516–4521.
- [27] C. Li, Q. Wang, Z. K. Zhao, *Green Chem.* **2008**, *10*, 177–182.
- [28] C. Li, Z. K. Zhao, *Adv. Synth. Catal.* **2007**, *349*, 1847–1850.
- [29] R. Rinaldi, R. Palkovits, F. Schüth, *Angew. Chem.* **2008**, *120*, 8167–8170; *Angew. Chem. Int. Ed.* **2008**, *47*, 8047–8050.
- [30] R. Rinaldi, N. Meine, J. vom Stein, R. Palkovits, F. Schüth, *ChemSusChem* **2010**, *3*, 266–276.
- [31] N. Meine, R. Rinaldi, F. Schüth, *ChemSusChem* **2012**, *5*, 1449–1454.
- [32] L. Vanoye, M. Fanselow, J. D. Holbrey, M. P. Atkins, K. R. Seddon, *Green Chem.* **2009**, *11*, 390–396.
- [33] T. E. Timell, *Can. J. Chem.* **1964**, *42*, 1456–1472.
- [34] S. R. Wann, M. M. Kreevoy, *J. Org. Chem.* **1981**, *46*, 419–423.
- [35] J. N. Bemiller, in *Advances in Carbohydrate Chemistry*, Vol. 22 (Eds.: L. W. Melville, R. S. Tipson), Academic Press, New York, **1967**, pp. 25–108.
- [36] J. M. Beck, S. M. Miller, M. W. Pecuh, C. M. Hadad, *J. Org. Chem.* **2012**, *77*, 4242–4251.
- [37] H. Satoh, H. S. Hansen, S. Manabe, W. F. van Gunsteren, P. H. Hünenberger, *J. Chem. Theory Comput.* **2010**, *6*, 1783–1797.
- [38] A. J. Kirby, *Acc. Chem. Res.* **1984**, *17*, 305–311.
- [39] H. Satoh, S. Manabe, Y. Ito, H. P. Lüthi, T. Laino, J. Hutter, *J. Am. Chem. Soc.* **2011**, *133*, 5610–5619.
- [40] R. B. Gupta, R. W. Franck, *J. Am. Chem. Soc.* **1987**, *109*, 6554–6556.
- [41] J. L. Liras, E. V. Anslyn, *J. Am. Chem. Soc.* **1994**, *116*, 2645–2646.
- [42] J. L. Liras, V. M. Lynch, E. V. Anslyn, *J. Am. Chem. Soc.* **1997**, *119*, 8191–8200.
- [43] D. R. McPhail, J. R. Lee, B. Fraser-Reid, *J. Am. Chem. Soc.* **1992**, *114*, 1905–1906.
- [44] T. L. Amyes, W. P. Jencks, *J. Am. Chem. Soc.* **1989**, *111*, 7888–7900.
- [45] C. W. Andrews, J. P. Bowen, B. Fraser-Reid, *J. Chem. Soc. Chem. Commun.* **1989**, 1913–1916.
- [46] C. W. Andrews, B. Fraser-Reid, J. P. Bowen, *J. Am. Chem. Soc.* **1991**, *113*, 8293–8298.
- [47] P. Deslongchamps, S. Li, Y. L. Dory, *Org. Lett.* **2004**, *6*, 505–508.
- [48] B. J. Smith, *J. Am. Chem. Soc.* **1997**, *119*, 2699–2706.
- [49] B. J. Smith, *J. Phys. Chem. A* **1998**, *102*, 4728–4733.
- [50] H. Dong, M. R. Nimlos, M. E. Himmel, D. K. Johnson, X. Qian, *J. Phys. Chem. A* **2009**, *113*, 8577–8587.
- [51] X. Liang, A. Montoya, B. S. Haynes, *J. Phys. Chem. B* **2011**, *115*, 10682–10691.
- [52] D. Liu, M. R. Nimlos, D. K. Johnson, M. E. Himmel, X. Qian, *J. Phys. Chem. A* **2010**, *114*, 12936–12944.
- [53] F. A. Momany, U. Schnupf, *Carbohydr. Res.* **2011**, *346*, 619–630.
- [54] R. H. Atalla, in *Advances in Chemistry Series*, Vol. 181 (Eds.: Jr. R. D. Brown, L. Jurasek), ACS, New York, **1979**, pp. 55–69.
- [55] J.-H. Q. Pinto, S. Kaliaguine, *AIChE J.* **1991**, *37*, 905–914.
- [56] Z.-E. Dadach, S. Kaliaguine, *Can. J. Chem. Eng.* **1993**, *71*, 880–891.
- [57] Gaussian 09, Revision A.1. M. J. Frisch, G. W. Trucks, H. B. Schlegel, G. E. Scuseria, M. A. Robb, J. R. Cheeseman, G. Scalmani, V. Barone, B. Mennucci, G. A. Petersson, H. Nakatsuji, M. Caricato, X. Li, H. P. Hratchian, A. F. Izmaylov, J. Bloino, G. Zheng, J. L. Sonnenberg, M. Hada, M. Ehara, K. Toyota, R. Fukuda, J. Hasegawa, M. Ishida, T. Nakajima, Y. Honda, O. Kitao, H. Nakai, T. Vreven, J. A. Montgomery, Jr., J. E. Peralta, F. Ogliaro, M. Bearpark, J. J. Heyd, E. Brothers, K. N. Kudin, V. N. Staroverov, R. Kobayashi, J. Normand, K. Raghavachari, A. Rendell, J. C. Burant, S. S. Iyengar,

- J. Tomasi, M. Cossi, N. Rega, J. M. Millam, M. Klene, J. E. Knox, J. B. Cross, V. Bakken, C. Adamo, J. Jaramillo, R. Gomperts, R. E. Stratmann, O. Yazyev, A. J. Austin, R. Cammi, C. Pomelli, J. W. Ochterski, R. L. Martin, K. Morokuma, V. G. Zakrzewski, G. A. Voth, P. Salvador, J. J. Dannenberg, S. Dapprich, A. D. Daniels, O. Farkas, J. B. Foresman, J. V. Ortiz, J. Cioslowski, D. J. Fox, Gaussian Inc., Wallingford CT, **2009**.
- [58] G. B. I. Csonka, A. D. French, G. P. Johnson, C. A. Stortz, *J. Chem. Theory Comput.* **2009**, *5*, 679–692.
- [59] Y. Zhao, B. J. Lynch, D. G. Truhlar, *J. Phys. Chem. A* **2004**, *108*, 2715–2719.
- [60] S. F. Sousa, P. A. Fernandes, M. J. Ramos, *J. Phys. Chem. A* **2007**, *111*, 10439–10452.
- [61] N. F. Brás, S. A. Moura-Tamames, P. A. Fernandes, M. J. Ramos, *J. Comput. Chem.* **2008**, *29*, 2565–2574.
- [62] N. F. Brás, P. A. Fernandes, M. J. Ramos, *J. Chem. Theory Comput.* **2010**, *6*, 421–433.
- [63] V. Barone, M. Cossi, *J. Phys. Chem. A* **1998**, *102*, 1995–2001.
- [64] A. V. Marenich, C. J. Cramer, D. G. Truhlar, *J. Phys. Chem. B* **2009**, *113*, 4538–4543.
- [65] C. Gonzalez, H. B. Schlegel, *J. Chem. Phys.* **1989**, *90*, 2154–2161.
- [66] C. Gonzalez, H. B. Schlegel, *J. Phys. Chem.* **1990**, *94*, 5523–5527.
- [67] A. D. Becke, *Phys. Rev. A* **1988**, *38*, 3098–3100.
- [68] A. D. Becke, *J. Chem. Phys.* **1993**, *98*, 1372–1377.
- [69] A. D. Becke, *J. Chem. Phys.* **1993**, *98*, 5648–5652.
- [70] C. Lee, W. Yang, R. G. Parr, *Phys. Rev. B* **1988**, *37*, 785–789.
- [71] Y. Zhao, N. E. Schultz, D. G. Truhlar, *J. Chem. Phys.* **2005**, *123*, 161103–161106.
- [72] NBO Version 3.1, TCI, E. D. Glendening, A. E. Reed, J. E. Carpenter, F. Weinhold, University of Wisconsin, Madison, **1998**.
- [73] E. Hatcher, E. Sävén, G. Widmalm, A. D. MacKerell, Jr., *J. Phys. Chem. B* **2011**, *115*, 597–608.
- [74] P. Zugenmaier, *Prog. Polym. Sci.* **2001**, *26*, 1341–1417.
- [75] a) T. Kurahashi, T. Mizutani, J. Yoshida, *J. Chem. Soc. Perkin Trans. I* **1999**, *1*, 465–473; b) G. Yang, E. A. Pidko, E. J. M. Hensen, *J. Catal.* **2012**, *295*, 122–132.
- [76] J. T. Ham, D. G. Williams, *Acta Crystallogr. Sect. B* **1970**, *26*, 1373–1383.
- [77] A. Rencurosi, J. Röhring, J. Pauli, A. Potthast, C. Jäger, S. Pérez, P. Kosma, A. Imberty, *Angew. Chem.* **2002**, *114*, 4453–4457; *Angew. Chem. Int. Ed.* **2002**, *41*, 4277–4281.
- [78] J. Ho, M. L. Coote, *Theor. Chem. Acc.* **2010**, *125*, 3–21.
- [79] K. S. Alongi, G. C. Shields in *Annual Reports in Computational Chemistry*, Vol. 6, (Ed.: A. W. Ralph), Elsevier, Amsterdam, **2010**, pp. 113–138.
- [80] TS(**18**→**21**): $\Delta H=2.4$ kcal mol⁻¹, $\Delta G=3.1$ kcal mol⁻¹, TS-((**18**-H₂O)→**25**): $\Delta H=0.6$ kcal mol⁻¹, $\Delta G=10.0$ kcal mol⁻¹.
- [81] Y. B. Tewari, R. N. Goldberg, *J. Biol. Chem.* **1989**, *264*, 3966–3971.
- [82] J. Hilgert, N. Meine, R. Rinaldi, F. Schüth, *Energy Environ. Sci.* **2013**, *6*, 92–96.
- [83] S. M. Hick, C. Griebel, D. T. Restrepo, J. H. Truitt, E. J. Buker, C. Bylda, R. G. Blair, *Green Chem.* **2010**, *12*, 468–474.

Received: April 11, 2013

Revised: August 13, 2013

Published online: October 18, 2013

CHEMISTRY

A EUROPEAN JOURNAL

Supporting Information

© Copyright Wiley-VCH Verlag GmbH & Co. KGaA, 69451 Weinheim, 2013

The Electronic Nature of the 1,4- β -Glycosidic Bond and Its Chemical Environment: DFT Insights into Cellulose Chemistry

Claudia Loerbroks, Roberto Rinaldi,* and Walter Thiel*^[a]

chem_201301366_sm_miscellaneous_information.pdf

Table of Contents

Theoretical methods.....	2
Results for the rotated conformer structure 41.....	7
Reaction mechanism A1 and A2 for 4-O-methyl-cellobiose.....	10
Results and reaction mechanism A1 for structure 2.....	13
Additional NBO data.....	17
PES Scans.....	18
Energy profiles for exo-cyclic mechanisms with different functionals and basis sets.....	21
Reaction scheme and energy profiles for endo-cyclic mechanism for structure 1.....	23
Additional Figures.....	24
Total energies of stationary points (Hartree).....	27
Cartesian coordinates (in Angstrom, BB1K/6-31++G**).....	31
Figures of optimized structures (BB1K/6-31++G**).....	65
References.....	69

Theoretical methods

General

All calculations were performed using the Gaussian09 suite of quantum chemical programs.¹ Density functional theory (DFT) was applied using the BB1K,² B97-1,³ B3LYP,⁴⁻⁷ and M06-2X⁸ functionals in combination with the 6-31++G** basis set. Geometry optimizations were carried out in the solvent phase (CPCM, UFF radii, water) for BB1K, B3LYP, and M06-2X without any constraints. Test calculations of pK_b values were done with the B97-1 functional and the SMD⁹ solvation model. The SMD model was generally used for the calculation of solvation energies. All calculations employed the tight convergence criteria and the ultrafine grid in Gaussian09. Harmonic vibrational frequency calculations were performed at the same level as the geometry optimizations. Zero-point energies (EZPC), enthalpies (H), and free energies (G) at 298.15 K and 1 atm were determined from these calculations. The number of imaginary modes was used to verify minima (no imaginary frequency) and transition states (one imaginary frequency). Intrinsic reaction coordinate (IRC)^{10,11} calculations were performed to confirm the direct connection between transition states and minima. The programs Molden¹² and Gaussview 3.5¹³ were used for visualization.

Energetics: Comparisons between different functionals

Unless noted otherwise, the results in the main paper come from BB1K/6-31++G(d,p) calculations. For comparison, additional calculations were done at the following levels: L1 = BB1K/6-311++G(3df,3pd), L2 = B3LYP/6-31++G(d,p), and L3 = M06-2X/6-31++G(d,p). The computed total energies are documented in Tables SI2-SI4, and selected energy profiles are shown in Figures SI7-SI10.

As pointed out in the main paper, the Gibbs relative free energies from BB1K/6-31++G(d,p) for structures **1**, **3-6** and **10-16** are well reproduced at the other levels, with small standard deviations of 2.3 (L1), 2.2 (L2), and 1.0 (L3) kcal/mol. In the case of structures **17-25**, geometry optimizations at levels L2-L3 sometimes failed (*e.g.*, when trying to locate the transition state for the required conformational change or C(1)O(1) dissociation); similar problems have been met in related systems.¹⁴ The comparisons for structures **17-25** are thus restricted to single-point calculations, which give standard deviations of 1.7 (L1), 4.2 (L2), and 10.2 (L3) kcal/mol relative to BB1K/6-31++G(d,p). The B3LYP results (L2) are consistent with the well-known tendency of this functional to underestimate barriers. In previous benchmarks for barrier heights, the following mean signed errors (MSE) relative to experiment were reported: BH42/04 database, $MSE(B3LYP/MG3S) = -4.4$ kcal/mol, $MSE(BB1K/MG3S) = -0.61$ kcal/mol;¹⁵ BH6 database, $MSE(B3LYP/MG3S) = -4.72$ kcal/mol, $MSE(BB1K/MG3S) = -1.03$ kcal/mol;¹⁵ HTBH38/04 and NHTBH38/04 database, $MSE(B3LYP/MG3S) = -4.15$ kcal/mol, $MSE(BB1K/MG3S) = -0.03$ kcal/mol.¹⁶ The large deviations of the M06-2X results (L3) for **17-25** are unexpected, however, since this functional usually provides rather accurate results for thermochemistry (TC177 database, mean unsigned errors: $MUE(B3LYP) = 1.39$ kcal/mol, $MUE(M06-2X) = 0.82$ kcal/mol) and for barrier heights (DBH76 database, $MUE(B3LYP) = 4.50$ kcal/mol, $MUE(M06-2X) = 1.22$ kcal/mol).¹⁷

Solvation model

We use the Conductor-like Polarizable Continuum Model (CPCM) for aqueous solvation. In a benchmark study¹⁸ of several solvation models, CPCM was found to give solvation free energies with the lowest mean absolute deviation (MAD) from the experimental values for a set of 70 small neutral and charged organic molecules (MAD = 3 kcal/mol), superior to those from a cluster-continuum model (MAD = 9 kcal/mol), COSMO (MAD = 9 kcal/mol), SM5.24R (MAD = 8 kcal/mol), PCM (MAD = 11 kcal/mol), and IPCM (MAD = 20 kcal/mol). For cations and neutral species that are studied presently, CPCM performs best using UAKS cavities (United Atom Topological Model applied on radii optimized for the PBE1PBE/6-31G(d) level of theory, $MAD_{\text{cation}} = 4$ kcal/mol, $MAD_{\text{neutral}} = 1$ kcal/mol). However, when using these UAKS cavities or other United Atom cavities (UAKS, UAHF, or UA0), geometry optimization on some of the charged species failed and the error on total polarization charges (value of the density outside of the generated cavity) exceeded 0.05 by far. On the other hand, these structures could be optimized with Pauling cavities (Merz-Kollman radii) and Bondi radii ($MAD_{\text{cation}} \approx 5$ kcal/mol, $MAD_{\text{neutral}} \approx 3$ kcal/mol), but the error on total polarization charges still exceeded 0.05. Only the use of universal force field (UFF) cavities (with explicit cavities for hydrogen atoms) yielded low errors on polarization charges, but led to larger deviations ($MAD_{\text{cation}} = 15$ kcal/mol, $MAD_{\text{neutral}} = 8$ kcal/mol) from experimental solvation free energies in the benchmark study.¹⁸ Therefore the CPCM model was used for calculations on the reaction pathway, but was not used for the calculation of the solvation energies (see below).

Table S11 lists CPCM solvation free energies for structures **1**, **3-6**, **10-16** and **41**, as obtained with UFF, Pauling, and Bondi cavities. Compared with the UFF-based values, we find standard deviations of 2.0 kcal/mol for Pauling cavities ($STD_{\text{neutral}} = 0.7$ kcal/mol; $STD_{\text{cation}} = 2.7$ kcal/mol) and of 1.5 kcal/mol for Bondi cavities ($STD_{\text{neutral}} = 1.1$ kcal/mol; $STD_{\text{cation}} = 1.8$ kcal/mol), which are much lower than expected from the errors mentioned above.

Table S11. Solvation free energies (kcal/mol) relative to structures **1** and **10** (BB1k/6-31++G(d,p), water, 298.15 K, 1 atm) for different choices of CPCM cavities (see text).

compound	UFF	Pauling	Bondi
41	3.5	2.7	2.7
1	0.0	0.0	0.0
3	0.3	-0.8	-0.7
4	-0.4	-0.8	-1.3
5	7.5	6.7	6.0
6	9.1	9.5	7.5
10	0.0	0.0	0.0
11	-3.2	-1.8	-3.6
12	-13.2	-10.6	-11.9
13	-16.0	-12.6	-13.6
14	-3.4	-1.2	-2.1
15	-14.8	-12.0	-12.6
16	-17.9	-13.7	-15.2

Transition states with low frequencies

In the transition states for the conformational changes of structure **10** to either **17**, **18**, or **19**, we find small imaginary frequencies ($\sim 60i \text{ cm}^{-1}$) that are typical for such low-barrier processes. The IRC calculations for these three transition states were unsuccessful, since they failed to converge after a few steps, even when the step sizes were varied between 0.05 to 0.2 Bohr. We note, however, that these three transition structures correspond to maxima of relaxed scans (see Figures SI1-SI3) and that optimizations starting from geometries obtained by manually displacing these structures along the transition vector in either direction end up either at **10** or at **17**, **18**, or **19**.

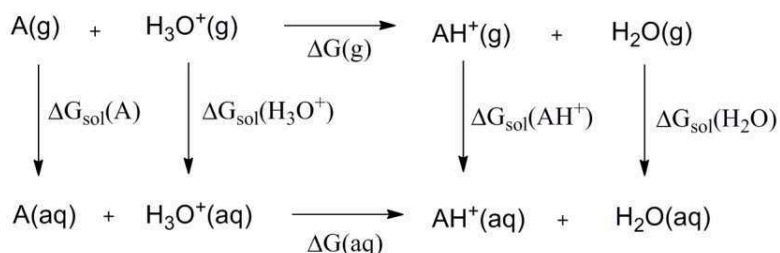
Calculations with thermodynamic pathways

Thermodynamic cycles were used to determine pK_b values, reaction free energies, and energies for bringing reactants together from infinity.

Calculation of pK_b values: The thermodynamic cycles corresponding to reaction (1) and (2) yield consistent pK_b values, with differences of 0.1 pK_b units or less (A= cellobiose).



Shown below is the thermodynamic pathway for reaction (2):



The required DFT calculations employed the BB1K functional. Previous benchmark calculations indicate that other functionals might provide more accurate solvation free energies: for example, in a comparative study on 30 acids using G-n and CBS methods as well as several DFT functionals, B97-1 performed best among the latter (MAD = 1 kcal/mol relative to experiment).¹⁹ Hence, we also carried out some B97-1 calculations for validation, but the corresponding pK_b values showed little improvement over the BB1K results, and therefore we adopted the BB1K functional also here, for the sake of consistency. Changes in solvation free energies were calculated by subtracting the BB1K free energy in vacuum from the BB1K free energy calculated with the SMD solvent model. The latter was chosen because its documented good performance for solvation free energies, for instance, in a benchmark study on a set of 51 drug-like molecules (RMSD = 2.5 kcal/mol relative to experiment).⁹ In the case of structure **10**, the gas-phase geometry optimization terminated because of SCF convergence problems, and the gas-phase energy was therefore estimated by a single-point calculation.

For the evaluation of the thermodynamic cycle, we used experimental values for the solvation free energy of hydronium ion, H^+ , and water molecule,^{20,21} and for the gas-phase free energy of H^+ :²² $\Delta G_{\text{sol},1\text{M}}(H_2O) = -6.32$ kcal/mol, $\Delta G_{\text{sol},1\text{M}}(H_3O^+) = -110.3$ kcal/mol, $\Delta G_{\text{sol},1\text{M}}(H^+) = -265.9$ kcal/mol, $\Delta G_{\text{g},1\text{atm}}(H^+) = -6.28$ kcal/mol. All energy values were converted to the standard state of 298 K and 1 M (1 mol/L). In the gas phase, equation (3), the change of 1 mole of ideal gas from 1 atm (24.46 L/mol) to 1 M gives rise to the following correction term:

$$\begin{aligned}\Delta G_{\text{g},1\text{M}} &= \Delta G_{\text{g},1\text{atm}} - T\Delta S \\ &= \Delta G_{\text{g},1\text{atm}} + RT\ln\left(\frac{V_{\text{g}}}{V_{\text{aq}}}\right) \\ &= \Delta G_{\text{g},1\text{atm}} + RT\ln(24.46) \\ &= \Delta G_{\text{g},1\text{atm}} + 1.89 \text{ kcal/mol}\end{aligned}\tag{3}$$

Likewise, bringing n water molecules from the concentration of 55.34 M in liquid water to 1M generates another correction term:

$$n \cdot \Delta G_{\text{aq},1\text{M}}^*(H_2O) = -n \cdot RT\ln(55.34) = -2.38 \cdot n \text{ kcal/mol}\tag{4}$$

Combining equations (3) and (4) with the thermodynamic cycle for reaction (2) leads to:

$$\begin{aligned}\Delta G(\text{aq}) &= \Delta G_{\text{g}} + \Delta\Delta G_{\text{sol}} + n\Delta G_{\text{aq},1\text{M}}^*(H_2O) \\ &= G_{\text{g}}(H_2O) + G_{\text{g}}(AH^+) - G_{\text{g}}(A) - G_{\text{g}}(H_3O^+) + \\ &\quad \Delta G_{\text{sol}}(H_2O) + \Delta G_{\text{sol}}(AH^+) - \Delta G_{\text{sol}}(A) - \Delta G_{\text{sol}}(H_3O^+) + 2.38 \text{ kcal/mol}\end{aligned}\tag{5}$$

The pK_b value is defined as:

$$pK_b = \frac{\Delta G(\text{aq})}{RT\ln(10)}\tag{6}$$

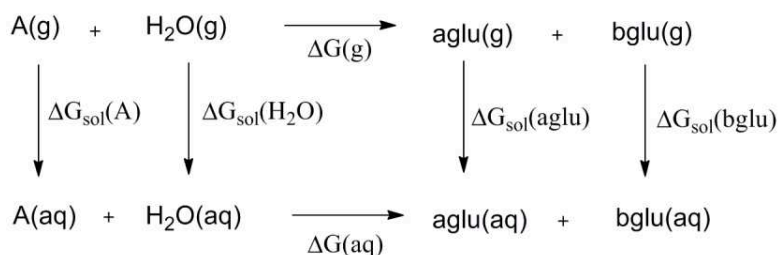
and pK_b differences between two molecules 1 and 2 are given by:

$$\Delta pK_b = \frac{\Delta G_1(\text{aq}) - \Delta G_2(\text{aq})}{RT\ln(10)}\tag{7}$$

Calculation of reaction free energy: To obtain the reaction free energy of reaction (8),



the following thermodynamic cycle was set up (aglu= α -glucose, bglu = β -glucose, A=cellobiose):

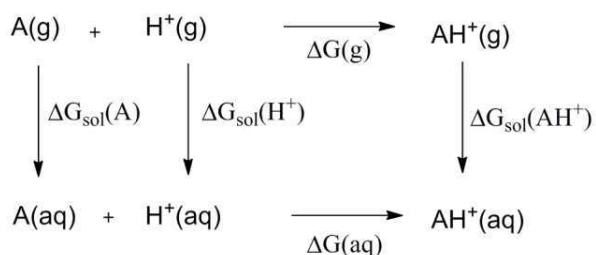


The reaction free energy is given by equation (9)

$$\begin{aligned} \Delta G(\text{aq}) &= \Delta G_{\text{g}} + \Delta \Delta G_{\text{sol}} + n \Delta G_{\text{aq},1\text{M}}^*(\text{H}_2\text{O}) \\ &= G_{\text{g}}(\text{aglu}) + G_{\text{g}}(\text{bglu}) - G_{\text{g}}(\text{A}) - G_{\text{g}}(\text{H}_2\text{O}) + \\ &\quad \Delta G_{\text{sol}}(\text{aglu}) + \Delta G_{\text{sol}}(\text{bglu}) - \Delta G_{\text{sol}}(\text{A}) - \Delta G_{\text{sol}}(\text{H}_2\text{O}) + 2.38 \text{ kcal/mol} \end{aligned} \quad (9)$$

The gas-phase free energies and the solvation free energies in this expression were calculated with the BB1K functional and the SMD solvent model. For water the experimental solvation energy was used (see above).

Calculation of the free energy needed to bring reactants together from infinity: In this case, the reactants are cellobiose (A) and a proton, which form species **10** in a protonation reaction (10). The gas-phase free energies and the solvation free energies in equation (11) were calculated with the BB1K functional and the SMD solvent model. For the proton the experimental solvation energy was used (see above).



$$\begin{aligned} \Delta G(\text{aq}) &= \Delta G_{\text{g}} + \Delta \Delta G_{\text{sol}} \\ &= G_{\text{g}}(\text{AH}^+) - G_{\text{g}}(\text{A}) - G_{\text{g}}(\text{H}^+) - 1.89 \text{ kcal/mol} + \\ &\quad \Delta G_{\text{sol}}(\text{AH}^+) - \Delta G_{\text{sol}}(\text{A}) - \Delta G_{\text{sol}}(\text{H}^+) \end{aligned} \quad (11)$$

Results for the rotated conformer structure 41

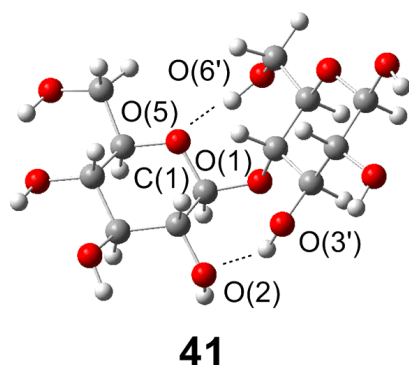


Figure S11. Optimized structure of **41** (BB1K/6-31++G**).

Structure **41** is one of the possible conformers of cellobiose, which can be reached from structure **1** by rotation around the C(1)-O(1) bond. It is often regarded as one of the most stable conformers of cellobiose in vacuum,^{23,24} but it is less relevant for the purposes of the present study. Therefore, we present computational results for **41** only in the Supporting Information. Its relative free energy, important bond lengths and dihedral angles (Table SI2), NBO data (Table SI3), and protonation energies (Table SI4) are given below in comparison to the other conformers **1** to **6**.

Conformer **41** contains the atoms H(1) and H(4') located *anti* to each other in the plane formed by the glycosidic linkage C(1)O(1)C(4'). It has two intramolecular H-bonds, O(5)⋯HO(6') and O(2)⋯HO(3'). NBO analysis reveals that the corresponding donor-acceptor interactions, $n_{O(5)} \rightarrow \sigma^*_{O(6')H}$ and $n_{O(2)} \rightarrow \sigma^*_{O(3')H}$, contribute 6.5 and 8.6 kcal mol⁻¹ to the stabilization of **41**, respectively (Table SI14, entry 41); the occupancies of $\sigma^*_{O(3')H}$ and $\sigma^*_{O(6')H}$ are 0.026 and 0.027 electrons (e). The exo-anomeric effect provides an even stronger interaction stabilizing **41** by 14.1 kcal mol⁻¹, with an occupancy of $\sigma^*_{C(1)O(5)}$ of 0.056 e .

By contrast, the endo-anomeric effect is only of marginal importance, as indicated by the low stabilization (3.9 kcal mol⁻¹) and the lower occupancy of $\sigma^*_{C(1)O(1)}$ (0.034 e). Rotation around the C(1)O(1) bond may convert conformer **41** into **1**. A relaxed scan for this rotation indicates an energy barrier of about 10 kcal mol⁻¹ (see the computed energy profile, Figure SI5), but the transition state could not be located precisely. Recent dynamic studies do not report transitions between **41** and **1**.^{23,25}

Table SI2. Gibbs free energies $\Delta\Delta G$ (kcal mol⁻¹) relative to structure **1**, selected torsional angles and bond lengths for structures **1** to **6** and **41** (BB1K/6-31++G**).

	$\Delta\Delta G$	Torsion angle (degree)			Bond length (Å)	
		ϕ	ψ	χ	C(1)O(1)	C(1)O(5)
1	0.0	-91.9	-144.5	-76.9	1.375	1.413
2	-1.1	-89.5	-139.6	-82.9	1.373	1.410
3	0.3	-77.5	-150.9	-168.9	1.374	1.410
4	-0.4	-73.9	-121.3	53.2	1.376	1.410
5	7.5	0	-141.8	-79.4	1.400	1.392
6	9.1	180	-141.6	-80.2	1.397	1.396
41	3.5	58.3	-121.8	-75.7	1.379	1.408

Table SI3. Selected NBO results for structures **1** to **6** and **41**.

Entry	<i>E</i> (2) donor-acceptor interactions (kcal mol ⁻¹)							
	Anomeric effect		H-bonding		Occupancy (e)			
	exo	endo			$\sigma^*_{C(1)O(5)}$	$\sigma^*_{C(1)O(1)}$	$\sigma^*_{O(3')H}$	$\sigma^*_{O(2)H}$
	$n_{O(1)} \rightarrow \sigma^*_{C(1)O(5)}$	$n_{O(5)} \rightarrow \sigma^*_{C(1)O(1)}$	$n_{O(5)} \rightarrow \sigma^*_{O(3')H}$	$n_{O(6')} \rightarrow \sigma^*_{O(2)H}$				
1	18.1	3.8	8.5	14.5	0.064	0.035	0.029	0.035
3	17.8	3.9	6.2	-	0.062	0.034	0.025	0.005
4	17.4	4.2	6.2	-	0.060	0.040	0.022	0.008
5	6.6	4.6	-	-	0.036	0.040	0.008	0.007
6	6.0	5.2	-	-	0.036	0.037	0.004	0.034
			$n_{O(5)} \rightarrow \sigma^*_{O(3')H}$	$n_{O(2)} \rightarrow \sigma^*_{O(6')H}$				$\sigma^*_{O(6')H}$
2	18.4	3.6	9.0	11.9	0.064	0.035	0.030	0.031
			$n_{O(5)} \rightarrow \sigma^*_{O(6')H}$	$n_{O(2)} \rightarrow \sigma^*_{O(3')H}$				$\sigma^*_{O(6')H}$
41	14.1	3.9	6.5	8.6	0.056	0.034	0.026	0.027

Table SI4. Relative Gibbs free energy of protonation for the oxygen sites in structures **1** to **6** and **41** (BB1K/6-31++G**, 298.15 K, kcal/mol). The values are relative to the O(1)-1 protonation site of each structure.

	Relative free energy of protonation, $\Delta\Delta G(298.15\text{ K}) / \text{kcal mol}^{-1}$						
	O(1)-1	O(1)-2	O(2)	O(3')	O(5)-1	O(5)-2	O(6')
1	0.0	-3.2*	-13.2*	-16.0	-3.4	-14.8	-17.9
2	0.0	-6.4*	-1.8	-15.6	-3.5	-16.2	-19.5
3	0.0	1.2	-8.4	-19.8	-7.6	-19.3	-13.0
4	0.0	-1.1	-6.1	-18.8	-3.8	-18.4	-18.4
5	0.0	-4.8	-3.9	-5.9	1.6*	9.1*	-5.1
6	0.0*	-15.3*	-1.7	-5.1	-0.6	-6.8	-16.4
41	0.0*	9.3*	-10.6	-11.6	12.1	-2.1*	-3.1

*[O(X)-H]⁺ distance fixed at 0.98 Å. In 5 and 6 the torsional angle ϕ is generally fixed at 0° and 180°, respectively.

Reaction mechanism A1 and A2 for 4-O-methyl-cellobiose

To validate the mechanism found for structure **1**, the A1 and A2 pathways were also calculated with a 4-O-methyl-cellobiose model to assess the influence of an additional methyl group. Results are collected in Table SI5 (energies), Figure SI2 (energy profile) and Figure SI3 (structures). The relative free energies of the pathways deviate by at most 1.8 kcal/mol (compared with **1**), and the overall trends are conserved.

Table SI5. Relative free energies for the A1 and A2 pathways for 4-O-methyl-cellobiose. BB1K/6-31++G**, CPCM water, 298.15 K, 1 atm.

B _{2,5} , A1		⁴ E, A1		^{2,5} B, A1		⁴ E, A2	
structure	ΔG (kcal mol ⁻¹)	structure	ΔG (kcal mol ⁻¹)	structure	ΔG (kcal mol ⁻¹)	structure	ΔG (kcal mol ⁻¹)
10	0.0	10	0.0	10	0.0	10	0.0
Ts(10-17)	2.4	Ts(10-18)	3.4	Ts(10-19)	6.3	Ts(10-18)	3.4
17	-5.0	18	1.9	19	3.6	18	1.9
		Ts(18-21)	3.4	Ts(19-22)	4.9	18+H₂O	7.9
		21	-2.4	22	1.3	Ts(18+H ₂ O-23)	9.9
		23	-3.8	23	-3.8	23	-3.8

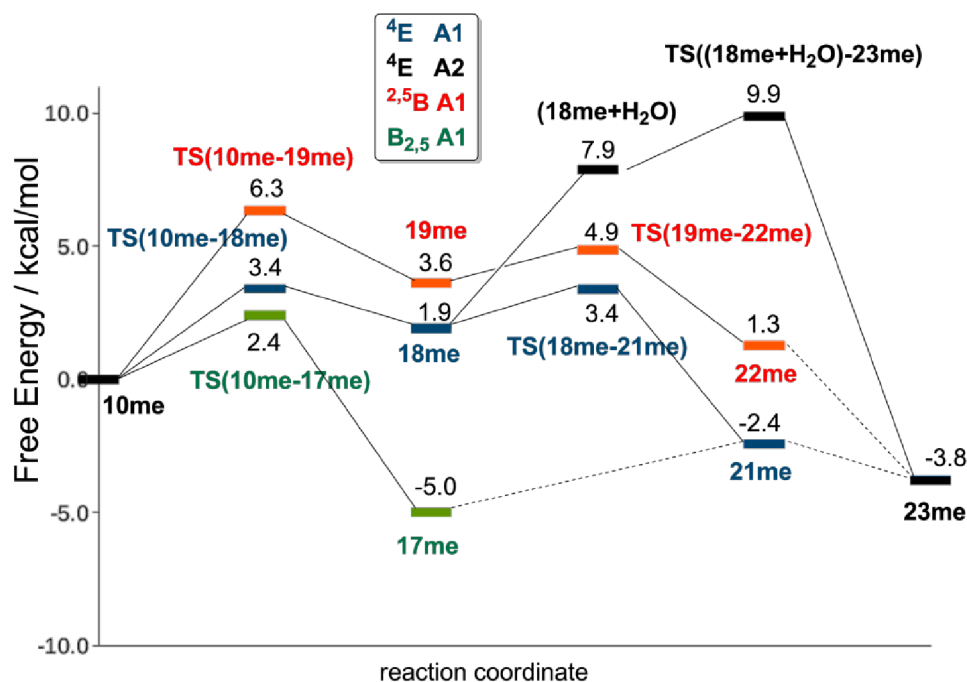


Figure SI2: Energy profile (BB1K/6-31++G(d,p)) for the exo-cyclic 4-O-methyl-cellobiose mechanism. Energies refer to structure **10me**.

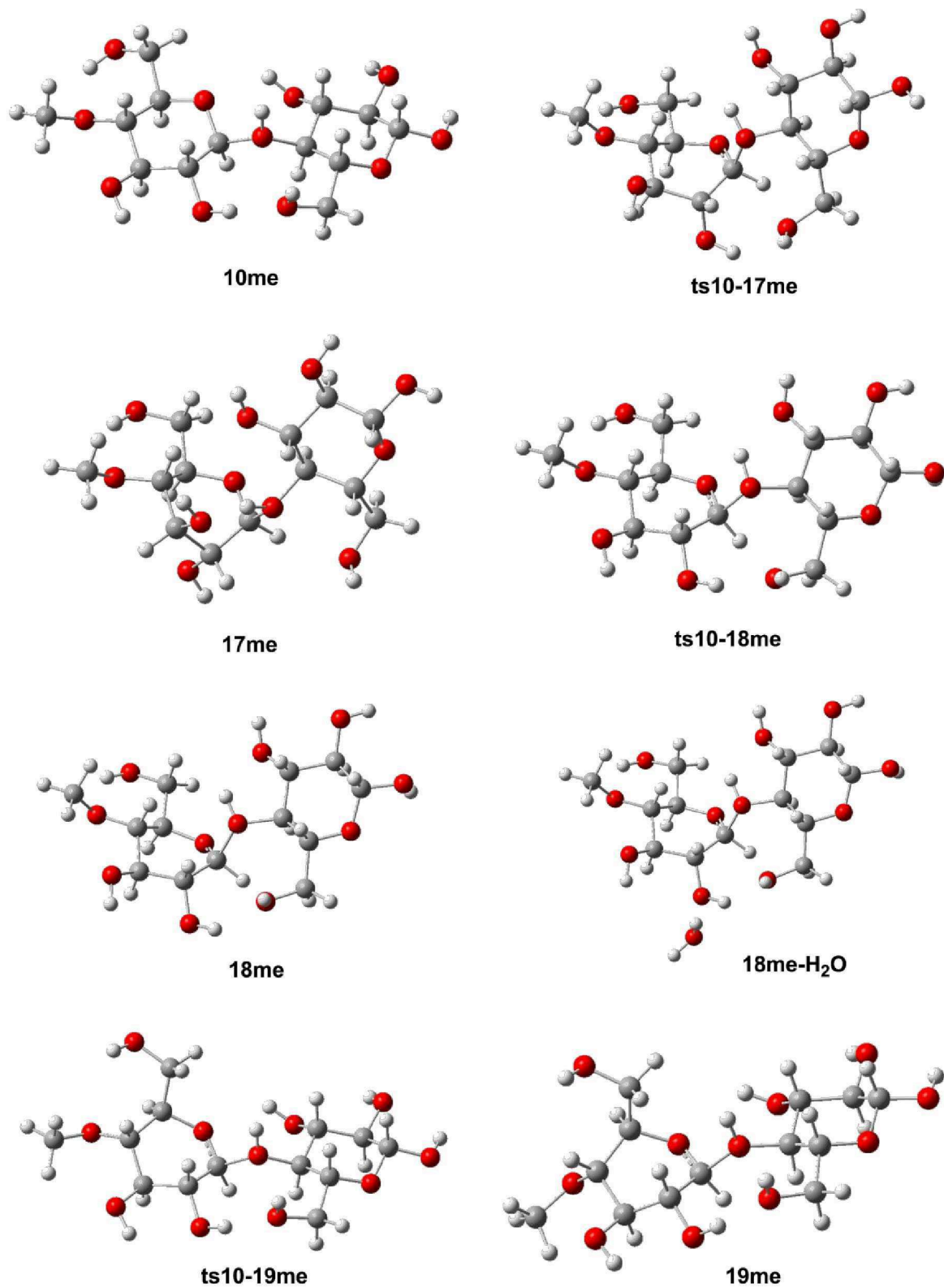


Figure S13-a: Structures (BB1K/6-31++G(d,p)) for the exo-cyclic 4-O-methyl-cellobiose mechanism.

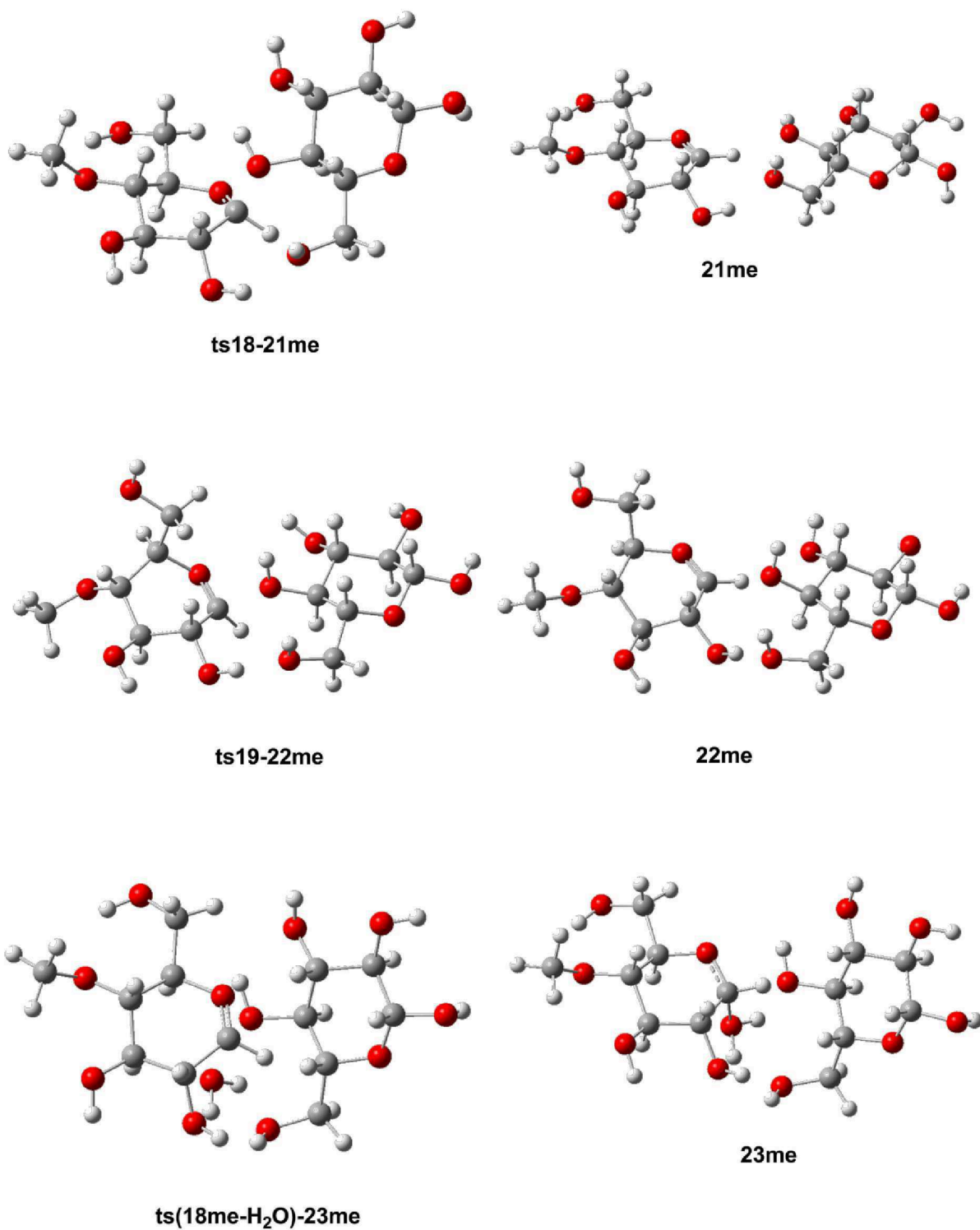


Figure S13-b: Structures (BB1K/6-31++G(d,p)) for the exo-cyclic 4-O-methyl-cellobiose mechanism.

Results and reaction mechanism A1 for structure 2

To validate the mechanism found for structure **1** (with an O(2)-H \cdots O(6') hydrogen bond) the A1 pathway was also calculated for structure **2** (with an O(2) \cdots H-O(6') hydrogen bond) to assess the influence of different hydrogen bond networks. Results are listed in Table SI6 (energies), Figure SI4 (energy profile), and Figure SI6 (structures). The energies along the pathways deviate by at most 2.6 kcal/mol (compared with **1**), and the overall trends are conserved.

No fully optimized structure for **TS(17'-20')** could be obtained, for the same reasons as discussed in the paper for structure **1**.

Figure SI5 shows the different hydrogen bond networks obtained upon protonation of O(2) in structures **1** and **2**.

Table SI6. Relative free energies for the A1 pathways for structure **2**. BB1K/6-31++G**, CPCM water, 298.15 K, 1 atm.

$B_{2,5}, A1$		${}^4E, A1$		${}^{2,5}B, A1$	
structure	ΔG (kcal mol $^{-1}$)	structure	ΔG (kcal mol $^{-1}$)	structure	ΔG (kcal mol $^{-1}$)
10'	0.0	10'	0.0	10'	0.0
Ts(10'-17')	2.7	Ts(10'-18')	4.5	Ts(10'-19')	6.9
17'	-5.7	18'	3.2	19'	3.1
		Ts(18'-21')	5.4	Ts(19'-22')	5.7
		21'	-1.2	22'	-0.4
		23	-3.5	23	-3.5

Table SI7. Selected bond lengths and results from the NBO analysis for structures **10'**, **17'**, **18'**, and **19'** (BB1K/6-31++G**).

Entry	Bond length (Å)		$E(2)$ donor-acceptor interactions (kcal mol $^{-1}$)				Charge at C(1) (e)	Occupancy (e)	
	C(1)O(1)	C(1)O(5)	H-bonding		Anomeric effect			$\sigma^*_{C(1)O(1)}$	$\sigma^*_{C(1)O(5)}$
			$n_{O(5)} \rightarrow \sigma^*_{O(3')H}$	$n_{O(2')} \rightarrow \sigma^*_{O(6)H}$	exo $n_{O(1)} \rightarrow \sigma^*_{C(1)O(5)}$	endo $n_{O(5)} \rightarrow \sigma^*_{C(1)O(1)}$			
2	1.373	1.410	9.0	11.9	18.4	3.6	0.408	0.034	0.061
10'	1.461	1.367	1.6	9.3	5.6	7.8	0.427	0.066	0.028
17'	1.480	1.443	-	-	8.7	29.0	0.421	0.103	0.037
18'	1.559	1.334	-	-	3.2	39.2	0.419	0.144	0.028
19'	1.564	1.331	-	11.4	2.9	38.8	0.419	0.152	0.022

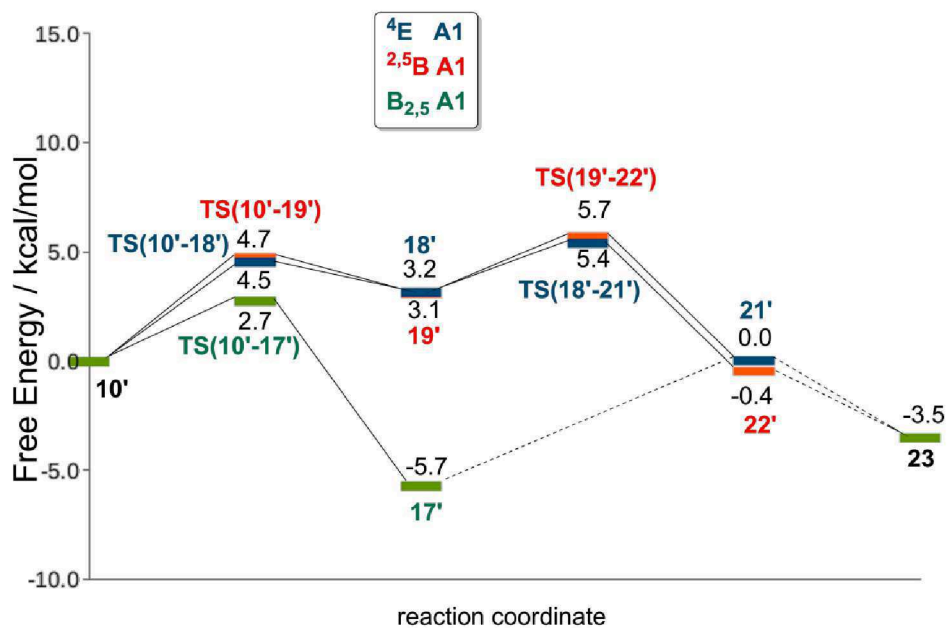


Figure S14: Energy profile (BB1K/6-31++G(d,p)) for the exo-cyclic cellobiose structure 2 mechanism. Energies refer to structure 10'.

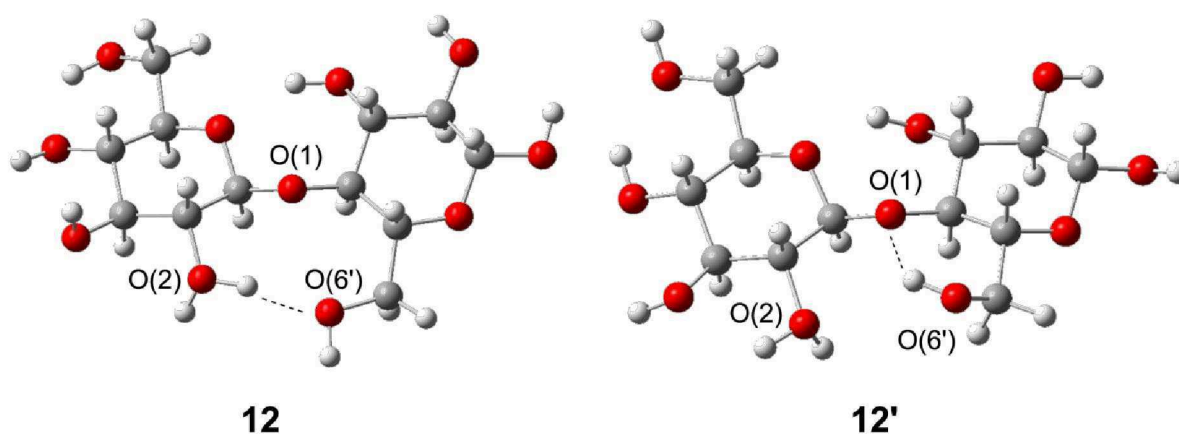


Figure S15: Structures 12 and 12' (BB1K/6-31++G(d,p)) showing the different hydrogen bonds formed upon protonation of O(2) in structures 1 and 2.

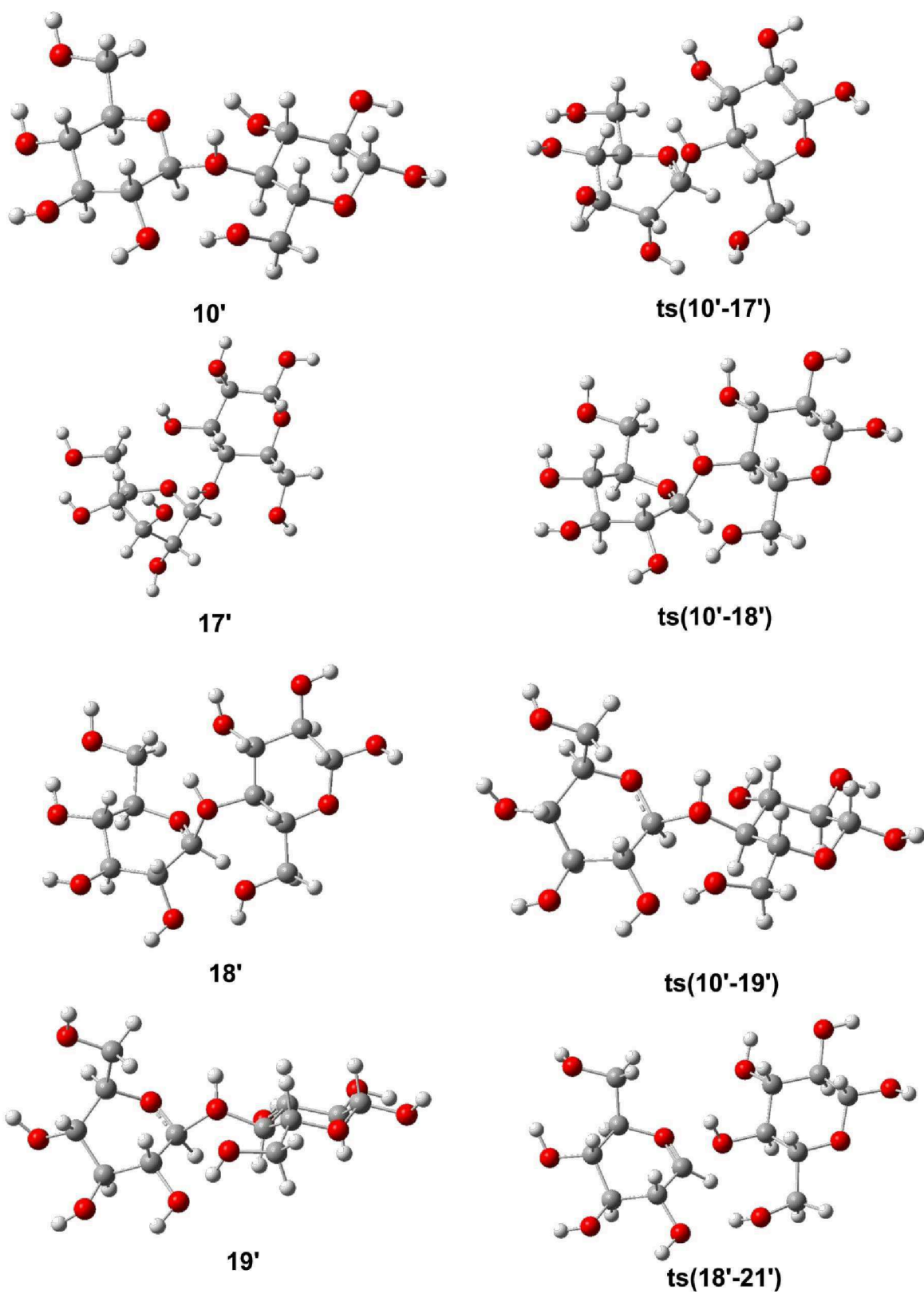


Figure S16-a: Structures 10' to 22' (BB1K/6-31++G(d,p)) for the exo-cyclic cellobiose structure 2 mechanism.

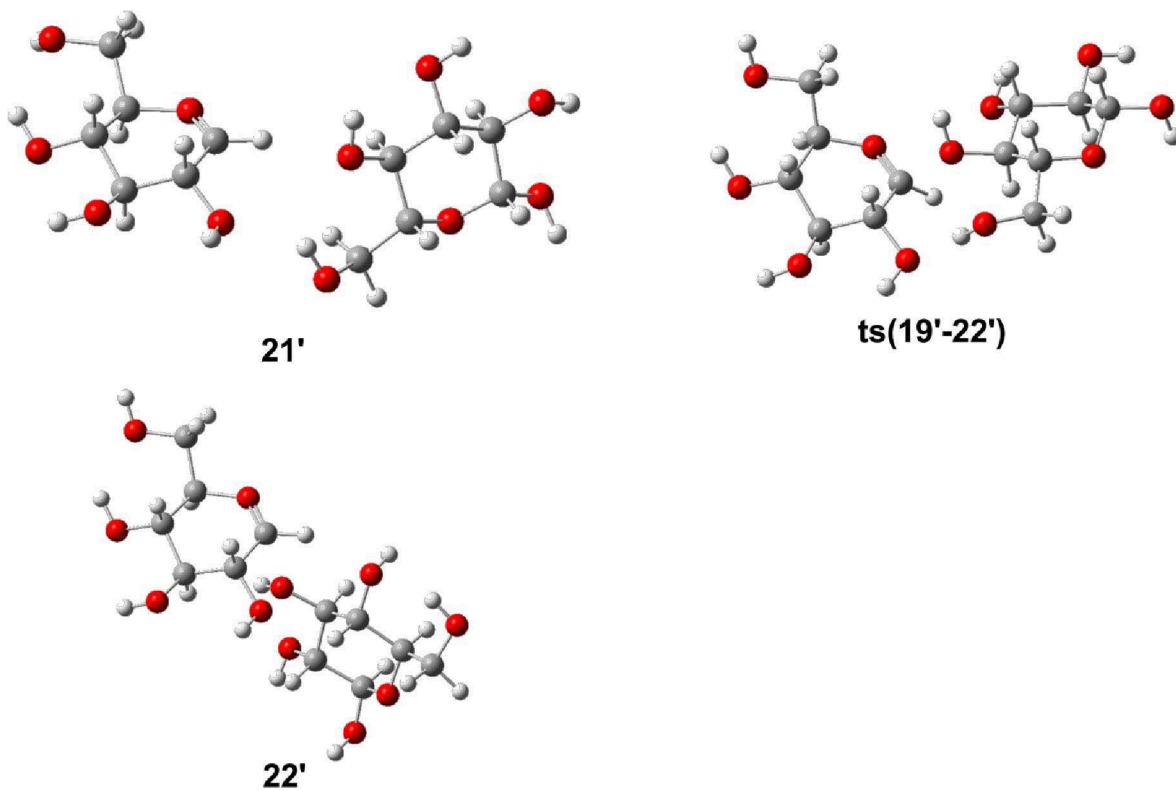


Figure S16-b: Structures **10'** to **22'** (BB1K/6-31++G(d,p)) for the exo-cyclic cellobiose structure **2** mechanism.

Additional NBO data

Table S18. NBO data for 4-O-methyl-cellobiose. BB1K/6-31++G**, CPCM water, 298.15 K, 1 atm.

	ΔG (kcal mol ⁻¹)	E(2) (kcal mol ⁻¹)		H-bonding		Bond length (Å)		Torsion angle (degree)	
		nO(1)→ $\sigma^*C(1)O(5)$	nO(5)→ $\sigma^*C(1)O(1)$	nO(6') → $\sigma^*O(2)H$	nO(3) → $\sigma^*O(X)H$	C(1)O(1)	C(1)O(5)	ϕ (O(5)C(1)O(1)C(4'))	χ (C(4')C(5')C(6')O(6'))
41me	3.5	14.0	4.0	8.1	6.4	1.379	1.406	57.8	-69.8
1me	0.0	18.0	3.9	14.6	2.9	1.375	1.411	-93.1	-76.8
3me	0.3	17.8	3.9	6.1	-	1.375	1.408	-78.0	-168.5
4me	0.0	17.4	4.2	6.26	-	1.376	1.409	-74.2	53.2
5me	9.3	6.6	4.6	-	-	1.400	1.391	0.0	-79.1
6me	9.3	6.0	5.5	-	-	1.398	1.395	-180.0	-80.3
10me	-	4.8	7.5	9.8	0.8	1.467	1.368	-104.9	-65.9
17me	-	7.0	28.7	-	59.6	1.502	1.351	-47.2	-61.3
18me	-	2.5	40.2	6.4	11.2	1.574	1.334	-91.3	-70.6
19me	-	5.7	36.6	12.5	0.5	1.54	1.336	-96.9	-66.3

Table S19: NBO data for structure 1 with water molecules. BB1K/6-31++G**, CPCM water, 298.15 K, 1 atm

Number and position of water molecules	E(2) (kcal mol ⁻¹)	
	nO(1)→ $\sigma^*C(1)O(5)$	nO(5)→ $\sigma^*C(1)O(1)$
0	18.1	3.8
1 at O(1) (frozen)	17.0	3.7
1 at O(3')	18.0	3.7
1 at O(5)	18.5	4.0
1 at O(6')/O(1)	17.4	4.0
2 at O(6'), O(5)	17.7	4.2
3 at O(1), O(5), O(6)	17.2	3.8

PES Scans

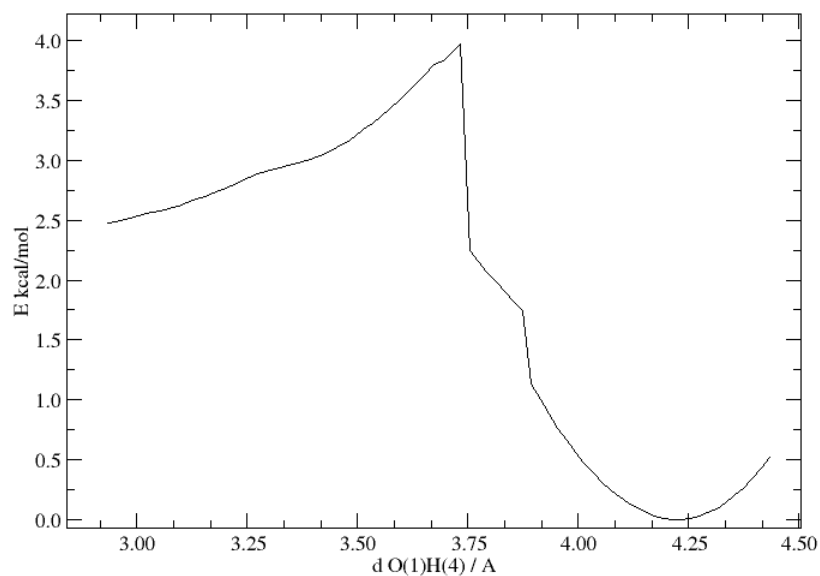


Figure S17: Relaxed PES scan energy profile (BB1K/6-31++G(d,p)). Elongation of O(1)H(4) distance in structure **18**. Energies refer to structure **10**. The abrupt change in energy at 3.73 Å is caused by the change from endo-sofa to chair conformation, with a shortening of the C(1)O(1) distance and a flip of C(6) from nearly axial to equatorial position.

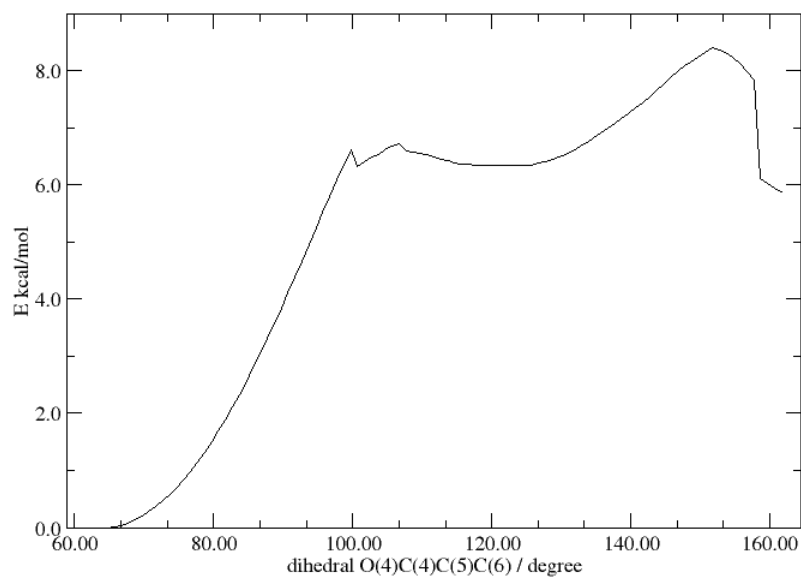


Figure S18: Relaxed PES scan energy profile (BB1K/6-31++G(d,p)). Rotation of O(4)C(4)C(5)C(6) dihedral in structure **10**. Energies refer to structure **10**.

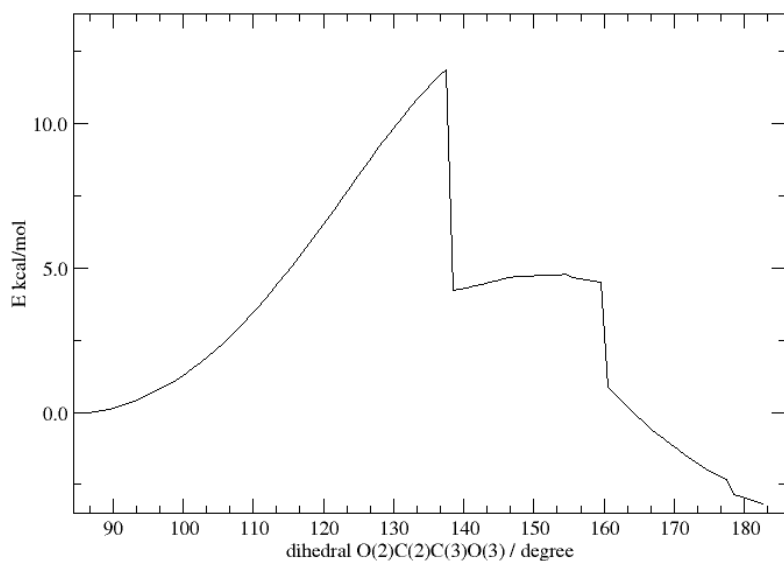


Figure S19: Relaxed PES scan energy profile (BB1K/6-31++G(d,p)). Rotation of O(2)C(2)C(3)O(3) dihedral in structure **10**. Energies refer to structure **10**. The abrupt energy change at 138° comes from O(2) moving into axial position and an increase of the C(1)O(1) distance. The abrupt change in energy at 160° is caused by the formation of a hydrogen bond between HO(1) and O(3).

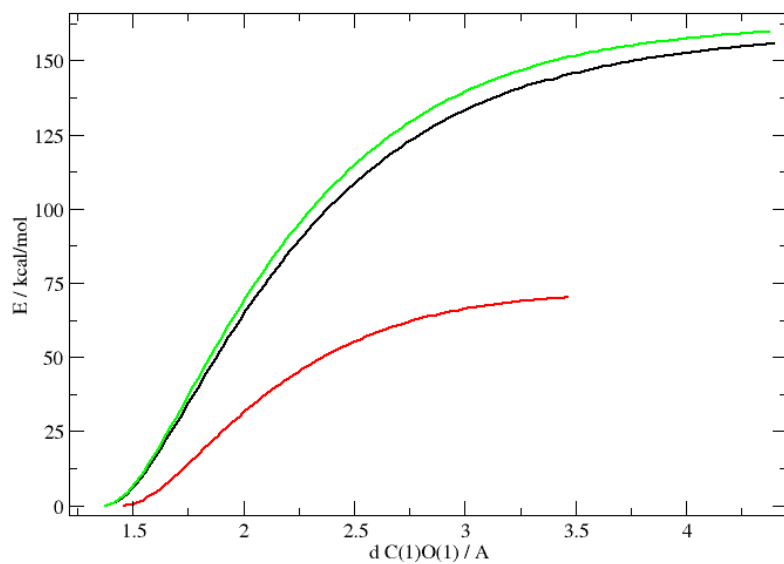


Figure S110: Unrelaxed open-shell PES scan energy profile (BB1K/6-31++G(d,p)). Elongation of C(1)O(1) distance in structures **1** (black), **10** (red), and **16** (green). Energies refer to starting structure.

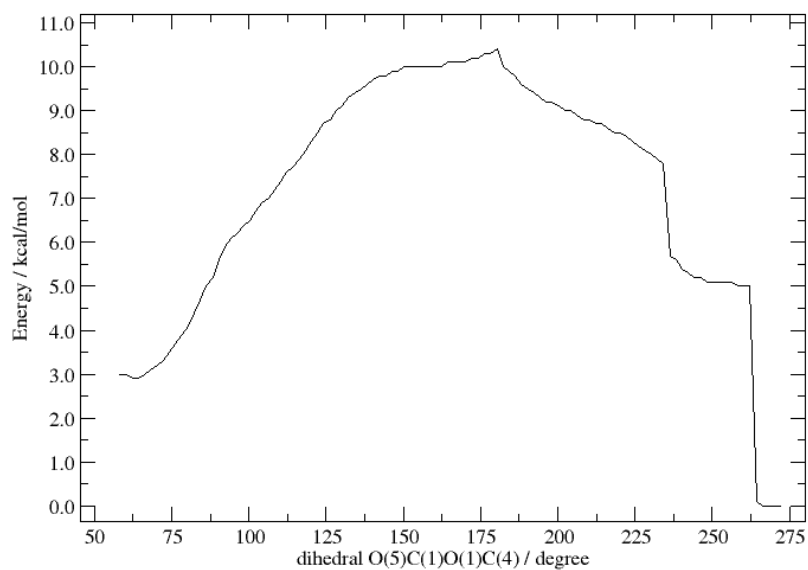


Figure S111: Relaxed PES scan energy profile (BB1K/6-31++G(d,p)). Rotation of O(5)C(1)O(1)C(4) dihedral in structure **41**. Energies refer to structure **1**. The abrupt changes in energy at 234° and 254° come from the formation of the O(6')O(2) and O(3')O(5) hydrogen bonds, respectively.

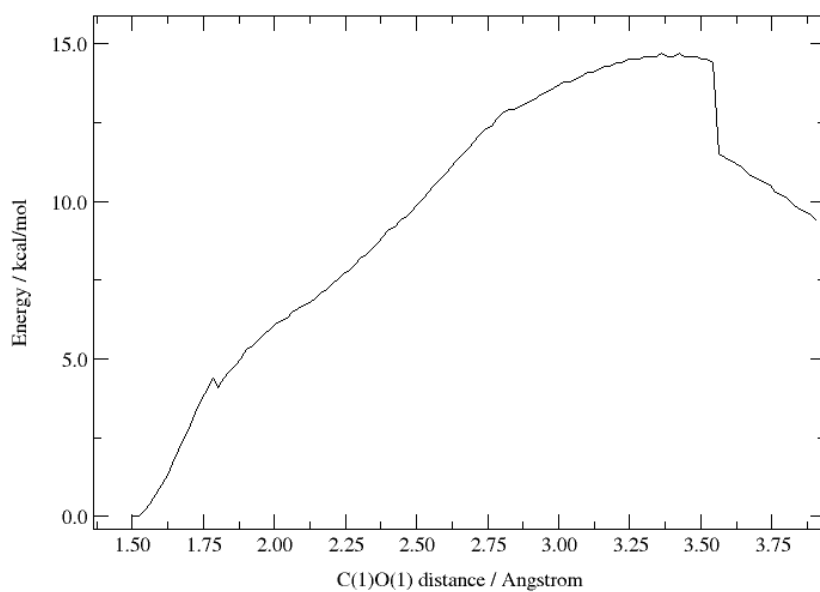


Figure S112: Relaxed PES scan energy profile (BB1K/6-31++G(d,p)). Elongation of C(1)O(1) distance in structure **17**. Energies refer to structure **17**. The abrupt energy change at 3.54 Å is caused by the formation of a hydrogen bond between HO(6') and O(1).

Energy profiles for exo-cyclic mechanisms with different functionals and basis sets

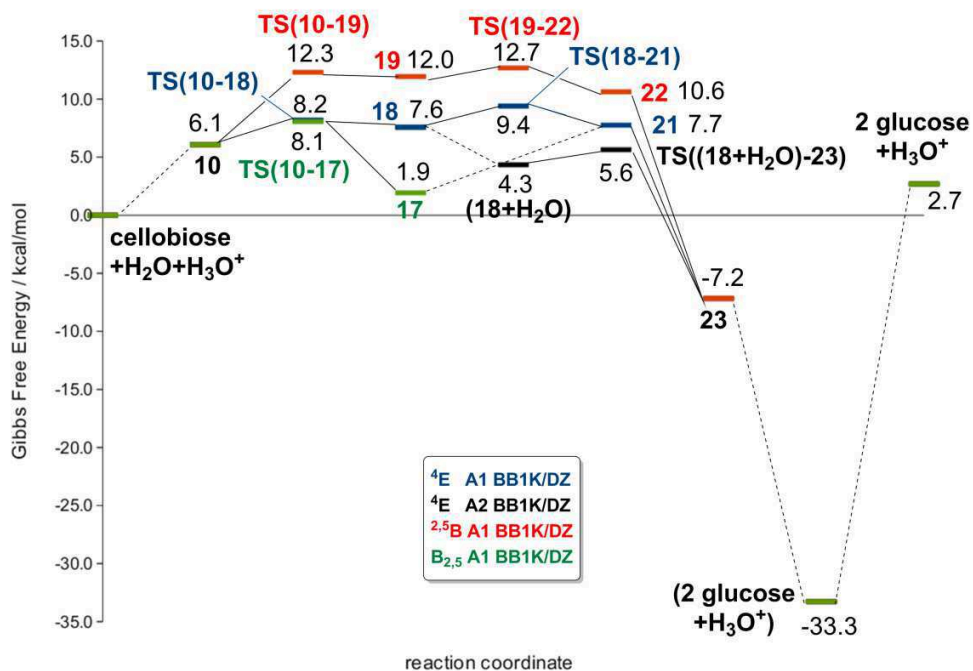


Figure S113: Energy profile (BB1K/6-31++G(d,p)) for exo-cyclic mechanisms. Energies refer to structure $1 + \text{H}_2\text{O} + \text{H}_3\text{O}^+$.

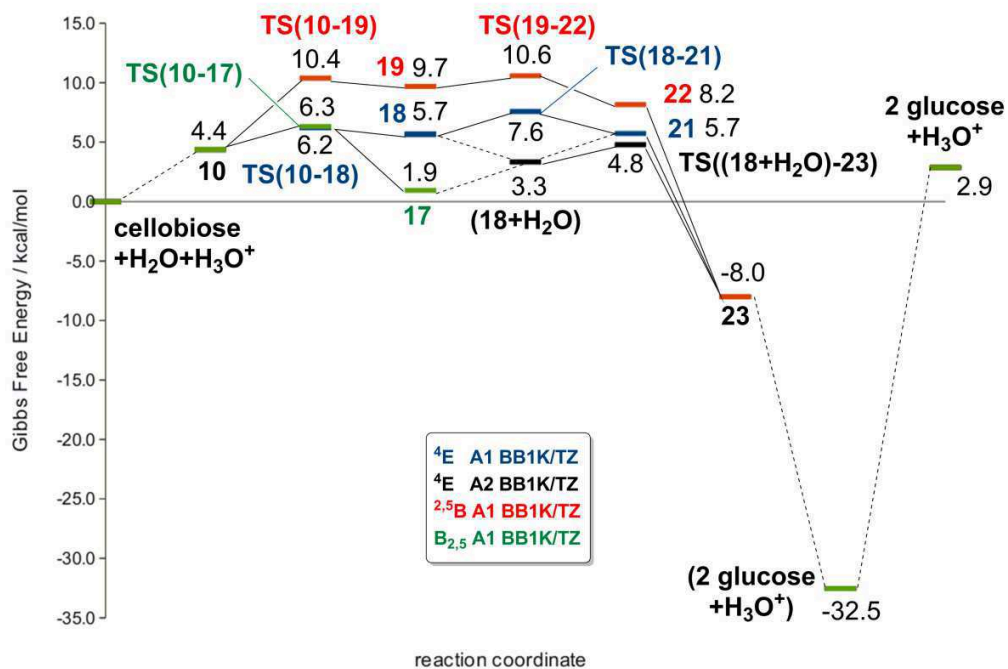
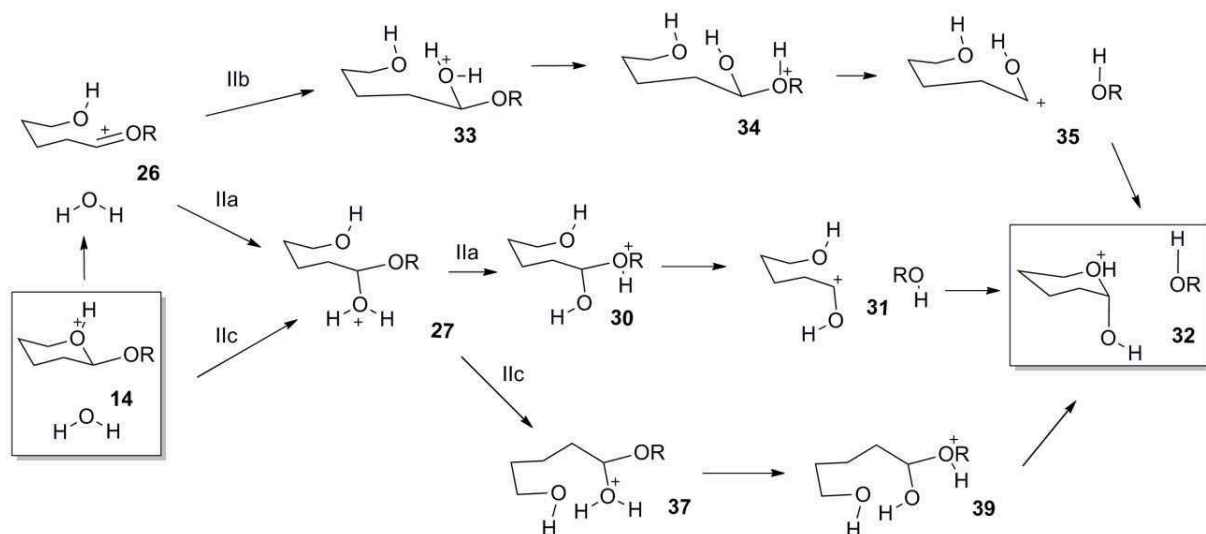


Figure S114: Single-point energy profile (BB1K/6-311++G(2df,2pd)) for exo-cyclic mechanisms. Energies refer to structure $1 + \text{H}_2\text{O} + \text{H}_3\text{O}^+$.

Reaction scheme and energy profiles for endo-cyclic mechanism for structure 1



Scheme S117. A1 and A2 pathways for cellobiose in the endo-cyclic mechanism.

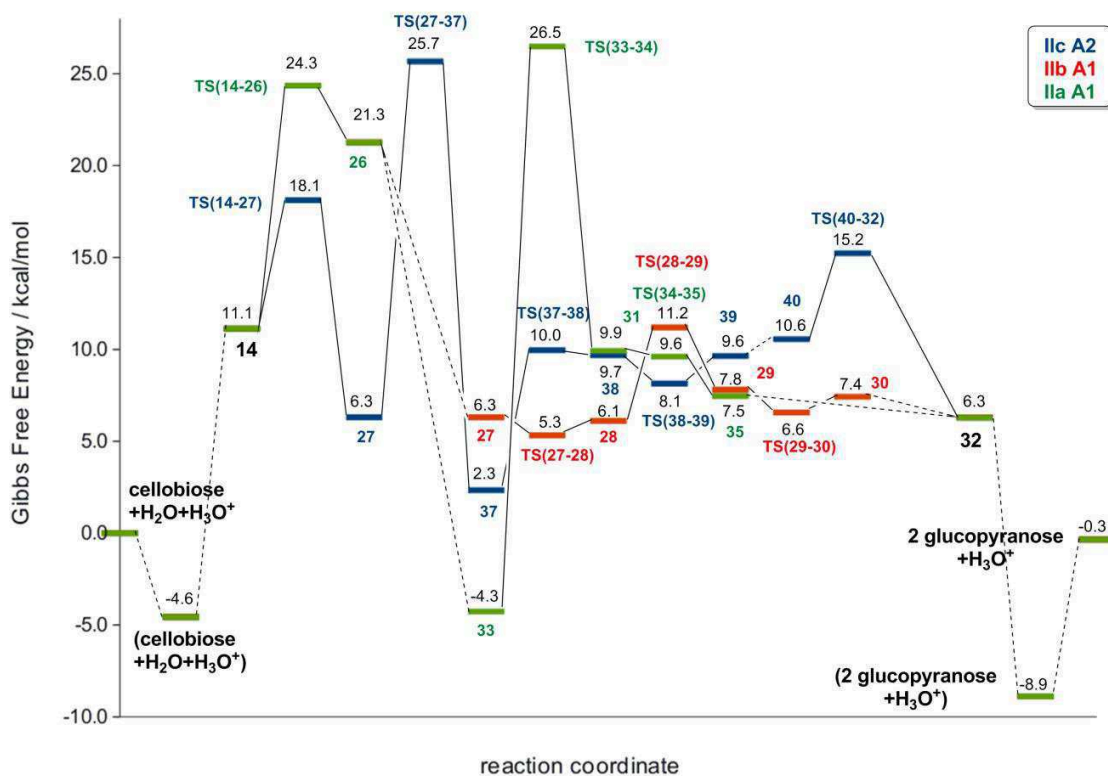


Figure S118. Energy profile for A1 and A2 pathways for cellobiose for the endo-cyclic mechanism (BB1K/6-31++G(d,p)).

Additional Figures

Figure SI14 shows an attempt to correlate the computed protonation free energy of structures **1**, **3** to **6** and **41** with the occupancy of the corresponding oxygen lone pairs.

Figures SI15 and SI16 are enlarged versions of Figures 4 and 8 of the main paper, respectively, that are included to provide a better view of these structures.

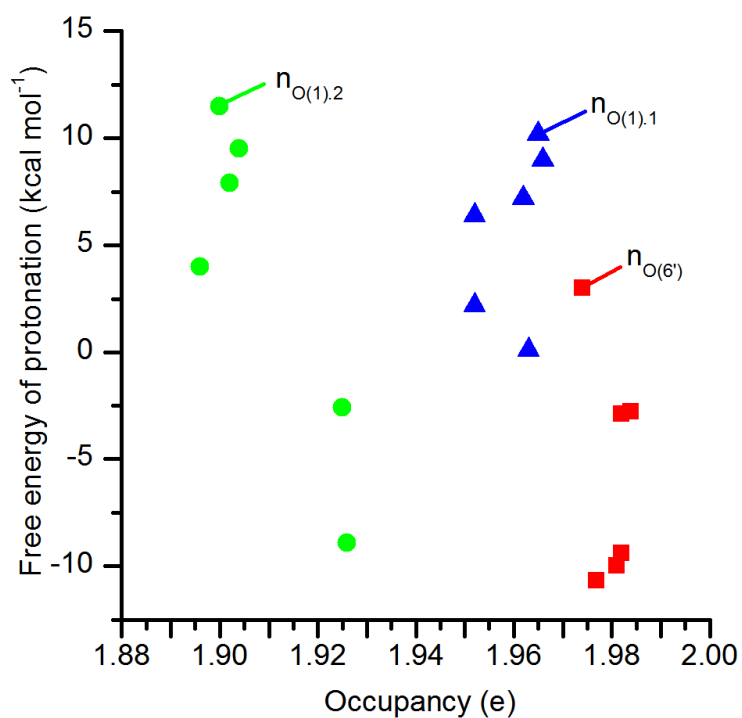


Figure SI19. Correlation of the free energy of protonation versus the occupancy of the O(1)-1, O(1)-2 and O(6) lone pairs in **1**, **3** to **6** and **41**.

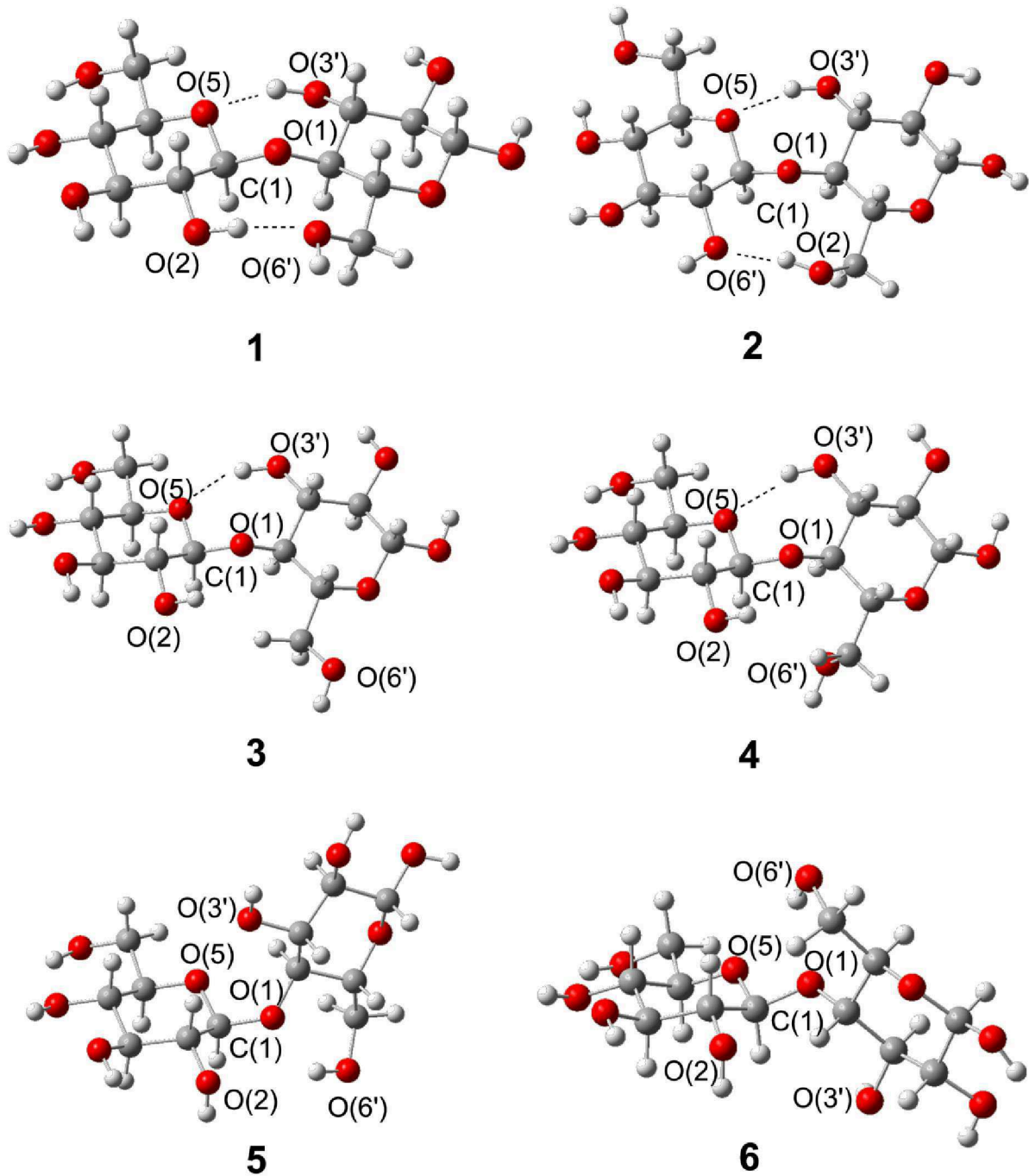


Figure S120. Optimized structures of the cellobiose conformers 1 to 6 (BB1K/6-31++G**).

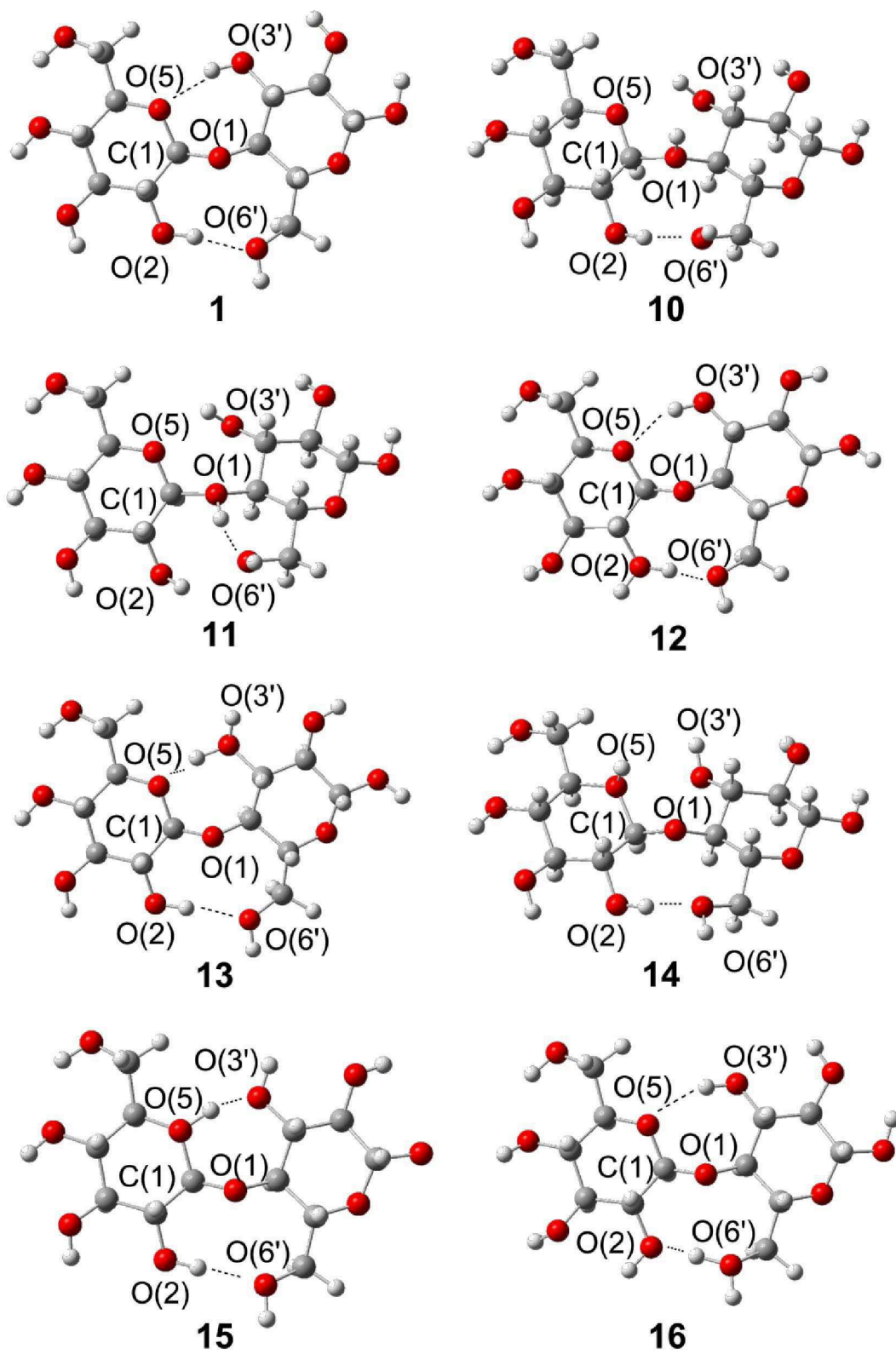


Figure S121. Optimized structures of **1** protonated at different sites (BB1K/6-31++G**).

Total energies of stationary points (Hartree)

Table SI10. BB1K/6-31++G**, CPCM water, 298.15 K, 1 atm.

compound	EZPC	H	G	spE(BB1K/6-31++G(3df,3pd))
H ₂ O	-76.381898	-76.378118	-76.399522	-76.4304370347
H ₃ O ⁺	-76.761283	-76.757457	-76.780387	-76.8212579647
α -glucose	-686.737489	-686.723827	-686.775481	
β -glucose	-686.738926	-686.725169	-686.777114	
1+H ₂ O+H ₃ O ⁺	-1450.281548	-1450.251585	-1450.341078	
α -glucose+ β -glucose+H ₃ O ⁺	-1450.286306	-1450.256975	-1450.347951	
41	-1297.096401	-1297.072112	-1297.147614	-1297.86818839
1	-1297.100801	-1297.076311	-1297.153244	-1297.87201564
2	-1297.102904	-1297.078618	-1297.154955	
3	-1297.099156	-1297.074911	-1297.152705	-1297.87014789
4	-1297.100289	-1297.075137	-1297.153846	-1297.87115728
5	-1297.087332	-1297.062337	-1297.141286	-1297.85859472
6	-1297.085026	-1297.060044	-1297.138701	-1297.85667333
7	-1221.905189	-1221.881679	-1221.956897	
8	-1221.913720	-1221.889704	-1221.965892	
9	-1146.717775	-1146.695146	-1146.767885	
12	-1297.493630	-1297.469930	-1297.543703	-1298.27988119
13	-1297.496645	-1297.472173	-1297.548188	-1298.28133209
10	-1297.469566	-1297.444240	-1297.522642	-1298.25586652
11	-1297.476602	-1297.452183	-1297.527793	-1298.25586652
14	-1297.474458	-1297.448955	-1297.528006	-1298.26387118
15	-1297.495049	-1297.470633	-1297.546290	-1298.28014517
16	-1297.499624	-1297.475243	-1297.551143	-1298.28391710

Table SI11. B3LYP/6-31++G**, CPCM water, 298.15 K, 1 atm (left) and M06-2X/6-31++G**, CPCM water, 298.15 K, 1 atm (right).

compound	EZPC	H	G	EZPC	H	G
H ₂ O	-76.421213	-76.417433	-76.438871	-76.382034	-76.378254	-76.399682
H ₃ O ⁺	-76.797051	-76.793223	-76.816185	-76.759155	-76.755325	-76.777247
41	-1297.678300	-1297.653557	-1297.730185	-1297.174687	-1297.150342	-1297.225914
1	-1297.684850	-1297.659921	-1297.737390	-1297.177971	-1297.153392	-1297.230200
3	-1297.682899	-1297.657262	-1297.737229	-1297.175367	-1297.150142	-1297.228962
4	-1297.683096	-1297.657522	-1297.737341	-1297.176625	-1297.151438	-1297.230028
5	-1297.670564	-1297.645959	-1297.722258	-1297.163250	-1297.139102	-1297.214311
6	-1297.675816	-1297.650912	-1297.728391	-1297.161215	-1297.136331	-1297.214853
10	-1298.054060	-1298.028305	-1298.107053	-1297.543264	-1297.518301	-1297.595602
11	-1298.059610	-1298.034601	-1298.111879	-1297.550115	-1297.525552	-1297.601624
12	-1298.076750	-1298.052418	-1298.127661	-1297.565098	-1297.540970	-1297.615524
13	-1298.081566	-1298.056666	-1298.133471	-1297.573734	-1297.549358	-1297.624897
14	-1298.060985	-1298.034878	-1298.115447	-1297.548314	-1297.522811	-1297.601789
15	-1298.080713	-1298.055714	-1298.132641	-1297.571686	-1297.547289	-1297.622872
16	-1298.083285	-1298.058455	-1298.135101	-1297.575639	-1297.551306	-1297.626843

Table SI12. Computed free energies relative to structure 1 in kcal/mol, CPCM water, 298.15 K, 1 atm.

compound	BB1K/ 6-31++G**	B3LYP/ 6-31++G**	M06-2X/ 6-31++G**	BB1K/ 6-311++G(3pd,3df)
41	3.5	4.5	2.7	2.4
1	0.0	0.0	0.0	0.0
3	0.3	0.1	0.8	1.2
4	-0.4	0.0	0.1	0.5
5	7.5	9.5	10.0	6.4
6	9.1	5.6	9.6	9.6
10	6.8	4.8	7.6	4.4
11	3.6	1.8	3.9	-0.6
12	-6.4	-8.1	-6.3	-10.7
13	-9.2	-11.8	-10.5	-11.6
14	3.4	-0.5	3.7	1.8
15	-8.1	-11.3	-9.5	-10.9
16	-11.1	-12.8	-12.0	-13.2

Table SI13. Absolute free energies in Hartree for structures 10, 12-14 and 16 (298.15 K, 1atm).

compound	G(B97-1/6- 31++G**, gas phase)	G(B97-1/6- 31++G**, SMD)	G(BB1K/6- 31++G**, gas phase)
10	-1297.653957	-1297.794645	-1297.419672
12	-1297.664611	-1297.811310	-1297.447881
13	-1297.669348	-1297.810924	-1297.452312
14	-1297.681326	-1297.796008	-1297.425601
16	-1297.667762	-1297.817733	-1297.449656

Table SI14. BB1K/6-31++G, CPCM water, 298.15 K, 1 atm: Pathway I.**

compound	EZPC	H	G	spE(B3LYP/6- 311++G(d,p))	spE(M06-2X/6- #11++G(d,p))	spE(BB1K/6- 311++G(3df,3pd))
TS(10-17)	-1297.466285	-1297.441989	-1297.517726	-1298.42199192	-1297.92288382	-1298.25276315
TS(10-18)	-1297.466204	-1297.441869	-1297.517808	-1298.42391927	-1297.92321569	-1298.25293669
TS(10-19)	-1297.459775	-1297.435187	-1297.511056	-1298.41805234	-1297.91657575	-1298.24627009
17	-1297.476617	-1297.451887	-1297.528588	-1298.42988056	-1297.93481896	-1298.26132724
18	-1297.466694	-1297.441683	-1297.519122	-1298.42329589	-1297.92435573	-1298.25381617
18+H ₂ O	-1373.849940	-1373.821601	-1373.906685	-1374.86919983	-1374.33668669	-1374.68797338
19	-1297.461441	-1297.435492	-1297.515964	-1298.41809229	-1297.91724589	-1298.24740007
20	-1297.457192	-1297.430081	-1297.515656			
TS(18-21)	-1297.465210	-1297.440329	-1297.517729	-1298.42596100	-1297.92007435	-1298.25077616
TS((18+H ₂ O)-23)	-1373.849630	-1373.821370	-1373.906298	-1374.87076504	-1374.33442826	-1374.68565119
TS(19-22)	-1297.461239	-1297.435679	-1297.515119	-1298.41978415	-1297.91527420	-1298.24597866
21	-1297.469130	-1297.442872	-1297.524923	-1298.43219746	-1297.92102355	-1298.25370889
21+H ₂ O	-1373.852209	-1373.821775	-1373.916678	-1374.87885536	-1374.32739856	-1374.68686515
22	-1297.465338	-1297.438712	-1297.522359	-1298.42750289	-1297.91706835	-1298.24983439
22+H ₂ O	-1373.852649	-1373.823062	-1373.912217	-1374.87881828	-1374.33323958	-1374.68839164
23	-1373.866997	-1373.839451	-1373.924562	-1374.88971587	-1374.35129560	-1374.70602874
24	-1373.860772	-1373.833206	-1373.917710	-1374.87913827	-1374.34803956	-1374.69806765

Table SI15. BB1K/6-31++G, CPCM water, 298.15 K, 1 atm: Pathway II.**

compound	EZPC	H	G
TS(14-26)	-1373.836626	-1373.807427	-1373.894834
TS(14-36)	-1373.849442	-1373.821647	-1373.904756
26	-1373.839373	-1373.809056	-1373.899749
27	-1373.869688	-1373.843741	-1373.923586
TS(27-28)	-1373.871420	-1373.845753	-1373.925152
28	-1373.869878	-1373.843803	-1373.923901
TS(28-29)	-1373.861661	-1373.835775	-1373.915780
29	-1373.866626	-1373.840161	-1373.921188
TS(29-30)	-1373.869033	-1373.842950	-1373.923171
30	-1373.867258	-1373.840765	-1373.921799
32	-1373.865198	-1373.837102	-1373.923610
33	-1373.886708	-1373.860750	-1373.940417
TS(33-34)	-1373.835964	-1373.809511	-1373.891439
34	-1373.862317	-1373.835344	-1373.917832
TS(34-35)	-1373.862738	-1373.836199	-1373.918334
35	-1373.864667	-1373.837255	-1373.921744
TS(27-37)	-1373.796689	-1373.771446	-1373.849225
37	-1373.875811	-1373.849729	-1373.929914
TS(37-38)	-1373.864037	-1373.838243	-1373.917753
38	-1373.863950	-1373.837728	-1373.918186
TS(38-39)	-1373.866196	-1373.840286	-1373.920652
39	-1373.863911	-1373.837619	-1373.918257
40	-1373.860199	-1373.832972	-1373.916809
TS(40-32)	-1373.853649	-1373.826647	-1373.909351

Table SI16. 4-O-methyl-cellobiose, BB1K/6-31++G, CPCM water, 298.15 K, 1 atm: Pathway I.**

compound	EZPC	H	G
10me	-1336.713408	-1336.686718	-1336.768549
TS(10me-17me)	-1336.711003	-1336.685258	-1336.764724
TS(10me-18me)	-1336.709750	-1336.684094	-1336.763108
TS(10me-19me)	-1336.704616	-1336.678483	-1336.758456
17me	-1336.723099	-1336.697070	-1336.776519
18me	-1336.710273	-1336.683711	-1336.765499
18me+H ₂ O	-1413.093766	-1413.063505	-1413.155529
19me	-1336.707080	-1336.679916	-1336.762758
TS(18me-21me)	-1336.708449	-1336.682111	-1336.763164
TS((18me+H ₂ O)-23me)	-1413.093559	-1413.063752	-1413.152300
TS(19me-22me)	-1336.705867	-1336.679277	-1336.760814
21me	-1336.712997	-1336.685010	-1336.772411
22me	-1336.708822	-1336.680809	-1336.766539
23me	-1413.112409	-1413.083117	-1413.174083

Table SI17. BB1K/6-31++G, CPCM water, 298.15 K, 1 atm: Protonation of structures 1, 41 and 3-6.**

compound	EZPC	H	G
41-O(1)-1	-1297.476248	-1297.451597	-1297.528283
41-O(1)-2	-1297.462110	-1297.437614	-1297.513420
41-O(2)	-1297.494349	-1297.470285	-1297.545157
41-O(3)	-1297.495925	-1297.471824	-1297.546776
41-O(5)-1	-1297.456806	-1297.431807	-1297.508953
41-O(5)-2	-1297.481394	-1297.457424	-1297.531557
41-O(6)	-1297.482503	-1297.458317	-1297.533271
3-O(1)-1	-1297.463731	-1297.438088	-1297.517285
3-O(1)-2	-1297.461924	-1297.436573	-1297.515314
3-O(2)	-1297.477455	-1297.452216	-1297.530710
3-O(3)	-1297.495885	-1297.470862	-1297.548798
3-O(5)-1	-1297.475624	-1297.449970	-1297.529392
3-O(5)-2	-1297.495779	-1297.470843	-1297.548038
3-O(6)	-1297.484562	-1297.459356	-1297.538061
4-O(1)-1	-1297.466624	-1297.440926	-1297.520440
4-O(1)-2	-1297.468759	-1297.443259	-1297.522121
4-O(2)	-1297.477047	-1297.451913	-1297.530092
4-O(3)	-1297.497304	-1297.472353	-1297.550427
4-O(5)-1	-1297.474051	-1297.448837	-1297.526460
4-O(5)-2	-1297.497451	-1297.472485	-1297.549799
4-O(6)	-1297.497997	-1297.473526	-1297.549721
5-O(1)-1	-1297.465373	-1297.440123	-1297.518586
5-O(1)-2	-1297.475277	-1297.451146	-1297.526292
5-O(2)	-1297.472335	-1297.447330	-1297.524857
5-O(3)	-1297.478064	-1297.454315	-1297.528005
5-O(5)-1	-1297.466099	-1297.442364	-1297.516044
5-O(5)-2	-1297.452834	-1297.428297	-1297.504147
5-O(6)	-1297.475229	-1297.451005	-1297.526782
6-O(1)-1	-1297.456759	-1297.431619	-1297.509360
6-O(1)-2	-1297.483111	-1297.459081	-1297.533746
6-O(2)	-1297.459128	-1297.434154	-1297.512045
6-O(3)	-1297.465265	-1297.440596	-1297.517526
6-O(5)-1	-1297.458135	-1297.433054	-1297.510395
6-O(5)-2	-1297.466747	-1297.441621	-1297.520167
6-O(6)	-1297.484199	-1297.459987	-1297.535440

Table SI18. Total Energies for pathway A1 for structure 2, BB1K/6-31++G, CPCM water, 298.15 K, 1 atm.**

compound	EZPC	H	G
10'	-1297.470223	-1297.445021	-1297.523070
TS(10'-17')	-1297.466512	-1297.442127	-1297.518287
TS(10'-18')	-1297.464306	-1297.439962	-1297.515844
TS(10'-19')	-1297.463446	-1297.438851	-1297.515519
17'	-1297.479193	-1297.454187	-1297.532172
18'	-1297.464620	-1297.439378	-1297.518023
19'	-1297.463843	-1297.438211	-1297.518099
TS(18'-21')	-1297.461728	-1297.436630	-1297.514439
TS(19'-22')	-1297.460726	-1297.435383	-1297.514040
21'	-1297.465028	-1297.438275	-1297.523043
22'	-1297.468822	-1297.442561	-1297.523787

References

- (1) Gaussian 09, Revision A.1, M. J. Frisch, G. W. Trucks, H. B. Schlegel, G. E. Scuseria, M. A. Robb, J. R. Cheeseman, G. Scalmani, V. Barone, B. Mennucci, G. A. Petersson, H. Nakatsuji, M. Caricato, X. Li, H. P. Hratchian, A. F. Izmaylov, J. Bloino, G. Zheng, J. L. Sonnenberg, M. Hada, M. Ehara, K. Toyota, R. Fukuda, J. Hasegawa, M. Ishida, T. Nakajima, Y. Honda, O. Kitao, H. Nakai, T. Vreven, J. A. Montgomery, Jr., J. E. Peralta, F. Ogliaro, M. Bearpark, J. J. Heyd, E. Brothers, K. N. Kudin, V. N. Staroverov, R. Kobayashi, J. Normand, K. Raghavachari, A. Rendell, J. C. Burant, S. S. Iyengar, J. Tomasi, M. Cossi, N. Rega, J. M. Millam, M. Klene, J. E. Knox, J. B. Cross, V. Bakken, C. Adamo, J. Jaramillo, R. Gomperts, R. E. Stratmann, O. Yazyev, A. J. Austin, R. Cammi, C. Pomelli, J. W. Ochterski, R. L. Martin, K. Morokuma, V. G. Zakrzewski, G. A. Voth, P. Salvador, J. J. Dannenberg, S. Dapprich, A. D. Daniels, Ö. Farkas, J. B. Foresman, J. V. Ortiz, J. Cioslowski, and D. J. Fox, Gaussian, Inc., Wallingford CT, 2009.
- (2) Zhao, Y.; Lynch, B. J.; Truhlar, D. G. *The Journal of Physical Chemistry A* **2004**, *108*, 2715.
- (3) Hamprecht, F. A.; Cohen, A. J.; Tozer, D. J.; Handy, N. C. *The Journal of Chemical Physics* **1998**, *109*.
- (4) Becke, A. D. *Phys. Rev. A* **1988**, *38*, 3098.
- (5) Lee, C.; Yang, W.; Parr, R. G. *Physical Review B* **1988**, *37*, 785.
- (6) Becke, A. D. *J. Chem. Phys.* **1993**, *98*, 1372.
- (7) Becke, A. D. *J. Chem. Phys.* **1993**, *98*, 5648.
- (8) Zhao, Y.; Schultz, N. E.; Truhlar, D. G. *J. Chem. Phys.* **2005**, *123*, 161103.
- (9) Marenich, A. V.; Cramer, C. J.; Truhlar, D. G. *The Journal of Physical Chemistry B* **2009**, *113*, 4538.
- (10) Gonzalez, C.; Schlegel, H. B. *J. Chem. Phys.* **1989**, *90*, 2154.
- (11) Gonzalez, C.; Schlegel, H. B. *J. Phys. Chem.* **1990**, *94*, 5523.
- (12) G.Schaftenaar; Noordik, J. H. *J. Comput.-Aided Mol. Design* **2000**, *14*, 123.
- (13) Dennington II, R.; Keith, T. J. M.; Eppinnett, K.; Hovell, W. L.; Gilliland, R. In *GaussView*; 3.0 ed.; Semichem, Inc., Shawnee Mission, KS: 2003.
- (14) Beck, J. M.; Miller, S. M.; Peczu, M. W.; Hadad, C. M. *J. Org. Chem.* **2012**, *77*, 4242.
- (15) Zhao, Y.; Truhlar, D. G. *The Journal of Physical Chemistry A* **2004**, *108*, 6908.
- (16) Zhao, Y.; González-García, N.; Truhlar, D. G. *J. Phys. Chem. A* **2005**, *109*, 2012.
- (17) Zhao, Y.; Truhlar, D. G. *Theoretical Chemistry Accounts* **2007**, *120*, 215.
- (18) Takano, Y.; Houk, K. N. *J. Chem. Theory Comput.* **2004**, *1*, 70.
- (19) Ho, J.; Coote, M. L. *Theoretical Chemistry Accounts* **2009**, *125*, 3.
- (20) Camaioni, D. M.; Schwerdtfeger, C. A. *The Journal of Physical Chemistry A* **2005**, *109*, 10795.
- (21) Kelly, C. P.; Cramer, C. J.; Truhlar, D. G. *The Journal of Physical Chemistry B* **2006**, *110*, 16066.
- (22) Liptak, M. D.; Shields, G. C. *J. Am. Chem. Soc.* **2001**, *123*, 7314.
- (23) Pincu, M.; Cocinero, E. J.; Mayorkas, N.; Brauer, B.; Davis, B. G.; Gerber, R. B.; Simons, J. P. *The Journal of Physical Chemistry A* **2011**, *115*, 9498.
- (24) Hardy, B. J.; Gutierrez, A.; Lesiak, K.; Seidl, E.; Widmalm, G. r. *J. Phys. Chem.* **1996**, *100*, 9187.
- (25) Christensen, N. J.; Hansen, P. I.; Larsen, F. H.; Folkerman, T.; Motawia, M. S.; Engelsen, S. B. *Carbohydrate Research* **2010**, *345*, 474.

Appendix B

Solvent Influence on Cellulose 1, 4- β -Glycosidic Bond Cleavage: A Molecular Dynamics and Metadynamics Study

Claudia Loerbroks, Eliot Boulanger, and Walter Thiel

Chemistry - A European Journal, 2014, submitted.

Carried out all calculations, analyzed the results, and wrote the draft of the manuscript

Solvent Influence on Cellulose 1,4- β -Glycosidic Bond Cleavage: A Molecular Dynamics and Metadynamics Study

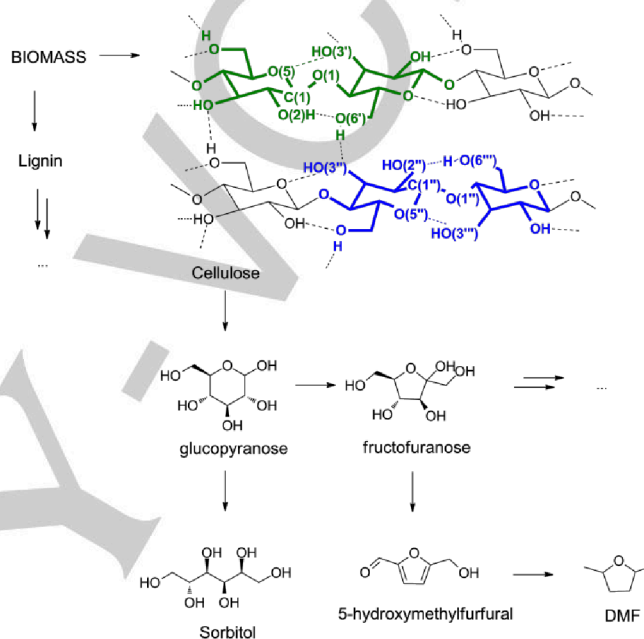
Claudia Loerbroks, Eliot Boulanger and Walter Thiel^{*[a]}

Abstract: We explore the influence of two solvents, water and the ionic liquid 1-ethyl-3-methylimidazolium acetate (EmimAc), on the conformations of two cellulose models (cellobiose and a chain of 40 glucose units) and their impact on glycosidic bond cleavage by acid hydrolysis using molecular dynamics and metadynamics simulations. We investigate the rotation around the glycosidic bond and ring puckering as well as the anomeric effect and hydrogen bonds in order to gauge the effect on the hydrolysis mechanism. We find that EmimAc eases hydrolysis by stronger solvent-cellulose interactions, which break structural and electronic barriers to hydrolysis. Our results indicate that hydrolysis in cellulose chains should start from the ends and not in the centre of the chain, which is less accessible to solvent.

Introduction

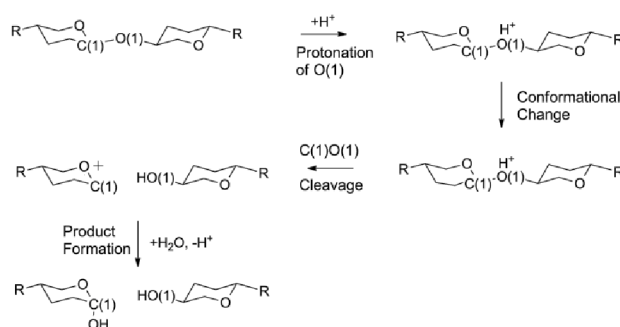
Cellulose is regarded as a potential alternative energy resource. It can be used to yield platform molecules for chemical industry like sorbitol and hydroxymethylfurfural (Scheme 1) and has thus received much attention in recent research.^[1] It can be decomposed by enzymatic reactions (using cellulases and cellobiases)^[2] and by acid hydrolysis; we focus on the latter process in this study. The rigid structure of native cellulose is difficult to break up.^[1a, b, 3] The hydrolysis has to overcome high energy barriers from cellulose to glucose (30 to 40 kcal mol⁻¹)^[4] and the reaction is carried out at high temperatures with the use of strong acids (pKa < -3).^[5] Since the early days of biomass hydrolysis, reaction conditions have been improved considerably, e.g. by changing the solvent from water to ionic liquids,^[6] by moving from strong acid catalysts like sulphuric acid to solid phase and metal catalysts,^[3e, 5c] and by introducing upstream processes like ball milling.^[7]

The necessity of harsh reaction conditions is attributed to the rigid structure of cellulose. In this article we focus on cellulose I β , which is abundant in nature (Scheme 1). It consists of 1,4- β -connected glucose chains, which are held together by hydrogen bonds and van der Waals forces.^[8] The glycosidic linkage C(1)-O(1), which is broken in acid hydrolysis, is surrounded by intramolecular hydrogen bonds (O(3')H \cdots O(5), O(2)H \cdots O(6'), and O(2) \cdots HO(6'')) and the intermolecular hydrogen bond O(6')H \cdots O(3'') that connects the chains.^[8]



Scheme 1: Possible conversion pathways starting from biomass and part of the cellulose I β structure with O(2)H \cdots O(6') (green) and O(2') \cdots HO(6'') (blue) hydrogen bonds.

In a recent study on cellobiose we used an implicit water solvent model and proposed an A1 type mechanism for dissociation into single glucose molecules,^[9] which proceeds as follows (Scheme 2): The glycosidic bond is activated by protonation of O(1) and a conformational change in the non-reducing ring,^[10] the C(1)-O(1) bond is cleaved, water is added at C(1), and deprotonation leads to the product.



Scheme 2: Proposed mechanism for the acid hydrolysis of cellulose.

[a] C. Loerbroks, E. Boulanger, Prof. Dr. W. Thiel
Max-Planck-Institut für Kohlenforschung
Kaiser-Wilhelm-Platz 1
45470 Mülheim an der Ruhr (Germany)
E-mail: thiel@kofo.mpg.de

Two activation steps, namely protonation and conformational change, are necessary to overcome not only the structural impediments to the reaction, like hydrogen bonds, but also the electronic ones, such as anomeric effects arising from the delocalisation of electronic density from and to the glycosidic bond (Figure 1). The exo-anomeric effect describes the donation from the O(1) lone pair into the anti-bonding C(1)-O(5) orbital ($n(O(1)) \rightarrow \sigma^*(C(1)-O(5))$). It is present if the lone pair (n) and the anti-bonding orbital (σ^*) are aligned in an anti-periplanar manner, as in chair conformers with equatorial C(1)-O(1) bonds that are found in cellulose. This interaction leads to a shortened C(1)-O(1) bond^[9, 11] and an energetically more demanding hydrolysis. The structural features causing the exo-anomeric effect can be removed with the two activation steps in the A1 hydrolysis mechanism.

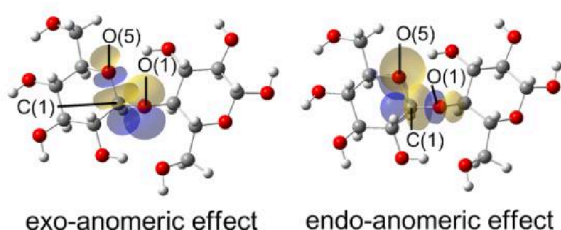


Figure 1: Orbital overlap responsible for anomeric effects in cellobiose.

Acting in the opposite direction is the endo-anomeric effect: it describes the donation of the O(5) lone pair into the anti-bonding C(1)-O(1) orbital ($n(O(5)) \rightarrow \sigma^*(C(1)-O(1))$) and lengthens the C(1)-O(1) bond, so hydrolysis becomes more facile. It operates in glucose conformers with an axial C(1)-O(1) bond, which can be generated by a conformational change of the non-reducing ring.

Several studies have addressed the dissolution of cellulose^[1c-f, 12] and the cleavage of the C(1)-O(1) glycosidic linkage.^[1g, 9, 13] Independent of the chosen model system, they have identified similar features that influence the utilization of cellulose: the puckering of the non-reducing glucose ring attached to the C(1)-O(1) bond, the charge on the C(1) atom, the axial or equatorial position of the C(1)-O(1) bond in the non-reducing ring, inter- or intramolecular hydrogen bonds, and the anomeric effect.^[1e, 9-10, 12, 14]

While previous molecular dynamics studies focused on the dissolution process of cellulose and the behaviour of conformers and hydrogen bonding in different solvents, the detailed impact of solvents on the pathway of acid hydrolysis, especially the impact on the electronic structure, received less attention. Our goal is therefore to unravel how different solvents influence the acid hydrolysis mechanism. We examine the structural changes (hydrogen bonds, ring flips, and rotations) in different positions of cellulose chains (40 glucose units) in water and in the ionic liquid 1-ethyl-3-methylimidazolium acetate (EmimAc) using molecular dynamics and metadynamics simulations. All relevant conformations are characterised with regard to populations and

free energy profiles, anomeric effects, hydrogen bonding, and correlations to other conformations.

Results and Discussion

To investigate solvent effects on cellulose structural properties, we considered two models: cellobiose and a cellulose chain of 40 glucose units. They were solvated in water and in the ionic liquid EmimAc (Figure 2). We first focus on cellobiose to get a general overview, and thereafter we discuss the cellulose chain with an emphasis on determining where hydrolysis preferably takes place.

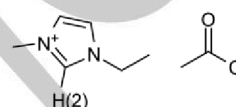


Figure 2: The ionic liquid 1-ethyl-3-methylimidazolium acetate (EmimAc); H(2) is the most acidic proton in the cation.

Several structural parameters are known to be relevant to cellulose hydrolysis because they influence the anomeric effects.^[9] Most important are the following (Figure 3): the O(5)-C(1)-O(1)-C(4') dihedral angle (ϕ) that takes into account the relative orientation of two adjacent glucose units and determines the magnitude of the $n(O(X)) \rightarrow \sigma^*(C(1)-O(Y))$ overlap and the exo-anomeric effect; the ring flip dihedral angle C(1)-O(5)-C(2)-C(4) (α_1) that characterises the conformation of the non-reducing glucose unit; and the orientation of the C(1)-O(1) bond relative to the ring [β_1 C(5)-O(5)-C(1)-O(1), β_2 C(3)-C(2)-C(1)-O(1)] which also depends on α_1 . The dihedral angles β_1 and β_2 determine whether an exo- ($n(O(1)) \rightarrow \sigma^*(C(1)-O(5))$) or an endo-anomeric effect ($n(O(5)) \rightarrow \sigma^*(C(1)-O(1))$) is present. In the following subsection, we will separately address each of these parameters before looking at their combined effects.

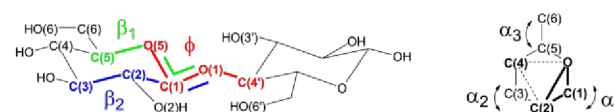


Figure 3: Dihedral angles β_1 , β_2 , ϕ , and α shown for cellobiose and a simplified glucose model.

Rotation ϕ : The rotation ϕ regulates the strength of the exo-anomeric effect. According to our previous study,^[9] the exo-anomeric effect reaches its maximum in the range from $\phi = -74^\circ$ to $\phi = -92^\circ$ and is three times smaller around $\phi = 0^\circ$ or $\phi = 180^\circ$. It was shown that the ϕ dihedral tends to remain around -90° even when the intra-molecular hydrogen bonds $O(3')H \cdots O(5)$ and $O(2) \cdots O(6')$ are broken. In the literature, ϕ values of -89° in crystal structure, -73° to -80° in water and -125° in EmimAc have been reported at the lowest minima.^[8d, 14-15]

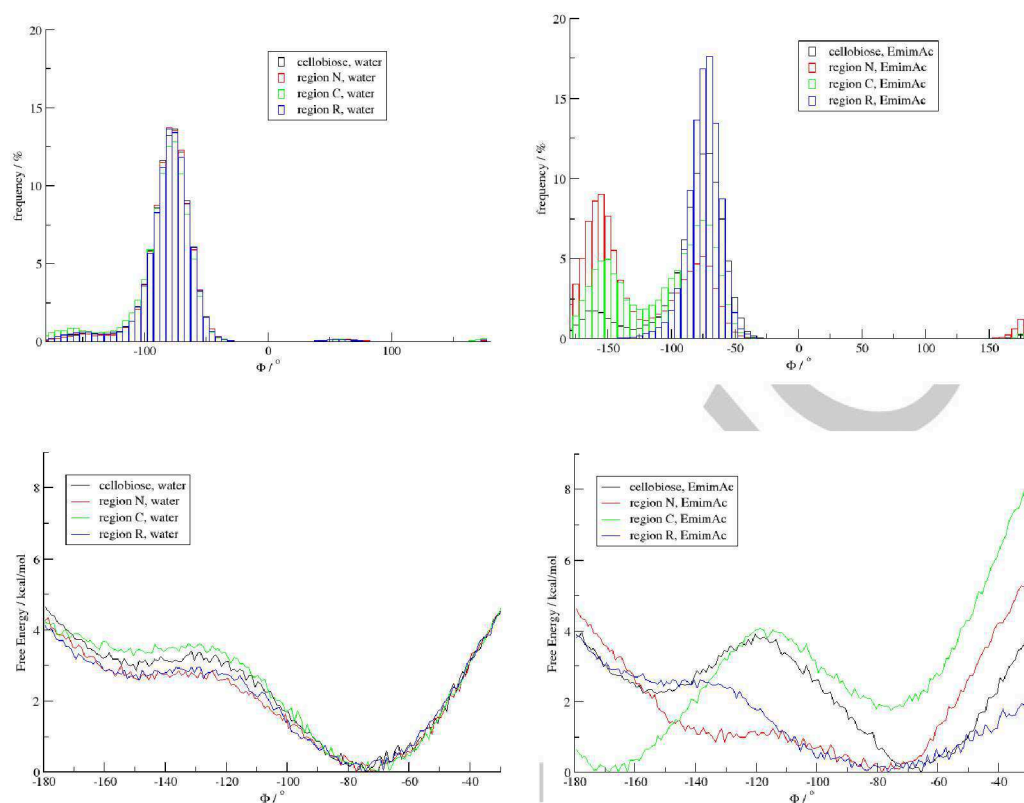


Figure 4: Distribution with respect to ϕ in water (top, left) and EmimAc (top, right) taken from 100 ns molecular dynamics simulations and corresponding free energy profiles taken from 20 ns metadynamics simulations at 420 K in water (bottom, left) and EmimAc (bottom, right): results for cellobiose and regions N, C, and R of the cellulose chain.

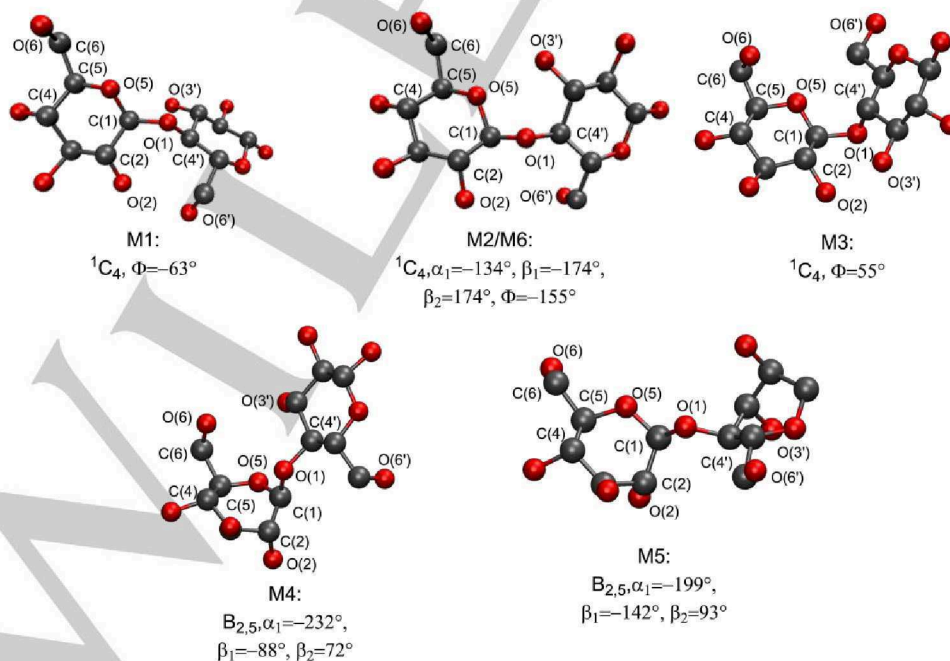


Figure 5: Exemplary structures for M1 to M6 and selected values of important dihedral angles. Hydrogen atoms are omitted for clarity.

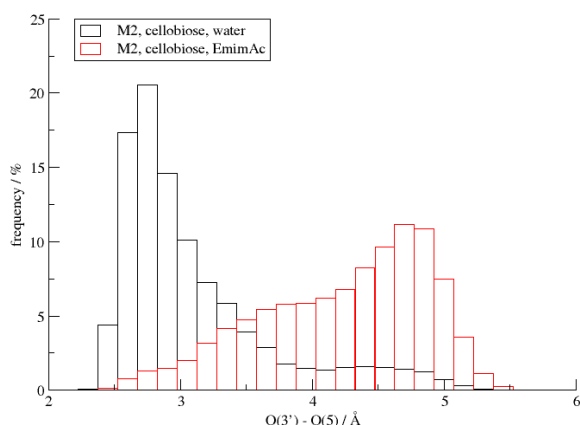


Figure 6: Correlation of the hydrogen bond distances $O(3')\cdots O(5)$ and the dihedral angle ϕ taken from 100 ns molecular dynamics simulations of cellobiose at 420 K in water and EmimAc.

The distributions and free energy profiles with respect to ϕ are shown for both cellulose models in Figure 4, while example structures are depicted in Figure 5. We first focus on cellobiose (black). Three population maxima can be seen: M1 around -150° (M1 population: water 3%, EmimAc 12%), M2 around -78° (M2 population: water 96%, EmimAc 88%), and M3 around 64° (M3 population: water 1%, EmimAc 0%). The location of M2 is slightly shifted in EmimAc (water -78° , EmimAc -66°). The higher the population, the deeper is the minimum and the higher is the barrier to the adjacent minima in the free energy profile, see e.g. M1 population in EmimAc 12% and water 3%, barrier in EmimAc $1.6 \text{ kcal mol}^{-1}$ and water $0.4 \text{ kcal mol}^{-1}$ (Figure 4, bottom, black). These data already show a first difference in the solvation between water and EmimAc: M1 has a higher population in EmimAc, and the positions of the minima are slightly shifted.

We are especially interested in the influence of the positions of the minima on the anomeric effect. Since the exo-anomeric effect is maximal in M2, any deviation from the best M2 dihedral angle (-78°) facilitates conformational changes and protonation of O(1), as the reduced $n(O(1))\rightarrow\sigma^*(C(1)-O(5))$ orbital overlap lengthens the C(1)-O(1) bond. In EmimAc deviations from the perfect dihedral are more likely considering the higher population of M1 and the shift in the optimum M2 dihedral angle, and hence EmimAc should be a superior solvent for hydrolysis.

Also of interest is the correlation between the hydrogen bond distances and the two major conformers M1 and M2. The presence of intra- or intermolecular hydrogen bonds influences hydrolysis and the anomeric effect. The most important intramolecular hydrogen bond is $O(3')\cdots O(5)$ close to the glycosidic linkage (the $O(2)\cdots O(6')$ hydrogen bond is discussed in the Supporting Information). In water this hydrogen bond is persistent ($O(3')\cdots O(5)$ population 70-80%),^[14-15] while in the ionic liquid it is replaced by intermolecular hydrogen bonds with the anion.^[12, 14-16] Therefore the anion provides the main driving force for structural changes in cellulose solutes, while interactions with the cation are of lesser importance.^[1c, 1f, 15b, 16c, 17]

The intramolecular hydrogen bond $O(3')\cdots O(5)$ and intermolecular solute-solvent interaction regulate the strength of the exo-anomeric effect.^[18] A hydrogen bond of the type solvent- $H\cdots O(X)-C(1)$ or $O(3')H\cdots O(5)-C(1)$ can increase the acceptor strength of $\sigma^*(O(X)-C(1))$, while a small solvent- $O\cdots O(Y)$ distance can increase the donation of electron density from the lone pair (n) of $O(Y)$ into $\sigma^*(O(X)-C(1))$.

The calculated distribution of the $O(3')\cdots O(5)$ distances in water and EmimAc for M1 and M2 are depicted in Figure 6. In water the $O(3')\cdots O(5)$ hydrogen bond is found only in M2. As the $O(3')\cdots O(5)$ distance increases upon rotation around the glycosidic linkage, it is broken in M1 (Figure 5). As expected, the number of intramolecular hydrogen bonds is reduced in EmimAc compared to water: for cellobiose, from 80% (water) to 13% (EmimAc) for the $O(3')\cdots O(5)$ hydrogen bond in M2.

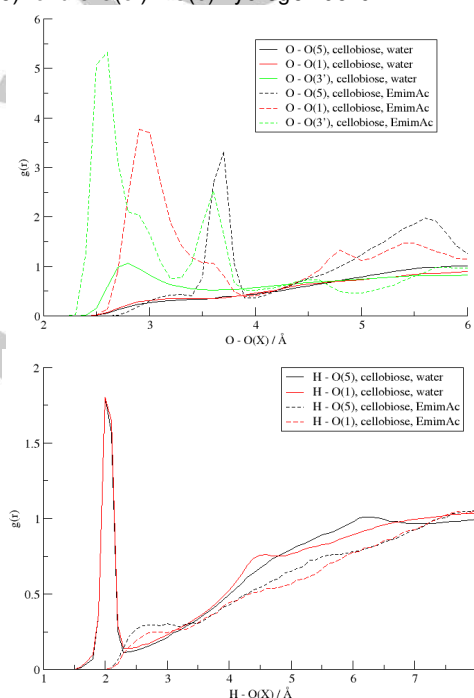


Figure 7: Radial distributions of selected $O\cdots O(X)$ (top) and $H\cdots O(X)$ (bottom) distances between solvent and solute for cellobiose at 420 K in water and EmimAc taken from 100 ns molecular dynamics simulations.

What are the consequences for hydrolysis? In water M2 will have a strong exo-anomeric effect, due to the frequent $O(3')\cdots O(5)$ hydrogen bonds. In M1 the exo-anomeric effect is weaker, since the $O(3')\cdots O(5)$ hydrogen bond is broken. In EmimAc we find a different picture: the intramolecular hydrogen bond is broken in M1 and M2, so that it can no longer impede the hydrolysis.

We now address the effect of intermolecular hydrogen bonding on hydrolysis. The radial distributions for $H_2O\cdots O(X)/AcO\cdots O(X)$ (top) and $OH_2\cdots O(X)/Emim-H(2)\cdots O(X)$ (bottom) are displayed in Figure 7 for both solvents and selected cellobiose oxygen atoms $O(X)$. Our results agree with literature data on the substitution of intramolecular hydrogen bonds by solute-anion hydrogen bonds^[12, 14-16] and the apparently low influence of the cation.^[1c, 1f, 15b, 16c, 17] In water the $O\cdots O(1)$ and $O\cdots O(5)$ as well as the $H\cdots O(1)$ and $H\cdots O(5)$ interactions are of similar strength,

and thus we do not expect any major influence on lone pair donation for the exo-anomeric effect. In EmimAc we find smaller $\text{Aco}\cdots\text{O}(1)$ than $\text{Aco}\cdots\text{O}(5)$ distances (maxima at 3.0 and 3.7 Å, respectively), probably due to the larger space available around O(1) than around O(5). This hints at a stronger donation from $n(\text{O}(1))$ and a stronger exo-anomeric effect in EmimAc, which would hinder hydrolysis.

In summary, there are two populated minima for ϕ , M1 and M2, in both solvents. While obstacles to hydrolysis exist in water (M2: maximal exo-anomeric effect and $\text{O}(3')\cdots\text{O}(5)$ hydrogen bond), they are not present in EmimAc, since the population of conformers with a reduced exo-anomeric effect is increased and all intramolecular hydrogen bonds are broken. The only effect that may impede hydrolysis is a closer $\text{O}(1)$ -Aco distance in EmimAc.

Ring flip α_1 and β_1 : In addition to the rotation around the glycosidic bond, we investigated the ring flip of the non-reducing glucose unit (α_1) and the orientation of the glycosidic bond towards the non-reducing ring (β_1 , β_2). With the help of these structural parameters we can distinguish whether the exo-anomeric effect (hindering hydrolysis) or the endo-anomeric effect (supporting hydrolysis) is present. Again we will first focus on cellobiose and evaluate the chain later.

In addition to α_1 two more dihedral angles (α_2 and α_3 , Figure 3) characterise the ring conformation. We concentrate on α_1 , as it is the only one of these three angles that controls the position of C(1)-O(1) relative to the ring and thus determines whether there is an exo- or endo-anomeric effect. Three major α_1 conformations are known in literature: The region around -

150° is the global minimum (e.g. ${}^4\text{C}_1$, ${}^{3,0}\text{B}$, and ${}^{2,5}\text{B}$ conformers), whereas the regions around -180° (e.g. skew conformers ${}^3\text{S}_5$, ${}^5\text{S}_3$) and around -230° (e.g. $\text{B}_{0,3}$, $\text{B}_{2,5}$, ${}^{1,4}\text{B}$, ${}^1\text{S}_3$, and ${}^1\text{S}_5$ conformers) support local minima.^[19] The population of local minima around -230° is higher in ionic liquids and the structure is more flexible.^[1c, 12, 15b, 20]

In our simulations we find similar results (Figure 8). The main conformation of α_1 is around -150° (M6) for both solvents (M6 population: water 93%, EmimAc 83%). The populations of M5 (-190°) and M4 (-230°) are much lower (M5, 3% in water and 6% in EmimAc; M4, 4% in water and 11% in EmimAc). Evidently, M4 and M5 have a somewhat higher population in EmimAc than in water. The higher population of M4 is also seen in the free energy profile, as the barrier to the nearest minima M5 and M6 in EmimAc is up to 2 kcal mol⁻¹ instead of < 1 kcal mol⁻¹ like in water. Exemplary structures for M4, M5, and M6 can be found in Figure 5.

Related to the conformational change in α_1 , the C(1)-O(1) bond can adopt an axial or equatorial position. The following analysis will focus on the more relevant β_1 dihedral (see Supporting Information for further details). The C(1)-O(1) bond is equatorial (eq) for β_1 around 180° and axial (ax) for β_1 close to 270°. In water and EmimAc the axial conformer is always in the minority (eq population: water 92%, EmimAc 83%, Figure 9). As seen from the free energy profile for cellobiose, the barrier and the relative energy (ax vs. eq) are lower in EmimAc than in water by 1 kcal mol⁻¹, consistent with the higher population of ax in EmimAc.

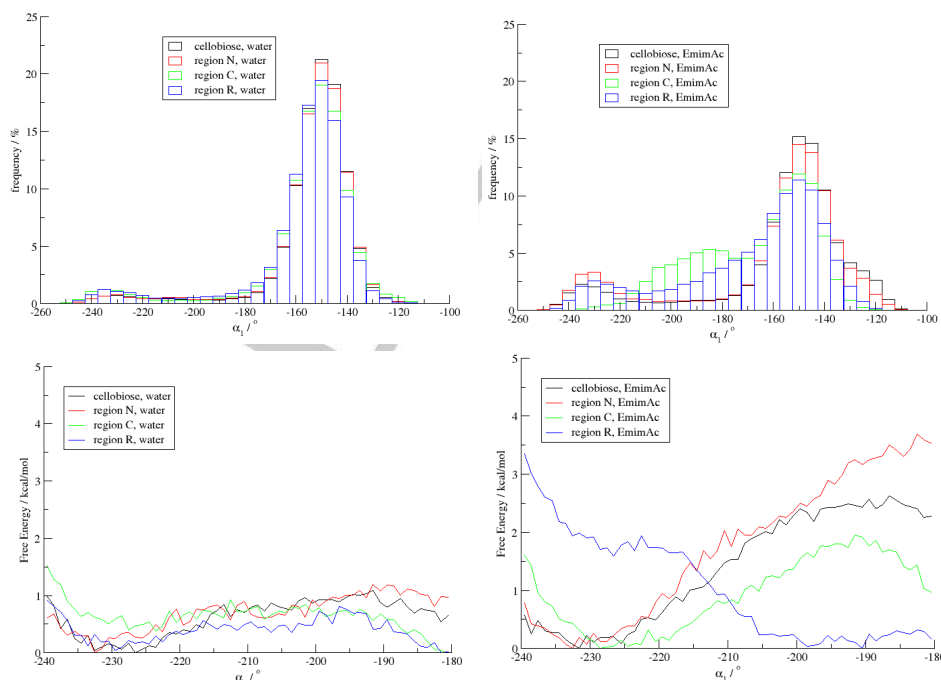


Figure 8: Distribution with respect to α_1 in water (top, left) and EmimAc (top, right) taken from 100 ns molecular dynamics simulations and corresponding free energy profiles taken from 20 ns metadynamics simulations at 420 K in water (bottom, left) and EmimAc (bottom, right): results for cellobiose and regions N, C, and R of the cellulose chain.

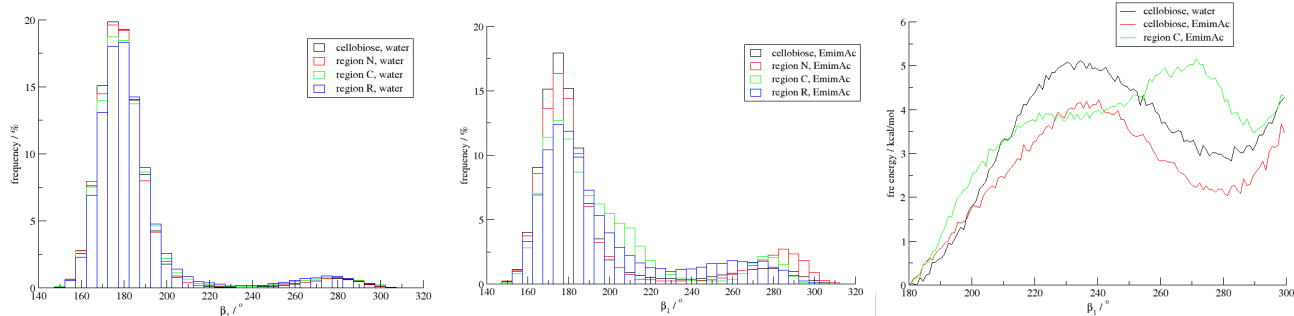


Figure 9: Distribution with respect to β_1 in water (left) and EmimAc (middle) taken from 100 ns molecular dynamics simulations and corresponding free energy profiles for β_1 (right) taken from 20 ns metadynamics simulations at 420 K in water and EmimAc: results for cellobiose and regions N, C, and R of the cellulose chain.

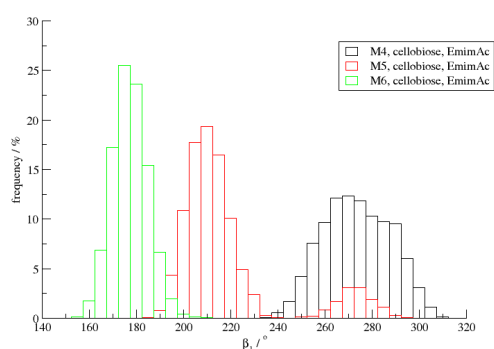


Figure 10: Correlation of β_1 and α_1 taken from a 100 ns molecular dynamics simulation of cellobiose at 420 K in EmimAc.

Since the structural parameters α_1 and β_1 determine the type of anomeric effect, it is interesting to correlate them (Figure 10). The C(1)-O(1) bond is always equatorial ($\beta_1=180^\circ$) in M6, mostly equatorial in M5 (87%), and completely axial ($\beta_1=270^\circ$) in M4. Example structures are shown in Figure 5. The endo-anomeric effect supporting hydrolysis operates only in the axial position (hence always in M4 and only to a minor extent in M5). As the population of M4 is higher in EmimAc, hydrolysis is favored in this solvent. Given that α_1 and β_1 are well correlated, we will focus on β_1 in the following correlations.

We already saw in the discussion of the rotation ϕ that the hydrogen bonds influence the anomeric effect and are therefore important for hydrolysis. However, as the ring conformers (α_1 , β_1) do not only determine the strength, but also the type of anomeric effect, we will now assess the influence of the hydrogen bonds on the anomeric effect and their ability to stabilise the minima M4 to M6.

For the axial and equatorial positions, there is an obvious difference in the distribution of the O(3')...O(6) bond distances (Figure 11). The corresponding hydrogen bond is formed mainly in the axial case (O(3')...O(6) distance < 3.5 Å; water, ax 53%, eq 15%), as the reducing ring is close to the non-reducing ring in the axial conformation (Figure 5). This has two positive effects on hydrolysis: The intramolecular O(3')...O(6) hydrogen bond stabilises the axial position and, as a corollary, O(3') is less likely to engage in an O(3')...O(5) hydrogen bond that would weaken the endo-anomeric effect. In EmimAc there are no significant differences between the O(3')...O(6) distances in the equatorial and axial conformers, as there is no such hydrogen bond in

either case. Nonetheless, in EmimAc there are more non-chair conformers M4 and M5 with an axial C(1)-O(1) bond, so the O(3')...O(6) hydrogen bond does not seem to play a crucial role in stabilising M4 or M5 in EmimAc, and O(6) is not competing with O(5) for hydrogen bonding with O(3')H.

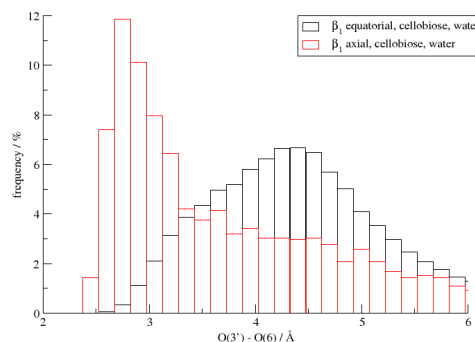


Figure 11: Correlation of hydrogen bond distances O(3')...O(6) and β_1 taken from 100 ns molecular dynamics simulations at 420 K in water: results for cellobiose and region C of the cellulose chain.

Solvent-solute interactions offer an alternative possibility for stabilising M4 or M5 in EmimAc. In our previous study, conformers M4 with an axial C(1)-O(1) bond were found to have an increased positive charge at C(1).^[9] The radial distribution between solvent oxygen atoms and the C(1) atom of the glycoside are shown in Figure 12. The O...C(1) interaction is stronger in EmimAc than in water, and the conformers M4 will thus be more frequent in EmimAc.

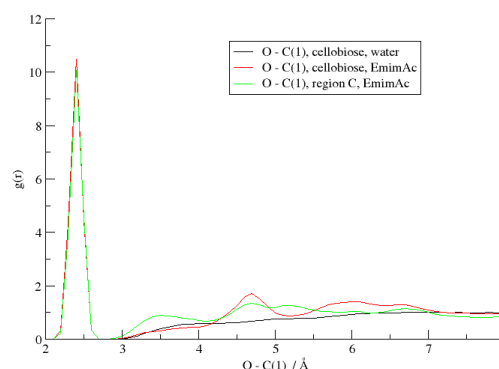


Figure 12: Radial distribution of selected O...C(1) distances between solvent and solute taken from 100 ns molecular dynamics simulations at 420 K in water and in EmimAc: results for cellobiose and region C of the cellulose chain.

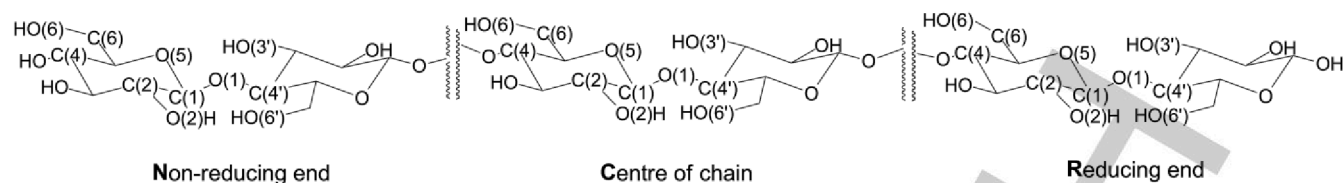


Figure 13: Simplified representation of the cellulose chain model and the nomenclature of the different regions.

Consequently, we find the following link between the conformation of the non-reducing ring and hydrolysis: In water and EmimAc there is one main conformer (M6) that has a low propensity to hydrolyse (because of the equatorial C(1)-O(1) bond). By contrast, the minor conformer (M4) contains an axial C(1)-O(1) bond and thus supports the endo-anomeric effect, which eases cellulose hydrolysis. M4 is stabilised in water by an intramolecular hydrogen bond, and in EmimAc by intermolecular interactions with the solvent. The population in M4 is higher in EmimAc, which is therefore a better solvent for hydrolysis.

The computed distributions for ϕ , α_1 , and β_1 in the two solvents can be summarized as follows: In water the main conformations contain a non-rotated glycosidic linkage (M2), O(3')...O(5) hydrogen bonds, chair conformations (M6) with a strong exo-anomeric effect, and an equatorial C(1)-O(1) bond (eq). These are factors that hinder hydrolysis. In EmimAc, the same conformers are still dominating, but there is a higher population of other local minima (M1, M4, M5, ax), which feature broken hydrogen bonds, a lower exo-anomeric effect, or an endo-anomeric effect and which thus ease cellulose hydrolysis.

Hydrolysis in different regions: So far we have mainly focused on solvent effects on the hydrolysis of cellobiose. Now we advance one step further and investigate how the solvent influences the hydrolysis of the cellulose chain model. We are especially interested in the question which part of the chain is easiest to hydrolyse (Figure 13): the non-reducing end (region N), the centre (region C), or the reducing end (region R).

We already know the main criteria that favor hydrolysis: reduction of the exo-anomeric effect (M1), breaking of the intramolecular hydrogen bonds O(3')...O(5) and O(2)...O(6'), and enhancement of the endo-anomeric effect (M4, ax). We will thus examine the cellulose chain model with regard to these properties. To estimate which region is easiest to cleave, we need to determine the factors most important for hydrolysis. In the proposed mechanism (Scheme 2) the endo-anomeric effect (M4, partly M5) is mandatory, since a conformational change is part of all hydrolysis pathways for cellulose.^[9-10, 21] A reduced exo-anomeric effect (M1) will ease the change to non-chair conformations and protonation, but this is not essential. The population of M4 is thus our main criterion for facile hydrolysis.

We first note that in water the regions of the cellulose chain behave almost like the cellobiose model (Table 1). This is not the case in EmimAc, where the conformer populations in the three regions of the chain change compared to cellobiose (Table 1). In the following we will therefore only discuss the situation in EmimAc.

It is evident from Table 1 that the conformers with reduced exo-anomeric effect (M1) are found in EmimAc more frequently in regions N (57%) and C (32%) than in cellobiose (12%). In contrast, M1 is not populated in region R, where the exo-anomeric effect is thus always close to maximum strength (Figure 4). The endo-anomeric effect is operating best in region N (16% ax and 15% M4), but the corresponding populations are only slightly higher than in cellobiose (Figure 8, Figure 9). In region C, the M4 conformers are less probable (6%), and the number of axial conformers is the same as in cellobiose (10%). Therefore the criteria for facile hydrolysis (M4 and ax) are satisfied in the following order: non-reducing end > reducing end >> centre of chain.

The centre of the chain clearly deviates from regions N and R and from cellobiose. We will now examine why M4 conformations are less accessible in region C than in regions N and R. As for cellobiose, we will analyse correlations involving the three dihedral angles ϕ , α_1 and β_1 as well as intra- and intermolecular hydrogen bonds.

Table 1: Conformer populations taken from 100 ns molecular dynamics simulations at 420 K in water and EmimAc: results for cellobiose and the regions N, C, and R of the cellulose chain.

		Water				EmimAc			
		cellobiose chain				cellobiose chain			
		cello.	N	C	R	cello.	N	C	R
ϕ	M1	3	3	7	4	12	57	32	0
	M2	96	96	92	95	88	43	68	100
	M3	1	1	1	1	0	0	0	0
α_1	M4	4	4	6	6	11	15	6	13
	M5	3	3	4	6	6	6	32	20
	M6	93	93	90	88	83	79	62	67
β_1	eq	92	91	89	87	83	78	68	69
	eqax	4	4	5	7	7	6	22	18
	ax	4	5	6	6	10	16	10	14

In Figure 14 we correlate β_1 and ϕ (top) as well as α_1 and ϕ (bottom). Bars in black show the distribution found in water for cellobiose, which is similar for all other models in water as well as for cellobiose and for regions N and R in EmimAc. Shown in red and green are the distributions for different conformers in region C. There are two differences: First, unlike in the other regions, conformers M2 with an axial C(1)-O(1) bond have a different maximum angle in region C (-90°, cellobiose -65°, Figure 14 top). Second, α_1 dihedral angles around -230° (connected with axial C(1)-O(1) bonds, Figure 10), are never populated in region C (Figure 14 bottom) by conformers M1

(green), and only slightly populated by conformers M2 (red); instead we find a higher population around $\alpha_1 = -190^\circ$ (M5). In summary, conformers M5 (mainly equatorial) are preferred over conformers M4 (only axial) for region C in EmimAc, and the ϕ dihedral angle is distorted in axial conformers.

We now turn to the hydrogen bonds. In spite of the capability of EmimAc to break hydrogen bonds (Figure 6), conformers M2 in region C still have weak $O(3')\cdots O(5)$ hydrogen bonds with the maximum of the distribution shifted from 2.8 Å (water) to 3.5 Å (EmimAc), and not to 4.7 Å like in the case of cellobiose in EmimAc (Figure 15, top). The unusual persistence of this hydrogen bonding is probably related to the $Aco\cdots O(X)$ interaction, which is less strong in region C than in cellobiose (judging from the radial distributions, see Figure 15, bottom) since region C is less accessible to larger solvent molecules. The preserved $O(3')\cdots O(5)$ hydrogen bond leads to a stronger exo-anomeric effect in the equatorial arrangement (impeding protonation of O(1) and conformational changes) and reduces the endo-anomeric effect in the axial arrangement.

To check this argument, we investigated the correlation of β_1 and the $O(3')\cdots O(5)$ hydrogen bond distance (Figure 16). In region C, distances of less than 3.5 Å are found in the equatorial position (red) 10% more often than in the axial position (green) and even 21% more often than in cellobiose, eq (black). The higher chance of having hydrogen bonds in the equatorial $C(1)-O(1)$ position might explain, why region C favors equatorial $C(1)-O(1)$ bonds and populates conformers M5 more than M4.

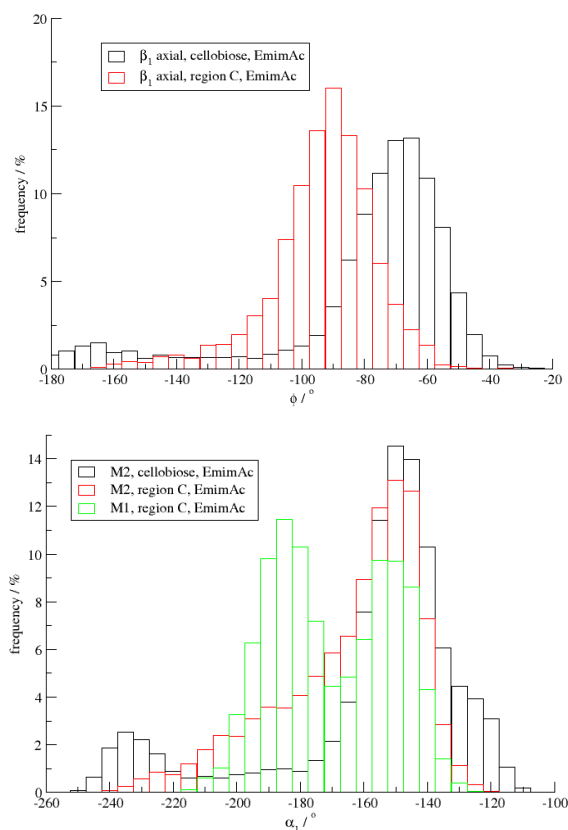


Figure 14: Correlation of β_1 and ϕ (top) and of α_1 and ϕ (bottom) taken from 100 ns molecular dynamics simulations of cellobiose in EmimAc at 420 K.

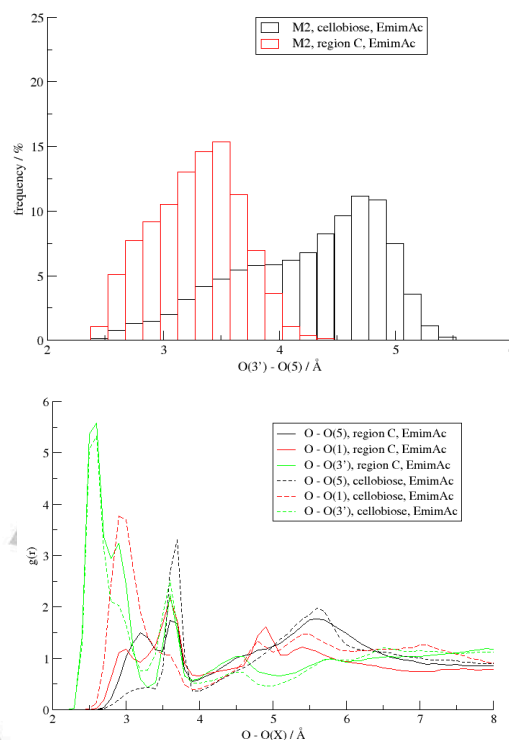


Figure 15: Top: Correlation of the hydrogen bond distances $O(3')\cdots O(5)$ in region C and cellobiose and the dihedral ϕ taken from 100 ns molecular dynamics simulations in EmimAc at 420 K. Bottom: Radial distribution of selected $O\cdots O(X)$ distances between solvent and solute for cellobiose and region C taken from 100 ns molecular dynamics simulations in EmimAc at 420 K.

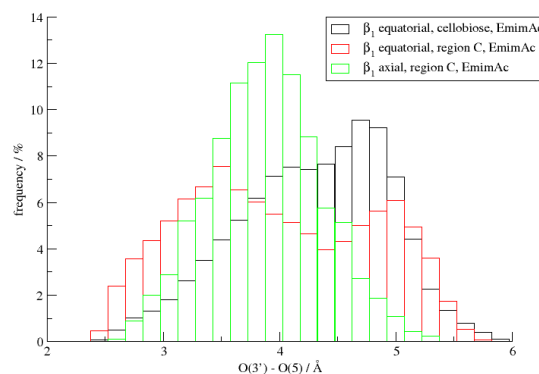


Figure 16: Correlation of the hydrogen bond distances $O(3')\cdots O(5)$ and the dihedral angle β_1 taken from 100 ns molecular dynamics simulations in EmimAc at 420 K: results for cellobiose and region C of the cellulose chain.

To summarize, the conformations of the cellulose chain differ from those of the cellobiose model only in EmimAc. Hydrolysis is expected to be easier in regions N and R because of more frequent non-chair conformations M4, but less favorable in region C. Even though rotation around the glycosidic linkage is possible in region C, the relevant non-chair conformers with axial $C(1)-O(1)$ bonds are less frequent. Likely reasons are the lower accessibility to solvent and the resulting persistence of the $O(3')\cdots O(5)$ hydrogen bond. The ends of the cellulose chain should thus be hydrolysed preferentially.

Conclusions

In this study we examined the effect of water and EmimAc solvents on the conformations of different cellulose models. We find that obstacles to cellulose hydrolysis are partly removed in EmimAc.

In water, the strong exo-anomeric effect involving the rather rigid glycosidic bond, the hydrogen bonds, and the dominance of chair conformers all combine to favor high activation barriers to hydrolysis. In EmimAc, there is more rotational freedom around the glycosidic bond (reduced exo-anomeric effect), most of the relevant intramolecular hydrogen bonds are broken, and ring flips from chair to non-chair conformers exhibiting the endo-anomeric effect become more likely. In contrast to water, conformers which are prone to hydrolysis are stabilised in EmimAc by strong solvent-solute interactions.

In EmimAc the conformer populations in the centre of a long cellulose chain are different from those in the end regions and in cellobiose: the non-chair conformers with axial C(1)-O(1) bonds are present less frequently. This difference can be attributed to weaker interactions with the solvent and more persistent O(3')...O(5) hydrogen bonds. Hydrolysis is thus expected to start at the end of cellulose chains.

Computational Section

We used the NAMD code^[22] for molecular dynamics (MD) and metadynamics simulations. Nonbonded interactions were truncated at a cut-off radius of 12 Å. The calculation of the electrostatic potential with periodic boundary conditions employed the particle mesh Ewald summation method.^[23] We applied the following setup procedure: energy minimisation, heating to 420 K with Langevin temperature control, and equilibration for 20 ns in the NPT ensemble with Langevin piston pressure control (1 atm). Thereafter, we carried out two types of production runs, namely classical MD simulations of 100 ns with the glycoside model inside the box (without restraints) and metadynamics simulations of 20 ns for a suitable range of collective variables. Since the energy barriers between chair and non-chair conformers are quite high (around 12 kcal mol⁻¹), metadynamics simulations were done only for non-chair conformers to ensure sufficient sampling for these local minima. The time step for the production runs was 2 fs, and every 2 ps a snapshot was taken saving energy, volume, and pressure.

Both for water and EmimAc, the size of the solvent box was chosen to be 50*50*50 Å³ for cellobiose and 50*50*265 Å³ for the cellulose chain. The sugar molecules were described by the GLYCAM06 force field, which has been demonstrated to give good results in comparison with other force fields.^[24] Water was represented by the TIP3P model, and the Amber force field GAFF was used for EmimAc, in view of its validation in a previous study.^[15b] The collective variables were chosen to be equivalent to dihedrals from previous work.^[19]

The simulations were performed at 420 K since the experiments were done at this temperature.^[6a, 25] In the analysis, we identified OH...O hydrogen bonds by the criterion of having O...O distances between 2.0 and 3.5 Å, in line with literature conventions.^[26] The plots of the radial distributions for various relevant interatomic distances were normalized to 1 at a cut-off distance of 10 Å. As a caveat, we note that some differences in the distributions found in EmimAc and in the metadynamics free energy profiles may stem from the limited simulation time, since it is

known that ionic liquids may stabilise certain conformers over nanoseconds.^[27]

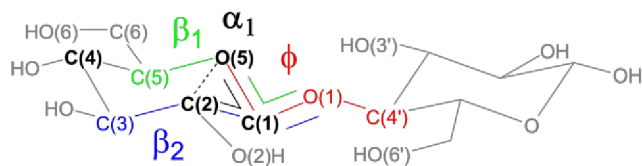
Acknowledgements

Financial support from the research cluster "Sustainable Chemical Synthesis—A Systems Approach (SusChemSys)" is also acknowledged. The project "Sustainable Chemical Synthesis (SusChemSys)" is co-financed by the European Regional Development Fund (ERDF) and the state of North Rhine-Westphalia, Germany, under the Operational Program "Regional Competitiveness and Employment" 2007–2013.

Keywords: Reaction mechanisms • Biomass • Solvent effects • Ionic Liquids • Molecular dynamics

- [1] a) R. Rinaldi and F. Schüth, *Energy Environ. Sci.* **2009**, *2*, 610-626; b) R. Rinaldi and F. Schüth, *ChemSusChem* **2009**, *2*, 1096-1107; c) H. M. Cho, A. S. Gross and J.-W. Chu, *J. Am. Chem. Soc.* **2011**, *133*, 14033-14041; d) K. Kulasinski, S. Keten, S. Churakov, D. Derome and J. Carmeliet, *Cellulose* **2014**, *1-14*; e) M. Bergensträhle, E. Thormann, N. Nordgren and L. A. Berglund, *Langmuir* **2009**, *25*, 4635-4642; f) A. Pinkert, K. N. Marsh and S. Pang, *Ind. Eng. Chem. Res.* **2010**, *49*, 11121-11130; g) W.-H. Hsu, Y.-Y. Lee, W.-H. Peng and K. C. W. Wu, *Catalysis Today* **2011**, *174*, 65-69.
- [2] a) R. R. Singhanian, A. K. Patel, R. K. Sukumaran, C. Larroche and A. Pandey, *Bioresour. Technol.* **2013**, *127*, 500-507. b) F. H. M. Souza, R. F. Inocentes, R. J. Ward, J. A. Jorge and R. P. M. Furiel, *J. Mol. Catal. B-Enzym* **2013**, *94*, 119-128.
- [3] a) G. T. Beckham, J. F. Matthews, B. Peters, Y. J. Bomble, M. E. Himmel and M. F. Crowley, *J. Phys. Chem B* **2011**, *115*, 4118-4127; b) C. M. Payne, M. E. Himmel, M. F. Crowley and G. T. Beckham, *J. Phys. Chem. Lett.* **2011**, *2*, 1546-1550; c) S. P. S. Chundawat, G. T. Beckham, M. E. Himmel and B. E. Dale, *Annu. Rev. Chem. Biomol. Eng.* **2011**, *2*, 121-145; d) P. Dhepe and A. Fukuoka, *ChemSusChem* **2008**, *1*, 969-975; e) H. Kobayashi, T. Komanoya, S. K. Guha, K. Hara and A. Fukuoka, *Appl. Catal. A: Gen.* **2011**, *409*, 13-20; f) L. R. Lynd, C. E. Wyman and T. U. Gerngross, *Biotechnol. Progr.* **1999**, *15*, 777-793; g) S. Van de Vyver, J. Geboers, P. A. Jacobs and B. F. Sels, *ChemCatChem* **2011**, *3*, 82-94; h) J. Verendel, T. Church and P. Andersson, *Synthesis* **2011**, *2011*, 1649-1677.
- [4] a) J.-H. Q. Pinto and S. Kaliaguine, *AIChE Journal* **1991**, *37*, 905-914; b) Z.-E. Dadach and S. Kaliaguine, *Can. J. Chem. Eng.* **1993**, *71*, 880-891; c) X. Liang, A. Montoya and B. S. Haynes, *J. Phys. Chem B* **2011**, *115*, 10682-10691.
- [5] a) C. Li, Q. Wang and Z. K. Zhao, *Green Chem.* **2008**, *10*, 177-177; b) C. Li and Z. K. Zhao, *Adv. Synth. Catal.* **2007**, *349*, 1847-1850; c) R. Rinaldi, N. Meine, J. vom Stein, R. Palkovits and F. Schüth, *ChemSusChem* **2010**, *3*, 266-276; d) R. Rinaldi, R. Palkovits and F. Schüth, *Angew. Chem Int. Ed.* **2008**, *47*, 8047-8050; e) N. Meine, R. Rinaldi and F. Schüth, *ChemSusChem* **2012**, *5*, 1449-1454; f) L. Vanoye, M. Fanselow, J. D. Holbrey, M. P. Atkins and K. R. Seddon, *Green Chem.* **2009**, *11*, 390-390; g) J. B. Binder and R. T. Raines, *P. Natl. Acad. Sci. USA* **2010**, *107*, 4516-4521.
- [6] a) R. P. Swatloski, S. K. Spear, J. D. Holbrey and R. D. Rogers, *J. Am. Chem. Soc.* **2002**, *124*, 4974-4975; b) R. Rinaldi, *Chem. Commun.* **2011**, *47*, 511-513; c) H. Liu, K. L. Sale, B. A. Simmons and S. Singh, *J. Phys. Chem B* **2011**, *115*, 10251-10258.
- [7] H. Zhao, J. H. Kwak, Y. Wang, J. A. Franz, J. M. White and J. E. Holladay, *Energy Fuels* **2005**, *20*, 807-811.

- [8] a) A. C. O'Sullivan, *Cellulose* **1997**, *4*, 173-207; b) Y. Nishiyama, P. Langan and H. Chanzy, *J. Am Chem. Soc.* **2002**, *124*, 9074-9082; c) Y. Nishiyama, J. Sugiyama, H. Chanzy and P. Langan, *J. Am Chem. Soc.* **2003**, *125*, 14300-14306; d) M. Jarvis, *Nature* **2003**, *426*, 611-612.
- [9] C. Loerbroks, R. Rinaldi and W. Thiel, *Chem-Eur. J.* **2013**, *19*, 16282-16294.
- [10] a) H. B. Mayes, L. J. Broadbelt and G. T. Beckham, *J. Am Chem. Soc.* **2013**, *136*, 1008-1022; b) C. B. Barnett and K. J. Naidoo, *Molecular Physics* **2009**, *107*, 1243-1250; c) B. M. Sattelle, S. U. Hansen, J. Gardiner and A. Almond, *J. Am Chem. Soc.* **2010**, *132*, 13132-13134.
- [11] G. A. Jeffrey, J. A. Pople, J. S. Binkley and S. Vishveshwara, *J. Am Chem. Soc.* **1978**, *100*, 373-379.
- [12] B. Mostdfian, X. Cheng and J. C. Smith, *J. Phys. Chem B* **2014**, *118*, 11037-11049.
- [13] a) Y. Nishimura, D. Yokogawa and S. Irlé, *Chem Phys. Lett.* **2014**, *603*, 7-12; b) K. L. Fleming and J. Pfaendtner, *J. Phys. Chem A* **2013**, *117*, 14200-14208.
- [14] L. Peric-Hassler, H. S. Hansen, R. Baron and P. H. Hünenberger, *Carbohydr. Res.* **2010**, *345*, 1781-1801.
- [15] a) C. S. Pereira, D. Kory, R. Baron, M. Müller, W. F. van Gunsteren and P. H. Hünenberger, *Biophys. J.* **2006**, *90*, 4337-4344; b) H. Liu, K. L. Sale, B. M. Holmes, B. A. Simmons and S. Singh, *J. Phys. Chem B* **2010**, *114*, 4293-4301; c) A. D. French and G. P. Johnson, *Can. J. Chem.* **2006**, *84*, 603-612.
- [16] a) N. J. Christensen, P. I. Hansen, F. H. Larsen, T. Folkerman, M. S. Motawia and S. B. Engelsens, *Carbohydr. Res.* **2010**, *345*, 474-486; b) E. Hatcher, E. Sävén, G. Widmalm and A. D. MacKerell, *J. Phys. Chem B* **2011**, *115*, 597-608; c) T. G. A. Youngs, J. D. Holbrey, C. L. Mullan, S. E. Norman, M. C. Lagunas, C. D'Agostino, M. D. Mantle, L. F. Gladden, D. T. Bowron and C. Hardacre, *Chem. Sci.* **2011**, *2*, 1594-1605.
- [17] a) Y. Zhao, X. Liu, J. Wang and S. Zhang, *Chem Phys. Chem* **2012**, *13*, 3126-3133; b) B. D. Rabideau, A. Agarwal and A. E. Ismail, *J. Phys. Chem. B* **2013**, *117*, 3469-3479; c) Y. Zhao, X. Liu, J. Wang and S. Zhang, *Carbohydr. Polym.* **2013**, *94*, 723-730; d) J. Zhang, H. Zhang, J. Wu, J. Zhang, J. He and J. Xiang, *Phys. Chem Chem. Phys.* **2010**, *12*, 1941-1947.
- [18] a) J. P. Praly and R. U. Lemieux, *Can. J. Chem.* **1987**, *65*, 213-223; b) R. U. Lemieux, *Pure Appl. Chem.* **1971**, *25*, 527-548.
- [19] H. S. Hansen and P. H. Hünenberger, *J. Comput. Chem.* **2010**, *31*, 1-23.
- [20] Z. Jarin and J. Pfaendtner, *J. Chem Theory Comput.* **2014**, *10*, 507-510.
- [21] N. F. Brás, M. J. Ramos and P. A. Fernandes, *J. Mol. Struct.-Theochem* **2010**, *946*, 125-133.
- [22] J. C. Phillips, R. Braun, W. Wang, J. Gumbart, E. Tajkhorshid, E. Villa, C. Chipot, R. D. Skeel, L. Kalé and K. Schulten, *J. Comput. Chem.* **2005**, *26*, 1781-1802.
- [23] T. Darden, D. York and L. Pedersen, *J. Chem Phys.* **1993**, *98*, 10089-10092.
- [24] V. Spiwok, B. Králová and I. Tvaroška, *Carbohydr. Res.* **2010**, *345*, 530-537.
- [25] A. P. Dadi, S. Varanasi and C. A. Schall, *Biotechnol. Bioeng.* **2006**, *95*, 904-910.
- [26] G. A. Jeffrey and S. Takagi, *Acc. Chem Res.* **1978**, *11*, 264-270.
- [27] T. G. A. Youngs, C. Hardacre and J. D. Holbrey, *J. Phys. Chem B* **2007**, *111*, 13765-13774.



How does solvation influence the acid hydrolysis mechanism of cellulose? Here we address this question with the help of molecular dynamics and metadynamics simulations for two solvents: water and 1-ethyl-3-methylimidazolium acetate. Solvent effects are compared in detail for cellobiose being the simplest cellulose model. The simulations for a 40-unit glucose chain indicate that hydrolysis will start at the ends of the chain.

*Claudia Loerbroks, Eliot Boulanger and
Walter Thiel**

Page No. – Page No.

**Solvent Influence on Cellulose 1,4- β -
Glycosidic Bond Cleavage: A
Molecular Dynamics and
Metadynamics Study**

Supporting Information

Rotation ϕ : Intramolecular hydrogen bond O(2)···O(6')

The intramolecular hydrogen bond O(2)···O(6') is of special importance for the first step of the acid hydrolysis mechanism. Since O(6)H is the most basic hydroxyl group, it might hinder protonation of the glycosidic oxygen, which is the energetically most demanding step of the reaction.^[8] The calculated distributions of the O(2)···O(6') distances in water and EmimAc for M1 and M2 are depicted in Figure S1. In water the O(2)···O(6') hydrogen bond is present in M1 and M2. Since the O(2)···O(6') hydrogen bond includes the exo-cyclic O(6') group of the reducing ring, it is more flexible with regard to the distance and can thus be maintained in M1 and M2 in contrast to the O(3')···O(5) hydrogen bond. As expected, the number of intramolecular hydrogen bonds is reduced in EmimAc compared to water: for cellobiose from 36% (water) to 5% (EmimAc) for the O(2)···O(6') hydrogen bond in M1. What are the consequences for hydrolysis? The low population of the O(2)···O(6') hydrogen bond should make protonation of O(1) easier in M2. In M1 on the other hand the O(2)···O(6') hydrogen bond is highly populated and protonation of O(1) is less likely.

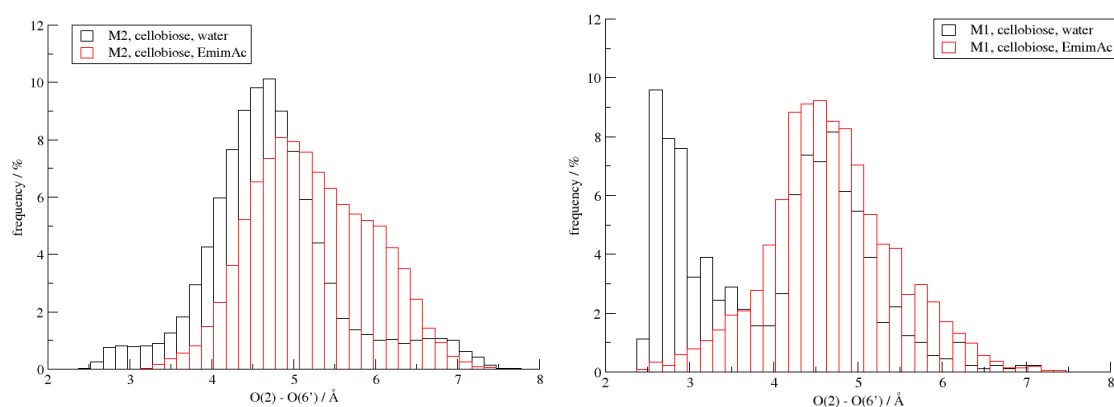


Figure S1: Correlation of the hydrogen bond distance O(2)···O(6') and the dihedral angle ϕ taken from 100 ns molecular dynamics simulations of cellobiose at 420 K in water and EmimAc.

Ring flip α_1 and β_1 : Correlation of α_1 and β_1

As the glycosidic linkage is only perfectly axial if both dihedrals β_1 (C(5)-O(5)-C(1)-O(1)) and β_2 (C(3)-C(2)-C(1)-O(1)) are at 90° or 270°, respectively, we correlate them in Figure S2. If β_1 is axial, β_2 is also axial, but this is not true vice versa. The analysis of this study focuses therefore on the more relevant β_1 dihedral.

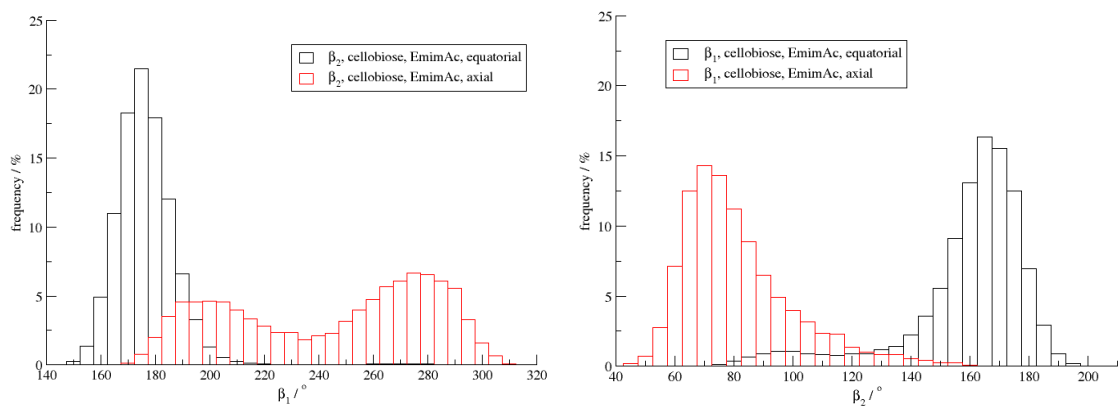


Figure S2: Correlation of β_1 and β_2 taken from a 100 ns molecular dynamics simulation of cellobiose at 420 K in EmimAc.

Appendix C

Spiroaminals – Crystal Structure and Computational Investigation of Conformational Preferences and Tautomerization Reactions

Claudia Loerbroks, Birte Böker, Jens Cordes, Anthony G. M. Barrett, and Walter Thiel

European Journal of Organic Chemistry, **2014**, 25, 5476 – 5486.

Carried out all calculations, analyzed the results, and wrote the draft of the manuscript

The cartesian coordinates were deleted from the Supporting Information and can be found in the published version of the manuscript.

Spiroaminals – Crystal Structure and Computational Investigation of Conformational Preferences and Tautomerization Reactions

Claudia Loerbroks,^[a] Birte Böker,^[b] Jens Cordes,^{[b,c][†]} Anthony G. M. Barrett,^[c] and Walter Thiel*^[a]

Keywords: Spiro compounds / Spiroaminals / Nitrogen heterocycles / Tautomerism / Computational chemistry / Conformation analysis

We report the first X-ray structure of a spiroaminal hydrochloride. The chiral spiroaminal crystallizes as a racemic hydrochloride in the monoclinic space group $P2_1/n$ and adopts the thermodynamically most stable conformation. Density functional calculations on several spiroaminals were used to establish correlations between trends in conformational energies, steric repulsions, and anomeric effects and to reveal the mechanism of the ring-opening tautomerization reaction. In the unsubstituted and backbone-substituted

spiroaminals, the aminal tautomer is thermodynamically preferred. *N*-Substituted spiroaminals favor the amine/imine form for steric reasons, except for those with bridging N,N' groups. The tautomerization from the aminal to the amine/imine is endergonic and kinetically hindered in the neutral species but quite facile after protonation. Anomeric effects lower the barriers but are less important than steric factors for relative energies.

Introduction

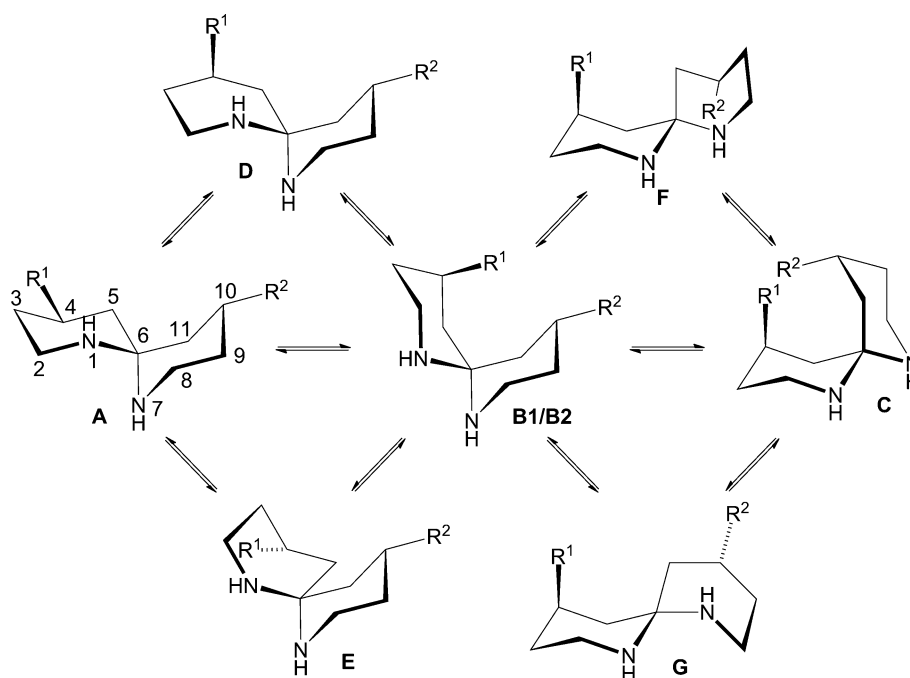
Spiroketals and their role in natural products are often the focus of experimental and computational investigations.^[1] By comparison, their nitrogen analogues, the spiroaminals, have been studied less intensively. Recently, the synthesis of spiroaminals and their reactivity towards electrophiles have been reported.^[2] Of special interest is the equilibrium of the spiroaminals with their open-ring tautomers, in which one nitrogen atom is of amine-type and the other one is of imine-type (Scheme 1). Some compounds were found to be spiroaminals [e.g., 1,7-diazaspiro[5.5]undecane (**1**, **2**)], whereas derivatives with substituted nitrogen atoms occur as imines [e.g., 1-allyl-1,7-diazaspiro[5.5]undecane (**3**, **4**)]. The tautomeric preferences of spiroaminals are of interest for further experimental work, for example, with regard to alkylation reactions and to fine tune them as ligands for metal–organic complexation reactions.

Spiroaminals can access a larger range of conformations than spiroketals. Like their carbohydrate analogues, they can assume different chair, twist, envelope, half-chair, and boat structures; in the following, the IUPAC nomenclature for the conformers of sugar molecules is used.^[3] The minimum-energy conformation for carbohydrates is the chair conformation. Owing to the presence of two heteroatoms and the connection of the two rings, the ¹chair₄ conformation is not equal to the ₁chair⁴ conformation for **1** and its analogues. Four different chair conformations are possible (Scheme 2, A–C). They can be distinguished by the orientation of the C⁶–N¹ and C⁶–N⁷ bonds relative to the other ring: A has two axial C–N bonds, B1/B2 has one axial and one equatorial C–N bond, and C has two equatorial C–N bonds. For aminals **1** and **7**, N¹ and N⁷ are equivalent; therefore, conformers B1 and B2 are simply called B. For aminals **3** and **5**, the conformation is called B1 or B2 depending on whether the allyl or isopropyl moiety is at the equatorial ring (N⁷ ring) or at the axial ring (N¹ ring). The chair conformers are in equilibrium with each other

- [a] Max-Planck-Institut für Kohlenforschung, Kaiser-Wilhelm-Platz 1, 45470 Mülheim an der Ruhr, Germany
E-mail: thiel@kofo.mpg.de
<http://www.kofo.mpg.de/de/forschung/theoretische-chemie>
- [b] Institut für Anorganische und Analytische Chemie, Technische Universität Carolo-Wilhemina zu Braunschweig, Hagenring 30, 38106 Braunschweig, Germany
- [c] Department of Chemistry, Imperial College London, London SW7 2AZ, United Kingdom
- [†] Current address: Hessisches Landesamt für Umwelt und Geologie, Ludwig-Mond-Straße 33, 34121 Kassel, Germany
- Supporting information for this article is available on the WWW under <http://dx.doi.org/10.1002/ejoc.201402576>.



Scheme 1. Tautomerism between aminal and amine/imine. R¹ = R² = R³ = H (**1**, **2**); R¹ = R² = H, R³ = allyl (**3**, **4**); R¹ = isopropyl, R² = R³ = H (**5**, **6**); R¹ = R² = isopropyl, R³ = H (**7**, **8**).



Scheme 2. Different chair and boat conformers of spiroaminals.

through ring flips and boat minima D–G (Scheme 2). For carbohydrates, the conformational changes can occur at room temperature. For molecules such as **1**, only conformer A was proposed to exist at room temperature, owing to an energy difference of 2 kcal/mol between the conformers.^[14]

The equilibrium between A, B, and C is influenced by the R¹ and R² substituents on the backbone. The R¹ and R² substituents are in equatorial positions in conformer A, one of them becomes axial in B, and both are axial in C. Axial positions raise the energy of conformers owing to 1,3 diaxial repulsion. In conformer C, both substituents are not only axial but also claim the same space and, thus, raise the energy even further.

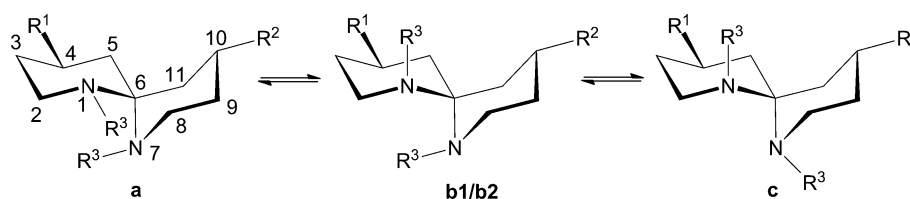
Moreover, for spirocycles with nitrogen atoms, the R³ substituents at the nitrogen atoms N¹ and N⁷ can assume equatorial (a and b) or axial (b and c) positions (Scheme 3). In conformer b, either the moiety at N¹ or at N⁷ can be axial or equatorial (b1, b2). The axial positions (c) are less favorable owing to the 1,2- and 1,3-diaxial interactions with neighboring hydrogen atoms and the CH₂ group. Substituents on the backbone of the ring have no influence on these conformations.

All conformational possibilities A–G and a–c influence the magnitude of the anomeric effect. The anomeric effect can stabilize certain conformations owing to electron delo-

calization and can contribute to the shortening or elongation of bonds. In spiroaminals, there are three types of hyperconjugation: $n(\text{N}) \rightarrow \sigma^*(\text{C}-\text{N})$, $n(\text{N}) \rightarrow \sigma^*(\text{C}-\text{C})$, and $n(\text{N}) \rightarrow \sigma^*(\text{C}-\text{H})$. To achieve maximum hyperconjugation, $n(\text{N})$ has to be antiperiplanar to the C–X bond. As the anomeric effect donates electron density into an antibonding orbital, the bond length $d(\text{C}-\text{X})$ increases with the anomeric effect. For our purposes, the $n(\text{N}) \rightarrow \sigma^*(\text{C}-\text{N})$ interaction will be most important, as we will focus on C–N bond cleavage in the tautomerization.

The combinations of the conformations a/c and A/B/C in which we may expect $n(\text{N}) \rightarrow \sigma^*(\text{C}-\text{N})$ hyperconjugation are shown in Figure 1. Two such interactions can be present in spiroaminal a-A, one can be present in a-B, and none can be present in a-C and all c-A/B/C conformers. Electron donation into the $\sigma^*(\text{C}-\text{C})$ and $\sigma^*(\text{C}-\text{H})$ orbitals is possible in all conformations, for example, $n(\text{N}^7)$ can donate into the $\sigma^*(\text{C}^6-\text{C}^{11})$ and $\sigma^*(\text{C}^8-\text{H})$ orbitals.

The aim of this study is to explain why some derivatives exist as spirocycles and others as amines/imines. Different conformers, the mechanism of the tautomerization, and the influence of the anomeric effect will be explored. Molecules with substituted backbones such as (4*R*)-4-isopropyl-1,7-diazaspiro[5.5]undecane (**5**, **6**) and (4*R*,10*R*)-4,10-diisopropyl-1,7-diazaspiro[5.5]undecane (**7**, **8**) were investigated



Scheme 3. Possible conformations of substituents at the nitrogen atoms for conformer A.

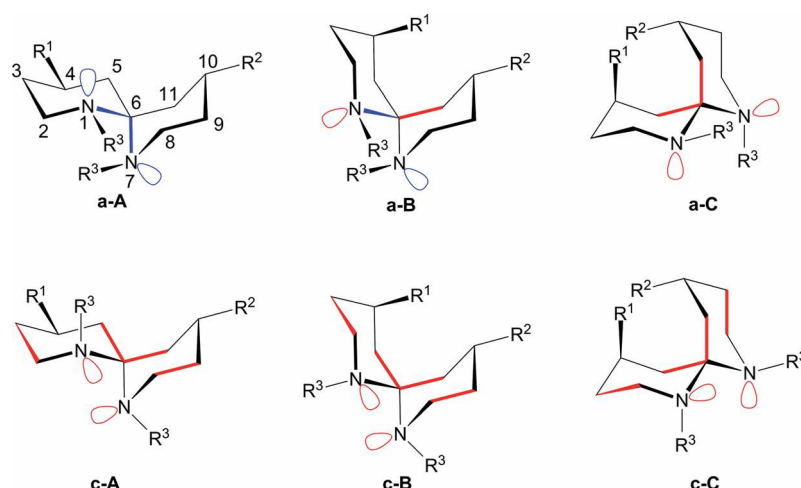


Figure 1. Position of the lone pairs and steric interactions in spiroaminals. Blue denotes $n(\text{N}) \rightarrow \sigma^*(\text{C}-\text{N})$ hyperconjugation, and red denotes $n(\text{N}) \rightarrow \sigma^*(\text{C}-\text{C})$ hyperconjugation.

in addition to the experimentally known compounds **1** and **4**.

Results and Discussion

The unsubstituted spiroaminal hydrochloride crystal structure (Figure 2) was used as the starting structure for the investigation of conformers and the ring-opening mechanism. The crystal structure is equivalent to a protonated **1a-A** structure, which is the energetically lowest minimum found for 1,7-diazaspiro[5.5]undecane. A typical C–N single bond length is ca. 1.47 Å.^[4] In the crystal, we find bond lengths of 1.433 Å for the unprotonated C–N bond (computed: 1.417 Å, 1% deviation from the crystal structure) and 1.559 Å for the protonated form (computed: 1.575 Å, 1% deviation from the crystal structure). The aminal C–N bond of the unprotonated nitrogen atom is shorter than expected for a C–N single bond owing to the

anomeric effect, which was calculated to be very strong (see below). The experimental and theoretical results agree well in these aspects.

Conformations of Spiroaminals

To study the equilibrium between aminals and amine/imines, the different conformers A–G and a–c (see above) were analyzed. The computed free energies (ΔG), a perturbational measure [$E(2)$] of the strength of the hyperconjugative interaction $n(\text{N}) \rightarrow \sigma^*(\text{C}-\text{N})$, and the C–N bond lengths of the conformers of 1,7-diazaspiro[5.5]undecane (**1**), 1-allyl-1,7-diazaspiro[5.5]undecane (**3**), 4-isopropyl-1,7-diazaspiro[5.5]undecane (**5**), and 4,10-diisopropyl-1,7-diazaspiro[5.5]undecane (**7**, Figure 3) are listed in Table 1. Only $E(2)$ values over 5 kcal/mol describe a significant donation and are listed. The conformers b were not investigated as they are a “mixture” of conformers a and c, and

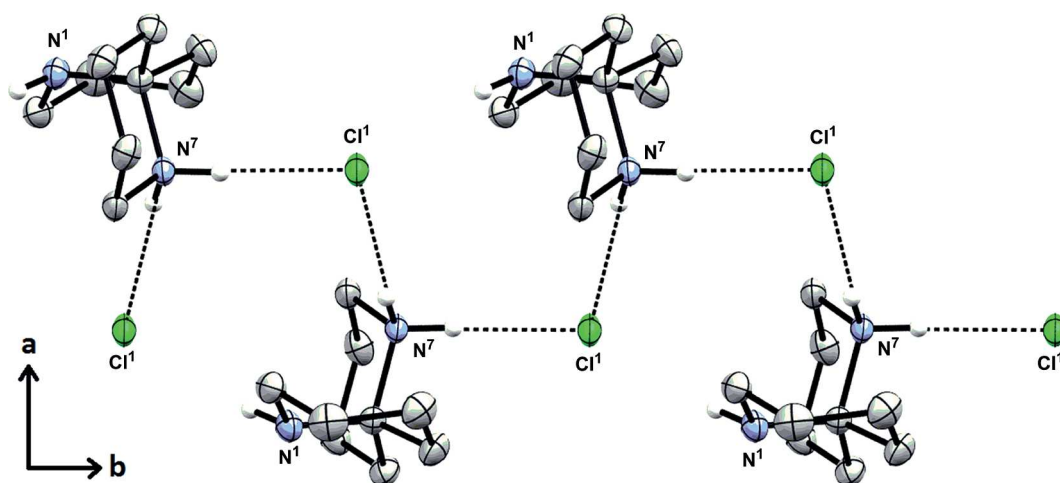


Figure 2. Crystal structure of individual spiroaminal molecules, which are linked through hydrogen bridges from N^7 to the chloride atoms to form a one-dimensional hydrogen-brided chain along b .

Table 1. Free energies ΔG [kcal/mol], magnitudes of the anomeric effect $E(2)$ [kcal/mol], and C–N bond lengths [\AA] of different conformers of the spiroaminals **1**, **3**, **5**, and **7** [M06-2X-D₃/TZVP,CPCM(water)]. B1 = ring flip of the unsubstituted ring. B2 = ring flip of the substituted ring.

	ΔG	$n(\text{N}^1) \rightarrow \sigma^*(\text{C}-\text{N}^7)$	$E(2)$ $n(\text{N}^7) \rightarrow \sigma^*(\text{C}-\text{N}^1)$	$d(\text{C}-\text{N}^1)$	Bond length $d(\text{C}-\text{N}^7)$	D_B [%] ^[a]
1: X = N, R¹ = R² = R³ = H						
1a-A	0.0	16.3	16.3	1.474	1.474	35.9
1c-A	0.5	–	–	1.470	1.470	21.7
1a-B	0.8	–	13.7	1.463	1.480	15.5
1c-B	1.2	–	–	1.469	1.472	10.4
1a-C	1.3	–	–	1.468	1.468	9.8
1c-C	1.8	–	–	1.471	1.471	6.1
1a-D	5.0	13.6	–	1.482	1.468	0.2
1a-E	5.6	15.7	16.3	1.469	1.478	0.1
1a-F	5.3	–	–	1.469	1.470	0.2
1a-G	5.2	–	11.1	1.467	1.478	0.2
3: X = N, R¹ = R² = H, R³ = allyl						
3a-A	0.0	17.0	15.4	1.468	1.490	1.0
3c-A	–2.6	–	–	1.474	1.482	12.5
3a-B1	–2.9	13.4	–	1.477	1.476	17.7
3c-B1	0.3	–	–	1.474	1.485	0.7
3a-B2	0.7	–	14.3	1.461	1.496	0.5
3c-B2	–2.7	–	–	1.468	1.483	15.1
3a-C	–3.9	–	–	1.469	1.482	49.7
3c-C	–1.0	–	–	1.471	1.485	2.8
5: X = N, R¹ = isopropyl, R² = R³ = H						
5a-A	0.0	16.4	16.2	1.475	1.471	41.3
5c-A	0.6	–	–	1.471	1.469	22.7
5a-B1	0.7	13.8	–	1.481	1.461	20.2
5c-B1	1.0	–	–	1.473	1.466	15.2
5a-B2	5.1	–	13.3	1.467	1.476	0.3
5c-B2	5.5	–	–	1.473	1.471	0.2
5a-C	5.7	–	–	1.470	1.466	0.1
5c-C	7.9	–	–	1.472	1.475	0.0
7: X = N, R¹ = R² = isopropyl, R³ = H						
7a-A	0.0	16.3	16.3	1.472	1.472	58.3
7c-A	0.4	–	–	1.468	1.468	40.6
7a-B	4.5	–	13.4	1.464	1.478	0.6
7c-B	5.0	–	–	1.470	1.472	0.4
7a-C	11.5	–	–	1.468	1.469	0.0
7c-C	12.5	–	–	1.475	1.475	0.0

[a] Boltzmann distribution at 298.15 K.

the general trends can be explained by conformers a and c. Conformers D–G are of high energy and were, therefore, only calculated for **1**.

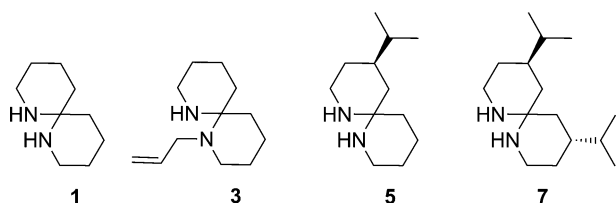


Figure 3. Spiroaminal tautomers of the investigated compounds **1** to **7**.

In our analysis of the results, we first focus on the differences in free energy and on the magnitude of hyperconjugation.

For **1**, **5**, and **7**, the free energy rises in the sequence $A < B < C$ for the same conformer a or c. Moreover, the

energy rises in the sequence $a < c$ for the same conformer A, B, or C. Spiroaminal **3** is the only exception: here, the energies follow no obvious trend with regard to A, B, and C or a and c.

The conformations of the spiroaminals determine the number of possible $n(\text{N}) \rightarrow \sigma^*(\text{C}-\text{N})$ hyperconjugative interactions. There are two in conformer a-A, one in conformer a-B, and none in conformer a-C. In the c conformers, there is in general no hyperconjugation. In the boat conformers D, E, F, and G, we again find zero, one, or two $n(\text{N}) \rightarrow \sigma^*(\text{C}-\text{N})$ interactions, which are of similar magnitude as those in the chair conformers A, B, and C. The strength of hyperconjugation is not influenced by the substituents R¹, R², and R³.

Some low-energy conformers show a strong $n(\text{N}) \rightarrow \sigma^*(\text{C}-\text{N})$ hyperconjugation, for example, **5a-A**, but there is no general correlation between energy and hyperconjugation (see, e.g., **5a-B2** vs. **5a-B1**). Apparently, strong

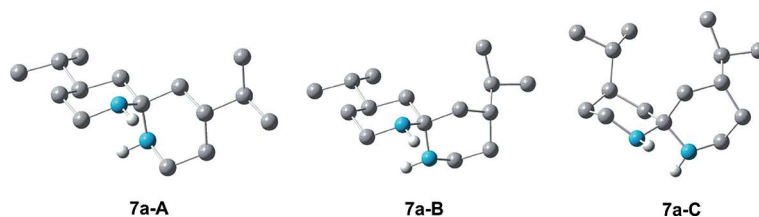


Figure 4. Change from equatorial to axial position of the two isopropyl groups on the backbone in the three chair conformers A, B, and C of **7**. Aliphatic hydrogen atoms are removed for clarity.

steric or electrostatic repulsions caused by conformations and substituents can override the influence of the anomeric effect when it comes to the selection of the minimum-energy conformation.^[5]

The energy differences between the a and c conformers of the same A–C species are often very small. For example, **5a-A** and **5c-A** are nearly of the same energy, even though the delocalization into a $\sigma^*(\text{C–N})$ orbital is only present in a and not c. One reason for these small energy differences may be additional hyperconjugation into the $\sigma^*(\text{C–C})$ and $\sigma^*(\text{C–H})$ orbitals. All conformers support this additional anomeric effect with $E(2) \approx 8\text{--}12$ kcal/mol. In conformers without $n(\text{N}) \rightarrow \sigma^*(\text{C–N})$ interactions, the electron density can be redistributed into the $\sigma^*(\text{C–C})$ and $\sigma^*(\text{C–H})$ orbitals. The ability of $n(\text{N})$ orbitals to donate into different antibonding orbitals is related to the lower electronegativity of nitrogen compared to oxygen. Thus, the electron density of the N lone pairs is more likely to be delocalized than that of O lone pairs, and electron donation into antibonding C–H orbitals is, therefore, more likely in spirocycles that contain nitrogen atoms rather than oxygen atoms. Additionally, this may explain why the energy differences between conformers A–C for spiroaminals without much steric repulsion (such as **1**) are low compared to the energy differences of more than 2 kcal/mol for the different chair conformers of the oxygen analogues.^[1d]

For **5** and **7**, the steric repulsion (Figure 4) correlates with the hyperconjugation. Conformations with equatorial isopropyl substituents also feature a strong anomeric effect (**7a-A**, **5a-A**). Owing to steric factors, the energy difference between conformers A–C is larger than that in the case of **1**.

Furthermore, steric repulsion offers an explanation for the anomalous energy features of **3**. In contrast to the other aminals **1**, **5**, and **7**, conformers A and B2 with axial substituents (**3c-A** and **3c-B2**) are lower in energy ($\Delta\Delta G = 2$ kcal/mol) than those with equatorial substituents (**3a-A** and **3a-B2**). Also, conformers **3a-B1** and **3a-C** are lower in energy than **3a-A** and also lower than **3c-B1** and **3c-C** ($\Delta\Delta G = 2\text{--}4$ kcal/mol). The steric reasons are best explained by inspection of **3a-A** and **3a-C** in Figure 5. The equatorial allyl groups and the opposite ring in the A and B2 conformers (**3a-A**) experience more repulsion than the axial allyl groups and the CH_2 groups, whereas no ring distortion is evident in the C and B1 conformers with equatorial allyl groups (**3a-C**).

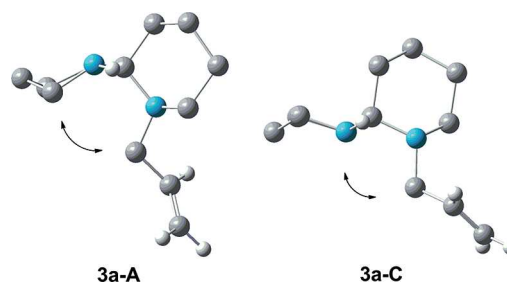


Figure 5. A and C chair conformers of **3**. Possible steric repulsions are shown with arrows. Aliphatic hydrogen atoms are removed for clarity.

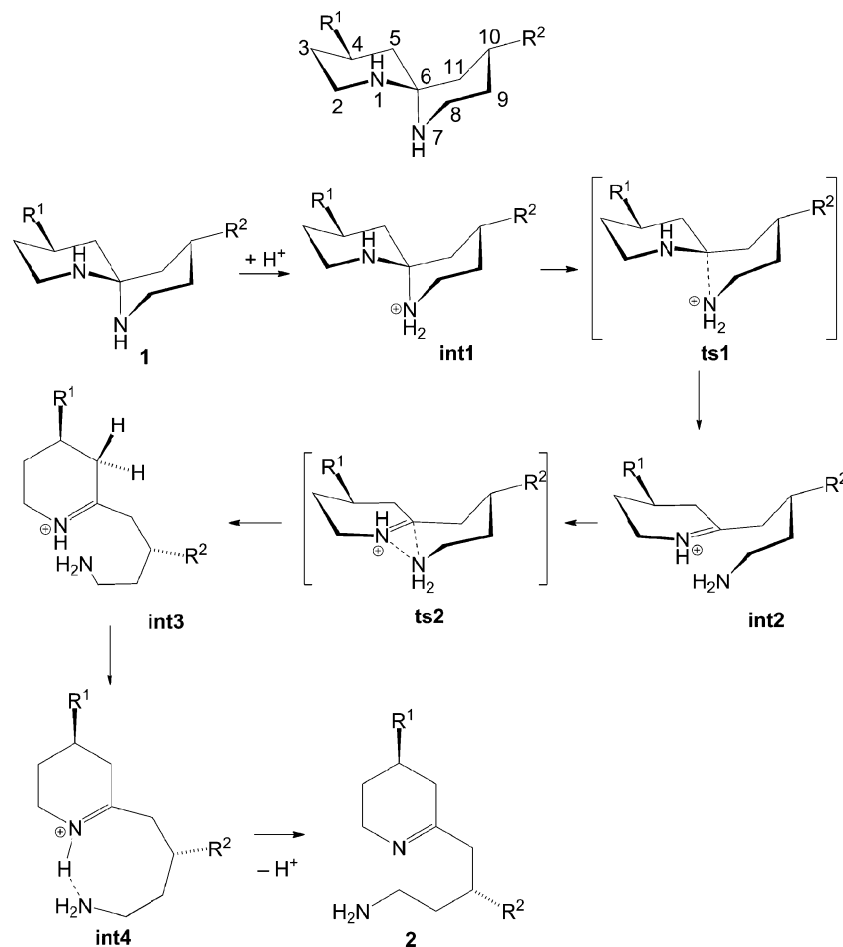
Therefore, a conformational change from A to C for the equatorial allyl groups lowers the relative energy. The conformation without an $n(\text{N}) \rightarrow \sigma^*(\text{C–N})$ interaction, a-C, is the lowest-energy conformer of **3** as the allyl group is in an equatorial position without perturbation of the ring conformation. For all the other spiroaminals **1**, **5**, and **7**, a-A is the lowest-energy conformer with maximum hyperconjugation.

With this knowledge in hand, we will now explore the mechanism of tautomerization.

Ring-Opening Mechanism

The mechanism was investigated for several conformers. We will present the results for conformers a-A/B/C of **1** and **3** and for the a-A conformers of **5** and **7**. The boat conformers D–G are not investigated here, as they are unlikely to be accessed at room temperature. However, we note that the strength of the hyperconjugation and the C–N bond lengths are generally similar in the chair and boat conformers.

All tautomerization pathways in the neutral species lead to unfeasibly high reaction barriers. Apparently, the C–N bond needs to be activated to make the tautomerization possible. One way to achieve this is to enhance the anomeric interactions and, thus, weaken one of the C–N bonds. Secondary amines are basic, so protonation should be a reasonable approach for activation. The free energy of protonation was calculated by a thermodynamic cycle, whereas the subsequent tautomerization of the protonated spiroaminals was studied by using standard procedures (see Computational Section). As protonation is necessary for the ring



Scheme 4. Proposed mechanism of the amination to amine/imine conversion for the reaction from **1** to **2**. R¹/R² = H.

opening, the C–N bond length in the neutral species is not important for the energy barriers.

The proposed mechanism is presented for spiroaminal **1** in Scheme 4 and proceeds as follows: First, one of the amine nitrogen atoms (N⁷ in **1**) is protonated to yield structure int1. The protonation leads to an elongation of the C⁶–N⁷ bond and an increased hyperconjugative interaction $n(\text{N}^1) \rightarrow \sigma^*(\text{C}^6\text{--N}^7)$. The next step is C⁶–N⁷ bond cleavage (int1 to int2). Depending on the spiroaminal reactant, this step may be a barrierless separation or go through a transition state (ts1), in which the unprotonated ring undergoes a conformational change from chair to envelope form. In the resulting minimum (int2), there is still a weak interaction between C⁶ and N⁷ (distances from 2.5 to 2.8 Å, Table S2), and the unprotonated ring is in the envelope conformation. The distance between C⁶ and N¹ decreases, and C⁶ becomes an sp² carbon atom. To reach tautomer **2** and, thus, lower the probability of a back reaction, C⁶ and N⁷ have to separate completely. To do so, the arm of the opened six-membered ring swings over to C⁵H₂ (via transition state ts2) and establishes a very weak N⁷–H–C⁵ hydrogen bond in some conformers (Table S2).^[6] Once in this position, the opened ring can uncoil further and assume different conformations. The lowest-energy conformer found (int4) has a N⁷–H–N¹ hydrogen bond.

To assess the reactivity of the spiroaminals, we successively discuss the free energies of the different unprotonated

Table 2. Relative free energies [kcal mol⁻¹] for unprotonated structures **1–8** [M06-2X-D3/TZVP, CPCM(water)] and free energies of protonation for structures **1**, **3**, **5**, and **7**. B1 = ring flip of the unsubstituted ring. B2 = ring flip of the substituted ring; ' denotes substituted ring protonated and opened.

Aminal→imine	ΔG (aminal)	ΔG (imine)	$\Delta\Delta G$ (imine-aminal)	ΔG (protonation)
1 → 2 : X = N, R ¹ = R ² = R ³ = H				
1a-A→ 2	0.0	5.0	5.0	-14.4
1a-B→ 2	0.8		4.2	-14.8
1a-C→ 2	1.3		3.7	-13.7
3 → 4 : X = N, R ¹ = R ² = H, R ³ = allyl				
3a-A→ 4	0.0	-0.6	-0.6	-15.7
3a-B1→ 4	-2.9		2.3	-13.0
3a-B2→ 4	0.7		-1.5	-15.5
3a-C→ 4	-3.9		3.3	-13.6
5 → 6 : X = N, R ¹ = isopropyl, R ² = R ³ = H				
5a-A→ 6	0.0	4.8	4.8	-14.6
5a-A→ 6'	0.0	10.0	10.0	-14.3
7 → 8 : X = N, R ¹ = R ² = isopropyl, R ³ = H				
7a-A→ 8	0.0	9.5	9.5	-14.5

spiroaminals and imines, the free energies needed to protonate the different spiroaminals, the protonated structures, and the kinetic barriers of the reaction.

The relative free energies for the unprotonated spiroaminals and imines considered are listed in Table 2. The aminal–imine conversions are all endergonic, except for those of the two allyl-substituted conformers **3a-A** and **3a-B2**, which are among the least populated conformers. The data indicate that the spiroaminal should be the preferred tautomer in all cases. On a relative scale, the open-ring form becomes more favorable in the following sequence: $7 \approx 5(A-2) < 5(A-1) \approx 1 < 3$.

Table 3. Relative free energies [kcal mol⁻¹] for the stationary points on the pathway to the tautomerization of protonated spiroaminals (int1 to int4), relevant hyperconjugative interactions $E(2)$ [kcal mol⁻¹], and C–N distances [Å] during the course of the reaction. Free energies are given relative to the lowest-energy protonated conformer int1 at the M06-2X-D3/TZVP, CPCM(water) level. B1 = ring flip of the unsubstituted ring. B2 = ring flip of the substituted ring; ' denotes substituted ring protonated and opened.

	ΔG	$E(2)$		$d(C-N^7)$
		$n(N^1) \rightarrow \sigma^*(C-N^7)$	$n(N^7) \rightarrow \sigma^*(C-N^1)$	
1 → 2 : X = N, R ¹ = R ² = R ³ = H				
1a-A		16.3	16.3	1.474
int1	0.0	31.2		1.575
ts1	–			
int2	4.0		14.4	2.575
ts2	–			
int3	5.4			
int4	–0.4			
3 → 4 : X = N, R ¹ = R ² = H, R ³ = allyl				
3a-C		2.1	1.8	1.482
int1	–1.0	4.6		1.549
ts1	4.3			
int2	0.5		7.9	2.738
ts2	2.8			
int3	0.1			
int4	–3.6			
5 → 6 : X = N, R ¹ = isopropyl, R ² = R ³ = H				
5a-A		16.4	16.2	1.475
int1	0.0	31.3		1.577
ts1	–			
int2	3.8		13.5	2.589
ts2	–			
int3	6.5			
int4	–0.7			
5a-A'		16.4	16.2	1.475
int1	0.3	30.5		1.569
ts1	–			
int2	6.3		17.8	2.514
ts2	–			
int3	–			
int4	1.4			
7 → 8 : X = N, R ¹ = R ² = isopropyl, R ³ = H				
7a-A		16.3	16.3	1.472
int1	0.0	30.7		1.570
ts1	–			
int2	6.0		16.3	2.535
ts2	–			
int3	–			
int4	3.1			

The protonation is exergonic for all spiroaminals, as expected for secondary amines with typical p*K*_a values of ca. 11 (for diethylamine).^[7] Moreover, the free energy of protonation, $\Delta G(\text{protonation})$, is nearly the same for all spiroaminals and ranges between –13 and –16 kcal/mol. Thus, the different substituents explored here do not significantly influence the basicity of the spiroaminals. Protonation is facile and evidently not a critical step towards the tautomeric equilibrium.

We will now explore the tautomerization mechanism, starting from the protonated spiroaminal int1 (Table 3). Structures int1a-A are taken as reference points. The proton was always placed on the nitrogen atom in the longest C–N bond.

For the protonated spiroaminals, the reaction from int1 to int4 is exergonic for the lowest-energy conformer **3a-C** (–2.6 kcal/mol), almost in equilibrium for **1a-A** (–0.4 kcal/mol) and **5a-A** (–0.7 kcal/mol), but endergonic for aminals **5a-A'** and **7a-A** (by 1.4 and 3.1 kcal/mol). Similarly to the unprotonated case, the ring opening becomes thermodynamically more favorable in the following sequence: $5(A' - \text{substituted ring protonated}) \approx 7 < 1 \approx 5(A - \text{unsubstituted ring protonated}) < 3$. In the following, we will first discuss the reactions for **1** and then for **3** and **5**.

Spiroaminal 1

The relative free energies of the protonated conformers **1-int1a-A/B/C** show the same energy trend as those of the unprotonated conformers **1a-A/B/C**. For all chair conformers A–C, the increase in the C⁶–N⁷ bond length upon protonation is similar [$\Delta d(C^6-N^7) = +0.09$ Å]. For int1-A and int1-B, the protonation results in one anomeric interaction of similar strength [with $\Delta E(2) = +15$ kcal/mol relative to the unprotonated conformers **1a-A** and **1a-B**], and there is still no hyperconjugation after the protonation of **1a-C** (which is higher in energy by ca. 2 kcal/mol compared to int1a-A). The differences in the relative free energies between A/B and C magnify in the next step of the reaction. Whereas the protonated conformers A and B undergo barrierless C⁶–N⁷ cleavage, the protonated conformer C faces a barrier of 8.4 kcal/mol, as there is no anomeric interaction that could support bond cleavage. Int2 is energetically similar for all conformers, but int2a-C has a longer C⁶–N⁷ distance [$\Delta d(C^6-N^7) = +0.15$ Å] and weaker $n(N^7) \rightarrow \sigma^*(C^6-N^1)$ hyperconjugation [$\Delta E(2) = 6$ kcal/mol] compared to those of int2-A/B. This is due to the different envelope conformations of the ring (Figure 6): A and B are ³E conformers, whereas C is a ³E conformer.^[3] The ³E conformer of int2-C has a rather long C⁶–N⁷ bond because of strong steric repulsion at shorter distances.

Beyond int2, the reaction pathways are similar for all conformers. There is a transition state (ts2) for conformers B and C, in which N⁷ moves away from C⁶ and establishes a weak C⁵H–N⁷ bond (distances of 2.76 to 2.83 Å). In conformer A, the C⁵H–N⁷ distance is much longer (3.6 Å), and the structure is less stabilized. The subsequent conforma-

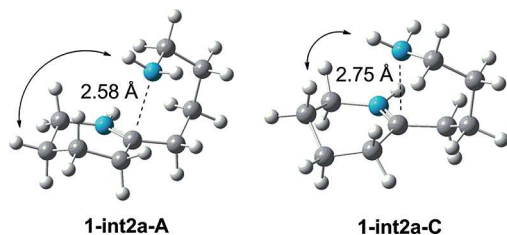


Figure 6. Two different envelope conformers 3E (left) and 3E (right) of **1-int2a**. Arrows indicate the possible steric repulsion.

tional change from **int3** to **int4** proceeds over several small barriers, which are not important kinetically.

Spiroaminal 3

Similar results were obtained for the allyl derivative **3**. The relative free energies of the protonated conformers **int1** are close to each other, and conformer **C** is still the lowest one. Nevertheless, the energy differences between the protonated **3a-A** and **3a-C** conformers are reduced compared to the unprotonated case, as the increase in the C^6-N^7 distance reduces the repulsion between the ring and the allyl moiety in **3a-A** (see above and Figure S1). The protonated conformers **A** and **B2** again show increased anomeric interactions ($\Delta E = +2-6$ kcal/mol) and an elongated C^6-N^7 bond [$\Delta d(C^6-N^7) = +0.09$ Å] compared to that of the unprotonated spiroaminal. The protonated conformers **B1** and **C** do not support anomeric interactions; the C^6-N^7 bond is still elongated upon protonation but less so than in **A** and **B2** (by 0.03 Å). All of the protonated conformers have to overcome small barriers for the initial step (ts1).

Those with hyperconjugative interactions (**A** and **B2**) have lower barriers than those without these interactions (by 2 kcal/mol). **Int2** has a longer C^6-N^7 distance for the **B1/C** conformers than for the **A/B2** conformers [$\Delta d(C^6-N^7) = +0.09$ Å], again because of the preference for different envelope conformers: **A/B2** is a 3E conformer, and **B1/C** is a 3E conformer. However, all **int2** conformers are energetically within 0.5 kcal/mol.

Analogous results have been obtained for the **5-A** and **7-A** conformers. There are strong anomeric effects in **int1** and **int2**, and the C^6-N^7 distances are similar for both conformers.

From a kinetic point of view, the tautomerization of the protonated spiroaminals is a facile process in all cases, as the individual steps are either barrierless or have small barriers in the range 2 to 8 kcal/mol.

The tautomerization of **3-int1** was calculated to be exergonic by -2.6 kcal/mol, which is consistent with the experimental result that the allyl-substituted system **3** exists as the amine/imine tautomer (Figure 7). The aminal and amine/imine forms are computed to have almost the same free energy for the parent molecule **1** and for the isopropyl-substituted derivative **5a-A**, so one would expect both forms to co-exist; experimentally, the aminal form is favored for **1**. The tautomerization of the other isopropyl-substituted spiroaminals **5a-A'** and **7** is predicted to be endergonic (no experimental data available).

Our calculations show that the allyl-substituted spiroaminal **3** is the most likely one to undergo ring opening upon protonation. Deprotonation will then generate the observed amine/imine product **4**. However, we note that there are two neutral spiroaminal conformers **3a-B1** and **3a-C**, which are computed to be slightly more stable than **4** (Table 2). The high population of **4** in the experiments indicates that the

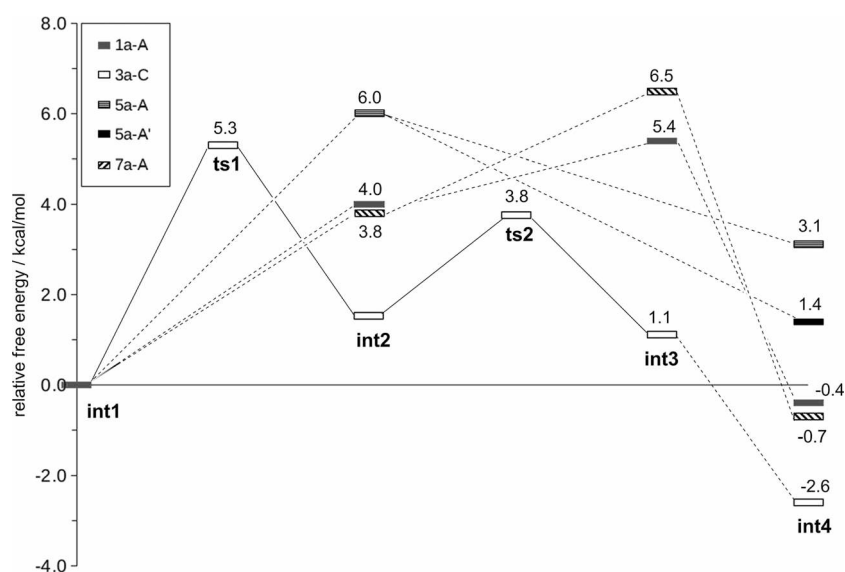


Figure 7. Free-energy profiles for the reaction from **int1** to **int4** for the lowest conformer of each protonated spiroaminal. The energies are given relative to that of **int1**. They were computed at the M06-2X-D3/TZVP,PCPM(water) level; ' denotes substituted ring protonated and opened.

back reaction is hindered. We have computed the back reaction from unprotonated **4** to **3** with a relaxed potential surface scan in vacuo and found a barrier of almost 60 kcal/mol between the aminal and the amine/imine tautomer (Figure 8). For comparison, we also report a scan for the reaction **2** to **1**, which revealed a slightly higher barrier for the back reaction without protonation. Thus, the closing of the ring in the neutral species is hindered for all spiroaminals. For the unprotonated parent compound **1**, the calculations correctly predict the spiroaminal form to be thermodynamically favored (Table 2).

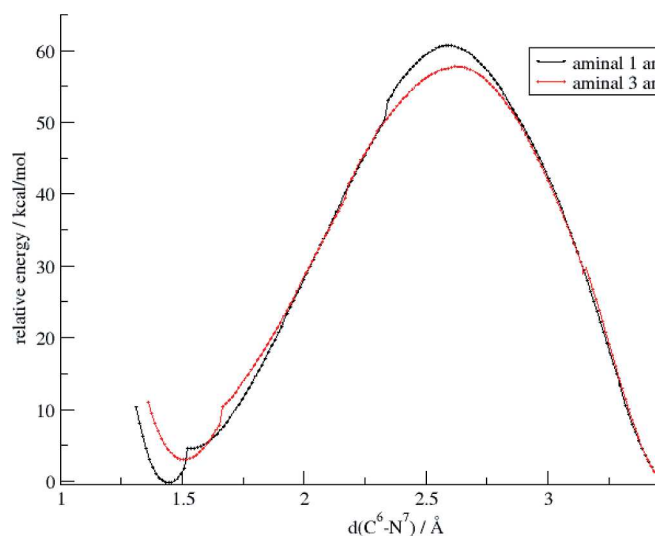


Figure 8. Energy profile of the reactions from unprotonated amine/imine tautomers (**2** and **4**) to spiroaminals (**1** and **3**) computed at the M06-2X/TZVP level. The unevenness in the scans is caused by conformational changes.

Conclusions

Several conformers of four different spiroaminals and their tautomerization mechanisms were studied by DFT [M06-2X-D3/TZVP, CPCM(water)]. Experimentally, the compound with an allyl substituent at the nitrogen atom (**3**) was observed as an amine/imine tautomer, and unsubstituted **1** was observed as a spiroaminal tautomer.

The calculations show that spiroaminals with substituted nitrogen atoms prefer a different minimum conformation (a-C) than unsubstituted spiroaminals or spiroaminals with substituted backbones (a-A). We find a strong $n(\text{N}) \rightarrow \sigma^*(\text{C}-\text{N})$ donation in the a-A conformers but not in the a-C conformers. Nevertheless, the C–N bond is still longer in **3a-C** than in the **1/5/7a-A** conformers, which indicates that steric repulsions influence the conformation even more strongly than the anomeric effect.

The computed ring-opening mechanism is similar for all spiroaminals. For the singly substituted spiroaminal (**5**), the opening of the unsubstituted ring is more facile and is energetically comparable that of the parent spiroaminal **1**. C–N cleavage is only possible upon prior protonation of one nitrogen atom. In all a-A conformers, the protonation leads

to an increased $n(\text{N}) \rightarrow \sigma^*(\text{C}-\text{N})$ donation and an elongated C–N bond. For a-C conformers without anomeric interactions, the increase of the C–N bond length upon protonation is less pronounced. The barriers for tautomerization are generally higher for C conformers than for A conformers by 2–4 kcal/mol. However, all barriers are small ($\Delta G = 2\text{--}8$ kcal/mol) and, therefore, the tautomerization of the protonated spiroaminals is feasible at room temperature in all cases. For the unprotonated spiroaminals, the reaction is always endergonic (and becomes less so in the sequence **7** > **5** > **1** > **3**). For the protonated spiroaminals, the reaction is computed to be exergonic for **3**, nearly thermoneutral for **1** and **5**, and endergonic for **7**.

Thus, the calculations show that spiroaminals with a substituted nitrogen atom (**3**) have a greater tendency to form the protonated open-ring tautomer than those with an unsubstituted nitrogen atom (**1/5/7**). There is a kinetic barrier that hinders the back reaction from the neutral imines to aminals for spirocycles. For the unsubstituted parent compound **1** and the backbone-substituted derivatives **5** and **7**, the calculations predict the spiroaminal tautomer to be thermodynamically favored.

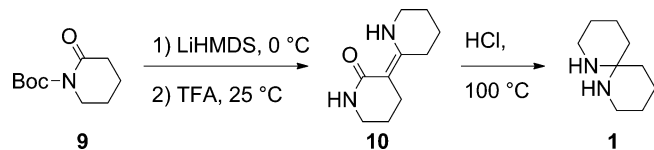
Computational Section

DFT calculations were performed by using the M06-2X density functional^[8] with D3 dispersion^[9] and the TZVP^[10] basis set as provided in the Gaussian09 program suite.^[11] Geometry optimizations were performed with an ultrafine grid by using the option `int = ultrafine` in Gaussian09 and without any constraints. Local minima (no imaginary mode) and transition states (one imaginary mode) were characterized by harmonic force constant analysis. Thermal corrections to obtain Gibbs free energies were determined at 1 bar and 298.15 K for all stationary points. The connectivities of transition states and minima were verified by intrinsic reaction coordinate (IRC)^[12] calculations. To estimate the energy of elusive transition states, scans of the potential energy surface (PES) were performed. Some scans were performed with Gaussian09 in the ChemShell package.^[13]

Solvent effects were treated by a polarizable continuum model (CPCM)^[14] with universal force field (UFF) cavities and water as solvent. The calculation of solvation free energies in thermodynamic cycles was performed with the solvent model density (SMD) approach, which was developed for this purpose.^[15] A natural bond orbital (NBO) analysis for selected structures was performed by using the NBO 3.1 package implemented in Gaussian09.^[16] The interactions of localized orbitals were quantified by second-order perturbation theory analysis, which characterizes the strength of the interaction in terms of the second-order energy $E(2)$ and the charge transfer from a donor to an acceptor orbital. Further details are given in the Supporting Information.

Experimental Section

General: Spiroaminal **1** was synthesized in three steps from *N*-Boc- δ -valerolactam (**9**, Boc = *tert*-butyloxycarbonyl) by the previously reported reaction sequence (Scheme 5).^[2] Upon the exposure of the spiroaminal to small amounts of HCl, which were allowed to slowly diffuse into the pure compound, crystals of the hydrochloride **11** suitable for crystal structure determination were obtained.^[17]

Scheme 5. Synthesis of spiroaminal **1**.

Crystallographic Structure Determination: Details of the data collection and processing, structure analysis, and refinement are summarized in Table 4. The diffraction data were collected with an Oxford Diffraction Nova A diffractometer by using mirror-focused Cu- K_{α} radiation. The structure was solved by direct methods (SHELXS-97) and refined anisotropically by full-matrix least-squares procedures on F^2 by using the SHELXL-97 program.^[18] Hydrogen atoms were (1) located and refined isotropically (hydrogen atoms attached to the nitrogen atoms) or (2) placed geometrically and allowed to ride on their attached carbon atoms (all other H atoms).

Table 4. Crystallographic data for unsubstituted spiroaminal hydrochloride **11**.

Empirical formula	C ₉ H ₁₉ ClN ₂
Formula weight	190.71
Crystal system	monoclinic
Space group	$P2_1/n$
a [Å]	9.0933(6)
b [Å]	7.4817(4)
c [Å]	15.3312(10)
α [°]	90
β [°]	90.205(6)
γ [°]	90
V [Å ³]	1043.03(11)
Z	4
Density (calculated) [mg m ⁻³]	1.214
Absorption coefficient [mm ⁻¹]	2.841
$F(000)$	416
θ Range for data collection [°]	4.86–73.96
Reflections collected	28567
Data/restraints/parameters	2116/0/122

The unsubstituted spiroaminal hydrochloride **11** crystallizes as a racemate in the monoclinic space group $P2_1/n$ with one molecule in the asymmetric unit. Its conformation is the thermodynamically stable conformer A (Scheme 2) with both rings in the chair conformation. In the molecular structure, the two nitrogen atoms can be clearly distinguished, and the protonation occurs at N⁷. The bond lengths to the central carbon atom are 1.433(2) Å for the unprotonated N¹ and 1.559(2) Å for the protonated N⁷. The individual spiroaminal molecules are linked through hydrogen bridges from N⁷ to the chloride atoms to form a one-dimensional hydrogen-bridged chain along b (Figure 2). The N⁷–Cl distances refined to 3.1662(15) and 3.1917(17) Å, which are slightly longer than the literature-reported value of 3.130(4) Å.^[19] The hydrogen atom at N¹ is oriented towards the nearest chloride atom with a N¹–Cl distance of 3.4019(17) Å.

CCDC-1001777 contains the supplementary crystallographic data for this paper. These data can be obtained free of charge from The Cambridge Crystallographic Data Centre via www.ccdc.cam.ac.uk/data_request/cif.

Supporting Information (see footnote on the first page of this article): Absolute energies and xyz structures of all important structures as well as detailed computational methods.

Acknowledgments

The authors thank the European Research Council (ERC) for generous financial support (to J. C and A. G. M. B.), GlaxoSmithKline for the Glaxo endowment (to A. G. M. B), and Prof. Martin Bröring (TU Braunschweig) for providing support and laboratory facilities.

- [1] a) S. Favre, P. Vogel, S. Gerber-Lemaire, *Molecules* **2008**, *13*, 2570–2600; b) S. K. Ghosh, R. P. Hsung, J. Liu, *J. Am. Chem. Soc.* **2005**, *127*, 8260–8261; c) K. T. Mead, B. N. Brewer, *Curr. Org. Chem.* **2003**, *7*, 227–256; d) P. Deslongchamps, D. D. Rowan, N. Pothier, J. K. Saunders, *Can. J. Chem.* **1981**, *59*, 1122–1131.
- [2] J. Cordes, P. R. D. Murray, A. J. P. White, A. G. M. Barrett, *Org. Lett.* **2013**, *15*, 4992–4995.
- [3] The notations of spiroaminal conformers in this paper follow the recommendations for comparable sugar compounds: *Conformational Nomenclature for Five- and Six-Membered Ring Forms of Monosaccharides and Their Derivatives, Recommendations, IUPAC-IUB Joint Commission on Biochemical Nomenclature (JCBN)*, **1980**; *Arch. Biochem. Biophys.* **1981**, *207*, 469–472; *Eur. J. Biochem.* **1980**, *111*, 295–298; *Pure Appl. Chem.* **1981**, *53*, 1901–1905.
- [4] A. F. Hollemann, E. Wiberg, N. Wiberg, *Hollemann-Wiberg, Lehrbuch der Anorganischen Chemie*, 101. Auflage, Walter de Gruyter, Berlin, **1995**.
- [5] C. Wang, Z. Chen, W. Wu, Y. Mo, *Chem. Eur. J.* **2013**, *19*, 1436–1444.
- [6] R. Taylor, O. Kennard, *J. Am. Chem. Soc.* **1982**, *104*, 5063–5070.
- [7] H. K. Hall, *J. Am. Chem. Soc.* **1957**, *79*, 5441–5444.
- [8] Y. Zhao, N. E. Schultz, D. G. Truhlar, *J. Chem. Theory Comput.* **2006**, *2*, 364–382.
- [9] S. Grimme, J. Antony, S. Ehrlich, H. Krieg, *J. Chem. Phys.* **2010**, *132*, 154104–154119.
- [10] A. Schäfer, C. Huber, R. Ahlrichs, *J. Chem. Phys.* **1994**, *100*, 5829–5835.
- [11] M. J. Frisch, G. W. Trucks, H. B. Schlegel, G. E. Scuseria, M. A. Robb, J. R. Cheeseman, G. Scalmani, V. Barone, B. Mennucci, G. A. Petersson, H. Nakatsuji, M. Caricato, X. Li, H. P. Hratchian, A. F. Izmaylov, J. Bloino, G. Zheng, J. L. Sonnenberg, M. Hada, M. Ehara, K. Toyota, R. Fukuda, J. Hasegawa, M. Ishida, T. Nakajima, Y. Honda, O. Kitao, H. Nakai, T. Vreven, J. A. Montgomery Jr., J. E. Peralta, F. Ogliaro, M. Bearpark, J. J. Heyd, E. Brothers, K. N. Kudin, V. N. Staroverov, R. Kobayashi, J. Normand, K. Raghavachari, A. Rendell, J. C. Burant, S. S. Iyengar, J. Tomasi, M. Cossi, N. Rega, J. M. Millam, M. Klene, J. E. Knox, J. B. Cross, V. Bakken, C. Adamo, J. Jaramillo, R. Gomperts, R. E. Stratmann, O. Yazyev, A. J. Austin, R. Cammi, C. Pomelli, J. W. Ochterski, R. L. Martin, K. Morokuma, V. G. Zakrzewski, G. A. Voth, P. Salvador, J. J. Dannenberg, S. Dapprich, A. D. Daniels, Ö. Farkas, J. B. Foresman, J. V. Ortiz, J. Cioslowski, D. J. Fox, *Gaussian 09*, revision A.1, Gaussian, Inc., Wallingford CT, **2009**.
- [12] a) C. Gonzalez, H. B. Schlegel, *J. Chem. Phys.* **1989**, *90*, 2154–2161; b) C. Gonzalez, H. B. Schlegel, *J. Phys. Chem.* **1990**, *94*, 5523–5527.
- [13] a) J. Kästner, J. M. Carr, T. W. Keal, W. Thiel, A. Wander, P. Sherwood, *J. Phys. Chem. A* **2009**, *113*, 11856–11865; b) *ChemShell, a Computational Chemistry Shell*, see: www.chemshell.org.
- [14] V. Barone, M. Cossi, *J. Phys. Chem. A* **1998**, *102*, 1995–2001.

- [15] A. V. Marenich, C. J. Cramer, D. G. Truhlar, *J. Phys. Chem. B* **2009**, *113*, 6378–6396.
- [16] *NBO*, v. 3.1, E. D. Glendening, A. E. Reed, J. E. Carpenter, F. Weinhold, University of Wisconsin, Madison.
- [17] This was achieved by storing a 1 mL vessel containing the spiroaminal (ca. 100 mg) in a cupboard next to chlorinated solvents. The crystals grew over the course of ca. 3 months. All direct attempts to obtain crystalline salts by reacting the spiroaminal with various acids were unsuccessful.
- [18] G. M. Sheldrick, *Acta Crystallogr., Sect. A* **2008**, *64*, 112–122.
- [19] T. Steiner, *Acta Crystallogr., Sect. B* **1998**, *54*, 456–463.

Received: May 14, 2014

Published Online: July 21, 2014

SUPPORTING INFORMATION

DOI: 10.1002/ejoc.201402576

Title: Spiroaminals – Crystal Structure and Computational Investigation of Conformational Preferences and Tautomerization Reactions

Author(s): Claudia Loerbroks, Birte Böker, Jens Cordes, Anthony G. M. Barrett, Walter Thiel*

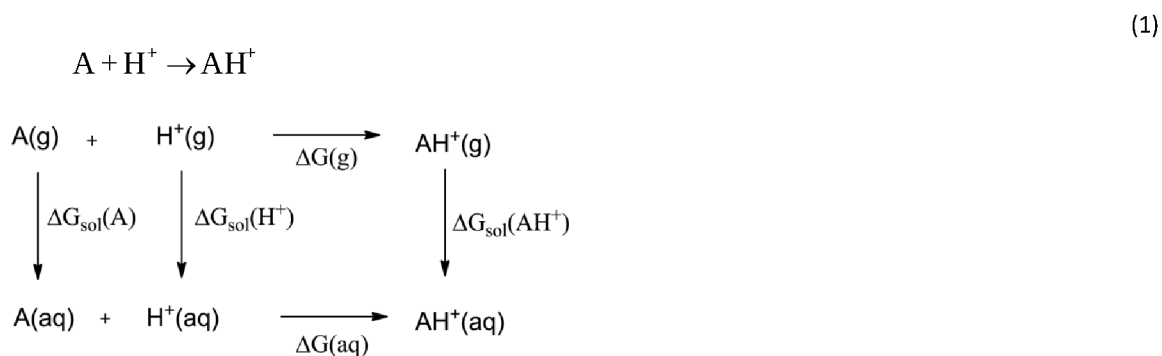
Computational Methods

DFT calculations were performed using the M06-2X density functional^[1] with D3 dispersion^[2] and the TZVP^[3] basis set as provided in the Gaussian09 program suite.^[4] The M06-2X functional is a hybrid functional (54% exchange), which was developed for main-group thermochemistry and kinetics. According to recent benchmarks, M06-2X is one of the best hybrid functionals with a weighted total mean absolute deviation of 2.2 kcal/mol for the GMTKN30 database (M06-2X-D3/(aug)-cc-pVQZ).^[5]

Geometry optimizations were carried out with an ultrafine grid, using the option int=ultrafine in Gaussian09, and without any constraints. Local minima (no imaginary mode) and transition states (one imaginary mode) were characterized by harmonic force constant analysis. Thermal corrections to obtain Gibbs free energies were determined at 1 bar and 298.15 K for all stationary points.

The connectivity of transition states and minima was verified by intrinsic reaction coordinate (IRC)^[6] calculations, unless mentioned otherwise. To estimate the energy of elusive transition states, scans of the potential energy surface (PES) were performed. Some scans were performed with Gaussian09 in the Chemshell package.

Solvent effects were treated by a polarizable continuum model (CPCM)^[7] with universal force field (UFF) cavities using water and chloroform as solvent. This model was applied since it gave the best results for solvated cationic species in previous validations.^[8] Thermodynamic cycles were used to calculate free energies of protonation:



For the evaluation of the thermodynamic cycle, we used the experimental values for the solvation free energy of the hydronium ion, H^+ , and for the gas-phase free energy of H^+ :^[9] $\Delta G_{sol,1M}(H^+) = -265.9$ kcal/mol, $\Delta G_{g,1atm}(H^+) = -6.28$ kcal/mol. All energy values were converted to the standard thermodynamic state of 298.15 K and 1 M (1 mol/L). In the gas phase, equation (2), the change of 1 mole of ideal gas from 1 atm (24.46 L/mol) to 1 M gives rise to the following correction term:

$$\begin{aligned}
\Delta G_{g,1M} &= \Delta G_{g,1atm} - T\Delta S \\
&= \Delta G_{g,1atm} + RT\ln\left(\frac{V_g}{V_{aq}}\right) \\
&= \Delta G_{g,1atm} + RT\ln(24.46) \\
&= \Delta G_{g,1atm} + 1.89 \text{ kcal/mol}
\end{aligned}
\tag{2}$$

The calculation of solvation free energies in thermodynamic cycles was done with the solvent model density (SMD) approach, which was developed for this purpose.^[10]

A natural bonding orbital (NBO) analysis for selected structures was performed using the NBO 3.1 package implemented in Gaussian09.^[11] The interactions of localized orbitals were quantified by the occupation of the orbitals and second-order perturbation theory analysis, which characterizes the strength of the interaction in terms of the second-order energy $E(2)$ and the charge transfer from a donor to an acceptor orbital.

The literature offers several models to describe the anomeric effect: hyperconjugation ($n(X) \rightarrow \sigma^*(C-Y)$),^[12] electrostatics (anti-parallel dipoles),^[13] hydrogen bonding with 1,3 axial CH groups,^[14] and redistribution of electron population from the hydrogen atoms of the central atom.^[15] Which factor contributes most is up to now a point of discussion,^[12] but mostly the electrostatic and hyperconjugation models are employed. In this report we will focus on hyperconjugation and also investigate steric factors.

The explanation of the anomeric effect by hydrogen bonds between the N lone pair and the 1,3 diaxial C-H groups (e.g. $n(N^7)$ and $C^{11}H$ and C^9H)^[14] does not apply to spiroaminals, as hydrogen bonding is not possible for steric reasons. In the conformers a, the hydrogen atoms on the nitrogen atoms point towards the CH bonds, and in the c conformers the C-N bond is not parallel to the CH groups and so the distance is too large.

Table S1: Relative free energies for all stationary points on the pathway to tautomerization of protonated spiroaminals (int1 to int4), relevant hyperconjugative interactions $E(2)$, and C-N distances during the course of the reaction. Free energies are given relative to the lowest-energy protonated conformer int1 at the M06-2X-D3/TZVP,CPCM(water) level. B1 = ring flip of the unsubstituted ring. B2 = ring flip of the substituted ring. ' = substituted ring protonated and opened.

	ΔG^a_j	$E(2)^{[a]}$		$d(C-N^1)^{[b]}$
		$n(N^1) \rightarrow \sigma^*(C-N^7)$	$n(N^1) \rightarrow \sigma^*(C-N^1)$	
1 → 2: X = N, R¹ = R² = R³ = H				
1a-A		16.3	16.3	1.474
int1	0.0	31.2		1.575
ts1	-			
int2	4.0		14.4	2.575
ts2	-			

int3	5.4			
int4	-0.4			
1a-B		13.7	1.8	1.480
int1	0.4	29.0		1.573
ts1	-			
int2	4.0		13.1	2.598
ts2	6.6			
int3	4.7			
int4	-0.4			
1a-C		1.7	1.7	1.468
int1	2.2	4.5		1.573
ts1	8.4			
int2	4.5		7.1	2.745
ts2	6.6			
int3	4.2			
int4	-0.4			
3 → 4: X = N, R¹ = R² = H, R³ = allyl				
3a-A		17.0	15.4	1.490
int1	0.0	19.5		1.582
ts1	2.5			
int2	0.1		12.0	2.642
ts2	-			
int3	2.9			
int4	-3.6			
3a-B1		13.4	1.8	1.477
int1	0.6	4.6		1.548
ts1	4.5			
int2	0.0		8.0	2.734
ts2	-			
int3	3.5			
int4	-3.6			
3a-B2		14.3	2.1	1.496
int1	-0.1	20.6		1.585
ts1	2.6			
int2	0.2		11.6	2.650
ts2	3.5			
int3	0.6			
int4	-3.6			
3a-C		2.1	1.8	1.482
int1	-1.0	4.6		1.549
ts1	4.3			
int2	0.5		7.9	2.738
ts2	2.8			
int3	0.1			
int4	-3.6			
5 → 6: X = N, R¹ = iso-propyl, R² = R³ = H				
5a-A		16.4	16.2	1.475
int1	0.0	31.3		1.577
ts1	-			
int2	3.8		13.5	2.589
ts2	-			
int3	6.5			
int4	-0.7			

5a-A'		16.4	16.2	1.475
int1	0.3	30.5		1.569
ts1	-			
int2	6.3		17.8	2.514
ts2	-			
int3	-			
int4	1.4			
7 → 8: X = N, R¹ = R² = iso-propyl, R³ = H				
7a-A		16.3	16.3	1.472
int1	0.0	30.7		1.570
ts1	-			
int2	6.0		16.3	2.535
ts2	-			
int3	-			
int4	3.1			

[a] kcal mol⁻¹; [b] Å

Table S2. Distances and angles in conformers int2 and int3 for the structures 1, 3, 5, and 7 in the protonated tautomerization mechanism.

	C ⁶ -N ⁷ in int2 / Å	C ⁵ H-N ⁷ in int3 / Å	C ⁵ -H-N ⁷ in int3 / °
1a-A	2.575	3.633	123
1a-B	2.598	2.764	163
1a-C	2.745	2.830	159
3a-A	2.642	3.176	132
3a-B1	2.734	2.619	159
3a-B2	2.650	2.503	165
3a-C	2.738	2.804	160
5a-A	2.589	2.897	134
5a-A'	2.514	-	-
7a-A	2.535	-	-

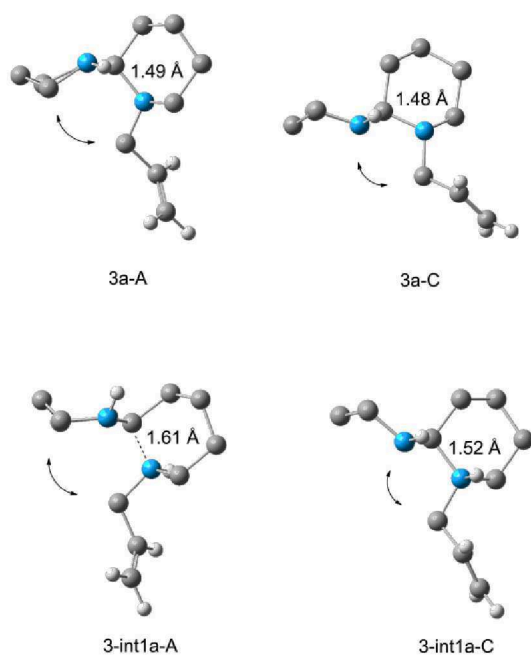


Figure S1. Protonated and unprotonated conformers 3a-A and 3a-C with their C¹-N⁷ distances.

Table S3. Absolute and relative energies for the conformers a-A and a-C and the species on the tautomerization pathway of 1-propyl-1,7-diazaspiro[5,5]undecane (8,9).

		E/ a.u.	E_ZPC / a.u.	H / a.u.	G/ a.u.	ΔE / kcal mol ⁻¹	ΔE_{ZPC} / kcal mol ⁻¹	ΔH / kcal mol ⁻¹	ΔG / kcal mol ⁻¹
unprotonated	8a-A	-581.156	-580.798	-580.784	-580.838	0.0	0.0	0.0	0.0
	8a-C	-581.163	-580.805	-580.791	-580.845	-4.5	-4.4	-4.5	-4.2
	9	-581.149	-580.795	-580.778	-580.841	4.1	2.1	3.2	-1.5
protonated 8a-A	int1	-581.620	-581.247	-581.232	-581.29	0.0	0.0	0.0	0.0
	ts1	-581.611	-581.242	-581.226	-581.28	5.3	3.2	3.4	2.6
	int2	-581.612	-581.243	-581.227	-581.29	4.7	2.3	3.1	0.7
	ts2	-	-	-	-				
	int3	-581.605	-581.236	-581.220	-581.28	9.2	6.7	7.7	4.1
	int4	-581.619	-581.250	-581.234	-581.29	0.6	-2.0	-1.3	-3.6
protonated 8a-C	int1	-581.623	-581.249	-581.235	-581.289	-1.9	-1.6	-1.8	-1.7
	ts1	-581.609	-581.239	-581.224	-581.280	6.7	4.8	4.9	4.4
	int2	-581.611	-581.242	-581.226	-581.285	5.4	2.9	3.8	1.2
	ts2	-581.603	-581.235	-581.219	-581.279	10.2	7.6	8.1	4.6
	int3	-581.608	-581.239	-581.223	-581.284	7.2	4.7	5.7	1.4
	int4	-581.619	-581.250	-581.234	-581.292	0.6	-2.0	-1.3	-3.6

Comparison with other methods

To verify the methods used, other methods have been employed to calculate the equilibrium structures (Table S4). In addition to water, chloroform was chosen as a solvent, since the NMR analysis took place in deuterated chloroform and the solvent influences the anomeric effect.^[16] Furthermore, the B3LYP functional as well as the MP2 hamiltonian with the aug-cc-pVTZ basis set was used.

Comparing all the reaction energies for the reactions **1** to **2** and **3** to **4**, it is obvious that the functionals do not agree in absolute values: For M06-2X-D3 and B3LYP-D3 an energy difference of about -2 kcal/mol between $\Delta\Delta G((\mathbf{4-3})-(\mathbf{2-1}))$ was detected, with the reaction **3** to **4** being less endothermic than the reaction **1** to **2**. For MP2 the reaction energies are the same ($\Delta G(\text{imine-aminol}) = 6 \text{ kcal/mol}$). B3LYP-D3 is the only functional which predicts the reactions to be exothermic. Since density functional theory seems not to be consistent about how endo- or exothermic this tautomeric reaction is, we prefer to compare relative energy trends rather than relative energies.

Table S4: Energy values for molecule 1-4 with different methods.

conformer	$\Delta E / \text{kcal mol}^{-1}$	$\Delta E_{\text{ZPC}} / \text{kcal mol}^{-1}$	$\Delta H / \text{kcal mol}^{-1}$	$\Delta G / \text{kcal mol}^{-1}$
M06-2X-D3/TZVP,CPCM(water)				
1a-A	0.0	0.0	0.0	0.0
2	11.3	8.5	10.1	5.0
3a-C	0.0	0.0	0.0	0.0
4	9.8	7.4	8.9	3.4
M06-2X-D3/TZVP,CPCM(chloroform)				
1a-A	0.0	0.0	0.0	0.0
2	11.7	9.0	10.5	5.7
3a-C	0.0	0.0	0.0	0.0
4	9.7	7.6	8.8	4.0
B3LYP-D3/TZVP,CPCM(chloroform)				
1a-A	0.0	0.0	0.0	0.0
2	6.1	3.5	5.0	-0.2
3a-C	0.0	0.0	0.0	0.0
4	3.7	1.6	2.9	-2.2
MP2/TZVP,CPCM(chloroform)				
1a-A	0.0	0.0	0.0	0.0
2	11.8	9.5	11.0	6.0
3a-C	0.0	0.0	0.0	0.0
4	11.8	10.1	11.3	6.3

Absolute Energies

Table S5: Absolute energies of unprotonated spiroaminal structures (M06-2X-D3/TZVP,CPCM(water)).

conformer	E/ kcal mol ⁻¹	E_ZPC / kcal mol ⁻¹	H / kcal mol ⁻¹	G/ kcal mol ⁻¹
1a-A	-463.256	-462.983	-462.973	-463.017
1c-A	-463.254	-462.982	-462.971	-463.016
1a-B	-463.254	-462.982	-462.971	-463.016
1c-B	-463.253	-462.981	-462.971	-463.015
1a-C	-463.254	-462.981	-462.971	-463.015
1c-C	-463.253	-462.98	-462.97	-463.014
1a-D	-463.247	-462.975	-462.964	-463.009
1a-E	-463.246	-462.974	-462.963	-463.008
1a-F	-463.246	-462.974	-462.964	-463.009
1a-G	-463.247	-462.975	-462.964	-463.009
3a-A	-579.928	-579.595	-579.581	-579.634
3c-A	-579.933	-579.6	-579.586	-579.638
3a-B1	-579.933	-579.599	-579.585	-579.639
3c-B1	-579.929	-579.595	-579.581	-579.634
3a-B2	-579.928	-579.594	-579.58	-579.633
3c-B2	-579.933	-579.6	-579.585	-579.639
3a-C	-579.935	-579.602	-579.587	-579.641
3c-C	-579.931	-579.597	-579.583	-579.636
5a-A	-581.178	-580.82	-580.806	-580.86
5c-A	-581.176	-580.819	-580.804	-580.859
5a-B1	-581.176	-580.819	-580.804	-580.859
5c-B1	-581.175	-580.818	-580.804	-580.858
5a-B2	-581.171	-580.813	-580.799	-580.852
5c-B	-581.17	-580.812	-580.798	-580.851
5a-C	-581.17	-580.812	-580.798	-580.851
5c-C	-581.166	-580.809	-580.794	-580.847
7a-A	-699.1	-698.658	-698.639	-698.702
7c-A	-699.098	-698.656	-698.637	-698.702
7a-B	-699.094	-698.651	-698.632	-698.695
7c-B	-699.092	-698.65	-698.631	-698.694
7a-C	-699.084	-698.641	-698.623	-698.684
7c-C	-699.083	-698.639	-698.621	-698.682

Table S6: Absolute energies of protonated spiroaminal structures and reaction mechanism from aminal to amine/imine

(M06-2X-D3/TZVP,CPCM(water)).

conformer	E/ kcal mol ⁻¹	E_ZPC / kcal mol ⁻¹	H / kcal mol ⁻¹	G/ kcal mol ⁻¹
1a-A-int1	-463.712820502	-463.425621	-463.414891	-463.459738
1a-A-int2	-463.700815659	-463.417138	-463.404905	-463.453404
1a-A-int3	-463.694492853	-463.411735	-463.39876	-463.451174
1a-A-int4	-463.706070216	-463.423237	-463.410907	-463.460317
1a-B-int1	-463.712099432	-463.424912	-463.414138	-463.459144
1a-B-int2	-463.69988231	-463.416589	-463.404199	-463.453366
1a-B-ts2	-463.695228662	-463.412402	-463.40045	-463.449249
1a-B-int3	-463.696771354	-463.413715	-463.400979	-463.452307
1a-B-int4	-463.706070216	-463.423237	-463.410907	-463.460317
1a-C-int1	-463.709876108	-463.421988	-463.411325	-463.456171
1a-C-ts1	-463.694961611	-463.411072	-463.399767	-463.446327
1a-C-int2	-463.698631161	-463.415555	-463.403024	-463.452626
1a-C-ts2	-463.696068234	-463.412885	-463.401079	-463.449251
1a-C-int3	-463.697641298	-463.414564	-463.401837	-463.453049
1a-C-int4	-463.706070216	-463.423237	-463.410907	-463.460317
3a-A-int1	-580.389304037	-580.040502	-580.025976	-580.080031
3a-A-ts1	-580.382102831	-580.035954	-580.021332	-580.075991
3a-A-int2	-580.383645683	-580.038131	-580.022398	-580.079862
3a-A-int3	-580.376916734	-580.031669	-580.015625	-580.075446
3a-A-int4	-580.387799281	-580.042961	-580.027164	-580.085765
3a-B1-int1	-580.389518611	-580.039817	-580.025622	-580.079121
3a-B1-ts1	-580.379497834	-580.033007	-580.018462	-580.072823
3a-B1-int2	-580.383273297	-580.037972	-580.022156	-580.080085
3a-B1-int3	-580.375802128	-580.030555	-580.014459	-580.074399
3a-B1-int4	-580.387799281	-580.042961	-580.027164	-580.085765
3a-B2-int1	-580.38934057	-580.040771	-580.02619	-580.080204
3a-B2-ts1	-580.381719891	-580.035812	-580.021117	-580.075895
3a-B2-int2	-580.383086499	-580.03762	-580.021844	-580.079734
3a-B2-ts2	-580.377654055	-580.032451	-580.017241	-580.074447
3a-B2-int3	-580.378840375	-580.033913	-580.017714	-580.079093
3a-B2-int4	-580.387799281	-580.042961	-580.027164	-580.085765
3a-C-int1	-580.391941138	-580.042469	-580.028259	-580.08166

3a-C-ts1	-580.37953264	-580.033327	-580.018695	-580.073203
3a-C-int2	-580.382457367	-580.03713	-580.021286	-580.079247
3a-C-ts2	-580.378595138	-580.033473	-580.018269	-580.075606
3a-C-int3	-580.379699233	-580.034795	-580.018625	-580.079904
3a-C-int4	-580.387799281	-580.042961	-580.027164	-580.085765
5a-A-int1	-581.634821643	-581.262787	-581.247787	-581.302557
5a-A-int2	-581.623100364	-581.25469	-581.238252	-581.296543
5a-A-int3	-581.617307085	-581.249273	-581.232469	-581.292195
5a-A-int4	-581.628902506	-581.261238	-581.244774	-581.303688
5a-A'-int1	-581.634545865	-581.262467	-581.247496	-581.302128
5a-A'-int2	-581.620124154	-581.251279	-581.235012	-581.292558
5a-A'-int4	-581.626261376	-581.258254	-581.241907	-581.300271
7a-A-int1	-699.556546371	-699.099704	-699.080429	-699.144973
7a-A-int2	-699.5424232	-699.088708	-699.068229	-699.135476
7a-A-int3	-699.545261809	-699.092331	-699.071833	-699.14011

Literature

- [1] Y. Zhao, N. E. Schultz and D. G. Truhlar, *J. Chem. Theory Comput.* **2006**, *2*, 364-382.
- [2] S. Grimme, J. Antony, S. Ehrlich and H. Krieg, *J. Chem. Phys.* **2010**, *132*, 154104-154119.
- [3] A. Schäfer, C. Huber and R. Ahlrichs, *J. Chem. Phys.* **1994**, *100*, 5829-5835.
- [4] Gaussian 09, Revision A.1, M. J. Frisch, G. W. Trucks, H. B. Schlegel, G. E. Scuseria, M. A. Robb, J. R. Cheeseman, G. Scalmani, V. Barone, B. Mennucci, G. A. Petersson, H. Nakatsuji, M. Caricato, X. Li, H. P. Hratchian, A. F. Izmaylov, J. Bloino, G. Zheng, J. L. Sonnenberg, M. Hada, M. Ehara, K. Toyota, R. Fukuda, J. Hasegawa, M. Ishida, T. Nakajima, Y. Honda, O. Kitao, H. Nakai, T. Vreven, J. A. Montgomery, Jr., J. E. Peralta, F. Ogliaro, M. Bearpark, J. J. Heyd, E. Brothers, K. N. Kudin, V. N. Staroverov, R. Kobayashi, J. Normand, K. Raghavachari, A. Rendell, J. C. Burant, S. S. Iyengar, J. Tomasi, M. Cossi, N. Rega, J. M. Millam, M. Klene, J. E. Knox, J. B. Cross, V. Bakken, C. Adamo, J. Jaramillo, R. Gomperts, R. E. Stratmann, O. Yazyev, A. J. Austin, R. Cammi, C. Pomelli, J. W. Ochterski, R. L. Martin, K. Morokuma, V. G. Zakrzewski, G. A. Voth, P. Salvador, J. J. Dannenberg, S. Dapprich, A. D. Daniels, Ö. Farkas, J. B. Foresman, J. V. Ortiz, J. Cioslowski, and D. J. Fox, Gaussian, Inc., Wallingford CT, **2009**.
- [5] L. Goerigk and S. Grimme, *Phys. Chem. Chem. Phys.* **2011**, *13*, 6670-6688.
- [6] a) C. Gonzalez and H. B. Schlegel, *J. Chem. Phys.* **1989**, *90*, 2154-2161; b) C. Gonzalez and H. B. Schlegel, *J. Phys. Chem.* **1990**, *94*, 5523-5527.
- [7] V. Barone and M. Cossi, *J. Phys. Chem. A* **1998**, *102*, 1995-2001.
- [8] Y. Takano and K. N. Houk, *J. Chem. Theory Comput.* **2004**, *1*, 70-77.
- [9] M. D. Liptak and G. C. Shields, *J. Am. Chem. Soc.* **2001**, *123*, 7314-7319.
- [10] A. V. Marenich, C. J. Cramer and D. G. Truhlar, *J. Phys. Chem. B* **2009**, *113*, 6378-6396.
- [11] NBO Version 3.1, E. D. Glendening, A. E. Reed, J. E. Carpenter, and F. Weinhold.
- [12] C. Wang, Z. Chen, W. Wu and Y. Mo, *Chem. – Eur. J.* **2013**, *19*, 1436-1444.
- [13] S. Gerber-Lemaire and P. Vogel in *Anomeric effects in pyranosides and related acetals*, (Eds.: A. Pilar Rauter and T. Lindhorst), Royal Society of Chemistry, Cambridge, *Vol. 35*, pp. 13-32.
- [14] O. Takahashi, K. Yamasaki, Y. Kohno, R. Ohtaki, K. Ueda, H. Suezawa, Y. Umezawa and M. Nishio, *Carbohydr. Res.* **2007**, *342*, 1202-1209.
- [15] A. Vila and R. A. Mosquera, *J. Comput. Chem.* **2007**, *28*, 1516-1530.
- [16] a) R. U. Lemieux, *Pure Appl. Chem.* **1971**, *25*, 527-548; b) R. Montagnani and J. Tomasi, *Int. J. Quantum Chem.* **1991**, *39*, 851-870; c) J. P. Praly and R. U. Lemieux, *Canad. J. Chem.* **1987**, *65*, 213-223.

Appendix D

Reactivity of Metal Catalysts in Glucose–Fructose Conversion

Claudia Loerbroks, Jeaphianne van Rijn, Marc-Philipp Ruby,
Qiong Tong, Ferdi Schüth, and Walter Thiel

Chemistry - A European Journal, **2014**, 38, 12298 – 12309.

Carried out most of the calculations, analyzed the results, and wrote the draft of the manuscript

The cartesian coordinates were deleted from the Supporting Information and can be found in the published version of the manuscript.

Transition Metals

Reactivity of Metal Catalysts in Glucose–Fructose Conversion

Claudia Loerbroks, Jeaphianne van Rijn, Marc-Philipp Ruby, Qiong Tong, Ferdi Schüth, and Walter Thiel*^[a]

Abstract: A joint experimental and computational study on the glucose–fructose conversion in water is reported. The reactivity of different metal catalysts (CrCl_3 , AlCl_3 , CuCl_2 , FeCl_3 , and MgCl_2) was analyzed. Experimentally, CrCl_3 and AlCl_3 achieved the best glucose conversion rates, CuCl_2 and FeCl_3 were only mediocre catalysts, and MgCl_2 was inactive. To explain these differences in reactivity, DFT calculations were performed for various metal complexes. The computed mechanism consists of two proton transfers and a hydrogen-atom transfer; the latter was the rate-determining step for all catalysts. The computational results were consistent

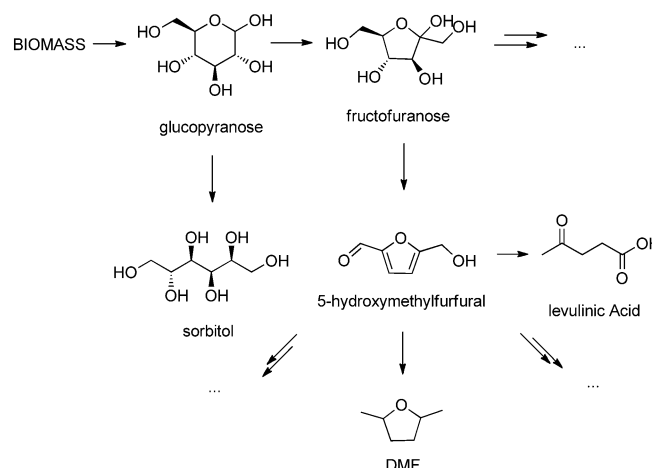
with the experimental findings and rationalized the observed differences in the behavior of the metal catalysts. To be an efficient catalyst, a metal complex should satisfy the following criteria: moderate Brønsted and Lewis acidity ($\text{p}K_{\text{a}}=4\text{--}6$), coordination with either water or weaker σ donors, energetically low-lying unoccupied orbitals, compact transition-state structures, and the ability for complexation of glucose. Thus, the reactivity of the metal catalysts in water is governed by many factors, not just the Lewis acidity.

Introduction

Biomass provides one of the renewable alternatives to fossil resources. The depolymerization of cellulosic and lignin-containing biomass yields platform molecules such as 5-hydroxymethylfurfural (HMF), which can be converted to other small organic molecules, such as levulinic acid (LA) and the biofuel dimethylfurfural (DMF), the latter in almost quantitative yield (Scheme 1).^[1] An important step in these processes is glucose–fructose isomerization.^[2] In technical applications, it is preferable to start from the educt glucose rather than fructose because of the lower price of glucose.

The isomerization was carried out experimentally in different solvents (ionic liquids,^[3] organic solvents,^[4] water)^[5] with various catalysts (acids,^[3a] metal salts)^[3,5a] and continues to be the topic of ongoing investigations. Among all systems tested, chromium(III) salts in ionic liquids were the most promising catalysts. The subsequent step of Brønsted acid catalyzed HMF formation from glucose has been studied thoroughly, both experimentally and computationally.^[6]

Recently, detailed experimental kinetic studies led to the conclusion that glucose–fructose conversion is catalyzed not only by the Lewis acidity of metal cations, but also by the Brønsted acidity of the water complexes of the cations.^[6g] The



Scheme 1. Possible pathways for the formation of platform molecules from biomass.

active species, a glucose–chromium(III)–water complex, was also investigated by Car–Parinello molecular dynamics (CPMD). An activation barrier of $15.5 \text{ kcal mol}^{-1}$ was estimated from an Arrhenius plot of the initial rate of glucose conversion with a 3:100 CrCl_3 /glucose ratio at 413 K.

Additionally, the formation of HMF from glucose in ionic liquids was studied by DFT. At the B3LYP/LANL2DZ//B3LYP/6-31 + G** level of theory, the glucose–fructose isomerization was found to be endothermic by $6.8 \text{ kcal mol}^{-1}$, with barriers of 20–40 kcal mol^{-1} depending on the chosen catalyst (WCl_3 , MoCl_3 , CrCl_3 , FeCl_3).^[7] Hensen and co-workers explored the isomerization by using CrCl_2 ,^[8] CrCl_3 ,^[8b] FeCl_2 ,^[8b] CuCl_2 ,^[8b] and SnCl_4 ^[9] as catalysts (PBE0/6-311 + + G**//PBE0/6-31 + G*). They proposed

[a] C. Loerbroks, J. van Rijn, M.-P. Ruby, Q. Tong, Prof. Dr. F. Schüth, Prof. Dr. W. Thiel
Max-Planck-Institut für Kohlenforschung
Kaiser-Wilhelm-Platz 1, 45470 Mülheim an der Ruhr (Germany)
Fax: (+49) 208-306-2996
E-mail: thiel@kofo.mpg.de

Supporting information for this article is available on the WWW under <http://dx.doi.org/10.1002/chem.201402437>.

that a dimeric complex catalyzes the reaction better than a monomeric catalyst and that chloride and hydroxyl ligands facilitate proton transfers during the reaction. The rate-determining step was identified as a hydrogen shift with a barrier of about 16 kcal mol⁻¹. According to their calculations and experiments, FeCl₂ and CuCl₂ are not active because the direct coordination of the corresponding active species to glucose is unfavorable. Reaction mechanisms for proton-catalyzed isomerizations were also the topic of extensive studies.^[5b, c, 6d, e, 10]

Despite all this previous work, the role of the metal salt in the reaction is still not fully understood, and to the best of our knowledge mechanisms have been studied in ionic liquids not water, which would most probably be the solvent of choice for any commercial process for cost-related reasons. To shed light on the activity of different metal salts in the glucose–fructose conversion in water, we have carried out a combined experimental and theoretical study, which made it possible to identify criteria for efficient catalysts that give high-conversion rates for glucose–fructose isomerization in water.

Computational details

DFT calculations were performed by using the PBE0 density functional^[11] and the 6-31 + G(d,p) basis set provided in the Gaussian 09 program suite.^[12] The basis set contains diffuse functions that are required for the correct description of intramolecular hydrogen bonds.^[13] The PBE0 hybrid functional has previously been found appropriate for the treatment of hydrogen-bonding complexes (mean unsigned error (MUE) = 0.34 kcal mol⁻¹) and their structures (angles: MUE = 1.11°, distances: mean average error = 0.0103 Å).^[14] Benchmark studies have documented the high accuracy of PBE0 for various transition-metal-catalyzed reactions with^[15] and without sugar molecules.^[16] For the sake of comparison, we carried out single-point calculations with other functionals and larger basis sets (see the Supporting Information), which gave results that agree well with those from the PBE0/6-31 + G(d,p) calculations.

Geometry optimizations were carried out without any constraints, unless noted otherwise. Local minima (no imaginary mode) and transition states (one imaginary mode) were characterized by harmonic force constant analysis. Thermal corrections to obtain Gibbs free energies were carried out at 1 bar and 298 K for all stationary points and at 70 bar and 413 K for rate-determining transition states and other important steps (see the Supporting Information). We observed only minimal changes in free energy at the higher temperature and pressure. The connectivity of transition states and minima was verified by intrinsic reaction coordinate (IRC) calculations,^[17] unless mentioned otherwise. To estimate the energy of elusive transition states, scans of the potential-energy surface (PES) were performed.

Solvent effects were treated by a polarizable continuum model (CPCM)^[18] with universal forcefield (UFF) cavities and water as the solvent. This model was applied because it gave the best results for cationic species in solution.^[19] The calculation of solvation free energies in thermodynamic cycles was performed with the solvent model density (SMD) approach,

which had been developed for this purpose.^[20] The role of the second hydration shell for the stabilization and constitution of the complexes had been examined previously: no exchange between the first and second hydration shell and no influence of the second hydration shell on the spin ordering could be detected, and therefore it was concluded that only the first hydration shell needs to be treated explicitly.^[21]

Different spin states were investigated for transition-metal complexes with different ligands (H₂O, Cl⁻, OH⁻) to identify the lowest-energy state. For all ligand systems, iron(III) cations prefer high-spin complexes (sextet), and chromium(III) cations prefer quartet rather than doublet spin states by about 26–35 kcal mol⁻¹. Copper(II) complexes favor the doublet state. These results are in agreement with the literature and are presented in the Supporting Information.^[22]

A natural bonding orbital (NBO) analysis for selected structures was performed by using the NBO 3.1 package implemented in Gaussian 09.^[23] The interactions of localized orbitals were quantified by the occupation of the orbitals and the natural charges.

All of the proposed mechanisms feature protonation and deprotonation reactions, which were treated by thermodynamic cycles (see the Supporting Information). This approach was also used for protonation reactions in a previous study on glucose protonation pathways.^[10]

Several possible mechanistic pathways were explored by consideration of different catalyst complexes, transition states in different protonation states, and also keto–enol tautomerization as a mechanistic alternative to hydrogen-transfer reactions. In the Results section, only the lowest pathways are shown. Data for all calculated pathways can be found in the Supporting Information.

Various metal–ligand systems were used in the calculations for iron(III), magnesium(II), aluminum(III), chromium(III), and copper(II) cations. If different choices were possible for the positioning of a ligand, different possibilities were examined and the lowest-energy structure of the starting glucopyranose–catalyst complex was selected (see the Supporting Information). Examples of metal catalysts and their coordination to glucose are shown in Figure 1. According to the literature, coordination of the O1/O2 hydroxyl groups is essential for the reaction.^[8b]

Results and Discussion

The experimental results are summarized in Table 1. The yields of fructose, HMF, and LA do not add up to the total conversion of glucose because acid-catalyzed side reactions of glucose with the products can occur. Due to the large variety and low yields of the side products, these were not analyzed.

The performance of the catalysts can be divided into three groups (Table 1). The first group consists of catalysts with high conversion rates: aluminum(III), zirconium(IV), and chromium(III). They also have reasonable yields of fructose, HMF, and/or LA. The second group includes bismuth(III)-, copper(II)-, and iron(III)-catalyzed reactions, which show low conversion and even lower product yields. The third group contains the reac-

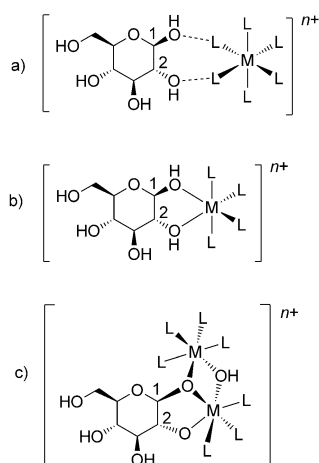


Figure 1. Glucose complexes of different metal cations with an octahedral ligand sphere: a) Hydrogen-bonding coordination, b) direct complexation of glucopyranose, and c) bonding of a dimeric catalyst.

Catalyst	Conv. [%]	HPLC yield [%]			pK _a	pH of reaction	
		Fructose	HMF	LA		Before	After
CrCl ₃ ·6H ₂ O	99	0	13	13	4.1	3.4	1.9
AlCl ₃ ·6H ₂ O	88	11	19	6	5.5	3.1	1.4
ZrCl ₄	69	7	5	13	-0.3	1.2	1.1
CuCl ₂ ·2H ₂ O	23	1	6	2	8.0	4.5	2.1
BiCl ₃	17	0.6	5	3	-3.5	1.3	1.3
FeCl ₃ ·6H ₂ O	12	0	3	0	2.2	2.0	1.6
MgCl ₂	2	1	0.8	0	11.4	7.4	3.3
CH ₃ COOH	0.1	0.8	0.6	0	4.8	3.1	3.2
uncatalyzed	0	0	0	0	15.7	-	-

tions with little or no conversion, i.e., the magnesium(II) and acetic acid catalyzed reactions and the uncatalyzed reaction.

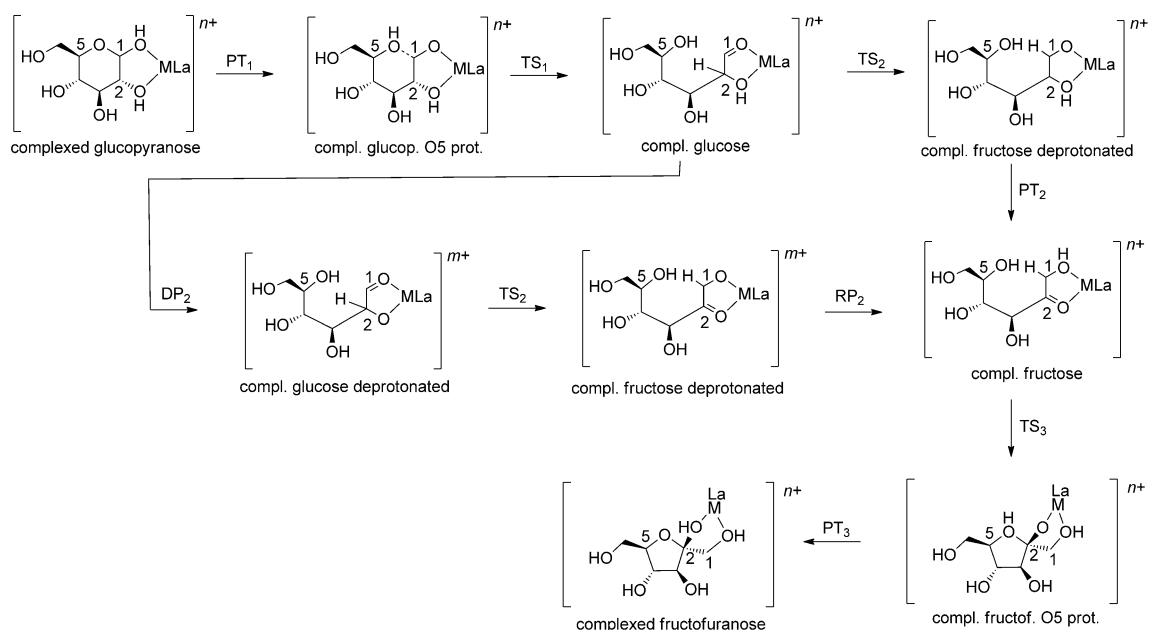
The experimental data indicate that Lewis acidity plays a role in this reaction because acetic acid is not a reactive catalyst, even though it has almost the same pK_a as chromium(III) or aluminum(III). But if Lewis acidity is important for the reaction, why do iron(III) and magnesium(II) not perform well, which are known as good Lewis acids? These experimental data already qualitatively suggest that the interplay between different factors is decisive for catalyst performance in the glucose–fructose conversion.

To answer this question in detail, the reaction was investigated computationally. Two examples from each group (Cr³⁺ and Al³⁺; Fe³⁺ and Cu²⁺; Mg²⁺ and no catalyst) were used to calculate the pathway from glucose to fructose. First, we present the general reaction mechanism, which was found to be lowest in energy for the glucose–fructose isomerization. Because multiple pathways and a variety of catalysts were investigated we will not dwell on the details of all pathways, but rather give an overview of the critical mechanistic steps within each group of catalysts. The focus will be on electronic, energetic, and geometrical trends that distinguish these groups and explain their reactivity.

The choice of cation environment for the single metal cations, alternatives to the general mechanism, and detailed descriptions of selected mechanistic pathways can be found in the Supporting Information.

Reaction mechanism

The lowest-energy pathways found consist of the steps shown in Scheme 2.



Scheme 2. Proposed mechanism for glucose to fructose isomerization. The example shown has α -glucose as a ligand.

Starting with a catalyst–glucopyranose complex, the first step is a proton transfer from O1 to O5 (PT₁) followed by C1–O5 bond cleavage (TS₁), which yields an open-chain glucose–catalyst complex. PT₁ can be separated into deprotonation of O1 and protonation of O5. In some cases PT₁ and TS₁ are concerted (uncatalyzed, magnesium(II)- and copper(II)-catalyzed pathways) and C1–O5 bond cleavage is, in most cases, a barrier-free process. In this initial step, the catalyst influences the C1–O1 and C1–O5 bond distances.

To form the open-chain fructose–catalyst complex, a hydrogen atom is transferred from C2 to C1 (TS₂) and a proton is transferred from O2 to O1 (PT₂). These steps were also identified from NMR experiments as part of the reaction pathway for solid Lewis acid catalysts in water.^[24] For the steps TS₂ and PT₂ there is an alternative: deprotonation of O2 (DP₂), hydrogen-atom transfer (TS₂), and re-protonation of O1 (RP₂). The deprotonation of O2 (DP₂) may be lower in energy as the negative charge on O2 eases the hydrogen transfer (TS₂) due to its positive inductive effect. This alternative pathway (DP₂, TS₂, RP₂) is favorable for the uncatalyzed pathway and for some of the [MO¹O²(H₂O)₄]ⁿ⁺ complexes and the dimeric catalysts. In the transition state TS₂ electron density is delocalized between the transferred hydrogen atom, the σ*(C–O) orbitals, and the orbitals of the metal or the metal–oxygen bonds.

To complete the fructose–fructofuranose transformation, the C2–O5 bond is formed (TS₃) and a proton transfer from O5 to O2 takes place (PT₃). All proton transfers proceed by a deprotonation followed by a protonation step. The C2–O5 bond formation is, in most cases, a barrier-free reaction.

Rate-determining steps

In all isomerization pathways, the first proton transfer (PT₁), the hydrogen-atom transfer (TS₂), and the separation of the catalyst from the product are possible critical steps. This section focuses on the comparison of these steps when different catalysts are used. Tables 2–4 below list the lowest energies found for these critical steps in each group. The rate-determining step for each mechanism is defined, and energies, NBO data, and natural charges are compared. Because the reaction takes place at 413 K, energies up to 36 kcal mol⁻¹ are assumed to be feasible; higher barriers would be difficult to overcome under these conditions.

The sum of the energies of [M(H₂O)₆]ⁿ⁺ and α-glucopyranose was taken as reference for all energies (ΔG) for a given metal M. No attempt was made to establish a common free-energy scale for all metals by calculations of the standard chemical potential at a given pH. The energy of the glucopyranose–catalyst complex (or, if lower, the sum of the energies of glucopyranose and the modified [M(H₂O)₆]ⁿ⁺ complex) serves as reference to determine the barriers for transition states TS₂ and PT₁ [ΔΔG(TS₂/PT₁)]. ΔΔG(separation) is the energy needed to separate fructofuranose from the catalyst; in this case, the reference is the energy of the fructofuranose–catalyst complex. ΔΔG(glucose–fructose) denotes the energy difference between the fructofuranose–catalyst complex and the glucopyranose–catalyst complex (relative to the latter).^[25]

The metal cations investigated will be discussed separately in three groups, according to their activity (see the Experimental section): group one (high conversion: Al³⁺, Cr³⁺), group two (low conversion: Cu²⁺, Fe³⁺), and group three (no conversion: uncatalyzed, Mg²⁺). For each group, we give a general overview over the cations then discuss the crucial proton transfers, hydrogen-atom transfers, and catalyst separation/reaction energies.

Group one: aluminum(III), chromium(III)

Group one comprises the best catalysts under the reaction conditions, for example, Al³⁺ and Cr³⁺, which yield 13–19% HMF and have high conversions of 88–99%. Analysis of their reactions should help us with finding criteria for good conversion.

For Al³⁺ and Cr³⁺, the catalysts [M(H₂O)₆]³⁺, [MO¹O²(H₂O)₄]³⁺, [MO¹O²(H₂O)₃OH]²⁺, [MO¹O²(H₂O)₃Cl]²⁺, and [M₂O¹O²(H₂O)₇OH]⁵⁺ were investigated. Reaction pathways with species [MO¹O²(H₂O)₂Cl₂]⁺ and [MO¹O²(H₂O)Cl₃] were only calculated for the chromium(III) cation. Under the reaction conditions aluminum(III) complexes with water ligands and chromium(III) complexes with one to three chloride ligands are most likely to appear. Deprotonated and dimeric complexes are also common for both metal cations in water.

Both metal complexes have similar Brønsted acidities (pK_a = 4.1 (Cr³⁺) and 5.5 (Al³⁺) in water) and both are regarded as hard Lewis acids.

Proton transfer

The proton transfer PT₁ was feasible for all Al³⁺ and Cr³⁺ complexes (Table 2). Low energies of 13–20 kcal mol⁻¹ were found for the [M(H₂O)₆]³⁺, [MO¹O²(H₂O)₄]³⁺, and [MO¹O²(H₂O)₆Cl₆]ⁿ⁺ pathways. In the [MO¹O²(H₂O)₃OH]²⁺ system, the barriers rise to 25 and 30 kcal mol⁻¹ for M = Cr³⁺ and Al³⁺, respectively. In general, PT₁ is higher in energy for the unbound catalyst

Table 2. Relative free energies [kcal mol⁻¹] at 298 K and 1 atm for critical steps (PT₁, TS₂, product/catalyst separation (sep.), and reaction energy for the complexed glucopyranose–fructofuranose (gluc.–fruc.) conversion) in the glucose–fructose isomerization with Al³⁺ and Cr³⁺ catalysts. PBE0/6-31 + G**, CPCM (water).

Catalyst	ΔΔG(PT ₁)	ΔΔG(TS ₂)	ΔΔG(sep.)	ΔΔG(gluc.–fruc.)
[Al(H ₂ O) ₆] ³⁺	17.0	29.2	9.4	-3.1
[AlO ¹ O ² (H ₂ O) ₄] ³⁺	13.3	23.0	15.4	-16.2
[AlO ¹ O ² (H ₂ O) ₃ OH] ²⁺	30.1	41.0	17.7	-14.1
[AlO ¹ O ² (H ₂ O) ₃ Cl] ²⁺	13.2	23.1	13.0	-11.8
[Al ₂ O ¹ O ² (H ₂ O) ₇ OH] ⁵⁺	-	40.1	-	-
[Cr(H ₂ O) ₆] ³⁺	13.9	26.9	13.0	-7.2
[CrO ¹ O ² (H ₂ O) ₄] ³⁺	16.2	18.0	18.3	-17.5
[CrO ¹ O ² (H ₂ O) ₃ OH] ²⁺	25.4	34.2	14.4	-10.9
[CrO ¹ O ² (H ₂ O) ₃ Cl] ²⁺	16.2	25.9	17.0	-13.5
[CrO ¹ O ² (H ₂ O) ₂ Cl ₂] ⁺	17.4	32.4	12.7	-8.0
[CrO ¹ O ² (H ₂ O)Cl ₃]	19.7	31.7	6.8	-4.3
[Cr ₂ O ¹ O ² (H ₂ O) ₇ OH] ⁵⁺	-	36.2	-	-

$[M(H_2O)_6]^{3+}$ and for complexes with non-water ligands compared to $[MO^1O^2(H_2O)_4]^{3+}$.

This can be explained by the diminished Brønsted acidity of O1 due to negatively charged ligand L^- in the metal cation ($[MO^1O^2(H_2O)_3OH]^{2+}$) and/or by the longer distance between the metal cation and the transferred proton ($[M(H_2O)_6]^{3+}$). The hydroxyl ligand has a stronger influence on the energy than the chloride ligand. The hydroxyl group oxygen atom should be a better σ - and π -electron donor than Cl^- because of the shorter M–L bond length (M–L = 1.79 and 2.19 Å for $[AlO^1O^2-(H_2O)_3OH]^{2+}$ and $[AlO^1O^2(H_2O)_3Cl]^{2+}$, respectively). Therefore, hydroxyl ligands diminish the Brønsted acidity more effectively than chloride ligands.

Hydrogen transfer

TS_2 is the rate-determining step for all catalysts in group one with $\Delta\Delta G(TS_2) = 18\text{--}41 \text{ kcal mol}^{-1}$. Only for $[CrO^1O^2(H_2O)_4]^{3+}$ is the product/catalyst separation energy in the same energy range as the TS_2 barrier.

The $[AlO^1O^2(H_2O)_3OH]^{2+}$ and $[Al_2O^1O^2(H_2O)_7OH]^{5+}$ catalyzed reactions are not feasible, with barriers around 40 kcal mol^{-1} for TS_2 ; all other aluminum(III) systems and the chromium(III)-catalyzed reactions are feasible. Only the TS_2 barrier for the dimer $[Cr_2O^1O^2(H_2O)_7OH]^{5+}$ is rather hard to overcome ($\Delta G(TS_2) = 36 \text{ kcal mol}^{-1}$). With more chloride ligands, the TS_2 barrier increases: 18.0 ($[CrO^1O^2(H_2O)_4]^{3+}$) < 25.9 ($[CrO^1O^2-(H_2O)_3Cl]^{2+}$) < 32.4 ($[CrO^1O^2(H_2O)_2Cl_2]^{+}$) $\approx 31.7 \text{ kcal mol}^{-1}$ ($[CrO^1O^2-(H_2O)_3Cl_3]$). Even more extreme is the rise in energy for the OH^- ligand, which increases the energy of TS_2 for aluminum(III) and chromium(III) catalysts by $16\text{--}18 \text{ kcal mol}^{-1}$ relative to $[MO^1O^2(H_2O)_4]^{3+}$.

Compared to water ligands, the higher TS_2 barrier in the case of OH^- and Cl^- ligands can be attributed to their negative charge and stronger σ - and π -electron donation, which diminishes the Lewis acidity of the metal complex. The lower acidity leads to less stabilization of the hydrogen-atom transfer, which can also be seen from geometry and NBO data (see below). We discuss three major effects: M–O1/2 bond elongation, reduced charge at M, and increased occupancy of the orbitals of M.

The introduction of OH^- and Cl^- ligands results in longer $M\cdots H_2O$ and $M\cdots O1/O2$ distances, which is expected due to the inductive effect of the negatively charged ligand(s) (Figure 2). For the Cl^- ligand, an increase of the $Al\cdots O2$ distance by 0.1 \AA is observed relative to the $[AlO^1O^2(H_2O)_4]^{3+}$ complex. Introduction of the OH^- ligand in $[CrO^1O^2(H_2O)_3OH]^{2+}$ leads to an increase of $\Delta d(Cr\cdots O2) = 0.2 \text{ \AA}$ compared to $[CrO^1O^2(H_2O)_4]^{3+}$. This elongation can be explained by the *trans* effect and the change in the nature of the ligand: water ligands are only weak σ -bonding ligands, whereas Cl^- and OH^- are σ - and potential π -donors. The latter anionic ligands shift more electron density to the metal center and weaken preferably the bonds in the *trans* position. With non-water ligands in axial or multiple positions the effect on the bond length is less pronounced, but the TS_2 energy still rises due to the higher electron density on the metal cation. Additionally, the cation is less capable of

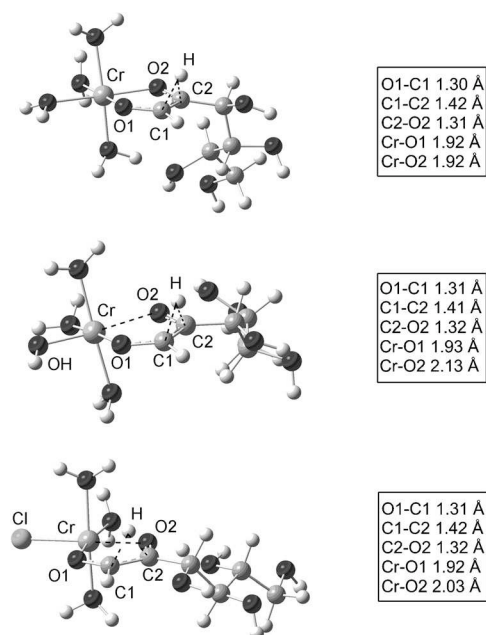


Figure 2. Hydrogen-atom transfer (TS_2) for (top) $[CrO^1O^2(H_2O)_4]^{3+}$, (middle) $[CrO^1O^2(H_2O)_3OH]^{2+}$ and (bottom) $[CrO^1O^2(H_2O)_3Cl]^{2+}$. PBE0/6-31+G**, CPCM (water).

accepting negative charge from the broken C–H bond because it has already taken up electron density from the ligands [natural charge on Cr: $1.18e$ ($[CrO^1O^2(H_2O)_4]^{3+}$) > $0.89e$ ($[CrO^1O^2-(H_2O)_3Cl]^{2+}$) > $0.59e$ ($[CrO^1O^2(H_2O)_2Cl_2]^{+}$)].

The TS_2 barriers increase with the electron density in the unoccupied d orbitals of the chromium(III) center (due to donation from the non-water ligands) and the d orbitals are destabilized, indicated by their orbital energies: $0.11e/-1.93 \text{ eV}$ ($[CrO^1O^2(H_2O)_4]^{3+}$), $0.14e/2.23 \text{ eV}$ ($[CrO^1O^2(H_2O)_3OH]^{2+}$), $0.12e/-0.27 \text{ eV}$ ($[CrO^1O^2(H_2O)_3Cl]^{2+}$), and $0.15e/0.49 \text{ eV}$ ($[CrO^1O^2-(H_2O)_2Cl_2]^{+}$). For aluminum(III), which does not have low-lying d orbitals, the π^*_{Al-O} orbitals are used instead (electron density in the π^*_{Al-O} orbitals rises by $0.01\text{--}0.07e$ for all bound catalysts $[MO^1O^2L_4]^{n+}$ relative to the unbound catalyst $[Al(H_2O)_6]^{3+}$).

Apparently, these explanations do not apply to the $[M_2O^1O^2-(H_2O)_7OH]^{5+}$ catalyzed reaction, which is not feasible even though the electronic structure is similar to $[MO^1O^2(H_2O)_4]^{3+}$. Its TS_2 structure (Figure 3) has a lengthened M–O1 bond to both metal centers (Cr: $\Delta d(Cr-O1) = +0.08 \text{ \AA}$ compared to $[CrO^1O^2-(H_2O)_4]^{3+}$) and a slightly shortened M–O2 bond (Cr: $\Delta d(Cr-$

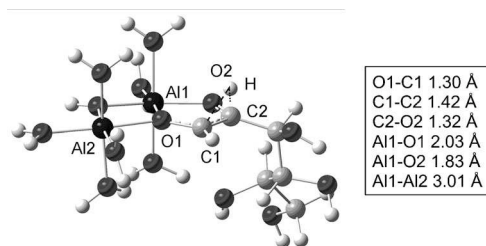


Figure 3. Hydrogen-atom transfer (TS_2) for $[Al_2O^1O^2(H_2O)_7OH]^{5+}$. PBE0/6-31+G**, CPCM (water).

O2) = -0.01 Å compared to [CrO¹O²(H₂O)₄]³⁺). Unlike all other TS₂ structures discussed above, the transferred hydrogen atom is closer to C2 than C1, which hints at an early transition state. Because the two positive metal centers repel each other, their distances to O1 must become longer. Therefore, the electron density is less stabilized in the C1–O1 orbitals and the hydrogen atom is bound to C2 instead of C1. The charge on both metal centers and the electron density in the π*_{Al–O} orbitals or *d* orbitals are nearly the same as for [MO¹O²(H₂O)₄]³⁺. Given these similarities in the electronic structure, the higher TS₂ energy does not stem from use of the dimer as the catalyst, but from the energy that is needed to form this dimer. For example, the glucose–catalyst complex is 26 kcal mol⁻¹ lower in energy with a monomeric rather than dimeric catalyst. The average dimer-formation energies for different doubly bridged aluminum(III) complexes were previously calculated to be 25–50 kcal mol⁻¹,^[26] and a CPMD simulation led to the separation of chromium(III) dimers into monomeric species.^[69] Also, no Al³⁺ dimer species was detected in our NMR experiments.

Catalyst separation, reaction energy

The catalyst/fructose separation is feasible for all catalysts (endothermic by 9–18 kcal mol⁻¹). It becomes more favorable when more chloride ligands are attached: 18.3 ([CrO¹O²(H₂O)₄]³⁺) > 17. ([CrO¹O²(H₂O)₃Cl]²⁺) > 12.7 ([CrO¹O²(H₂O)₂Cl₂]⁺) > 6.8 kcal mol⁻¹ ([CrO¹O²(H₂O)Cl₃]).

The energy difference between the glucopyranose–catalyst and fructofuranose–catalyst complexes is negative (exothermic) for all catalysts, but becomes less so as the number of chloride ligands increases: -17.5 ([CrO¹O²(H₂O)₄]³⁺) > -13.5 ([CrO¹O²(H₂O)₃Cl]²⁺) > -8.0 ([CrO¹O²(H₂O)₂Cl₂]⁺) > -4.3 kcal mol⁻¹ ([CrO¹O²(H₂O)Cl₃]). The separation energies and the energy differences for glucopyranose–fructofuranose conversion show that the complexes become less stable when non-water ligands are present.

Experimentally, the aluminum(III) and chromium(III) catalysts mediate the glucopyranose–fructofuranose transformation with 88–99% conversion. This is consistent with the computed barriers of 18–34 kcal mol⁻¹, which are high but still feasible at 413 K. According to the calculations, chloride or hydroxyl ligands have a significant impact on the reaction barriers. The more non-water ligands are attached to the catalyst, the higher the barriers PT₁ and TS₂ and the less exothermic the reaction. Another effect of non-water ligands is destabilization of the product complex.

Because Al³⁺ and Cr³⁺ are not prone to attract hydroxyl ligands (due to medium Brønsted acidity) and the reaction is still feasible with some chloride ligands (due to good Lewis acidity and empty *d* orbitals), the isomerization has high conversions with these catalysts.

Group two: iron(III), copper(II)

The criteria we found for group one were applied to less productive cations: the group two catalysts copper(II) and iron(III) with 3–6% HMF yield and a conversion rate of 12–23%.

For iron(III), we investigated the systems [Fe(H₂O)₆]³⁺, [FeO¹O²(H₂O)₄]³⁺, [FeO¹O²(H₂O)₃OH]²⁺, [FeO¹O²(H₂O)₂(OH)₂]⁺, [FeO¹O²(H₂O)₃Cl]²⁺, [FeO¹O²(H₂O)₂(OH)Cl]⁺, [FeO¹O²(H₂O)₂Cl₂]⁺, [FeO¹O²(H₂O)(OH)Cl₂], [FeO¹O²(H₂O)Cl₃], [FeO¹O²(OH)Cl₃]⁻, and [Fe₂O¹O²(H₂O)₇OH]⁵⁺. Most likely, iron(III) is present in the chloride complexes, the dimers, and the deprotonated species. For copper(II), different catalysts were found in water: [Cu(H₂O)₆]²⁺, [CuO¹O²(H₂O)₄]²⁺, [CuO¹O²L₂], and [CuO¹O²(H₂O)Cl]⁺. The ligands depend on the concentration of CuCl₂·2H₂O. Experimentally, a concentration of 19.9 g L⁻¹ was used, which seems low compared to the maximum solubility of 1150 g L⁻¹ in water at 20 °C.^[27] Therefore, copper(II) complexes with water ligands are expected to be preferred.

As can be seen from the diverse complexation preferences, iron(III) and copper(II) differ in their properties. Iron(III) complexes are hard Lewis acids with high Brønsted acidity (pK_a = 2.2), whereas copper(II) complexes are soft Lewis acids with low Brønsted acidity (pK_a = 8.0). Despite these differences both show low reactivity for the glucose to fructose conversion.

Proton transfer

The differences in Brønsted acidity become evident in the energies for PT₁ (Table 3). This step is feasible for most of the

Table 3. Relative free energies [kcal mol⁻¹] at 298 K and 1 atm for critical steps (PT₁, TS₂, product/catalyst separation, and reaction energy for the complexed glucopyranose–fructofuranose conversion) for the glucose–fructose isomerization with Fe³⁺ and Cu²⁺ catalysts. PBE0/6-31+G**, CPCM (water).

Catalyst	ΔΔG(PT ₁)	ΔΔG(TS ₂)	ΔΔG(sep.)	ΔΔG(gluc.–fruc.)
[Fe(H ₂ O) ₆] ³⁺	16.9	25.5	13.0	-7.1
[FeO ¹ O ² (H ₂ O) ₄] ³⁺	14.9	20.3	17.2	-17.9
[FeO ¹ O ² (H ₂ O) ₃ OH] ²⁺	18.0	32.3	13.1	-9.6
[FeO ¹ O ² (H ₂ O) ₂ (OH) ₂] ⁺	44.8	53.9	13.1	-4.3
[FeO ¹ O ² (H ₂ O) ₃ Cl] ²⁺	15.1	30.2	16.0	-10.7
[FeO ¹ O ² (H ₂ O) ₂ (OH)Cl] ⁺	30.1	42.0	13.8	-4.9
[FeO ¹ O ² (H ₂ O) ₂ Cl ₂] ⁺	15.9	35.4	11.5	-4.8
[FeO ¹ O ² (H ₂ O)(OH)Cl ₂]	39.1	51.6	9.5	-1.4
[FeO ¹ O ² (H ₂ O)Cl ₃]	19.3	31.7	3.0	0.0
[FeO ¹ O ² (HO)Cl ₃] ⁻	-	60.4	-	-
[Fe ₂ O ¹ O ² (H ₂ O) ₇ OH] ⁵⁺	-	31.1	-	-
[Cu(H ₂ O) ₆] ²⁺	-	36.4	4.5	-2.3
[CuO ¹ O ² (H ₂ O) ₄] ²⁺	-	36.5	6.1	-2.1
[CuO ¹ O ² (H ₂ O) ₂] ²⁺	20.1	38.2	10.5	-1.6
[CuO ¹ O ² (H ₂ O)Cl] ⁺	20.2	43.3	6.6	0.1
[CuO ¹ O ² Cl ₂]	28.5	42.7	8.3	0.6

iron(III) catalysts (uphill by 15–30 kcal mol⁻¹) and unfeasible only for [FeO¹O²(H₂O)₂(OH)₂]⁺ and [FeO¹O²(H₂O)₂(OH)Cl₂] (uphill by 39–45 kcal mol⁻¹). Iron(III) behaves similarly to chromium(III) with regards to energy trends and their explanations for PT₁: the more non-water ligands attached to the cation, the lower the Brønsted acidity and the higher the PT₁ barrier (see group one, above).

The PT₁ energies for copper(II) complexes range from 20–30 kcal mol⁻¹ and are, therefore, slightly higher than those for the previously discussed Al³⁺, Cr³⁺, and Fe³⁺ catalysts with simi-

lar ligands, due to the generally lower Brønsted acidity of the copper(II) complexes. PT_1 could not be calculated for $[Cu(H_2O)_6]^{2+}$ and $[CuO^1O^2(H_2O)_4]^{2+}$, because water ligands dissociated during the calculation of the thermodynamic cycle (see the Supporting Information).

Hydrogen transfer

As for group one, TS_2 is the rate-determining step. For iron(III) complexes with only water ligands ($[Fe(H_2O)_6]^{3+}$ and $[FeO^1O^2(H_2O)_4]^{3+}$) the energy for the isomerization is as low as for aluminum(III) and chromium(III) complexes ($\Delta\Delta G(TS_2) = 20\text{--}25\text{ kcal mol}^{-1}$). For catalysts with chloride or hydroxyl ligands, the TS_2 energy is in the range $30\text{--}35\text{ kcal mol}^{-1}$, slightly higher than for the corresponding group one catalysts with one or two chloride ligands ($[MO^1O^2(H_2O)_3Cl]^{2+}$: 25.9 (Cr) versus $30.2\text{ kcal mol}^{-1}$ (Fe); $[MO^1O^2(H_2O)_2Cl_2]^{+}$: 32.4 (Cr) versus $35.4\text{ kcal mol}^{-1}$ (Fe)). As for chromium(III) catalysts, the TS_2 energy rises further when more chloride or hydroxyl ligands are present. If the complex contains two hydroxyl ligands or both hydroxyl and chloride ligands, the TS_2 barrier exceeds 40 kcal mol^{-1} and the reaction becomes unfeasible.

In the case of copper(II) catalysts, the TS_2 energies with one or two chloride ligands are also too high ($38\text{--}43\text{ kcal mol}^{-1}$). Reactions with the catalysts $[Cu(H_2O)_6]^{2+}$ and $[CuO^1O^2(H_2O)_4]^{2+}$ are barely feasible because they have barriers of $36\text{--}37\text{ kcal mol}^{-1}$.

The reasons for the increased TS_2 energies for catalysts with non-water ligands and for the dimeric catalyst are analogous to those discussed for the chromium(III) catalysts. We find an elongated M–O2 bond for the monomeric catalysts if chloride or hydroxyl ligands are attached (Figure 4). Here, the M–O2

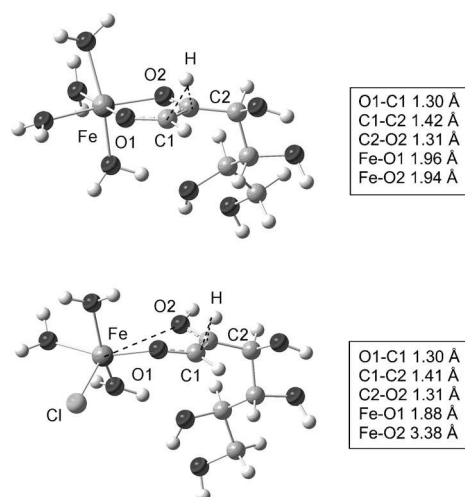


Figure 4. Hydrogen-atom transfer (TS_2) for (top) $[FeO^1O^2(H_2O)_4]^{3+}$ and (bottom) $[FeO^1O^2(H_2O)_3Cl]^{2+}$. PBE0/6-31 + G**, CPCM (water).

bond is not simply weakened, but broken with M...O2 distances of 2.81 ($[FeO^1O^2(H_2O)_2Cl_2]^{+}$), 2.97 ($[CuO^1O^2L_2]$), and 3.38 Å ($[FeO^1O^2(H_2O)_3Cl]^{2+}$). After cleavage of the M–O2 bond, the metal cation no longer has octahedral coordination but adopts a roughly pentacoordinate structure, which leads to lower d

orbitals in the $x\text{--}y$ plane and higher d orbitals with z -axis contributions. Because each iron(III) d orbital is occupied by one electron, additional electron density from the hydrogen transfer is partly shifted to the $4s^*$ and $4p^*$ orbitals. However, unlike the group one case, catalysts with chloride ligands do not have higher electron density in the antibonding orbitals. Instead, the population in the s^* orbitals is higher for the $[FeO^1O^2(H_2O)_4]^{3+}$ than the $[FeO^1O^2(H_2O)_3Cl]^{2+}$ catalyst (0.15e/0.24 eV and 0.10e/0.16 eV, respectively). The reason for the higher population might be that the M–O2 bond is still present in $[FeO^1O^2(H_2O)_4]^{3+}$ but is broken in $[FeO^1O^2(H_2O)_3Cl]^{2+}$. The orbital energies show that it is energetically expensive to put electron density into virtual orbitals. Additionally, the charge on the metal cation is decreased [natural charge on Fe: 1.39e ($[FeO^1O^2(H_2O)_4]^{3+}$) > 1.31e ($[FeO^1O^2(H_2O)_3Cl]^{2+}$) > 0.61e ($[FeO^1O^2(H_2O)_2Cl_2]^{+}$)]. The situation for copper(II) complexes is analogous to that for iron(III) complexes with axial ligands (or with both OH^- and Cl^- ligands).

The substitution of water ligands with hydroxyl or chloride ligands may have a larger effect on iron(III) and copper(II) than on chromium(III) because for copper(II) and iron(III) all d orbitals are filled with one or two electrons according to ligand field theory for quadratic planar and octahedral complexes, respectively (high-spin complexes). Therefore, there is no vacant low-energy metal orbital that can accept additional electron density from the transferred hydrogen atom and, hence, the M–O2 bond is broken.

The broken M–O2 bond in complexes with non-water ligands creates another problem for the group two catalysts. Because the reaction is performed under high pressure, a transition state with a higher volume should be less favorable. Under high pressure the M...O2 bond distance will probably shrink, which will tend to raise the barrier because more electron density is donated into the already filled d orbitals and the high-energy s^* orbitals of the metal cations.

For the iron(III) dimer, the TS_2 energy is as low as for the monomeric complex. Unlike the cases of aluminum(III) and chromium(III), complex formation through deprotonation of water ligands is favorable for iron(III) due to the high acidity of its complexes. Iron(III) dimers bound to glucose molecules were also found experimentally.^[28]

Catalyst separation, reaction energy

The separation of the catalyst from fructofuranose is endothermic in all cases. The separation becomes easier for the iron(III) catalysts when more chloride and hydroxyl ligands are attached: 17.2 ($[FeO^1O^2(H_2O)_4]^{3+}$) > 16.0 ($[FeO^1O^2(H_2O)_3Cl]^{2+}$) > 11.5 ($[FeO^1O^2(H_2O)_2Cl_2]^{+}$) > 3.0 kcal mol^{-1} ($[FeO^1O^2(H_2O)Cl_3]$). No such trend was found for copper(II) complexes. Analogously to chromium(III), the difference in free energy between the gluco-pyranose and fructofuranose complexes was negative for most iron(III) catalysts. However, with an increasing number of chloride ligands, the reaction becomes less exoergic (for $[FeO^1O^2(H_2O)Cl_3]$ and $[CuO^1O^2(H_2O)Cl]^{+}$ $\Delta\Delta G(\text{glucose-fructose}) = 0\text{ kcal mol}^{-1}$).

The lower HMF yields and conversions for group two catalysts can be explained on the basis of this data. The iron(III)-catalyzed isomerization does not have similar barriers to the chromium(III)-catalyzed reaction because the higher Brønsted acidity of the Fe^{III} complexes prevents the formation of advantageous ligand systems. In water, a pK_a value of 2.2 and strong Lewis acidity favors coordination of multiple hydroxyl and chloride ligands to the metal cation, which raises the TS₂ barrier. Furthermore, the high-spin nature of the iron(III) catalysts leads to breaking of the M–O2 bond in the rate-determining transition state TS₂, which will disfavor the reaction at high pressure.

For copper(II) the problem is rather the low Lewis acidity. Even though only water ligands are present at low concentrations of copper(II) complexes, the TS₂ barrier is high (around 36 kcal mol⁻¹).

In summary, the disadvantages of the group two relative to the group one metal cations arise from their Lewis acidity (either too high or too low) and from their high-spin electronic structure.

Group three: magnesium(II), uncatalyzed

For group three we may expect similar reasons for the low reactivity as for the group two cations. We examined the uncatalyzed reaction and the magnesium(II)-catalyzed reactions.

For magnesium(II), the catalysts [Mg(H₂O)₆]²⁺ and [MgO¹O²(H₂O)₄]²⁺ were investigated (Table 4). Magnesium(II) complexes

Table 4. Relative free energies [kcal mol⁻¹] at 298 K and 1 atm for critical steps (PT₁, TS₂, product/catalyst separation, and reaction energy for the complexed glucopyranose–fructofuranose conversion) for the glucose–fructose isomerization catalyzed by Mg²⁺ complexes and for the uncatalyzed reaction. PBE0/6-31 + G**, CPCM (water).

Catalyst	ΔΔG(P _{T1})	ΔΔG(T _{S2})	ΔΔG(sep.)	ΔΔG(gluc.–fruc.)
[Mg(H ₂ O) ₆] ²⁺	33.7	40.1	-0.4	-0.3
[MgO ¹ O ² (H ₂ O) ₄] ²⁺	25.5	35.1	7.4	-5.2
uncatalyzed	38.1	78.2	1.5	1.5

are hard Lewis acids, but weak Brønsted acids (pK_a=11.4). Most likely the [Mg(H₂O)₆]²⁺ complex is present; it was found experimentally that magnesium(II) does not attach glucose as a ligand.^[29] The uncatalyzed reaction has only water (pK_a=15.7) to stabilize its intermediates.

In all of the group three reaction pathways, the reactions via PT₁/TS₁ are concerted because the O5-protonated intermediate is not sufficiently stabilized and the C1–O5/C2–O5 bond opens immediately upon protonation of the pyranic oxygen. Whereas a proton is detached in the uncatalyzed reaction before reaching TS₂, it is energetically preferable for the [Mg(H₂O)₆]²⁺ and [MgO¹O²(H₂O)₄]²⁺ catalyzed pathways to retain the proton on O2 until after TS₂.

Proton transfer

PT₁ is high in energy for the uncatalyzed reaction (38 kcal mol⁻¹) and for the two magnesium(II) catalysts with (26 and 34 kcal mol⁻¹ for [MgO¹O²(H₂O)₄]²⁺ and [Mg(H₂O)₆]²⁺, respectively). Due to the low Brønsted acidity, this step requires more energy than for other catalysts with water ligands. Thus, the proton transfers are already close to the limit of what is feasible under the reaction conditions.

Hydrogen transfer

Even higher barriers were found for the rate-determining step via TS₂: 78 (uncatalyzed), 40 ([Mg(H₂O)₆]²⁺), and 35 kcal mol⁻¹ ([MgO¹O²(H₂O)₄]²⁺).

In the [MgO¹O²(H₂O)₄]²⁺ catalyzed reaction, the structure of TS₂ is similar to those for the iron(III)- and copper(II)-chloride catalysts, and different from those for the aluminum(III) and chromium(III) cases (Figure 5). The M–O2 bond is broken

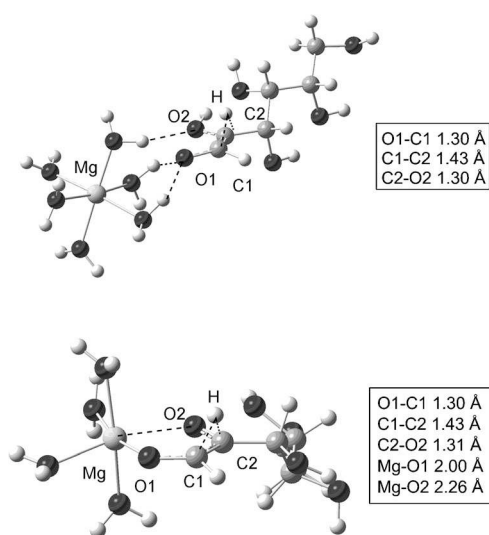


Figure 5. Hydrogen-atom transfer (TS₂) for the (top) hydrogen-bonded catalyst [Mg(H₂O)₆]²⁺ and (bottom) glucose-bonded catalyst [MgO¹O²(H₂O)₄]²⁺. PBE0/6-31 + G**, CPCM (water).

(2.26 Å), whereas the M–O1 bond is still intact (2.00 Å). This TS₂ structure should also be less favorable under the reaction conditions of 60 bar because of the large M···O2 distance. The donation of electron density into antibonding orbitals is even higher than for [FeO¹O²(H₂O)₄]³⁺ (0.18e in 4s*): 0.22e are found in the s* orbital (7.07 eV) of [MgO¹O²(H₂O)₄]²⁺, with a similar value for [Mg(H₂O)₆]²⁺. There is no analogous occupation of an s* orbital in the aluminum(III) catalysts, which also lack d orbitals. Apparently, the acidity is too low to stabilize the electron density in this case, which explains why the magnesium(II) catalyst with only water ligands has the highest TS₂ barrier of all the [M(H₂O)₆]²⁺ complexes studied.

Moreover, this might rationalize why the association of glucose hydroxyl groups or other non-water ligands is unfavorable for magnesium(II) relative to the other metal catalysts. If

water ligands with their weak σ donation can already fill anti-bonding orbitals, ligands with stronger σ -donation ability will destabilize the complex even more so that the complexation of glucose by magnesium(II) becomes unfavorable. However, this is not reflected in the energy of the glucopyranose– $[\text{MgO}^1\text{O}^2(\text{H}_2\text{O})_4]^{2+}$ complex, which lies below the separated catalyst and glucopyranose thanks to the entropic contribution ($\Delta G = -0.7 \text{ kcal mol}^{-1}$, $\Delta H = 5.9 \text{ kcal mol}^{-1}$), whereas the formation of glucopyranose– $[\text{Mg}(\text{H}_2\text{O})_6]^{2+}$ is endoergic ($\Delta G = 2.1 \text{ kcal mol}^{-1}$, $\Delta H = -9.8 \text{ kcal mol}^{-1}$).

Catalyst separation, reaction energy

The separation of the fructose complex is barely exoergic for $[\text{Mg}(\text{H}_2\text{O})_6]^{2+}$ and is endoergic for $[\text{MgO}^1\text{O}^2(\text{H}_2\text{O})_4]^{2+}$. For the latter complex, the glucose–fructose conversion is slightly exoergic ($\Delta G = -5.2 \text{ kcal mol}^{-1}$), whereas the uncatalyzed reaction is endoergic by $1.5 \text{ kcal mol}^{-1}$. Thus, the metal catalyst affords stabilization of the final product complex, which may help prevent the formation of side products.

In summary, the main problem of the magnesium(II) complexes is their low acidity and the missing association of the hydroxyl groups of glucopyranose, which renders the reaction inefficient. Unlike for the group two catalysts, non-water ligands are not a problem in this case.

Analysis of PT_1 and TS_2 energies

Further to the discussion of the individual metal cations (and their complexes) and explanation of their reactivity, we present a general comparison between the three groups. To provide a better overview of the influence of the acidity and the ligand systems on the critical steps, PT_1 (deprotonation of O1 and protonation of O5) and TS_2 , the computed relative free energies are related to the experimental $\text{p}K_a$ values (Figure 6).

Proton transfer

The $\text{p}K_a$ value of the metal cation in water is plotted against the deprotonation energy of O1 in PT_1 (Figure 6, ●) for the $[\text{MO}^1\text{O}^2(\text{H}_2\text{O})_4]^{n+}$ mechanism. As expected, lower energies were found for lower $\text{p}K_a$ values. However, comparison of iron(III) to aluminum(III) ($\Delta\text{p}K_a = 3.3$) shows that the deprotonation energy is only slightly lower for iron(III) ($\Delta\Delta G(\text{PT}_1\text{-deprot}) = 0.7 \text{ kcal mol}^{-1}$). The corresponding energy gain from copper(II) to aluminum(III) ($\Delta\text{p}K_a = 2.5$) is distinctively larger ($\Delta\Delta G(\text{PT}_1\text{-deprot}) = 6.2 \text{ kcal mol}^{-1}$).

The influence of the metal complex on the protonation of O5 in PT_1 was also plotted (Figure 6, ■). Compared to the uncatalyzed reaction, the protonation energy rises with decreasing $\text{p}K_a$ values, but the influence of the metal cation is less ap-

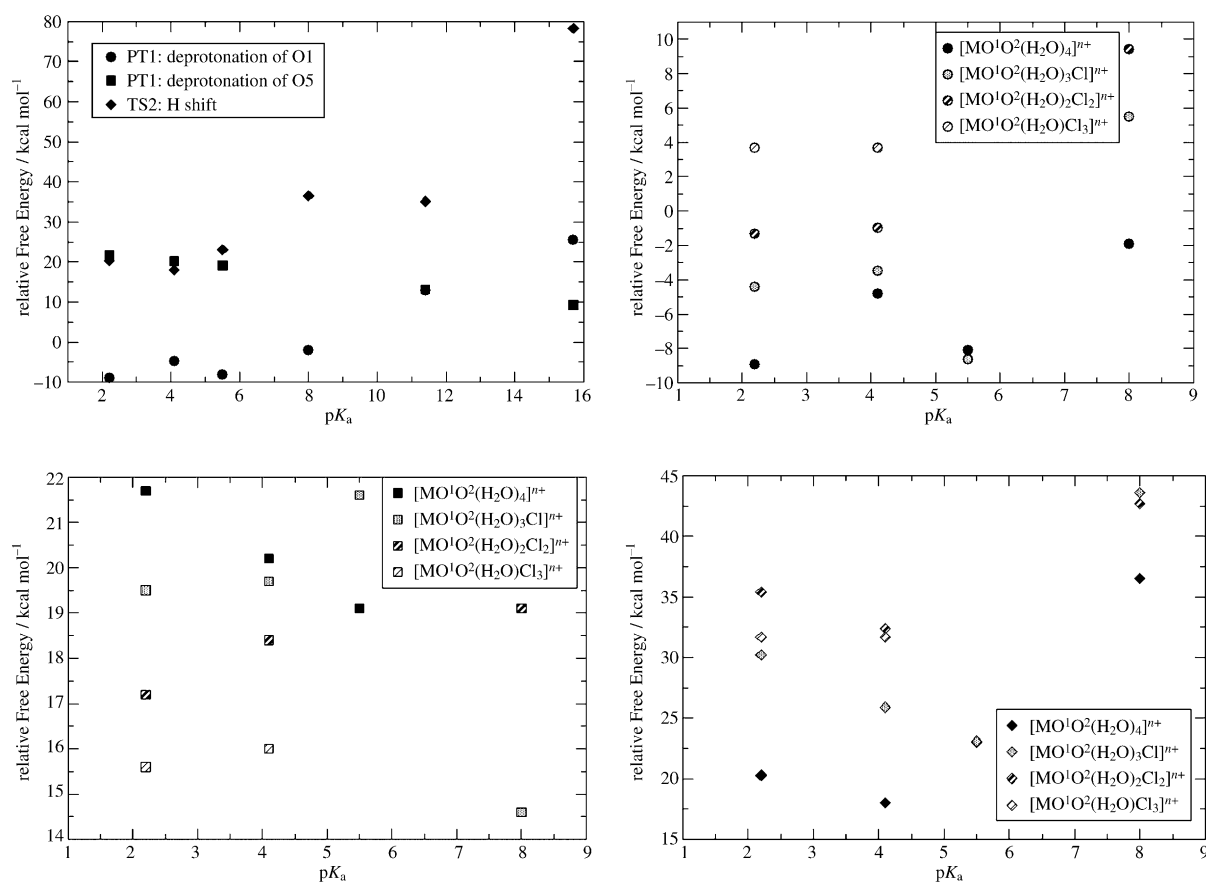


Figure 6. Relative free energy of the PT_1 (O1 deprotonation (●), O5 protonation (■)) and TS_2 steps (◆) for $[\text{MO}^1\text{O}^2(\text{H}_2\text{O})_a]^{n+}$ (top, left) and $[\text{MO}^1\text{O}^2(\text{H}_2\text{O})_{4-a}\text{Cl}_a]^{n+}$, $a = 0-3$ (top, right and bottom). $\text{p}K_a$ of metal complex: $\text{Fe}^{3+} = 2.2$, $\text{Cr}^{3+} = 4.1$, $\text{Al}^{3+} = 5.5$, $\text{Cu}^{2+} = 8.0$, $\text{Mg}^{2+} = 11.4$, water = 15.7. PBE0/6-31 + G**, CPCM (water).

parent than in the case of deprotonation. Acidic metal cations that also have a high Lewis acidity better stabilize the deprotonated O1 atom of the glucopyranose complex. This results in a longer C1–O1 and a shorter C1–O5 bond, which makes it harder to protonate O5 [(C1–O5 bond lengths = 1.41 (uncatalyzed) > 1.38 ([MgO¹O²(H₂O)₄]²⁺) > 1.35 ([AlO¹O²(H₂O)₄]³⁺) ≈ 1.35 ([CrO¹O²(H₂O)₄]³⁺) ≈ 1.36 Å ([FeO¹O²(H₂O)₄]³⁺)]. Again, the difference between the cations iron(III) and aluminum(III) is rather small when the difference in their p*K*_a values is considered (ΔΔ*G*(PT₁-prot) = 2.6 kcal mol⁻¹), whereas 5.9 kcal mol⁻¹ are gained for aluminum(III) versus copper(II).

Hydrogen transfer

Analogously to the deprotonation of O1, the TS₂ barrier is lower for metal complexes with a lower p*K*_a value (Figure 6, ♦). For p*K*_a < 6 the change in transition-state energy is less pronounced than for higher p*K*_a values. For example, 13.5 kcal mol⁻¹ are gained when going from Cu²⁺ to Al³⁺ (Δp*K*_a = 2.5), whereas only 2.7 kcal mol⁻¹ are gained between Al³⁺ and Fe³⁺ (Δp*K*_a = 3.3).

The same analysis has been performed for ligand systems with 0–3 chloride ligands (Figure 6). Chloride ligands increase the energy for the deprotonation of O1 and for TS₂, but slightly lower the energy for the protonation of O5. This is to be expected because chloride ligands lower the Brønsted and Lewis acidity of the catalysts. The same holds for hydroxyl ligands.

It seems that once a certain Lewis and Brønsted acidity is reached (p*K*_a = 4–6), the influence of the metal cation on a given ligand system is small and a limit of improvement is approached. Low yields for acidic catalysts below this p*K*_a threshold must be explained by other factors, for example, their ligand system or electron configuration. Catalysts with lower p*K*_a values can also access other pathways (mainly proton catalyzed).

We conclude that aluminum(III) and chromium(III) cations work successfully for the reaction, because their Brønsted and Lewis acidity is high enough to catalyze the PT₁ and TS₂ steps well, but not so high that they would exist mainly in their deprotonated form and attract multiple chloride ligands. These cations also have empty orbitals, which allows them to accept electron density during the reaction (when needed). On the other hand, iron(III) seems to be too acidic, thus favors complexes with too many hydroxyl and chloride ligands, and its prevalent high-spin complexes are not well suited to act as electron acceptors. Copper(II) and magnesium(II) do not have sufficient Lewis acidity to be effective.

To conclude this report, we return to the experimental results. More metal cations were investigated experimentally than were explored in the computational study, thus we checked if our qualitative notions could rationalize the results for these additional cations.

Zirconium(IV) is a group one cation (high conversion, but only 5% HMF) with a p*K*_a value of –0.3 and empty *d* orbitals. In aqueous solution, zirconium(IV) has the coordination number 8 and is coordinated by water and hydroxyl ligands.^[22] The high Brønsted acidity should hinder the reaction, whereas

the empty *d* orbitals appear perfectly suited for the reaction. Because zirconium(IV) has a high conversion rate but only a low HMF yield [similar to copper(II) and iron(III)] and a high yield of LA, we assumed, in view of the strong Brønsted acidity of the cation complex, that the reaction is acid catalyzed and thus takes a pathway different from the one described in this study; there may also be subsequent acid-catalyzed reactions that reduced the yield of HMF.

Bismuth(III) is a group two cation. Experimentally, the cation is coordinated in water with three hydroxyl and three water ligands at pH 7.^[22] Its strong Brønsted acidity makes it likely that the reaction again follows proton-catalyzed pathways.

Comparison with previous computational studies

The only previous study performed in water^[69] employed CPMD simulations to investigate two Cr³⁺ species [Cr(H₂O)₅OH]²⁺ together with one glucose molecule in a box of water. Similar to our case, the first solvation shell around the metal cation consisted of six oxygen atoms, with the O1 and O2 hydroxyl groups of glucose able to bind to the metal cation. For the monomeric complex, an association with glucose was found to be more favorable than a hydrogen-bonding interaction. The dimeric catalyst complex did not coordinate to glucose, but separated into two monomers during the course of the simulation. These results are in agreement with our findings of an unfavorably high energy for dimer formation and higher TS₂ barriers for chromium(III) dimers compared to monomers. However, there are also differences. In the previous study,^[69] a metal complex with one hydroxyl ligand was proposed as the active catalyst. The hydroxyl ligand was reported to deprotonate O2 before TS₂ and to protonate O1 after TS₂, analogous to our findings for the proton transfers DP₂ and RP₂. From an Arrhenius plot, the activation energy was estimated to be 15 kcal mol⁻¹ at 413 K. In our calculations for a reasonable analogue, the [CrO¹O²(H₂O)₃OH]²⁺ catalyst, the deprotonation step PT₂ (after TS₂) was found to require less energy than the steps DP₂, TS₂, and RP₂. Using thermodynamic cycles to treat the proton transfers, we arrived at an activation barrier of 34 kcal mol⁻¹ for the rate-determining step, with the hydrogen transfer alone already requiring an activation of 27 kcal mol⁻¹ (relative to an open-chain glucose molecule). Because our experiments detected only slow or no conversion at temperatures lower than 120 °C, barriers around 30 kcal mol⁻¹ would seem reasonable, whereas a barrier of 15 kcal mol⁻¹ could already be easily overcome at room temperature. There is no clear explanation for the large difference between the two computed activation energies (except for noting the obvious, namely that the chosen computational procedures are quite different).

All other previous computational studies were carried out in ionic liquids.^[7,8] In these solvents, there are different active species (MCl₄²⁻), and imidazole cations and chloride ligands are assumed to support the reaction, unlike the situation in water.^[16] Therefore, the chemistry and the barriers are expected to be different in these systems (see the Supporting Information for further comments).

There have also been many studies on the proton-catalyzed reactions.^[5b,c,6d,e,10] They conclude that under highly acidic conditions different hydroxyl groups of glucopyranose, which are more basic than the pyranic oxygen, can be protonated.^[30] After such protonation, the water moieties formed can leave as neutral species, followed by a cationic rearrangement of the pyranose ring to give different products. These results are relevant for metal complexes that act as a Brønsted acid rather than a Lewis acid because these proton-catalyzed pathways can lead to HMF without a fructose intermediate.^[8b]

Conclusion

We calculated the preferred mechanism for the uncatalyzed and metal-catalyzed glucose–fructose isomerization in water by using DFT. This allowed us to rationalize many of the available experimental results and suggest criteria for an effective catalyst.

Metal cations with moderate Lewis acidity and moderate Brønsted acidity ($pK_a=4-6$) are good catalysts. Ideally, they have only water ligands attached, or ligands further up the spectrochemical series that are weak σ donors and can accept π back donation (e.g. CN^- and CO). The ligands should be moderately strong π acceptors at most; π -acceptor ligands will increase the ligand field separation and, thus, may hinder acceptance of electron density during the hydrogen-transfer step of the reaction. Bad ligands are strong σ - and π -donors, such as halogenides. Low-lying unoccupied orbitals that can accept electron density, for example, unoccupied metal d orbitals are helpful. It is also an advantage if the metal complex allows co-ordination of glucose as a ligand because this lowers the energy relative to catalysts with hydrogen bonding to glucose.

Aluminum(III) and chromium(III) fulfill these criteria, hence, they yield more HMF than iron(III), copper(II), and magnesium(II). Dimeric catalysts are less effective because the energy for complex formation is high for aluminum(III) and chromium(III) and it is entropically less favorable for glucose to meet two metal cations rather than one. The high temperature of the experiments is necessary to overcome the computed barriers for the different catalysts investigated (20–35 kcal mol⁻¹).

Experimental Section

The reactions were carried out as follows: glucose (0.616 mmol) and catalyst (0.070 mmol) were dissolved in distilled water (3 mL). The reaction vessel was placed in an autoclave (22 mL) with a glass inlet. The autoclave was closed and filled with nitrogen (60 bar), then depressurized to expel oxygen. The autoclave was filled again with nitrogen (60 bar) and heated to 413 K with stirring. The reaction mixture was stirred at 413 K for 1 h. The reaction was stopped by letting the autoclave cool down rapidly in an ice bath. The experiment was repeated several times with different catalysts and the yields were reproduced within analytical accuracy.

The products were analyzed by HPLC by using a Shimadzu instrument equipped with a Shimadzu CBM-20A controller, an organic acid resin column (300 × 8 mm), two pumps (Shimadzu LC-20AB & LC-20AD), an auto injector (Shimadzu SIL-20AC), and a column oven (Shimadzu CTO-20A). HMF was detected with a UV detector

(Shimadzu SPD-M20A & SPD-M30A). All other compounds were analyzed with a refractive index (RI) detector (Shimadzu LC-10A). Tri-fluoroacetic acid (2 mM) in water was used as the eluent at 40 °C with a flow rate of 1.0 mL min⁻¹.

Acknowledgements

Financial support from the research cluster Sustainable Chemical Synthesis—A Systems Approach (SusChemSys) is acknowledged. SusChemSys is co-financed by the European Regional Development Fund (ERDF) and the state of North Rhine-Westphalia, Germany, under the Operational Program Regional Competitiveness and Employment 2007–2013.

Keywords: biomass • computer chemistry • Lewis acids • reaction mechanisms • sustainable chemistry

- [1] G.-H. Wang, J. Hilgert, F. H. Richter, F. Wang, H.-J. Bongard, B. Spliethoff, C. Weidenthaler, F. Schüth, *Nat. Mater.* **2014**, *13*, 293–300.
- [2] A. A. Rosatella, S. P. Simeonov, R. F. M. Frade, C. A. M. Afonso, *Green Chem.* **2011**, *13*, 754–793.
- [3] a) T. Ståhlberg, W. Fu, J. M. Woodley, A. Riisager, *ChemSusChem* **2011**, *4*, 451–458; b) G. Yong, Y. Zhang, J. Y. Ying, *Angew. Chem.* **2008**, *120*, 9485–9488; *Angew. Chem. Int. Ed.* **2008**, *47*, 9345–9348; c) S. Hu, Z. Zhang, J. Song, Y. Zhou, B. Han, *Green Chem.* **2009**, *11*, 1746–1749; d) H. Zhao, J. E. Holladay, H. Brown, Z. C. Zhang, *Science* **2007**, *316*, 1597–1600.
- [4] J. B. Binder, R. T. Raines, *J. Am. Chem. Soc.* **2009**, *131*, 1979–1985.
- [5] a) T. Wang, Y. J. Pagán-Torres, E. J. Combs, J. A. Dumesic, B. H. Shanks, *Top. Catal.* **2012**, *55*, 657–662; b) X. Qian, M. R. Nimlos, M. Davis, D. K. Johnson, M. E. Himmel, *Carbohydr. Res.* **2005**, *340*, 2319–2327; c) T. Ståhlberg, S. Rodríguez-Rodríguez, P. Frstrup, A. Riisager, *Chem. Eur. J.* **2011**, *17*, 1456–1464.
- [6] a) Y. Roman-Leshkov, J. N. Chheda, J. A. Dumesic, *Science* **2006**, *312*, 1933–1937; b) Y.-N. Li, J.-Q. Wang, L.-N. He, Z.-Z. Yang, A.-H. Liu, B. Yu, C.-R. Luan, *Green Chem.* **2012**, *14*, 2752–2758; c) S. Caratzoulas, D. G. Vlachos, *Carbohydr. Res.* **2011**, *346*, 664–672; d) R. S. Assary, P. C. Redfern, J. Greeley, L. A. Curtiss, *J. Phys. Chem. B* **2011**, *115*, 4341–4349; e) R. S. Assary, T. Kim, J. J. Low, J. Greeley, L. A. Curtiss, *Phys. Chem. Chem. Phys.* **2012**, *14*, 16603–16611; f) M. J. Antal, W. S. L. Mok, G. N. Richards, *Carbohydr. Res.* **1990**, *199*, 91–109; g) V. Choudhary, S. H. Mushrif, C. Ho, A. Anderko, V. Nikolakis, N. S. Marinkovic, A. I. Frenkel, S. I. Sandler, D. G. Vlachos, *J. Am. Chem. Soc.* **2013**, *135*, 3997–4006.
- [7] J. Guan, Q. Cao, X. Guo, X. Mu, *Comput. Theor. Chem.* **2011**, *963*, 453–462.
- [8] a) E. A. Pidko, V. Degirmenci, R. A. van Santen, E. J. M. Hensen, *Angew. Chem.* **2010**, *122*, 2584–2588; *Angew. Chem. Int. Ed.* **2010**, *49*, 2530–2534; b) E. A. Pidko, V. Degirmenci, E. J. M. Hensen, *ChemCatChem* **2012**, *4*, 1263–1271.
- [9] G. Yang, E. A. Pidko, E. J. M. Hensen, *ChemSusChem* **2013**, *6*, 1688–1696.
- [10] G. Yang, E. A. Pidko, E. J. M. Hensen, *J. Catal.* **2012**, *295*, 122–132.
- [11] C. Adamo, V. Barone, *J. Chem. Phys.* **1999**, *110*, 6158–6169.
- [12] Gaussian 09, Revision B.1, M. J. Frisch, G. W. Trucks, H. B. Schlegel, G. E. Scuseria, M. A. Robb, J. R. Cheeseman, G. Scalmani, V. Barone, B. Menucci, G. A. Petersson, H. Nakatsuji, M. Caricato, X. Li, H. P. Hratchian, A. F. Izmaylov, J. Bloino, G. Zheng, J. L. Sonnenberg, M. Hada, M. Ehara, K. Toyota, R. Fukuda, J. Hasegawa, M. Ishida, T. Nakajima, Y. Honda, O. Kitao, H. Nakai, T. Vreven, J. A. Montgomery, Jr., J. E. Peralta, F. Ogliaro, M. Bearpark, J. J. Heyd, E. Brothers, K. N. Kudin, V. N. Staroverov, R. Kobayashi, J. Normand, K. Raghavachari, A. Rendell, J. C. Burant, S. S. Iyengar, J. Tomasi, M. Cossi, N. Rega, J. M. Millam, M. Klene, J. E. Knox, J. B. Cross, V. Bakken, C. Adamo, J. Jaramillo, R. Gomperts, R. E. Stratmann, O. Yazyev, A. J. Austin, R. Cammi, C. Pomelli, J. W. Ochterski, R. L. Martin, K. Morokuma, V. G. Zakrzewski, G. A. Voth, P. Salvador, J. J. Dannenberg, S. Dapprich, A. D. Daniels, Ö. Farkas, J. B. Foresman, J. V. Ortiz, J. Cio-slowski, D. J. Fox, Gaussian, Inc., Wallingford CT, **2009**.

- [13] G. I. Csonka, A. D. French, G. P. Johnson, C. A. Stortz, *J. Chem. Theory Comput.* **2009**, *5*, 679–692.
- [14] S. F. Sousa, P. A. Fernandes, M. J. Ramos, *J. Phys. Chem. A* **2007**, *111*, 10439–10452.
- [15] a) J. M. del Campo, J. L. Gázquez, S. B. Trickey, A. Vela, *J. Chem. Phys.* **2012**, *136*, 104108; b) Y. Zhao, D. G. Truhlar, *Acc. Chem. Res.* **2008**, *41*, 157–167; c) Y. Zhao, D. G. Truhlar, *J. Chem. Theory Comput.* **2009**, *5*, 324–333.
- [16] E. A. Pidko, V. Degirmenci, R. A. van Santen, E. J. M. Hensen, *Inorg. Chem.* **2010**, *49*, 10081–10091.
- [17] a) C. Gonzalez, H. B. Schlegel, *J. Chem. Phys.* **1989**, *90*, 2154–2161; b) C. Gonzalez, H. B. Schlegel, *J. Phys. Chem.* **1990**, *94*, 5523–5527.
- [18] V. Barone, M. Cossi, *J. Phys. Chem. A* **1998**, *102*, 1995–2001.
- [19] Y. Takano, K. N. Houk, *J. Chem. Theory Comput.* **2005**, *1*, 70–77.
- [20] A. V. Marenich, C. J. Cramer, D. G. Truhlar, *J. Phys. Chem. B* **2009**, *113*, 6378–6396.
- [21] S. A. Bogatko, E. J. Bylaska, J. H. Weare, *J. Phys. Chem. A* **2010**, *114*, 2189–2200.
- [22] A. F. Hollemann, N. Wiberg, *Lehrbuch der Anorganischen Chemie, Vol. 101*, Walter de Gruyter, Berlin, New York, **1995**.
- [23] NBO Version 3.1, E. D. Glendening, A. E. Reed, J. E. Carpenter, F. Weinhold, University of Wisconsin, Madison, **1998**.
- [24] Y. Román-Leshkov, M. Moliner, J. A. Labinger, M. E. Davis, *Angew. Chem.* **2010**, *122*, 9138–9141; *Angew. Chem. Int. Ed.* **2010**, *49*, 8954–8957.
- [25] TS₁, PT₂, TS₃, and PT₃ were not analyzed because they are generally lower in energy or of the same energy as PT₁ and TS₂. The energy for separation of the open-chain fructose–catalyst complex was not determined because the ring closure (TS₃) requires more activation for the uncatalyzed than for the catalyzed reaction. The ring has to be established if HMF is to be formed later in the reaction. The deprotonated and protonated species involved in the proton transfers are not taken as reference points because they are not stable minima in the reaction; their energies were generated with a thermodynamic cycle.
- [26] S. Bogatko, P. Geerlings, *Phys. Chem. Chem. Phys.* **2012**, *14*, 8058–8066.
- [27] Entry of Merck Millipore for CAS 10125–13–0, copper(II) chloride dihydrate.
- [28] L. Nagy, H. Ohtaki, T. Yamaguchi, M. Nomura, *Inorg. Chim. Acta* **1989**, *159*, 201–207.
- [29] J. Briggs, P. Finch, M. C. Matulewicz, H. Weigel, *Carbohydr. Res.* **1981**, *97*, 181–188.
- [30] T. Kurahashi, T. Mizutani, J. Yoshida, *J. Chem. Soc. Perkin Trans. 1* **1999**, 465–474.

Received: March 1, 2014

Published online on August 26, 2014

CHEMISTRY

A European Journal

Supporting Information

© Copyright Wiley-VCH Verlag GmbH & Co. KGaA, 69451 Weinheim, 2014

Reactivity of Metal Catalysts in Glucose–Fructose Conversion

Claudia Loerbroks, Jeaphianne van Rijn, Marc-Philipp Ruby, Qiong Tong, Ferdi Schüth, and Walter Thiel*^[a]

chem_201402437_sm_miscellaneous_information.pdf

Comparison with other computational methods

For comparison the glucose to fructose isomerization with the $[\text{AlO}^1\text{O}^2(\text{H}_2\text{O})_4]^{3+}$ catalyst was calculated at the B3LYP/6-31+G(d,p), the M06/6-31+G(d,p) and the PBE0/6-311+G(d,p) level. The energy trends are comparable to the PBE0/6-31+G(d,p) level used in this study (Table 18, Table 1). The only exception is the final fructofuranose-catalyst complex, which is less stabilized with the other functionals.

Table 1: Relative free energies of different functionals for the isomerization with $[\text{AlO}^1\text{O}^2(\text{H}_2\text{O})_4]^{3+}$ catalyst comparison with used method. Energy reference is glucosepyranose + $[\text{Al}(\text{H}_2\text{O})_6]^{3+}$.

	$\Delta\text{G}(\text{B3LYP}/6-31+\text{G}^{**}, \text{CPCM}(\text{water})) / \text{kcal mol}^{-1}$	$\Delta\text{G}(\text{M06}/6-31+\text{G}^{**}, \text{CPCM}(\text{water})) / \text{kcal mol}^{-1}$	$\Delta\text{G}(\text{PBE0}/6-311+\text{G}^{**}, \text{CPCM}(\text{water})) / \text{kcal mol}^{-1}$	$\Delta\text{G}(\text{PBE0}/6-31+\text{G}^{**}, \text{CPCM}(\text{water})) / \text{kcal mol}^{-1}$
glucosepyranose + $[\text{Al}(\text{H}_2\text{O})_6]^{3+}$	0.0	0.0	0.0	0.0
glucopyranose	6.4	3.0	0.8	2.3
PT1				
glucopyranose O5 prot.	11.0	10.8	6.9	11.0
TS1				
glucose	5.1	8.0	4.7	7.0
DP2				
deprot. glucose	12.0	10.1	9.2	10.4
TS2	27.1	26.2	21.1	23.0
deprot. fructose	9.0	8.8	5.1	6.4
RP2				
fructose	-1.7	-2.4	-3.0	-1.3
TS3	5.8	6.2	4.9	7.0
fructofuranose O5 prot.	6.0	4.4	-0.1	0.7
PT3				
fructofuranose	0.1	-1.4	-5.1	-13.9
fructofuranose + $[\text{Al}(\text{H}_2\text{O})_6]^{3+}$	2.7	2.8	1.5	1.5

Influence of temperature and pressure

The computations reported in this study include thermal corrections for standard conditions (298 K and 1 bar). The experiments were carried out around 413 K and 80 bar. Therefore additional frequency calculations have been performed for exemplary aluminum(III) and iron(III) catalysts (Table 2, Table 19). Higher temperature will increase the importance of the entropic contributions, and higher pressure will favor more compact transition states. Nevertheless, only marginal to small differences are found (0.1 to 5.0 kcal/mol) for the relative TS2 barriers. Since temperature and pressure are not included in the optimization of the structures, the computed energy changes do not reflect all the effects of the experimental conditions.

Table 2: Relative free energies at 298 K and 1 bar and at 413 K and 70 bar for critical steps (TS2 and product catalyst separation) in the glucose-fructose isomerization with selected Al³⁺ and Fe³⁺ catalysts (PBE0/6-31+G, CPCM(water)).**

		$\Delta G(\text{TS2})$ / kcal mol ⁻¹	$\Delta\Delta G(\text{TS2})$ / kcal mol ⁻¹	$\Delta\Delta G(\text{separation})$ / kcal mol ⁻¹
reference→		glucopyranose + [M(H ₂ O) ₆] ³⁺	lowest minimum before TS2	glucopyranose-catalyst complex
catalyst ↓				
[Al(H ₂ O) ₆] ³⁺	298 K, 1 bar	24.4	29.2	9.4
	413 K, 70 bar	25.2	28.7	--
[AlO ¹ O ² (H ₂ O) ₄] ³⁺	298 K, 1 bar	23.0	23.0	15.4
	413 K, 70 bar	23.5	23.5	--
[AlO ¹ O ² (H ₂ O) ₃ Cl] ²⁺	298 K, 1 bar	5.7	23.1	13.0
	413 K, 70 bar	0.9	23.4	11.2
[Fe(H ₂ O) ₆] ³⁺	298 K, 1 bar	21.0	25.4	13.0
	413 K, 70 bar	27.4	30.4	--
[FeO ¹ O ² (H ₂ O) ₄] ³⁺	298 K, 1 bar	20.3	20.3	17.2
	413 K, 70 bar	21.3	21.3	--
[FeO ¹ O ² (H ₂ O) ₃ Cl] ²⁺	298 K, 1 bar	-5.4	30.2	16.0
	413 K, 70 bar	-6.0	30.1	14.1

Thermodynamic cycles

All mechanisms feature protonation and deprotonation reactions at hydroxyl groups and at the pyranic oxygen O5 (proton transfer 1 (PT1) from O1 to O5, proton transfer 2 (PT2) from O2 to O1, and proton transfer 3 (PT3) from O5 to O2, Figure 1). For the transition states of these transfers, we considered (a) direct proton transfer (intramolecular, concerted) and (b) proton transfers assisted by one to three water molecules (intermolecular, two steps). Mechanism (a) always led to the highest barriers. In the transition state for this intramolecular proton transfer, the O-H-O angle is very strained (for example, in the uncatalyzed reaction, PT1: $\gamma(\text{C1-H-O5}) = 120^\circ$) whereas this angle is nearly linear in unconstrained proton transfers. Additionally, the chair conformation of the glucopyranose is distorted towards a boat conformation, thus raising the energy. In mechanism (b), the energy of the transition state is lowered the more waters are attached. The associated barriers depend on the number and position of the water molecules.

Free energies of proton transfer were calculated with the use of appropriate thermodynamic cycles (see below). The corresponding values in the Results section were always determined from such cycles. This approach was also used in a previous study on glucose protonation pathways.^[1]

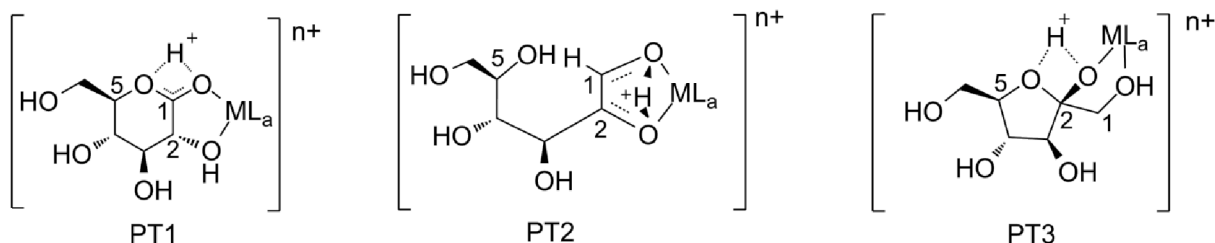
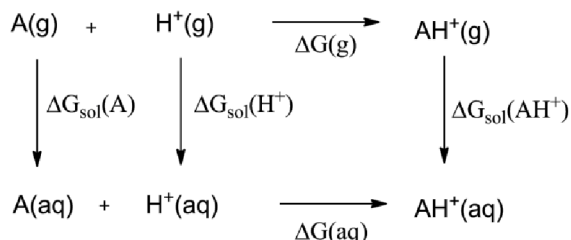


Figure 1: The three proton transfers in the proposed glucose to fructose isomerization mechanism. PT1 from O1 to O5, PT2 from O2 to O1, and PT3 from O5 to O2.

For the thermodynamic cycles the protonation reaction (1) was used or in case of deprotonations the back reaction of (1).



Changes in solvation free energies were calculated by subtracting the PBE0 free energy in vacuum from the PBE0 free energy calculated with the SMD solvent model. The latter was chosen because its documented good performance for solvation free energies, for instance, in a benchmark study on a set of 51 drug-like molecules (RMSD = 2.5 kcal/mol relative to experiment).^[2] For the evaluation of the thermodynamic cycle, we used experimental values for the solvation free energy of hydronium ion, H^+ , and water molecule,^[3] and for the gas-phase free energy of H^+ .^[4] $\Delta G_{\text{sol},1M}(H_2O) = -6.32$ kcal/mol, $\Delta G_{\text{sol},1M}(H_3O^+) = -110.3$ kcal/mol, $\Delta G_{\text{sol},1M}(H^+) = -265.9$ kcal/mol, $\Delta G_{g,1atm}(H^+) = -6.28$ kcal/mol. All energy values were converted to the standard state of 298 K and 1 M (1 mol/L). In the gas phase, equation (2), the change of 1 mole of ideal gas from 1 atm (24.46 L/mol) to 1 M gives rise to the following correction term:

$$\begin{aligned}
 \Delta G_{g,1M} &= \Delta G_{g,1atm} - T\Delta S \\
 &= \Delta G_{g,1atm} + RT \ln\left(\frac{V_g}{V_{aq}}\right) \\
 &= \Delta G_{g,1atm} + RT \ln(24.46) \\
 &= \Delta G_{g,1atm} + 1.89 \text{ kcal/mol}
 \end{aligned} \quad (2)$$

Likewise, bringing water molecules from the concentration of 55.34 M in liquid water to 1M generates another correction term:

$$n \cdot \Delta G_{aq,1M}^*(H_2O) = -n \cdot RT \ln(55.34) = -2.38 \cdot n \text{ kcal/mol} \quad (3)$$

Metal salt complexes in water

The complex formation of metal salts MCl_x in water depends on many factors: the metal cation, temperature, the pK_a of the complex, the pH of the solution, the available ligands (here: H_2O , Cl^- , OH^- , hydroxyl groups of glucose), and the ligand exchange rate. Under these diverse conditions, the investigated metal cations (Al^{3+} , Mg^{2+} , Cr^{3+} , Fe^{3+} , Cu^{2+}) can form different complexes in water, but they have in common that they can all form octahedral complexes with six water ligands (Figure 2).

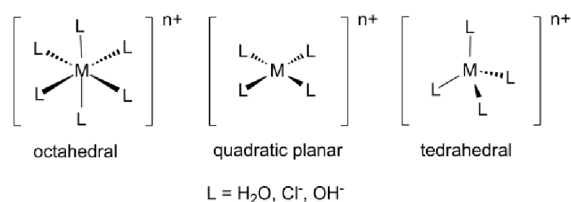
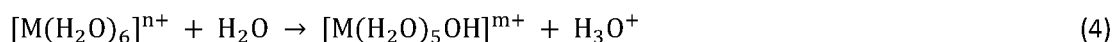


Figure 2: Possible metal-ligand complexes of chloride salts in water.

Which ligands are associated depends on the metal cation.^[5] For Cr³⁺ at high temperatures and for Fe³⁺, it is common to exchange one to three water ligands for chloride ligands, whereas Al³⁺ and Mg²⁺ prefer water ligands. Copper(II) cations often have four ligands, favoring a tetrahedral (quadratic) arrangement for chloride (oxygen) ligands. The geometry of the actually formed copper(II) complexes depends on the concentration of salt in the solution, with tetrahedral CuCl₄²⁻ complexes at high salt concentrations and [Cu(H₂O)₂Cl₂] and [Cu(H₂O)₆]²⁺ complexes at lower salt concentrations.

If a metal complex is acidic enough, the water ligands of the metal cation can act as proton donors, transforming a water ligand into a hydroxyl ion ligand (eq. 4).



Using a thermodynamic cycle the energy of a deprotonation reaction like equation (4) was calculated for metal cations [M(H₂O)₆]ⁿ⁺ (Table 3). As expected, the computed energy ranges correlate qualitatively with the pK_a of the metal cations. The values for Cu²⁺ and Al³⁺/Cr³⁺ cations do not match the pK_a values perfectly, as the thermodynamic cycle is not accurate enough for quantitative results in this case.^[6] Complexes with exothermic reaction energies (Cr³⁺, Al³⁺, Fe³⁺) are more likely to be found deprotonated in water. For example, iron(III) hexaqua-complexes are only stable at pH values lower than zero, and at higher pH values one to three water ligands are deprotonated.^{[5a],[7]} Analogous relations are found for hexaqua-aluminum(III) and chromium(III) complexes. As the experiment takes place in water at pH 7, deprotonation reactions become likely for these three metal complexes.

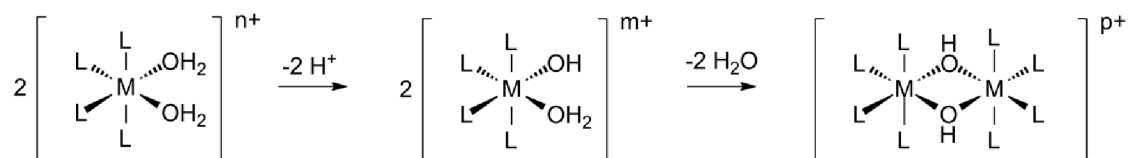
Table 3: Free energies of deprotonation for [M(H₂O)₆]ⁿ⁺ complexes in water calculated with a thermodynamic cycle (PBE0/6-31+G).**

Metal cation	pK _a in water, 298 K	ΔG(deprot) / kcal mol ⁻¹
Cu ²⁺	8.0	26.3*
H ₂ O	15.7	23.5
Mg ²⁺	11.4	20.3
Cr ³⁺	4.1	-0.5
Al ³⁺	5.5	-2.1
Fe ³⁺	2.2	-4.7

*calculated at the frozen geometry, since deprotonation leads to significant structural changes in [Cu(H₂O)₆]²⁺

As can be seen in Table 3, the deprotonation reaction is endothermic for metal cation complexes that hardly catalyze the glucose to fructose isomerization (Cu^{2+} , Mg^{2+} , water), whereas for good catalysts (Cr^{3+} , Al^{3+}) and Fe^{3+} the deprotonation reaction is exothermic. The influence of the Brønsted acidity of the different metal complexes will be discussed in the context of the mechanism in the Results section.

Depending on the pH of the solution binuclear complexes can also be formed (Scheme 1). Dimers can be found with single, double or triple chloride, hydroxo or oxo bridges, but most likely are doubly bridged hydroxo systems.^[8] The higher the pH of the solution, the more probable is the formation of dimeric complexes, as dimers are predeceased by a deprotonation of water ligands. For example, the μ -hydroxyl bridged catalysts are found for chromium(III) and iron(III) complexes, and in low amounts also for aluminum(III) in aqueous systems.^{[5a],[7]} Like the monomeric catalysts some dimers are able to bind to glucose: Extended x-ray absorption fine structure (EXAFS) spectroscopy found Fe^{3+} - dimers with the hydroxyl groups of glucose acting as ligands.^[9] For the dimeric catalyst, only the rate determining steps were explored in the Results section.



Scheme 1: Formation of a dimeric complexes with μ -water hydroxyl bridges.

If sugar molecules are added to the metal complexes in water, they can act as bidentate ligands or can form hydrogen bonded complexes (Figure 3). The direct binding to glucose is entropically favored as two water ligands are detached (chelate effect). The position closest to the reaction centre for isomerization is the O^1O^2 position in glucose. For the $[\text{M}(\text{H}_2\text{O})_4]^{n+}$ catalyst, the coordination sites O^1O^2 , O^2O^3 , O^3O^4 , O^3O^4 and O^4O^6 were investigated, and their energies are displayed in Table 4. We did not perform such a study for $[\text{M}(\text{H}_2\text{O})_6]^{n+}$, because a hydrogen bonded catalyst seems more unlikely in the high-pressure environment of the experimental setup since it has higher energies for the rate determining steps (see Results section). According to the literature, different percentages of complexed glucose are found for different metal cations in water: Mg^{2+} 0%, Fe^{3+} 8%, Al^{3+} 9%, Cr^{3+} 12% and Cu^{2+} 14%.^[10]

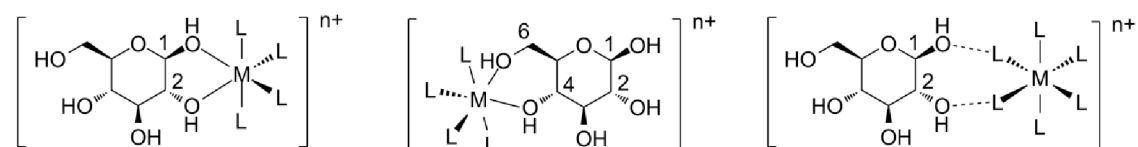


Figure 3: Octahedral metal-ligand complexes with β -glucose as a bidentate ligand. O^1O^2 coordination (left), O^4O^6 coordination (middle) or attached to β -glucose via hydrogen bonds (right).

Table 4: Relative binding free energies between tetraaqua-metal complexes and α - and β -glucopyranose for different coordination sites (PBE0/6-31+G, CPCM(water)).**

Coordination	$\Delta G / \text{kcal mol}^{-1}$				
α -glucose	$\text{Al}(\text{H}_2\text{O})_4^{3+}$	$\text{Fe}(\text{H}_2\text{O})_4^{3+}$	$\text{Cr}(\text{H}_2\text{O})_4^{3+}$	$\text{Mg}(\text{H}_2\text{O})_4^{2+}$	$\text{Cu}(\text{H}_2\text{O})_4^{2+}$
O^1O^2	0.0	0.0	0.0	0.0	0.0
O^2O^3	-0.3	-1.6	-0.1	-2.4	-4.2
O^3O^4	1.7	-0.3	-0.4	-0.2	-4.6
O^4O^6	-3.0	-4.8	-5.3	-1.5	-5.9
O^6O^5	2.6	-0.9	-3.3	0.5	-5.8
β -glucose	$\text{Al}(\text{H}_2\text{O})_4^{3+}$	$\text{Fe}(\text{H}_2\text{O})_4^{3+}$	$\text{Cr}(\text{H}_2\text{O})_4^{3+}$	$\text{Mg}(\text{H}_2\text{O})_4^{2+}$	$\text{Cu}(\text{H}_2\text{O})_4^{2+}$
O^1O^2	0.0	0.0	0.0	0.0	0.0
O^2O^3	-3.0	-3.9	-4.3	-0.9	0.4
O^3O^4	-0.4	0.3	-1.3	0.7	0.3
O^4O^6	-5.3	-5.5	-6.1	-0.7	-1.1
O^6O^5	-5.8	-5.2	-5.1	0.9	-1.0

According to Table 4, the O^4O^6 coordination is preferred in the majority of cases, as in this position a second six-membered ring can be formed between the metal complex and glucopyranose. The O^1O^2 and O^3O^4 coordination are least favorable for most metals. Nevertheless, the isomerization was investigated for O^1O^2 coordination of α -glucopyranose in this study. This coordination site is closest to the reactive centre of the glucose to fructose isomerization and should therefore help lower the barriers most efficiently. In addition, we note that the complexes with O^1O^2 coordination remain accessible because they are only 1-6 kcal/mol above the lowest-energy complex. In experiments with O1 methylated glucose, no isomerization was detected for CrCl_2 in ionic liquids.^[11] This was taken as evidence that the isomerization can only be carried out if O1 is free for coordination, and hence only O1 coordination was regarded relevant in this study. The rate determining step (TS2) of the isomerization was investigated for the coordination site lowest in energy (O^4O^6), but no stable transition state was found.

In addition to the coordination site of glucose, the energy of the complex is also influenced by the ligand arrangement. Axial (ax1, ax2) and equatorial positions (eq1, eq2) were calculated for different numbers of chloride and hydroxyl ligands in the iron(III), chromium(III), and aluminum(III) complexes $[\text{MO}^1\text{O}^2(\text{H}_2\text{O})_4]^{n+}$. For copper(II) the ligand positions in the complex $[\text{CuO}^1\text{O}^2(\text{H}_2\text{O})\text{Cl}]^+$ were investigated. Since hydroxyl and chloride ligands are not likely for magnesium(II) complexes in water, no calculations were done with magnesium(II) and these ligands. Exemplary results are summarized in Table 5. For the subsequent mechanistic studies, we always chose the lowest-energy position. The energy of the rate determining steps was also spot-checked for different ligand positions, and the results (Table 7) agree mainly with the data in Table 5. In general the equatorial positions are lowest in energy, although the energy differences are only small for the different constitutions.

Table 5: Relative free energies of α -glucose metal complexes with different chloride, hydroxide, and water ligands (PBE0/6-31+G, CPCM(water)).**

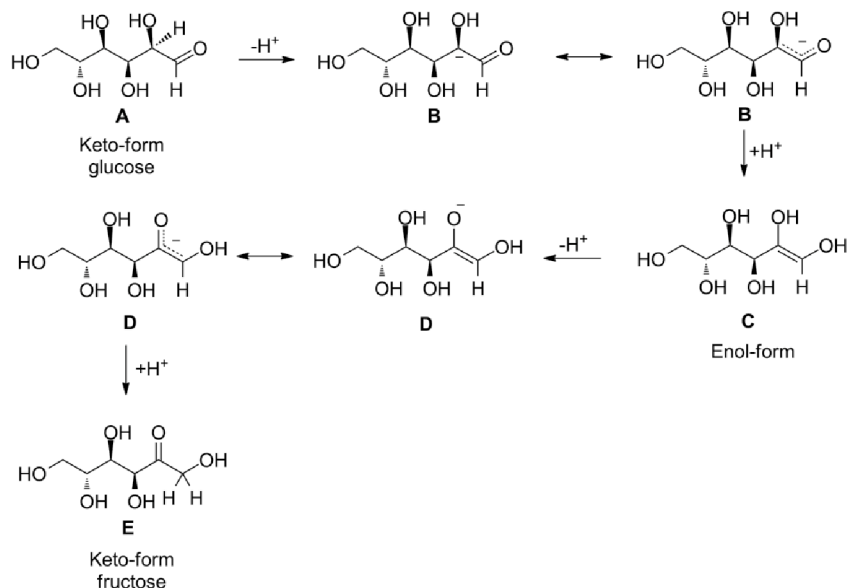
complex	$\Delta G / \text{kcal mol}^{-1}$	$\Delta G / \text{kcal mol}^{-1}$	$\Delta G / \text{kcal mol}^{-1}$
catalyst \rightarrow coordination \downarrow	$\text{Al}(\text{H}_2\text{O})_3\text{Cl}^{2+}$	$\text{Fe}(\text{H}_2\text{O})_3\text{Cl}^{2+}$	$\text{Cr}(\text{H}_2\text{O})_3\text{Cl}^{2+}$
ax1	0.0	0.0	0.0
ax2	-1.0	-0.5	-0.1
eq1	-1.9	-1.5	-0.6
eq2	-1.6	-2.6	-2.0
	$\text{Al}(\text{H}_2\text{O})_2\text{Cl}_2^+$	$\text{Fe}(\text{H}_2\text{O})_2\text{Cl}_2^+$	$\text{Cr}(\text{H}_2\text{O})_2\text{Cl}_2^+$
ax1-ax2	--	0.0	0.0
eq1-eq2	--	-3.1	-1.6
eq1-ax1	--	-0.8	0.8
eq1-ax2	--	-1.9	1.2
eq2-ax1	--	-1.5	1.2
eq2-ax2	--	-1.1	0.1
	$\text{Al}(\text{H}_2\text{O})_3\text{OH}^{2+}$	$\text{Fe}(\text{H}_2\text{O})_3\text{OH}^{2+}$	$\text{Cr}(\text{H}_2\text{O})_3\text{OH}^{2+}$
ax1	0.0	0.0	0.0
ax2	-2.1	-0.9	-1.0
eq1	-1.8	-2.4	-1.2
eq2	-3.3	-3.2	-2.8
		$\text{Fe}(\text{H}_2\text{O})\text{Cl}_3$	$\text{Cr}(\text{H}_2\text{O})\text{Cl}_3$
fac	--	0.0	0.0
mer	--	-2.2	-1.4

Since it is hard to determine which of the complex configurations are most likely under the experimental conditions and how fast they change, the reaction mechanism was calculated for the most probable ligands for each metal cation.

In this study, all free energies refer to the sum of the free energies of $[\text{M}(\text{H}_2\text{O})_6]^{n+}$ and α -glucopyranose. Free energies of reactants with chloride or hydroxyl ligands were adjusted to this reference by including the corresponding free energy of ligand exchange, as obtained from calculations at the same level of theory for water, hydronium, and chloride.

Alternative pathway Keto-Enol-Tautomerization

An alternative to the hydrogen transfer TS2 is the keto-enol tautomerization. The tautomerization involves various de- and reprotonations via intermediates stabilized by charge delocalization in the keto- and enol-forms (Scheme 2). The relative reaction free energy for protonation and deprotonation reactions between the sugar molecule and the solvent were calculated with thermodynamic cycles (see above). This pathway was found to be higher in energy by 3 kcal/mol for the $[\text{Al}(\text{H}_2\text{O})_4]^{3+}$ catalyzed pathway because of the higher energy for the proton addition from structure B to the enol-form C. Therefore this pathway was not further investigated. The H shift mechanism was also found to be preferred in enzymes according to the literature.^[12]



Scheme 2: Keto-enol-Tautomerization as an alternative to the hydrogen shift TS2.

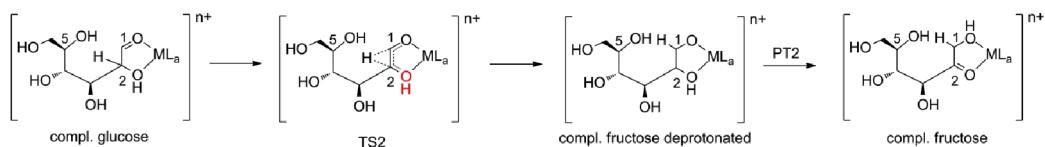
Table 6: Relative free Energies for the hydrogen transfer TS2 versus the Keto-Enol-Tautomerization. Energy references is glucopyranose + $[Al(H_2O)_6]^{3+}$. Prot. barrier describes the energy needed for the protonation or deprotonation (PBE0/6-31+G, CPCM(water)).**

Hydrogen transfer	ΔG / kcal/mol	Keto-Enol-tautomerization	ΔG / kcal/mol
glucopyranose+ $[Al(H_2O)_6]^{3+}$	0.0	glucopyranose+ $[Al(H_2O)_6]^{3+}$	0.0
glucose- $[AlO^1O^2(H_2O)_4]^{3+}$	7.0	glucose- $[AlO^1O^2(H_2O)_4]^{3+} = A$	7.0
glucose deprot.- $[AlO^1O^2(H_2O)_4]^{3+}$	10.4	B	20.2
		prot. barrier	25.9
TS2	23.0	C	17.5
fructose deprot.- $[AlO^1O^2(H_2O)_4]^{3+}$	6.4	D	17.8
fructose- $[AlO^1O^2(H_2O)_4]^{3+}$	-1.3	E	-2.5

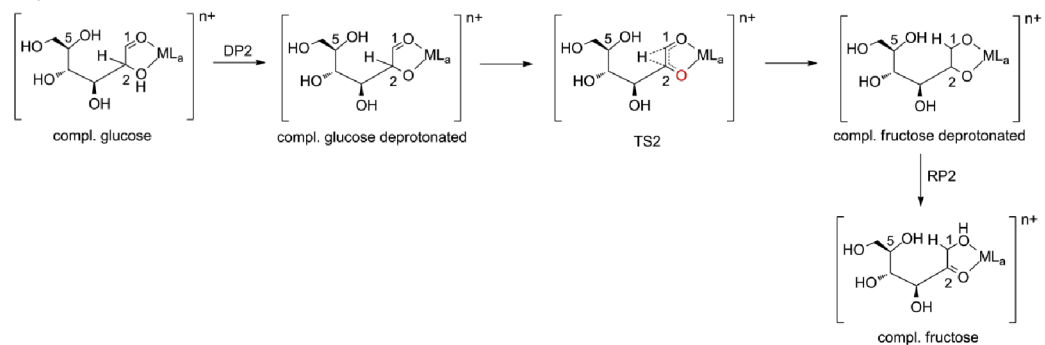
Alternative pathway TS2-PT2 versus DP2-TS2-RP2:

One step of the glucose to fructose isomerization is a hydrogen shift (TS2), with a hydrogen atom being transferred from C2 to C1. The shift can be carried out with O2 being protonated or deprotonated (Scheme 3). Protonated and deprotonated forms of the transition states were calculated for exemplary ligand constitutions and metals (Table 7). The lowest-energy form is always given in the Results section. If the transition state is protonated, the proton transfer from O2 to O1 occurs after the transition state (PT2). If the hydrogen transfer occurs in the deprotonated form, the O2 deprotonation (DP2) takes place before TS2 and the O1 protonation afterwards (RP2).

Deprotonation after TS2:



Deprotonation before TS2:



Scheme 3: Possible intermediates before and after TS2, depending on the protonation state of O2 (marked in red) in the complexed glucose.

Table 7: Relative free energies for hydrogen transfer transition states with different ligand positions and protonation states (PBE0/6-31+G, CPCM(water)).**

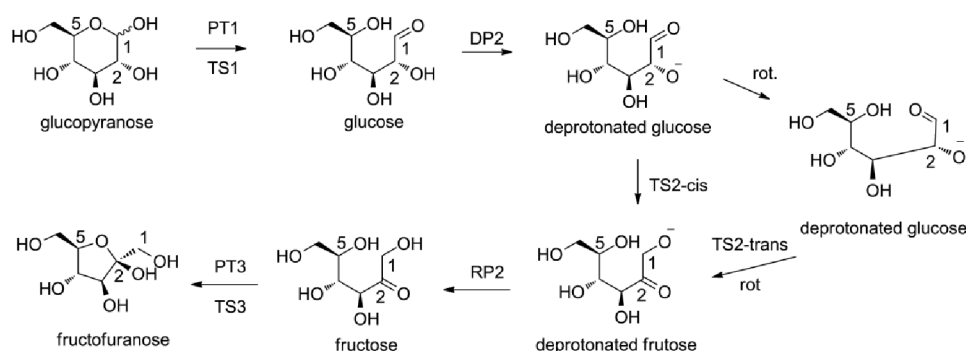
TS2	$\Delta G / \text{kcal mol}^{-1}$	$\Delta G / \text{kcal mol}^{-1}$	$\Delta G / \text{kcal mol}^{-1}$
catalyst \rightarrow coordination \downarrow	$\text{Al}(\text{H}_2\text{O})_3\text{Cl}^{2+}$	$\text{Fe}(\text{H}_2\text{O})_3\text{Cl}^{2+}$	$\text{Cr}(\text{H}_2\text{O})_3\text{Cl}^{2+}$
TS2 - ax1	--	-6.8	--
TS2 - ax1 - deprot	10.4	-1.3	1.2
TS2 - ax2	13.3	-8.0	--
TS2 - ax2 - deprot	--	3.4	--
TS2 - eq1	1.8	-4.3	--
TS2 - eq1 - deprot	--	-0.5	--
TS2 - eq2	10.7	-5.4	-4.0
TS2 - eq2 - deprot	--	-1.6	0.2
		$\text{Fe}(\text{H}_2\text{O})\text{Cl}_3$	
TS2 - eq1ax12	--	-42.2	--
TS2 - eq12ax2	--	-46.3	--
	$\text{Al}(\text{H}_2\text{O})_3\text{OH}^{2+}$	$\text{Fe}(\text{H}_2\text{O})_3\text{OH}^{2+}$	$\text{Cr}(\text{H}_2\text{O})_3\text{OH}^{2+}$
TS2 - ax1 - deprot	55.8	44.9	--
TS2 - ax2	41.7	--	--
TS2 - ax2 - deprot	--	--	46.7
TS2 - eq1 - deprot	48.3	--	--
TS2 - eq2	41.0	32.3	34.2
TS2 - eq2 - deprot	48.4	42.5	44.6
	$\text{Al}(\text{H}_2\text{O})_6^{3+}$		
TS2	24.4	--	--
TS2 - deprot.	40.6	--	--
	$\text{Al}(\text{H}_2\text{O})_4^{3+}$	$\text{Fe}(\text{H}_2\text{O})_4^{3+}$	$\text{Cr}(\text{H}_2\text{O})_4^{3+}$
TS2	34.7	24.7	19.3
TS2 - deprot.	23.0	20.3	18.0
	$\text{Al}_2(\text{H}_2\text{O})_8(\text{OH})_2^{4+}$		
TS2	57.8	--	--
TS2 - deprot.	40.1	--	--

Detailed description of mechanisms

Example 1: Glucopyranose to fructofuranose conversion mechanism without catalyst

To estimate the influence of the different metal catalysts, the uncatalyzed mechanism of the glucose to fructose conversion was calculated starting from α - and β -glucopyranose (Scheme 4, Figure 5, Table 8). Only the energies of PT1 and TS1 are different for the two anomeric forms of glucopyranose, as free rotation around the C1-C2 bond is assumed after ring opening.

All energies refer to α -glucopyranose.



Scheme 4: Mechanism for the uncatalyzed pathway of glucose to fructose isomerization.

The reaction starts with protonation of O5 and deprotonation of O1 (PT1) to facilitate the ring opening of the pyranose ring (Scheme 4, PT1). Overall, these de- and reprotonation reactions are endothermic by 38.1 kcal/mol for α -glucopyranose and by 33.7 kcal/mol for β -glucopyranose. After protonation of O5, a spontaneous ring opening by C1-O5 bond cleavage leads to glucose (TS1).

The next step is the deprotonation of O2 (DP2), which is necessary for the uncatalyzed mechanism as the negative charge on O2 eases the hydrogen transfer to C1 due to its positive inductive effect. The deprotonation energy was calculated to be 23.3 kcal/mol.

Thereafter, hydrogen transfer from C2 to C1 transforms the hydroxyl group at O2 into a keto group and O1 into a hydroxyl group (TS2, Figure 4). This reaction (Figure 4, TS2) can occur with the hydroxyl groups at the C1-C2 carbon bond in the *cis* ($\Delta G(\text{TS2})=78.2$ kcal/mol) or *trans* ($\Delta G(\text{TS2})=88.9$ kcal/mol) conformation. The *cis* transition state is lower in energy by ca. 10 kcal/mol, which might be due to the better charge delocalization in the more planar geometry of the *cis* structure (3° versus 17° in the O1-C1-C2-O2 dihedral angle). According to NBO analysis the electrons of the former C2-H bond are distributed between the s_{H} orbital (0.799 e) of the transferred hydrogen atom and the two $\pi^*_{\text{C1-O1}}$ and $\pi^*_{\text{C2-O2}}$ orbitals (0.584 and 0.562 e). The hydrogen atom donates electron density into the $\pi^*_{\text{C-O}}$ orbitals. It carries a positive charge of 0.198 e.

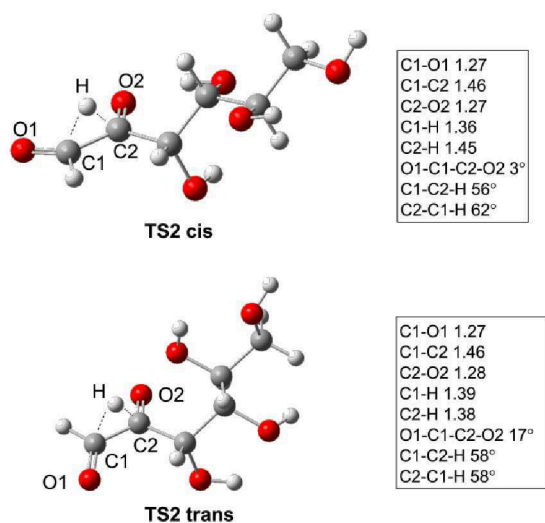


Figure 4: Transition states for the uncatalyzed hydrogen atom transfer from C2 to C1 in the *cis* (top) and *trans* (bottom) conformation. Distances are given in Ångstrom (PBE0/6-31+G, CPCM(water)).**

Beyond TS2, the O1 atom is protonated (RP2). Since the negative charge is mainly located at O1, this oxygen atom is a reasonable target for protonation, which is exothermic by -26.1 kcal/mol.

The last step involves ring closure (TS3) and proton transfer (PT3). The hydroxyl group at O5 attacks C2 and transfers the HO5 proton to O2, forming fructofuranose. The bond formation and the proton transfer occur in a concerted manner. After bond formation, 33.9 kcal/mol are needed for deprotonation of O5, and -41.5 kcal/mol are gained by protonation of O2.

The hydrogen atom transfer is the rate determining step, with an energy of 78.2 kcal/mol for TS2. It is clearly unfeasible even at 413 K. The overall reaction is endothermic by 1.5 kcal/mol. These findings are in agreement with experiments that show no conversion for the uncatalyzed reaction. A catalyst should lower the energies of PT1 and PT2 due to its Brønsted acidity as well as the transition state TS2 due to its Lewis acidity.

Table 8: Relative free energies for the uncatalyzed reaction from glucopyranose to fructofuranose. The energy reference is α -glucopyranose (PBE0/6-31+G, CPCM(water)).**

	$\Delta G / \text{kcal mol}^{-1}$	$\Delta G / \text{kcal mol}^{-1}$
structure	α -glucopyranose	β -glucopyranose
glucopyranose	0.0	-0.2
PT1 – deprot.	25.5	24.1
PT1 – prot.	38.1	33.4
TS1		
glucose	11.4	10.9
DP2	34.2	34.8
deprot. glucose	72.5	77.8
TS2	78.2 (cis)	88.9 (trans)
deprot. fructose	69.4	75.4
RP2	43.3	49.3
fructose	7.2	
TS3		
PT3 – deprot.	41.1	
PT3 – prot.	-0.3	
fructofuranose	1.5	

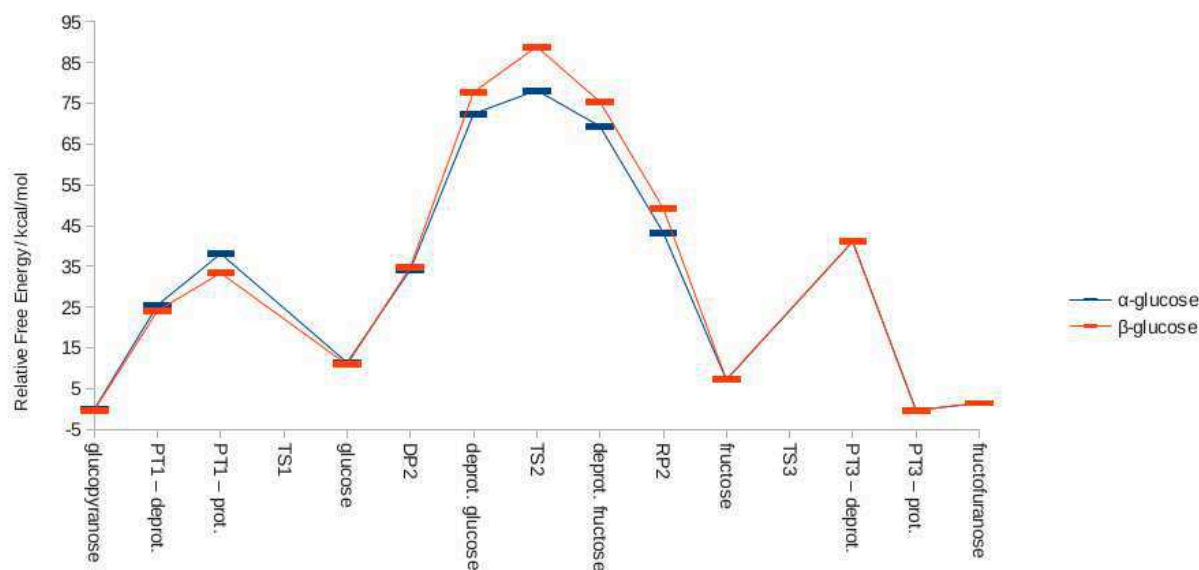


Figure 5: Relative free energy profile in kcal mol^{-1} for the uncatalyzed reaction pathway from glucopyranose to fructofuranose. Energy reference is α -glucopyranose (PBE0/6-31+G, CPCM(water)).**

Example 2: The $[\text{Al}(\text{H}_2\text{O})_6]^{3+}$ catalyzed glucopyranose fructofuranose isomerization

One way to catalyze the isomerization is to attach the catalyst with hydrogen bonds to glucopyranose. As an example, we address $[\text{Al}(\text{H}_2\text{O})_6]^{3+}$ as a catalyst (Table 9, Figure 10) pointing out similarities and differences with respect to the uncatalyzed reaction.

The first step is the formation of the weak $[\text{Al}(\text{H}_2\text{O})_6]^{3+}$ - α -glucopyranose complex, which stabilizes the system by -4.8 kcal/mol . In this complex, the aluminum(III) catalyst is coordinated via hydrogen bonds to the O^1 and O^2 hydroxyl groups of the glucopyranose molecule (Figure 6). Water ligands with hydrogen

bonds to glucopyranose [water(1) and water(2)] have somewhat shorter water-Al³⁺ distances than the other water ligands without such hydrogen bonds. Compared to the uncatalyzed mechanism, the C1-O1 bond is elongated [$\Delta d(\text{C1-O1})=+0.02 \text{ \AA}$], whereas the C1-O5 bond is shortened [$\Delta d(\text{C1-O5})=-0.02 \text{ \AA}$].

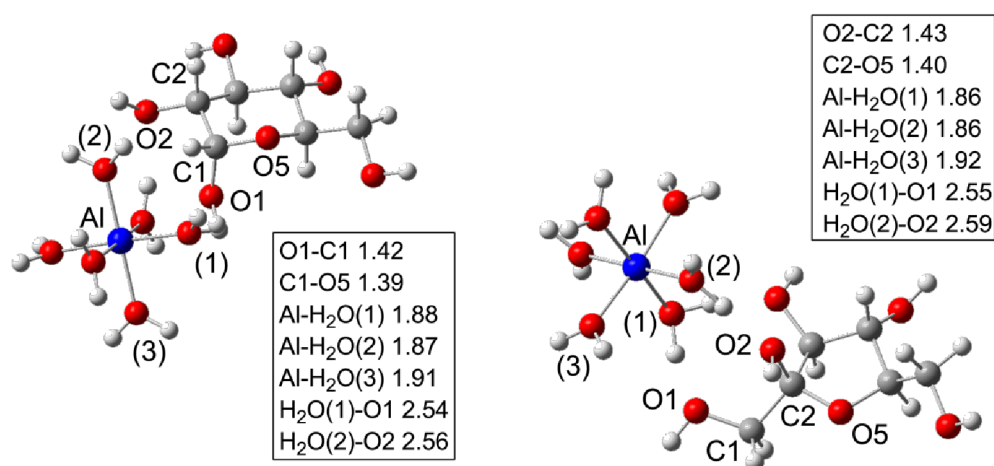


Figure 6: Glucopyranose (left) and fructofuranose (right) form weak complexes with $[\text{Al}(\text{H}_2\text{O})_6]^{3+}$. Distances are given in Ångstrom (PBE0/6-31+G, CPCM(water)).**

In contrast to the uncatalyzed case, the initial deprotonation and reprotonation occur stepwise. The O1 deprotonation energy is -2.8 kcal/mol compared to 25.5 kcal/mol in the uncatalyzed mechanism, while the subsequent O5 protonation is endothermic by 19.8 kcal/mol (similar to the uncatalyzed case). The proton transfer (PT1) leads to a stable O5 protonated glucopyranose. The attached Al³⁺-complex stabilizes the unprotonated hydroxyl group O1, and the C1-O5 bond is shorter than in the uncatalyzed case by 0.13 Å. After surmounting a small barrier of 8.3 kcal/mol, the ring is opened by C1-O5 cleavage (TS1) leading to glucose; TS1 is slightly lower than the energy of the previous minimum due to the inaccuracy of the thermal correction in combination with negative frequencies in Gaussian09.

The following step is the hydrogen atom transfer (TS2, Figure 7). With the $[\text{Al}(\text{H}_2\text{O})_6]^{3+}$ catalyst, TS2 is 10 kcal/mol lower in energy when O2 is protonated rather than deprotonated. While the hydrogen atom is transferred from C2 to C1, O1 is protonated by one of the water ligands of the Al³⁺ complex. Due to the complexation the C1-C2 bond is fixed in the *cis* position; this is advantageous considering that the *cis* transition state was already found to be lower in energy than its *trans* counterpart in the uncatalyzed mechanism (see above). NBO analysis shows that, unlike the uncatalyzed case, s_{H} does not donate into the $\pi^*_{\text{Cx-Oy}}$ orbitals, but the $\pi^*_{\text{Cx-Oy}}$ orbitals donate into s_{H} orbital, leading to an occupancy of 0.633e in s_{H} . The electronic population is 0.695e in the $\pi^*_{\text{C1-O1}}$ orbital and 0.611e in $\pi^*_{\text{C2-O2}}$. The positive charge on the hydrogen atom (0.365 e) is higher than in the uncatalyzed case. Electron density is also transferred into the $\sigma^*_{\text{M-O}}$ orbitals, which have an occupancy that is higher by 0.02 to 0.07e than in the unbound metal complex. The energy of TS2 is 24.4 kcal/mol.

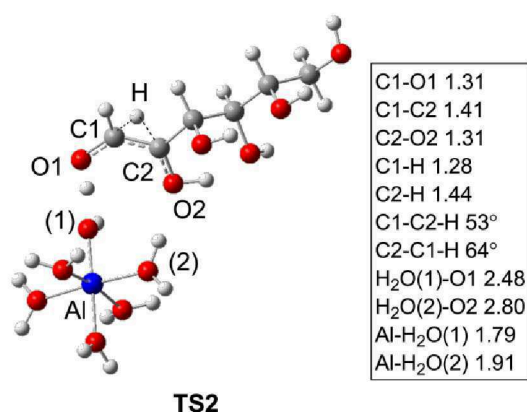


Figure 7: Hydrogen atom transfer (TS2) with attached $[Al(H_2O)_6]^{3+}$ complex. Distances are given in Ångstrom (PBE0/6-31+G**, CPCM(water)).

To obtain the open-chain fructose structure, another protons transfer (PT2) is needed, transferring the proton on O2 to the hydroxyl ligand (1) of the aluminum(III) complex. The deprotonation of O2 gains 19.1 kcal/mol, whereas the protonation of the hydroxyl ligand needs 4.3 kcal/mol.

With a keto group at O2, the structure is now prepared for forming fructofuranose via TS3. Like PT1 and TS1, TS3 and PT3 are stepwise processes. The open chain has to coil up, bringing O5 close to C2 for bond formation. The barrier for C2-O5 bond formation is 8.7 kcal/mol. The O5 deprotonation energy is -19 kcal/mol, the protonation of O2 needs 0.3 kcal/mol.

In the presence of the hydrogen bonded catalyst, the overall reaction becomes exothermic by 3.1 kcal/mol for the glucopyranose to fructofuranose conversion, whereas the uncatalyzed reaction is endothermic. However, the separation of catalyst and fructofuranose needs another 9.4 kcal/mol.

The rate determining transition state of the $[Al(H_2O)_6]^{3+}$ catalyzed isomerization mechanism is the same as in the uncatalyzed reaction: TS2, the hydrogen atom transfer. With $\Delta\Delta G(TS2) = 29$ kcal/mol this barrier is feasible under the reaction conditions.

Example 3: The $[AlO^1O^2(H_2O)_4]^{3+}$ catalyzed glucopyranose fructofuranose isomerization

An alternative to $[Al(H_2O)_6]^{3+}$ is the directly bonded complex $[AlO^1O^2(H_2O)_4]^{3+}$, which includes the hydroxyl groups O1 and O2 as ligands (Figure 11, Table 9). The isomerization mechanism with this catalyst will be compared to the uncatalyzed and the $[Al(H_2O)_6]^{3+}$ catalyzed mechanism.

The first step is the formation of the $[AlO^1O^2(H_2O)_4]^{3+}$ - α -glucopyranose complex, in which two of the formerly coordinating water ligands are exchanged for the two hydroxyl groups at O¹ and O² of α -glucopyranose (Figure 8). The replaced water molecules are not included in the calculation explicitly for simplicity. The complex formation leads to a rise in energy of 2.3 kcal/mol. Due to the association of glucopyranose to the metal center, the chair conformer is slightly distorted bringing O¹ in a more equatorial and O² in a more axial position than in the uncatalyzed case. Continuing the previously observed trend, the C1-O1 bond is elongated [$\Delta d(C1-O1) = +0.07$ Å] and the C1-O5 bond is shortened [$\Delta d(C1-O5) = -0.04$ Å] compared to the hydrogen bonded complex $[Al(H_2O)_6]^{3+}$.

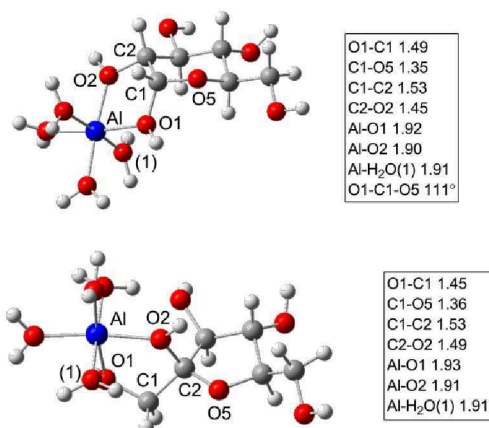


Figure 8: Glucopyranose (top) and fructofuranose (bottom) form weak complexes with $[\text{Al}(\text{H}_2\text{O})_4]^{3+}$. Distances are given in Ångstrom (PBE0/6-31+G, CPCM(water)).**

Analogous to the $[\text{Al}(\text{H}_2\text{O})_6]^{3+}$ mechanism, the initial deprotonation and reprotonation (TS1, PT1) occur stepwise. The deprotonation of O1 becomes even more exothermic with -8.1 kcal/mol, while the O5 protonation reaction energy is 19.1 kcal/mol and thus close to those obtained in examples 1 and 2. No transition state could be located for C1-O5 bond breaking, and scans show no barrier for this cleavage.

For the $[\text{AlO}^1\text{O}^2(\text{H}_2\text{O})_4]^{3+}$ catalyzed isomerization, the sequence DP2, TS2, RP2 is lower in energy by 12 kcal/mol compared to the sequence TS2, PT2. The O2 deprotonation energy in DP2 is -8.8 kcal/mol. The structure of TS2 is different from the $[\text{Al}(\text{H}_2\text{O})_6]^{3+}$ transition state (Figure 9). As O2 is deprotonated, there is no hydrogen bond between the hydroxyl group O3 and O2. Instead, the chain is bent so that water ligand (1) can form a hydrogen bond with O5. It was found that isomerizations with deprotonated O2 prefer ligand-O5 hydrogen bonds, whereas transition states with protonated O2 have O2-O3 hydrogen bonds. The NBO results for TS2 with the bonded catalyst are very similar to TS2 with the hydrogen bonded catalyst: Two electrons are delocalized between $\pi^*_{\text{C1-O1}}$ (0.640e), $\pi^*_{\text{C2-O2}}$ (0.714), and the s orbital of the hydrogen atom (0.650e). The charge on the hydrogen atom is 0.348e. As in the hydrogen bonded catalyst, electron density is pushed into the $\sigma^*_{\text{M-O}}$ orbitals. Their occupation is 0.02-0.03e higher compared to the $[\text{Al}(\text{H}_2\text{O})_6]^{3+}$ catalyzed reaction path. The TS2 energy is only slightly lower than the one of $[\text{Al}(\text{H}_2\text{O})_6]^{3+}$, with $\Delta G(\text{TS2}) = 23.0$ kcal/mol.

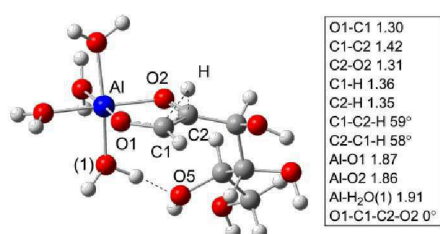


Figure 9: Hydrogen atom transfer (TS2) with the $[\text{Al}(\text{H}_2\text{O})_4]^{3+}$ complex. Distances are given in Ångstrom (PBE0/6-31+G, CPCM(water)).**

After the H-shift O1 is protonated with an energy gain of -9.5 kcal/mol, leading to fructose.

In TS3 the O5-C2 bond is formed with a barrier of 7.0 kcal/mol. The following O5 deprotonation lowers the energy significantly by -18.2 kcal/mol, and the protonation of O2 raises the energy by 5.3 kcal/mol, leading to fructofuranose. The reaction from complexed glucopyranose to fructofuranose is exothermic by -16 kcal/mol. The fructofuranose catalyst separation needs 15 kcal/mol.

Like in examples 1 and 2, the hydrogen atom transfer (TS2) is the rate determining step. The energy for TS2 is lower than for the $[\text{Al}(\text{H}_2\text{O})_6]^{3+}$ catalyzed reaction (23 vs. 29 kcal/mol). The fructofuranose-catalyst complex has an energy of -14 kcal/mol and is thus more stable than in the former examples.

The three examples show the following: The metal complex supports the proton transfers and the hydrogen atom shift, by accepting the electron density from deprotonated oxygen atoms and the broken C2-H bond. The deprotonation of O1 becomes more exothermic and the TS2 energy is lowered. The closer the metal cation to the C1-C2 bond, the better both are stabilized. How much this stabilization changes with different metal cations and ligands will now be investigated.

Comparison with previous computational studies

Mu *et al.*^[13] proposed a mechanism in ionic liquids that requires only direct proton transfers and keto-enol-tautomerization, similar to what we considered as an alternative mechanism (see Supporting Information). In our systems, such pathways were found to be higher in energy than our preferred pathway, and hence we did not investigate this alternative further.

The studies by van Santen^[14] and Hensen^[11, 15] in ionic liquids proposed a mechanism similar to ours. It differs only in that the proton transfers are not considered explicitly, with the focus being on the hydrogen shift (TS2). The authors found that O2 has to be deprotonated in TS2 (sequence DP2, TS2, RP2 in our study) and that the transition state barrier is lowered by using a dimeric complex. This is in contrast to our results in water: for some catalysts, the deprotonation before TS2 is unfavorable and a dimeric chromium(III) complex is higher in energy compared to the monomeric species. The differences might stem from the different stabilization of the stationary points by the solvent (ionic liquids vs. water).

Iron(II) and copper(II) catalysts yield a low conversion both in water and in ionic liquids. In the previous studies in ionic liquids, the inactivity of these metal cations was attributed to the inability of the MCl_4^{2-} species to coordinate to the sugar, instead a nonselective deprotonation of glucose by the Cl^- ligands was proposed. Again, there are differences to our results in water, where the formation of copper(II)- and iron(III)-glucose complexes is favorable (and only slightly unfavorable if hydroxyl ligands are attached).

These comparisons show that the solvent influences the reaction: While dimers and chloride ligands are helpful in the case of ionic liquids, they are obstructive in water. Despite these differences the rate determining step, a hydrogen shift, is the same in all studies.

Overview over all mechanisms

In the preceding example section, two types of metal catalyzed reaction mechanisms were described. Metal catalysts that are bonded to glucose, catalyze the reaction in the same way as $[\text{AlO}^1\text{O}^2(\text{H}_2\text{O})_4]^{3+}$, while hydrogen bonded catalysts take the same pathway as $[\text{Al}(\text{H}_2\text{O})_6]^{3+}$. The sequence DP2, TS2, RP2 is found for the $[\text{MO}^1\text{O}^2(\text{H}_2\text{O})_4]^{3+}$ and $\text{M}_2(\text{H}_2\text{O})_8(\text{OH})_2^{4+}$ catalysts, whereas the pathway TS2, PT2 applies for all other complexes and all magnesium(II) complexes. As an overview over the computational results, we present energy tables and energy diagrams of the lowest pathways for all metals with different ligand constitutions (Table 9 - Table 16, Figure 10 - Figure 18). Thereafter, the rate determining steps will be discussed in detail and compared for individual catalysts.

The complete mechanism was calculated for most of the complexes. In some cases, computations were performed only for the most important steps (TS2, PT1) and for the catalyst-glucopyranose and catalyst-fructofuranose complexes.

Aluminum

Table 9: Relative free energies for allisomerizations catalyzed by an aluminum(III) complex. Energy reference is the sum of the energies of the $[\text{Al}(\text{H}_2\text{O})_6]^{3+}$ complex and α -glucopyranose (PBE0/6-31+G, CPCM(water)).**

catalyst →	$\text{Al}(\text{H}_2\text{O})_6^{3+}$	$\text{Al}(\text{H}_2\text{O})_3\text{OH}^{2+}$	$\text{Al}(\text{H}_2\text{O})_3\text{Cl}^{2+}$		$\text{Al}(\text{H}_2\text{O})_4^{3+}$	$\text{Al}_2(\text{H}_2\text{O})_8(\text{OH})_2^{4+}$
structure ↓	$\Delta\text{G} / \text{kcal mol}^{-1}$	$\Delta\text{G} / \text{kcal mol}^{-1}$	$\Delta\text{G} / \text{kcal mol}^{-1}$	structure	$\Delta\text{G} / \text{kcal mol}^{-1}$	$\Delta\text{G} / \text{kcal mol}^{-1}$
$\text{Al}(\text{H}_2\text{O})_6^{3+} + \text{glucop.}$	0.0	0.0	0.0	$\text{Al}(\text{H}_2\text{O})_6^{3+} + \text{glucop.}$	0.0	0.0
modified cat. ref.		15.7	-21.3	modified cat. ref.		
compl. gluc.	-4.8	13.6	-21.1	compl. gluc.	2.3	
PT1 – deprot	-7.6	11.4	-29.6	PT1 – deprot	-5.8	
PT1 – prot	12.2	30.1	-8.0	PT1 – prot	13.3	
glucop. O5 prot.	8.0	27.4	-11.9	glucopyranose O5 prot.	11.0	
TS1	8.3			TS1		
glucose	-0.1	19.1	-18.7	glucose	7.0	
				DP2	-4.4	
				deprot. glucose	10.4	36.0
TS2	24.4	41.0	1.8	TS2	23.0	40.1
deprot. fructose	13.8	28.9	-12.6	deprot. fructose	6.4	10.0
PT2 – deprot.	-5.3	11.9	-28.5	RP2	16.0	
PT2 – prot.	-1.0	15.8	-21.1			
fructose	2.5	9.7	-20.4	fructose	-1.3	
TS3	8.7	17.5	-13.8	TS3	7.0	
fructofuranose O5 prot.	9.4	16.4	-16.6	fructofuranose O5 prot.	0.7	
PT 3 – deprot.	-9.5	-1.5	-35.3	PT 3 – deprot.	-17.5	
PT 3 – prot.	-9.8	0.5	-26.3	PT 3 – prot.	-12.2	
fructofuranose	-7.9	-0.5	-32.8	fructofuranose	-13.9	
sep. compl.		17.2	-19.8	sep. compl.		
$\text{Al}(\text{H}_2\text{O})_6^{3+} + \text{fructop.}$	1.5	1.5	1.5	$\text{Al}(\text{H}_2\text{O})_6^{3+} + \text{fructop.}$	1.5	1.5

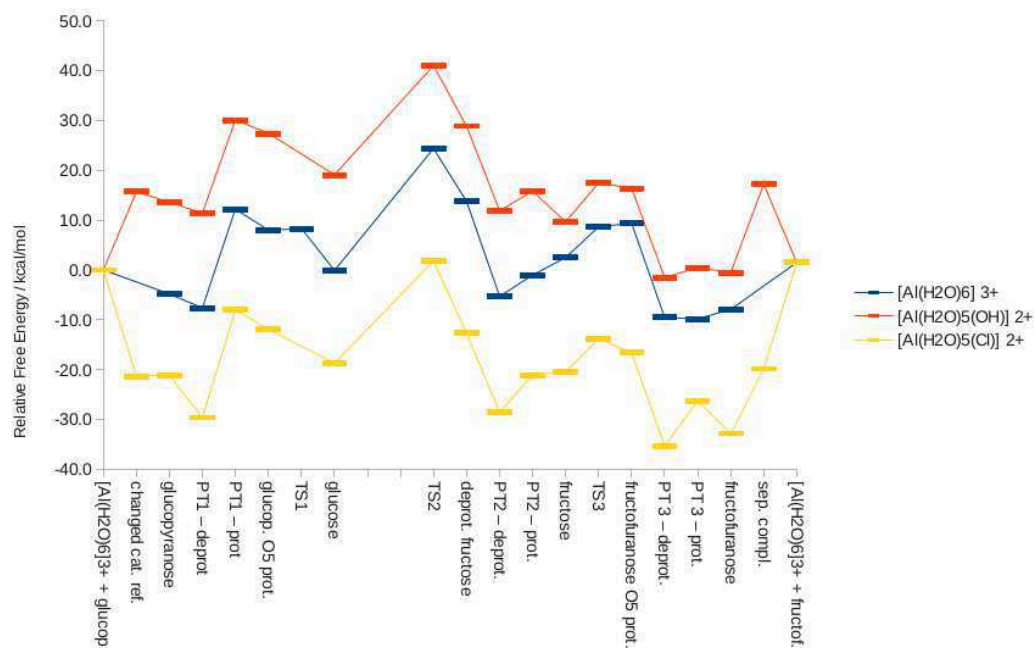


Figure 10: Relative free energy profiles (kcal mol⁻¹) for isomerization catalyzed by an aluminum(III) complex, sequence TS2, PT2. Energy reference is the sum of the energies of the [Al(H₂O)₆]³⁺ complex and α-glucopyranose (PBE0/6-31+G**, CPCM(water)).

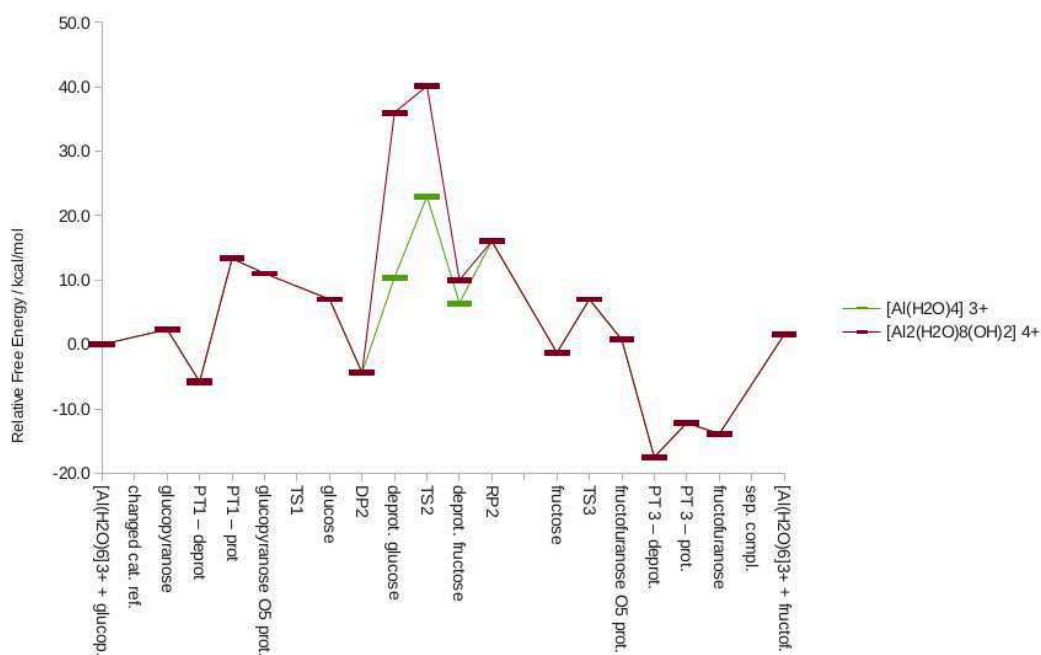


Figure 11: Relative free energy profiles (kcal mol⁻¹) for isomerizations catalyzed by an aluminum(III) complex, sequence DP2, TS2, RP2. Energy reference is the sum of the energies of the [Al(H₂O)₆]³⁺ complex and α-glucopyranose (PBE0/6-31+G**, CPCM(water)).

Chromium

Table 10: Relative free energies for all isomerizations catalyzed by a chromium(III) complex, sequence: TS2, PT2. Energy reference is the sum of the energies of the $[\text{Cr}(\text{H}_2\text{O})_6]^{3+}$ complex and α -glucopyranose (PBE0/6-31+G, CPCM(water)).**

catalyst →	$\text{Cr}(\text{H}_2\text{O})_6^{3+}$	$\text{Cr}(\text{H}_2\text{O})_3\text{OH}^{2+}$	$\text{Cr}(\text{H}_2\text{O})_3\text{Cl}^{2+}$	$\text{Cr}(\text{H}_2\text{O})_2\text{Cl}_2^+$	$\text{Cr}(\text{H}_2\text{O})\text{Cl}_3$
structure ↓	$\Delta G / \text{kcal mol}^{-1}$	$\Delta G / \text{kcal mol}^{-1}$	$\Delta G / \text{kcal mol}^{-1}$	$\Delta G / \text{kcal mol}^{-1}$	$\Delta G / \text{kcal mol}^{-1}$
$\text{Cr}(\text{H}_2\text{O})_6^{3+}$ + glucop.	0.0	0.0	0.0	0.0	0.0
modified cat. ref.		8.5	-27.8	-50.2	-64.4
compl. gluc.	-4.4	6.4	-29.9	-53.5	-65.4
PT1 – deprot	-5.9	6.3	-33.4	-54.5	-61.8
PT1 – prot	13.9	25.4	-13.8	-36.1	-45.7
glucop. O5 prot.	5.5	20.5	-17.3	-37.1	
TS1	7.2				
glucose	-2.6	7.0	-24.9	-46.2	-61.7
TS2	22.5	34.2	-4.0	-21.1	-33.8
deprot. fructose	9.4	20.8	-18.0	-32.6	-41.2
PT2 – deprot.	-9.8	5.0	-38.1	-49.7	
PT2 – prot.	-5.9	3.1	-31.8	-49.1	
fructose	2.4	8.3	-32.6	-50.1	
TS3	6.8	16.1	-22.7		
fructofuranose O5 prot.	6.5	14.3	-26.1	-42.2	
PT 3 – deprot.	-11.3	11.2	-34.5	-57.7	
PT 3 – prot.	-10.7	9.6	-30.7	-59.0	
fructofuranose	-11.6	-4.5	-43.4	-61.5	-69.8
sep. compl.		9.9	-26.4	-48.7	-63.0
$\text{Cr}(\text{H}_2\text{O})_6^{3+}$ + fructop.	1.5	1.5	1.5	1.5	1.5

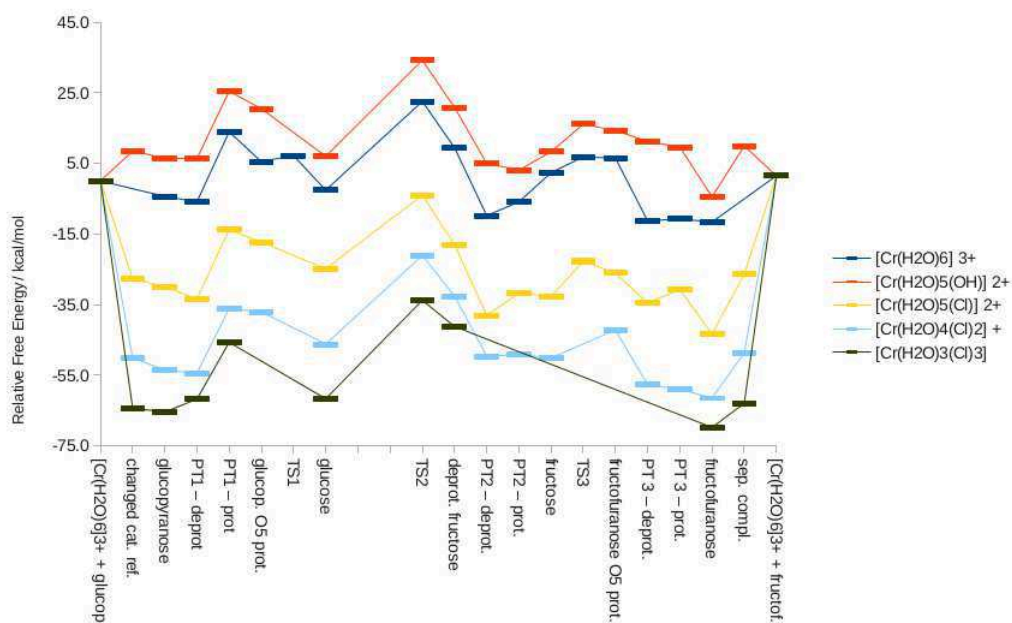


Figure 12: Relative free energy profiles (kcal mol^{-1}) for isomerizations catalyzed by a chromium(III) complex, sequence TS2, PT2. Energy reference is the sum of the energies of the $[\text{Cr}(\text{H}_2\text{O})_6]^{3+}$ complex and α -glucopyranose (PBE0/6-31+G**, CPCM(water)).

Table 11: Relative free energies for all isomerizations catalyzed by a chromium(III) complex, sequence: DP2,TS2, RP2. Energy reference is the sum of the energies of the $[\text{Cr}(\text{H}_2\text{O})_6]^{3+}$ complex and α -glucopyranose (PBE0/6-31+G**, CPCM(water)).

structure ↓	catalyst →	$\text{Cr}(\text{H}_2\text{O})_4^{3+}$ $\Delta G / \text{kcal mol}^{-1}$	$\text{Cr}_2(\text{H}_2\text{O})_8(\text{OH})_2^{4+}$ $\Delta G / \text{kcal mol}^{-1}$
$\text{Cr}(\text{H}_2\text{O})_6^{3+} + \text{glucop.}$		0.0	0.0
modified cat. ref.			
compl. gluc.		0.7	
PT1 – deprot		-4.1	
PT1 – prot		16.2	
glucopyranose O5 prot.		4.9	
TS1			
glucose		0.9	
DP2		-7.5	
deprot. glucose		4.4	32.3
TS2		18.0	36.2
deprot. fructose		0.2	5.8
RP2		9.3	
fructose		-4.6	
TS3		2.8	
fructofuranose O5 prot.		-2.9	
PT 3 – deprot.		-24.8	
PT 3 – prot.		-18.6	
fructofuranose		-16.8	
sep. compl.			
$\text{Cr}(\text{H}_2\text{O})_6^{3+} + \text{fructop.}$		1.5	1.5

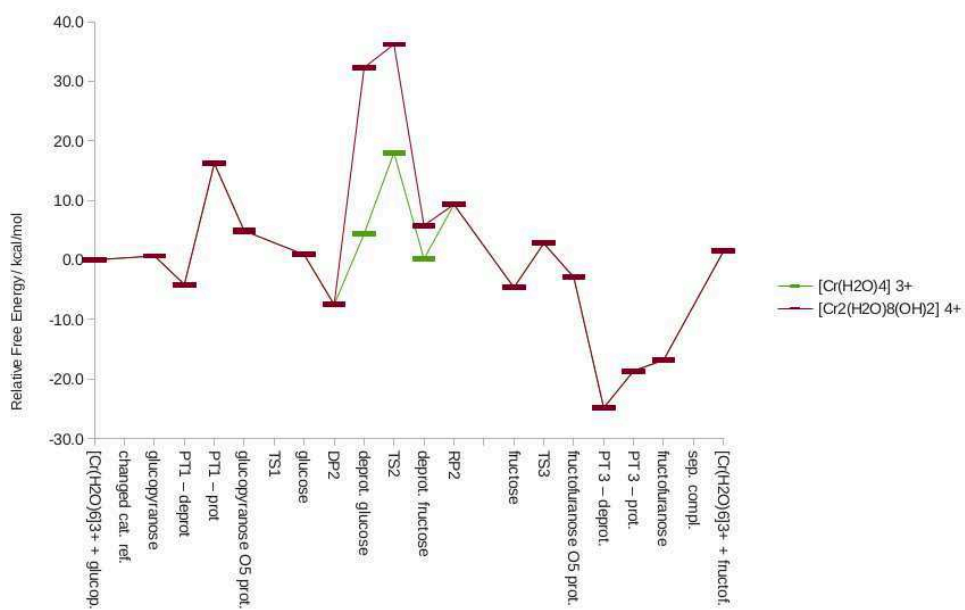


Figure 13: Relative free energy profiles (kcal mol⁻¹) for isomerizations catalyzed by a chromium(III) complex, sequence DP2, TS2, RP2. Energy reference is the sum of the energies of the [Cr(H₂O)₆]³⁺ complex and α-glucopyranose (PBE0/6-31+G**, CPCM(water)).

Iron

Table 12: Relative free energies for all isomerizations catalyzed by an iron(III) complex, sequence: TS2, PT2. Energy reference is the sum of the energies of the $[\text{Fe}(\text{H}_2\text{O})_6]^{3+}$ complex and α -glucopyranose (PBE0/6-31+G, CPCM(water)).**

catalyst →	$\text{Fe}(\text{H}_2\text{O})_3\text{Cl}^{2+}$	$\text{Fe}(\text{H}_2\text{O})_2(\text{OH})\text{Cl}^+$	$\text{Fe}(\text{H}_2\text{O})_2\text{Cl}_2^+$	$\text{Fe}(\text{H}_2\text{O})(\text{OH})\text{Cl}_2$	$\text{Fe}(\text{H}_2\text{O})\text{Cl}_3$	$\text{Fe}(\text{OH})\text{Cl}_3^-$
structure ↓	$\Delta G / \text{kcal mol}^{-1}$	$\Delta G / \text{kcal mol}^{-1}$	$\Delta G / \text{kcal mol}^{-1}$	$\Delta G / \text{kcal mol}^{-1}$	$\Delta G / \text{kcal mol}^{-1}$	$\Delta G / \text{kcal mol}^{-1}$
$\text{Fe}(\text{H}_2\text{O})_6^{3+}$ glucop.	0.0	0.0	0.0	0.0	0.0	0.0
modified cat. ref.	-31.8	-31.8	-55.2	-55.2	-72.3	-70.1
modified cat. ref. 2		-13.5		-28.4		
compl. gluc.	-35.6	-21.0	-60.4	-35.1	-73.9	
PT1 – deprot	-40.0	-18.4	-61.8	-30.7	-70.2	
PT1 – prot	-20.5	-1.7	-44.6	-16.1	-54.6	
glucop. O5 prot.	-24.3		-44.3			
TS1						
glucose	-27.8	-12.9	-51.7	-27.3	-68.1	
TS2	-5.4	10.2	-25.0	-3.6	-42.2	-9.6
deprot. fructose	-13.8	-3.6	-49.0	-15.9	-58.8	
PT2 – deprot.	-36.8		-59.7			
PT2 – prot.	-29.8		-54.8			
fructose	-37.2		-50.4			
TS3						
fructofuranose O5 prot.	-29.3		-48.8			
PT 3 – deprot.	-46.6		-59.1			
PT 3 – prot.	-45.7		-58.1			
fructofuranose	-46.4	-25.9	-65.3	-36.5	-73.9	
sep. compl.	-30.3	-12.0	-53.7	-27.0	-70.9	
$\text{Fe}(\text{H}_2\text{O})_6^{3+}$ fructop.	1.5	1.5	1.5	1.5	1.5	

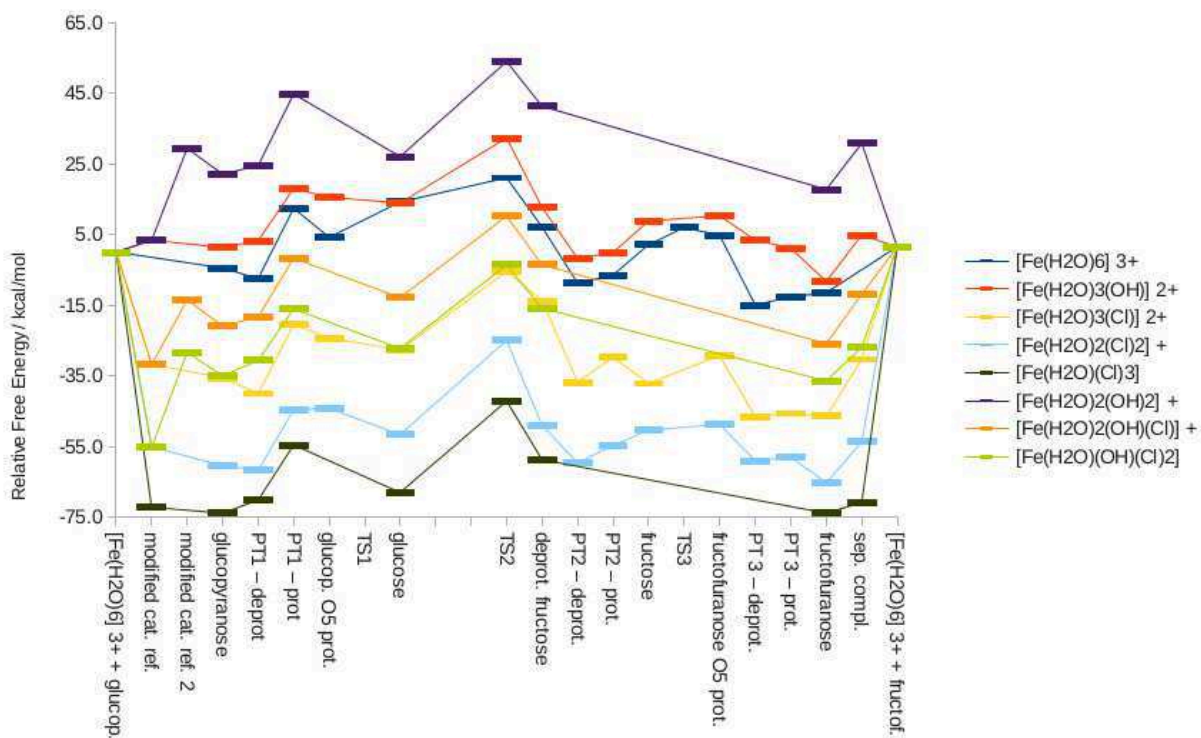


Figure 14: Relative free energy profiles (kcal mol⁻¹) for isomerizations catalyzed by an iron(III) complex, sequence TS2, PT2. Energy reference is the sum of the energies of the [Fe(H₂O)₆]³⁺ complex and α-glucopyranose (PBE0/6-31+G**, CPCM(water)).

Table 13: Relative free energies for all isomerizations catalyzed by an iron(III) complex, sequence: TS2, PT2 (left); DP2, TS2, RP2 (right). Energy reference is the sum of the energies of the $[\text{Fe}(\text{H}_2\text{O})_6]^{3+}$ complex and α -glucopyranose (PBE0/6-31+G, CPCM(water)).**

catalyst →	$\text{Fe}(\text{H}_2\text{O})_6^{3+}$	$\text{Fe}(\text{H}_2\text{O})_3\text{OH}^{2+}$	$\text{Fe}(\text{H}_2\text{O})_2(\text{OH})_2^+$		$\text{Fe}(\text{H}_2\text{O})_4^{3+}$	$\text{Fe}_2(\text{H}_2\text{O})_8(\text{OH})_2^{4+}$
structure ↓	$\Delta\text{G} / \text{kcal mol}^{-1}$	$\Delta\text{G} / \text{kcal mol}^{-1}$	$\Delta\text{G} / \text{kcal mol}^{-1}$	structure	$\Delta\text{G} / \text{kcal mol}^{-1}$	$\Delta\text{G} / \text{kcal mol}^{-1}$
$\text{Fe}(\text{H}_2\text{O})_6^{3+}$ + glucop.	0.0	0.0	0.0	$\text{Fe}(\text{H}_2\text{O})_6^{3+}$ + glucop.	0.0	0.0
modified cat. ref.		3.3	3.3	modified cat. ref.		
modified cat. ref. 2			29.4			
compl. gluc.	-4.5	1.3	22.0	compl. gluc.	2.1	
PT1 – deprot	-7.5	3.2	24.5	PT1 – deprot	-6.9	
PT1 – prot	12.4	18.0	44.8	PT1 – prot	14.9	
glucop. O5 prot.	4.2	15.5		glucopyranose O5 prot.	2.1	
TS1				TS1	5.0	
glucose	14.2	13.9	27.0	glucose	-5.1	
				DP2		
				deprot. glucose	1.6	23.5
TS2	21.0	32.3	53.9	TS2	20.3	31.1
deprot. fructose	7.1	12.6	41.3	deprot. fructose	-2.8	3.1
PT2 – deprot.	-8.8	-1.8		RP2	7.8	
PT2 – prot.	-6.5	-0.1				
fructose	2.1	8.8		fructose	-4.1	
TS3	6.9			TS3	3.8	
fructofuranose O5 prot.	4.8	10.3		fructofuranose O5 prot.	1.6	
PT 3 – deprot.	-15.0	3.4		PT 3 – deprot.	-21.1	
PT 3 – prot.	-12.7	1.1		PT 3 – prot.	-15.4	
fructofuranose	-11.5	-8.3	17.7	fructofuranose	-15.8	
sep. compl.		4.8	30.8	sep. compl.		
$\text{Fe}(\text{H}_2\text{O})_6^{3+}$ + fructop.	1.5	1.5	1.5	$\text{Fe}(\text{H}_2\text{O})_6^{3+}$ + fructop.	1.5	1.5

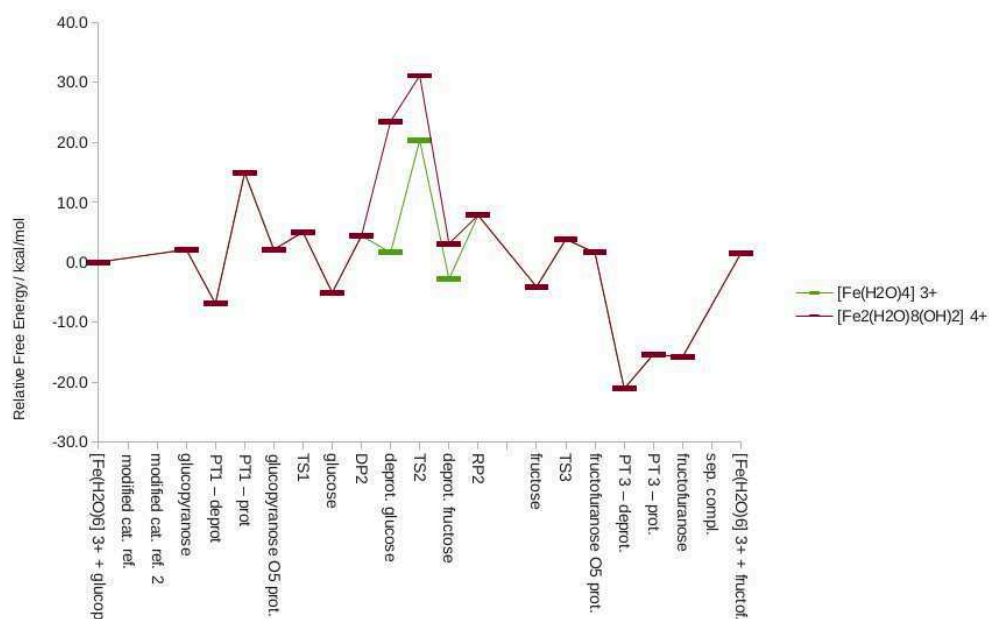


Figure 15: Relative free energy profiles (kcal mol⁻¹) for isomerizations catalyzed by an iron(III) complex, sequence DP2, TS2, RP2. Energy reference is the sum of the energies of the [Fe(H₂O)₆]³⁺ complex and α -glucopyranose (PBE0/6-31+G**, CPCM(water)).

Copper

Table 14: Relative free energies for all isomerizations catalyzed by a copper(II) complex, sequence: TS2, PT2. Energy reference is the sum of the energies of the [Cu(H₂O)₆]²⁺ complex and α -glucopyranose (PBE0/6-31+G**, CPCM(water)).

catalyst →	Cu(H ₂ O) ₆ ²⁺	Cu(H ₂ O)Cl ⁺	CuCl ₂
structure ↓	$\Delta G / \text{kcal mol}^{-1}$	$\Delta G / \text{kcal mol}^{-1}$	$\Delta G / \text{kcal mol}^{-1}$
Cu(H ₂ O) ₆ ²⁺ + glucop.	0.0	0.0	0.0
modified cat. ref.		-26.5	-42.4
compl. gluc.	-1.2	-31.7	-49.9
PT1 - deprot		-26.2	-40.4
PT1 - prot		-11.6	-21.3
glucop. O5 prot.			
TS1			
glucose	4.9	-20.1	-37.8
TS2	35.5	11.5	-7.2
deprot. fructose	24.4	5.3	-11.8
PT2 - deprot.			
PT2 - prot.			
fructose			-45.9
TS3			
fructofuranose O5 prot.			
PT 3 - deprot.			
PT 3 - prot.			
fructofuranose	-3.5	-31.6	-49.2
sep. compl.		-25.1	-40.9
Cu(H ₂ O) ₆ ²⁺ + fructop.	1.5	1.5	1.5

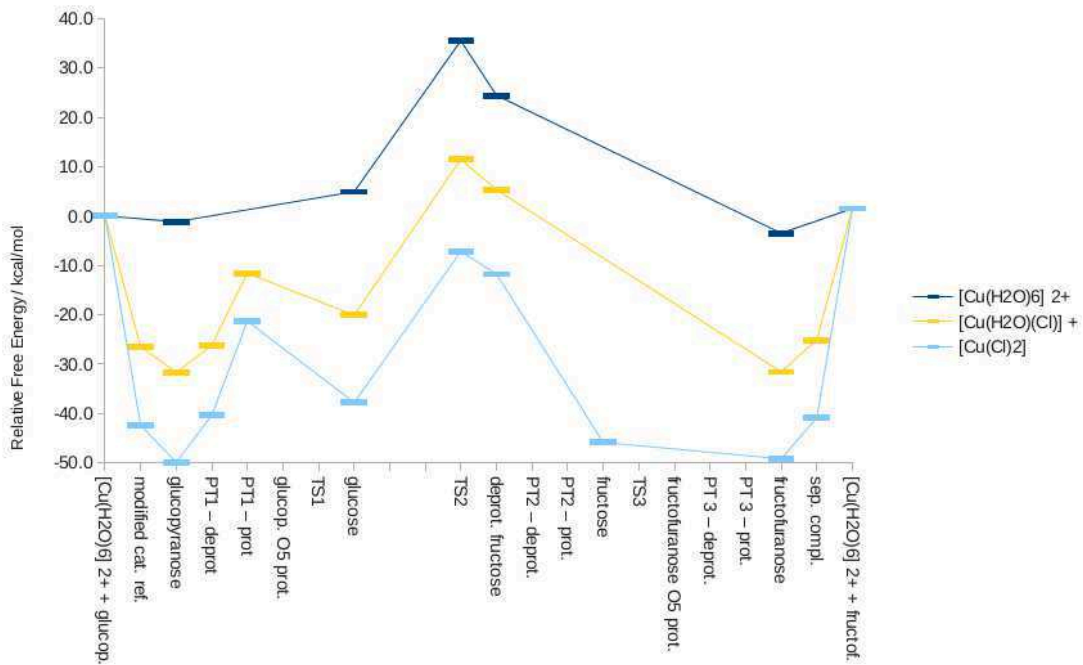


Figure 16: Relative free energy profiles (kcal mol^{-1}) for isomerizations catalyzed by a copper(II) complex, sequence TS2, PT2. Energy reference is the added energy of the $[\text{Cu}(\text{H}_2\text{O})_6]^{3+}$ complex and α -glucopyranose (PBE0/6-31+G**, CPCM(water)).

Table 15: Relative free energies for all isomerizations catalyzed by a copper(II) complex, sequence: DP2, TS2, RP2. Energy reference is the sum of the energies of the $[\text{Cu}(\text{H}_2\text{O})_6]^{2+}$ complex and α -glucopyranose (PBE0/6-31+G, CPCM(water)).**

catalyst →	$\text{Cu}(\text{H}_2\text{O})_4^{2+}$	$\text{Cu}(\text{H}_2\text{O})_2^{2+}$
structure ↓	$\Delta\text{G} / \text{kcal mol}^{-1}$	$\Delta\text{G} / \text{kcal mol}^{-1}$
$\text{Cu}(\text{H}_2\text{O})_6^{2+}$ + glucop.	0.0	0.0
modified cat. ref.		
compl. gluc.	-0.4	-7.4
PT1 – deprot	-2.3	-2.9
PT1 – prot		12.7
glucopyranose O5 prot.		
TS1		
glucose	2.5	
DP2		
deprot. glucose	23.0	18.6
TS2	36.1	30.8
deprot. fructose	18.6	13.2
RP2		
fructose	-4.6	
TS3		
fructofuranose O5 prot.		
PT 3 – deprot.		
PT 3 – prot.		
fructofuranose	-2.5	-9.0
sep. compl.		
$\text{Cu}(\text{H}_2\text{O})_6^{2+}$ + fructop.	1.5	1.5

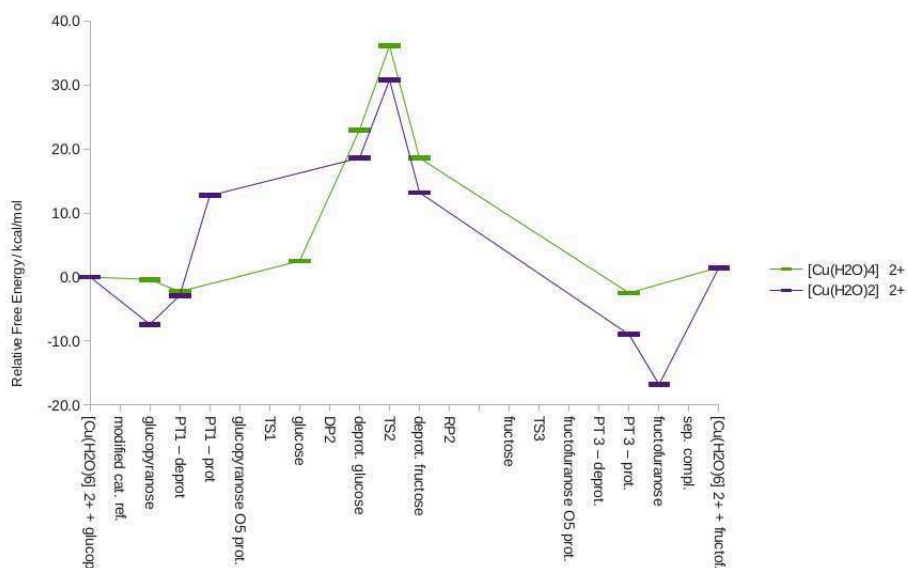


Figure 17: Relative free energy profiles (kcal mol^{-1}) for isomerizations catalyzed by a copper(II) complex, sequence DP2, TS2, RP2. Energy reference is the sum of the energies of the $[\text{Cu}(\text{H}_2\text{O})_6]^{2+}$ complex and α -glucopyranose (PBE0/6-31+G, CPCM(water)).**

Magnesium

Table 16: Relative free energies for all isomerizations catalyzed by a magnesium(II) complex, sequence: TS2, PT2. Energy reference is the sum of the energies of the $[\text{Mg}(\text{H}_2\text{O})_6]^{2+}$ complex and α -glucopyranose (PBE0/6-31+G**, CPCM(water)).

catalyst →	$[\text{Mg}(\text{H}_2\text{O})_6]^{2+}$	$[\text{Mg}(\text{H}_2\text{O})_4]^{2+}$		
structure ↓	$\Delta\text{G} / \text{kcal mol}^{-1}$	$\Delta\text{G} / \text{kcal mol}^{-1}$		
$\text{Mg}(\text{H}_2\text{O})_6^{2+}$ + glucop.	0.0	0.0		
modified cat. ref.				
compl. gluc.	2.1	-0.7		
PT1 – deprot	13.3	12.3		
PT1 – prot	33.7	25.5		
glucop. O5 prot.				
TS1				
glucose	9.1	4.7		
TS2	40.1	34.4		
deprot. fructose	34.0	27.5		
PT2 – deprot.	19.4	31.3		
PT2 – prot.	6.3	26.4		
fructose	8.1	0.2		
TS3				
fructofuranose O5 prot.	38.6	42.6		
PT 3 – deprot.	24.7	-2.8		
PT 3 – prot.	11.9	-14.9		
fructofuranose	1.9	-5.9		
sep. compl.				
$\text{Mg}(\text{H}_2\text{O})_6^{2+}$ + fructop.	1.5	1.5		

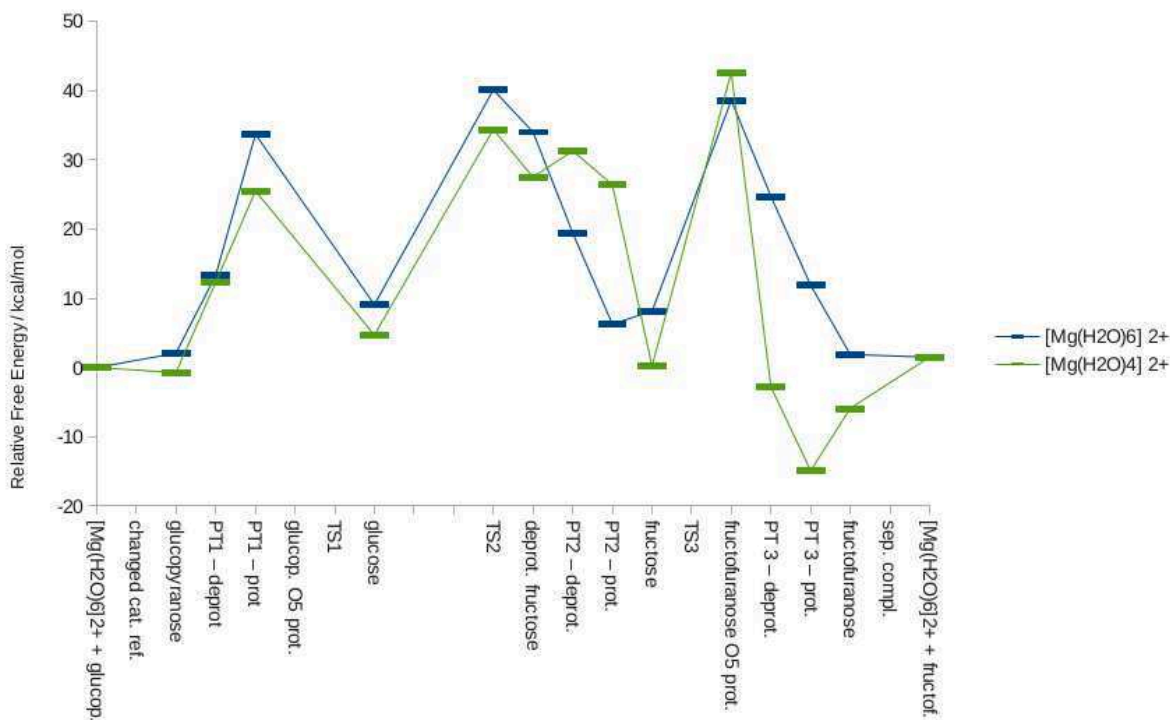


Figure 18: Relative free energy profiles (kcal mol⁻¹) for isomerizations catalyzed by a magnesium(II) complex, sequence TS2, PT2. Energy reference is the sum of the energies of the [Mg(H₂O)₆]²⁺ complex and α-glucopyranose (PBE0/6-31+G**, CPCM(water)).

Absolute energies of important structures

Table 17: Absolute free energies, solvated and in vacuum, for the calculation of the deprotonation of [M(H₂O)₆]ⁿ⁺ catalysts by a thermodynamic cycle.

	G_vacuum(PBE0/6-31+G**) / a.u.	G_solvated(PBE0/6-31+G**, SMD) / a.u.
[Cu(H ₂ O) ₆] ²⁺	-2097.559	-2097.907
[Cu(H ₂ O) ₅ OH] ⁺	-2097.330	-2097.435
H ₃ O ⁺	-76.610	literature value (see above)
H ₂ O	-76.346	literature vale (see above)
[Mg(H ₂ O) ₆] ²⁺	-657.619	-657.947
[Mg(H ₂ O) ₅ OH] ⁺	-657.362	-657.484
[Cr(H ₂ O) ₆] ³⁺	-1501.196	-1501.947
[Cr(H ₂ O) ₅ OH] ²⁺	-1501.151	-1501.517
[Al(H ₂ O) ₆] ³⁺	-699.379	-700.110
[Al(H ₂ O) ₅ OH] ²⁺	-699.327	-699.682
[Fe(H ₂ O) ₆] ³⁺	-1720.334	-1721.093
[Fe(H ₂ O) ₅ OH] ²⁺	-1720.302	-1720.670

Table 18: Absolute free energies of different functionals for the isomerization with $[\text{AlO}^1\text{O}^2(\text{H}_2\text{O})_4]^{3+}$ catalyst comparison with used method.

	G(B3LYP/6-31+G**) / a.u.	G(M06/6-31+G**) / a.u.	G(PBE0/6-311+G**) / a.u.
glucopyranose	-687.087	-686.729	-686.551
fructofuranose	-687.083	-686.725	-686.548
$[\text{Al}(\text{H}_2\text{O})_6]^{3+}$	-700.656	-700.432	-700.217
H_2O	-76.439	-76.403	-76.382
H_3O^+	-76.816	-76.779	-76.761
glucosepyranose + $[\text{Al}(\text{H}_2\text{O})_6]^{3+}$	-1387.743	-1387.161	-1386.767
glucopyranose	-1234.854	-1234.350	-1234.002
PT1			
glucopyranose O5 prot.	-1234.847	-1234.338	-1233.992
TS1			
glucose	-1234.856	-1234.342	-1233.996
DP2			
deprot. glucose	-1234.469	-1233.962	-1233.610
TS2	-1234.445	-1233.937	-1233.591
deprot. fructose	-1234.474	-1233.965	-1233.616
RP2			
fructose	-1234.867	-1234.359	-1234.008
TS3	-1234.855	-1234.345	-1233.996
fructofuranose O5 prot.	-1234.855	-1234.348	-1234.004
PT3			
fructofuranose	-1234.864	-1234.357	-1234.012
fructofuranose + $[\text{Al}(\text{H}_2\text{O})_6]^{3+}$	-1387.739	-1387.157	-1386.765

Table 19: Absolute energies at 413 K and 80 bar for critical steps in the glucose-fructose isomerization with selected Al^{3+} and Fe^{3+} catalysts (PBE0/6-31+G, CPCM(water)).**

	E / a.u.	E_ZPC / a.u.	H / a.u.	G / a.u.
glucose	-686.502	-686.304	-686.280	-686.359
fructose	-686.498	-686.301	-686.276	-686.357
$[\text{Al}(\text{H}_2\text{O})_6]^{3+}$	-700.153	-699.996	-1083.877	-700.050
$[\text{Al}(\text{H}_2\text{O})_5\text{Cl}]^{2+}$	-1084.034	-1083.903	-1083.877	-1083.958
$[\text{Fe}(\text{H}_2\text{O})_6]^{3+}$	-1721.088	-1720.937	-1720.907	-1720.999
$[\text{Fe}(\text{H}_2\text{O})_5\text{Cl}]^{2+}$	-2104.989	-2104.861	-2104.833	-2104.924
H_2O	-76.357	-76.336	-76.331	-76.357
H_3O^+	-76.750	-76.714	-76.709	-76.737
Cl^-	-460.213	-460.213	-460.210	-460.230
glucopyranose- $[\text{Al}(\text{H}_2\text{O})_6]^{3+}$	-1386.685	-1386.327	-1386.276	-1386.415
glucopyranose- $[\text{AlO}^1\text{O}^2(\text{H}_2\text{O})_4]^{3+}$	-1233.920	-1233.614	-1233.571	-1233.691
glucopyranose- $[\text{AlO}^1\text{O}^2(\text{H}_2\text{O})_3\text{Cl}]^{2+}$	-1617.809	-1617.526	-1617.485	-1617.600
TS2- $[\text{Al}(\text{H}_2\text{O})_6]^{3+}$	-1386.630	-1386.279	-1386.228	-1386.369
TS2- $[\text{AlO}^1\text{O}^2(\text{H}_2\text{O})_4]^{3+}$	-1233.490	-1233.202	-1233.161	-1233.277
TS2- $[\text{AlO}^1\text{O}^2(\text{H}_2\text{O})_3\text{Cl}]^{2+}$	-1617.761	-1617.488	-1617.446	-1617.565
fructofuranose- $[\text{AlO}^1\text{O}^2(\text{H}_2\text{O})_3\text{Cl}]^{2+}$	-1617.83	-1617.55	-1617.51	-1617.62
glucopyranose- $[\text{Fe}(\text{H}_2\text{O})_6]^{3+}$	-2407.620	-2407.268	-2407.215	-2407.363
glucopyranose- $[\text{FeO}^1\text{O}^2(\text{H}_2\text{O})_4]^{3+}$	-2254.861	-2254.558	-2254.513	-2254.638
glucopyranose- $[\text{FeO}^1\text{O}^2(\text{H}_2\text{O})_3\text{Cl}]^{2+}$	-2638.77	-2638.49	-2638.45	-2638.57
TS2- $[\text{Fe}(\text{H}_2\text{O})_6]^{3+}$	-2407.564	-2407.216	-2407.162	-2407.314
TS2- $[\text{FeO}^1\text{O}^2(\text{H}_2\text{O})_4]^{3+}$	-2254.434	-2254.149	-2254.106	-2254.229
TS2- $[\text{FeO}^1\text{O}^2(\text{H}_2\text{O})_3\text{Cl}]^{2+}$	-2638.713	-2638.441	-2638.398	-2638.525
fructofuranose- $[\text{FeO}^1\text{O}^2(\text{H}_2\text{O})_3\text{Cl}]^{2+}$	-2638.79	-2638.51	-2638.47	-2638.59

Table 20: Absolute binding energies between tetraqua-metal complexes and α -glucopyranose for different coordination sites (PBE0/6-31+G, CPCM(water)).**

α -glucopyranose	coordination site	E / a.u.	E_ZPC / a.u.	H / a.u.	G / a.u.
[Al(H ₂ O) ₄] ³⁺	O ¹ O ²	-1233.920	-1233.614	-1233.589	-1233.664
	O ² O ³	-1233.92486628	-1233.616911	-1233.593087	-1233.665215
	O ³ O ⁴	-1233.92083493	-1233.613066	-1233.588966	-1233.661981
	O ⁴ O ⁶	-1233.93052670	-1233.621721	-1233.598082	-1233.669538
	O ⁵ O ⁶	-1233.92309188	-1233.613300	-1233.589979	-1233.660552
[Fe(H ₂ O) ₄] ³⁺	O ¹ O ²	-2254.861	-2254.558	-2254.532	-2254.610
	O ² O ³	-2254.86637811	-2254.561403	-2254.536585	-2254.612737
	O ³ O ⁴	-2254.86218636	-2254.557711	-2254.532388	-2254.610769
	O ⁴ O ⁶	-2254.87124223	-2254.566390	-2254.541386	-2254.617832
	O ⁵ O ⁶	-2254.86336128	-2254.559149	-2254.533768	-2254.611663
[Cr(H ₂ O) ₄] ³⁺	O ¹ O ²	-2035.731	-2035.424	-2035.400	-2035.475
	O ² O ³	-2035.73204409	-2035.424454	-2035.400401	-2035.475435
	O ³ O ⁴	-2035.73253568	-2035.425346	-2035.401188	-2035.475878
	O ⁴ O ⁶	-2035.74127933	-2035.433248	-2035.409439	-2035.483615
	O ⁵ O ⁶	-2035.73591048	-2035.429116	-2035.404703	-2035.480479
[Mg(H ₂ O) ₄] ²⁺	O ¹ O ²	-1191.786	-1191.485	-1191.457	-1191.539
	O ² O ³	-1191.78893433	-1191.488128	-1191.460445	-1191.543260
	O ³ O ⁴	-1191.78670280	-1191.485220	-1191.457760	-1191.539773
	O ⁴ O ⁶	-1191.79185344	-1191.489092	-1191.462424	-1191.541804
	O ⁵ O ⁶	-1191.78989099	-1191.486784	-1191.460319	-1191.538677
[Cu(H ₂ O) ₄] ²⁺	O ¹ O ²	-2631.720	-2631.418	-2631.391	-2631.474
	O ² O ³	-2631.72930934	-2631.426090	-2631.399568	-2631.480749
	O ³ O ⁴	-2631.73159889	-2631.427519	-2631.401589	-2631.481358
	O ⁴ O ⁶	-2631.73314918	-2631.429816	-2631.403482	-2631.483439
	O ⁵ O ⁶	-2631.73461720	-2631.430462	-2631.404651	-2631.483338

Table 21: Absolute binding energies between tetraaqua-metal complexes and β -glucopyranose for different coordination sites (PBE0/6-31+G, CPCM(water)).**

β -glucopyranose	coordination site	E / a.u.	E_ZPC / a.u.	H / a.u.	G / a.u.
[Al(H ₂ O) ₄] ³⁺	O ¹ O ²	-1233.91368131	-1233.606777	-1233.582327	-1233.656375
	O ² O ³	-1233.91946074	-1233.612345	-1233.588232	-1233.661150
	O ³ O ⁴	-1233.91533046	-1233.608083	-1233.583858	-1233.657009
	O ⁴ O ⁶	-1233.92552784	-1233.616963	-1233.593231	-1233.664770
	O ⁵ O ⁶	-1233.92517332	-1233.617390	-1233.593613	-1233.665597
[Fe(H ₂ O) ₄] ³⁺	O ¹ O ²	-2254.85458427	-2254.552417	-2254.526186	-2254.606767
	O ² O ³	-2254.86044820	-2254.558122	-2254.531884	-2254.612967
	O ³ O ⁴	-2254.85674033	-2254.553290	-2254.527642	-2254.606270
	O ⁴ O ⁶	-2254.86613380	-2254.562551	-2254.536994	-2254.615453
	O ⁵ O ⁶	-2254.86586756	-2254.562240	-2254.536706	-2254.615038
[Cr(H ₂ O) ₄] ³⁺	O ¹ O ²	-2035.72467301	-2035.418785	-2035.394220	-2035.469488
	O ² O ³	-2035.73007941	-2035.424270	-2035.399713	-2035.476340
	O ³ O ⁴	-2035.72690707	-2035.420767	-2035.396270	-2035.471526
	O ⁴ O ⁶	-2035.73631767	-2035.428981	-2035.404939	-2035.479179
	O ⁵ O ⁶	-2035.73584391	-2035.428428	-2035.404750	-2035.477675
[Mg(H ₂ O) ₄] ²⁺	O ¹ O ²	-1191.78266651	-1191.482118	-1191.454361	-1191.536936
	O ² O ³	-1191.78429280	-1191.483647	-1191.455986	-1191.538309
	O ³ O ⁴	-1191.78213422	-1191.481349	-1191.453683	-1191.535888
	O ⁴ O ⁶	-1191.78743220	-1191.485205	-1191.458389	-1191.538056
	O ⁵ O ⁶	-1191.78349407	-1191.481720	-1191.454557	-1191.535573
[Cu(H ₂ O) ₄] ²⁺	O ¹ O ²	-2631.72679291	-2631.423496	-2631.397163	-2631.477429
	O ² O ³	-2631.72634434	-2631.423126	-2631.396854	-2631.476765
	O ³ O ⁴	-2631.72620035	-2631.422689	-2631.396511	-2631.476926
	O ⁴ O ⁶	-2631.72863324	-2631.425563	-2631.399133	-2631.479196
	O ⁵ O ⁶	-2631.73035257	-2631.426007	-2631.400292	-2631.479010

Table 22: Absolute energies of different aluminum(III)-complexes (PBE0/6-31+G, CPCM(water)).**

	non-water ligand position	E / a.u.	E_ZPC / a.u.	H / a.u.	G / a.u.
[Al(H ₂ O) ₄] ³⁺		-547.322	-547.217	-547.206	-547.250
[Al(H ₂ O) ₆] ³⁺		-700.153	-699.996	-699.980	-700.033
[Al(H ₂ O) ₅ Cl] ²⁺		-1084.03	-1083.903	-1083.887	-1083.941
[Al(H ₂ O) ₅ OH] ²⁺		-699.737	-699.592	-699.577	-699.629
α -glucopyranose-[Al(H ₂ O) ₆] ³⁺		-1386.685	-1386.327	-1386.298	-1386.384
α -glucopyranose-[Al(H ₂ O) ₄] ³⁺		-1233.920	-1233.614	-1233.589	-1233.664
α -glucopyranose-[Al(H ₂ O) ₅ Cl] ²⁺	ax1	-1617.805	-1617.523	-1617.499	-1617.572
	ax2	-1617.806	-1617.525	-1617.501	-1617.574
	eq1	-2419.627	-2419.345	-2419.322	-1617.575
	eq2	-1617.809	-1617.526	-1617.503	-1617.575
α -glucopyranose-[Al(H ₂ O) ₅ OH] ²⁺	ax1	-1233.507	-1233.213	-1233.189	-1233.262
	ax2	-1233.511	-1233.216	-1233.193	-1233.266
	eq1	-1233.511	-1233.217	-1233.193	-1233.265
	eq2	-1233.513	-1233.219	-1233.195	-1233.268

Table 23: Absolute energies of different chromium(III)-complexes (PBE0/6-31+G, CPCM(water)).**

	non-water ligand position	E / a.u.	E_ZPC / a.u.	H / a.u.	G / a.u.
$[\text{Cr}(\text{H}_2\text{O})_6]^{3+}$	dublett	-1501.917	-1501.762	-1501.746	-1501.801
$[\text{Cr}(\text{H}_2\text{O})_6]^{3+}$	quartett	-1501.959	-1501.803	-1501.787	-1501.842
$[\text{Cr}(\text{H}_2\text{O})_5\text{Cl}]^{2+}$		-1885.852	-1885.721	-1885.705	-1885.761
$[\text{Cr}(\text{H}_2\text{O})_5\text{OH}]^{2+}$		-1501.551	-1501.409	-1501.392	-1501.449
$[\text{Cr}(\text{H}_2\text{O})_4\text{Cl}_2]^+$	cis	-2269.734	-2269.628	-2269.613	-2269.668
$[\text{Cr}(\text{H}_2\text{O})_4\text{Cl}_2]^+$	trans	-2269.736	-2269.630	-2269.615	-2269.670
$[\text{Cr}(\text{H}_2\text{O})_3\text{Cl}_3]$	mer	-2653.607	-2653.526	-2653.512	-2653.567
$[\text{Cr}(\text{H}_2\text{O})_3\text{Cl}_3]$	fac	-2653.605	-2653.524	-2653.510	-2653.565
α -glucopyranose- $[\text{Cr}(\text{H}_2\text{O})_5\text{Cl}]^{2+}$	ax1	-2419.627	-2419.345	-2419.322	-2419.397
	ax2	-2419.627	-2419.346	-2419.322	-2419.399
	eq1	-2035.323	-2035.030	-2035.006	-2035.081
	eq2	-2035.325	-2035.032	-2035.008	-2035.083
α -glucopyranose- $[\text{Cr}(\text{H}_2\text{O})_5\text{OH}]^{2+}$	ax1	-2035.326	-2035.032	-2035.008	-2035.083
	ax2	-2035.328	-2035.035	-2035.010	-2035.086
	eq1	-2803.512	-2803.256	-2803.232	-2803.307
	eq2	-2803.514	-2803.258	-2803.234	-2803.310
α -glucopyranose- $[\text{Cr}(\text{H}_2\text{O})_4\text{Cl}_2]^+$	ax1ax2	-2803.509	-2803.253	-2803.230	-2803.305
	eq1eq2	-2803.510	-2803.254	-2803.231	-2803.306
	eq1ax2	-2803.511	-2803.256	-2803.232	-2803.307
	eq1ax1	-2803.509	-2803.254	-2803.230	-2803.305
	eq2ax2	-2419.627	-2419.345	-2419.322	-2419.397
	eq2ax1	-2419.627	-2419.346	-2419.322	-2419.399

Table 24: Absolute energies of different iron(III)-complexes (PBE0/6-31+G, CPCM(water)).**

	non-water ligand position	E / a.u.	E_ZPC / a.u.	H / a.u.	G / a.u.
[Fe(H ₂ O) ₆] ³⁺	dublett	-1721.044	-1720.885	-1720.871	-1720.922
[Fe(H ₂ O) ₆] ³⁺	sextett	-1721.088	-1720.937	-1720.919	-1720.979
[Fe(H ₂ O) ₅ Cl] ²⁺		-2104.989	-2104.861	-2104.844	-2104.904
[Fe(H ₂ O) ₅ OH] ²⁺		-1720.689	-1720.550	-1720.532	-1720.595
[Fe(H ₂ O) ₄ Cl ₂] ⁺	cis	-2488.876	-2488.772	-2488.756	-2488.816
	trans	-2488.875	-2488.771	-2488.755	-2488.813
[Fe(H ₂ O) ₃ Cl ₃]	mer	-2872.750	-2872.671	-2872.657	-2872.713
	fac	-2872.755	-2872.675	-2872.660	-2872.717
[Fe(H ₂ O) ₄ ClOH] ⁺	cis	-2104.571	-2104.455	-2104.439	-2104.497
	trans	-2104.568	-2104.453	-2104.436	-2104.496
[Fe(H ₂ O) ₃ Cl ₂ OH]	cis	-2488.442	-2488.352	-2488.336	-2488.394
	trans OH	-2488.439	-2488.348	-2488.332	-2488.390
	trans Cl	-2488.441	-2488.350	-2488.335	-2488.392
[Fe(H ₂ O) ₂ Cl ₂ OH ₂]	cis	-1720.259	-1720.132	-1720.115	-1720.174
	trans	-1720.255	-1720.129	-1720.111	-1720.172
α-glucoopyranose-[Fe(H ₂ O) ₅ Cl] ²⁺	ax1	-2638.764	-2638.486	-2638.461	-2638.539
	ax2	-2638.766	-2638.486	-2638.461	-2638.540
	eq1	-2638.766	-2638.487	-2638.462	-2638.541
	eq2	-2638.768	-2638.489	-2638.464	-2638.543
α-glucoopyranose-[Fe(H ₂ O) ₅ OH] ²⁺	ax1	-2254.465	-2254.174	-2254.149	-2254.226
	ax2	-2254.467	-2254.176	-2254.151	-2254.228
	eq1	-2254.466	-2254.176	-2254.151	-2254.230
	eq2	-2254.467	-2254.177	-2254.152	-2254.231
α-glucoopyranose-[Fe(H ₂ O) ₄ Cl ₂] ⁺	ax1ax2	-3022.655	-3022.401	-3022.377	-3022.453
	eq1eq2	-3022.659	-3022.405	-3022.380	-3022.458
	eq1ax2	-3022.655	-3022.400	-3022.376	-3022.454
	eq1ax1	-3022.656	-3022.402	-3022.378	-3022.456
	eq2ax2	-3022.657	-3022.402	-3022.378	-3022.455
	eq2ax1	-3022.654	-3022.400	-3022.376	-3022.455

Table 25: Absolute energies of different copper(II)-complexes (PBE0/6-31+G, CPCM(water)).**

	non-water ligand position	E / a.u.	E_ZPC / a.u.	H / a.u.	G / a.u.
[Cu(H ₂ O) ₄] ²⁺	quadratic-planar	-1945.203	-1945.099	-1945.087	-1945.136
[Cu(H ₂ O) ₆] ²⁺		-2097.949	-2097.796	-2097.778	-2097.839
[CuCl ₄] ²⁻	tedrahedral	-3480.691	-3480.688	-3480.679	-3480.725
[Cu(H ₂ O)Cl ₃] ⁻	tedrahedral	-2329.089	-2329.011	-2329.000	-2329.047
[Cu(H ₂ O) ₂ Cl ₂]	quadratic planar	-2712.964	-2712.911	-2712.900	-2712.947

Table 26: Absolute energies of different magnesium(II)-complexes (PBE0/6-31+G, CPCM(water)).**

	non-water ligand position	E / a.u.	E_ZPC / a.u.	H / a.u.	G / a.u.
[Mg(H ₂ O) ₄] ²⁺		-547.322	-547.217	-547.206	-547.250
[Mg(H ₂ O) ₆] ²⁺		-658.009	-657.860	-657.840	-657.904
TS2 - [MgO ⁺ O ²⁻ (H ₂ O) ₄] ²⁺		-1191.721	-1191.427	-1191.400	-1191.484
	deprotonated	-1191.299	-1191.016	-1190.989	-1191.070

Table 27: Absolute energies for hydrogen transfer transition states with different ligand positions (PBE0/6-31+G, CPCM(water)).**

		E / a.u.	E_ZPC / a.u.	H / a.u.	G / a.u.
Al(H ₂ O) ₆ ³⁺	TS2	-1386.630	-1386.279	-1386.249	-1386.337
	TS2 – deprot.	-1386.211	-1385.876	-1385.847	-1385.932
Al(H ₂ O) ₄ ³⁺	TS2	-1233.863	-1233.562	-1233.537	-1233.612
	TS2 – deprot.	-1233.520	-1233.202	-1233.179	-1233.252
Al(H ₂ O) ₃ Cl ²⁺	TS2 – eq1	-1617.761	-1617.488	-1617.464	-1617.539
	TS2 – ax1 - deprot	-1617.360	-1617.097	-1617.074	-1617.146
	TS2 – ax2	-1617.744	-1617.469	-1617.445	-1617.520
	TS2 – eq2	-1617.749	-1617.473	-1617.450	-1617.525
Al(H ₂ O) ₃ OH ²⁺	TS2 – eq2	-1233.458	-1233.173	-1233.149	-1233.223
	TS2 – ax2	-1233.456	-1233.171	-1233.147	-1233.222
	TS2 – eq1 – deprot	-1233.058	-1232.783	-1232.759	-1232.832
	TS2 – ax1 - deprot	-1233.046	-1232.770	-1232.747	-1232.820
	TS2 – eq2 – deprot	-1233.058	-1232.783	-1232.759	-1232.832
Al ₂ (H ₂ O) ₈ OH ⁴⁺	TS2	-1780.860	-1780.462	-1780.428	-1780.521
	TS2 – deprot.	-1780.499	-1780.113	-1780.080	-1780.170
Fe(H ₂ O) ₄ ³⁺	TS2	-2254.818	-2254.521	-2254.495	-2254.574
	TS2 – deprot.	-2254.434	-2254.149	-2254.124	-2254.202
Fe(H ₂ O) ₃ Cl ²⁺	TS2 – eq1	-2638.714	-2638.441	-2638.416	-2638.494
	TS2 – eq1 - deprot	-2638.316	-2638.056	-2638.031	-2638.109
	TS2 – ax1	-2638.715	-2638.444	-2638.419	-2638.499
	TS2 – ax1 - deprot	-2638.316	-2638.056	-2638.032	-2638.110
	TS2 – ax2	-2638.718	-2638.447	-2638.422	-2638.500
	TS2 – ax2 - deprot	-2638.306	-2638.047	-2638.021	-2638.103
	TS2 – eq2	-2638.713	-2638.441	-2638.416	-2638.496
	TS2 – eq2 - deprot	-2638.316	-2638.056	-2638.032	-2638.111
Fe(H ₂ O) ₃ OH ²⁺	TS2 – eq2	-2254.412	-2254.128	-2254.103	-2254.183
	TS2 – eq2 – deprot	-2254.005	-2253.733	-2253.708	-2253.787
	TS2 – ax1 - deprot	-2253.999	-2253.728	-2253.702	-2253.784
Fe(H ₂ O)Cl ₃	TS2 – eq1ax12	-3406.468	-3406.246	-3406.222	-3406.303
	TS2 – eq12ax2	-3406.476	-3406.254	-3406.230	-3406.310
Cr(H ₂ O) ₄ ³⁺	TS2	-2035.693	-2035.394	-2035.369	-2035.446
	TS2 – deprot.	-2035.305	-2035.017	-2034.993	-2035.068
Cr(H ₂ O) ₃ OH ²⁺	TS2 – eq2	-2035.274	-2034.990	-2034.965	-2035.042
	TS2 – eq2 – deprot	-2034.869	-2034.595	-2034.571	-2034.647
	TS2 – ax2 - deprot	-2034.864	-2034.591	-2034.566	-2034.643
Cr(H ₂ O) ₃ Cl ²⁺	TS2 – eq2	-2419.576	-2419.304	-2419.279	-2419.357
	TS2 – eq2 – deprot	-2419.181	-2418.919	-2418.895	-2418.971
	TS2 – ax2 - deprot	-2419.179	-2418.917	-2418.894	-2418.969

Table 28: Absolute energies for isomerization catalyzed by an [Mg(H₂O)₆]²⁺ complex (PBE0/6-31+G, CPCM(water)).**

catalyst →	[Mg(H ₂ O) ₆] ²⁺			
structure ↓	E / a.u.	E_ZPC / a.u.	H / a.u.	G / a.u.
compl. gluc.	-1344.531	-1344.180	-1344.146	-1344.244
glucose	-1344.518	-1344.169	-1344.135	-1344.232
TS2	-1344.468	-1344.122	-1344.090	-1344.183
deprot. fructose	-1344.480	-1344.131	-1344.099	-1344.193
fructose	-1344.521	-1344.172	-1344.138	-1344.234
fructofuranose O5 prot.	-1344.482	-1344.131	-1344.101	-1344.185
fructofuranose	-1344.537	-1344.185	-1344.153	-1344.244

Table 29: Absolute energies for isomerization catalyzed by an $[\text{Mg}(\text{H}_2\text{O})_4]^{2+}$ complex (PBE0/6-31+G, CPCM(water)).**

catalyst →	$[\text{Mg}(\text{H}_2\text{O})_4]^{2+}$			
structure ↓	E / a.u.	E_ZPC / a.u.	H / a.u.	G / a.u.
compl. gluc.	-1191.786	-1191.485	-1191.457	-1191.539
glucose	-1191.774	-1191.475	-1191.447	-1191.531
TS2	-1191.721	-1191.427	-1191.400	-1191.484
deprot. fructose	-1191.732	-1191.437	-1191.410	-1191.495
fructose	-1191.780	-1191.482	-1191.453	-1191.538
fructofuranose O5 prot.	-1191.323	-1191.037	-1191.010	-1191.091
fructofuranose	-1191.797	-1191.495	-1191.469	-1191.548

Table 30: Absolute energies for isomerization catalyzed by an $[\text{Cu}(\text{H}_2\text{O})_4]^{2+}$ complex (PBE0/6-31+G, CPCM(water)).**

catalyst →	$\text{Cu}(\text{H}_2\text{O})_4^{2+}$			
structure ↓	E / a.u.	E_ZPC / a.u.	H / a.u.	G / a.u.
compl. gluc.	-2631.720	-2631.418	-2631.391	-2631.474
glucose	-2631.716	-2631.415	-2631.388	-2631.469
deprot. glucose	-2631.286	-2631.000	-2630.973	-2631.058
TS2	-2631.264	-2630.981	-2630.954	-2631.037
deprot. fructose	-2631.294	-2631.008	-2630.981	-2631.065
fructose	-2631.725	-2631.425	-2631.398	-2631.481
fructofuranose	-2631.726	-2631.424	-2631.399	-2631.477

Table 31: Absolute energies for isomerization catalyzed by an $[\text{Cu}(\text{H}_2\text{O})_2]^{2+}$ complex (PBE0/6-31+G, CPCM(water)).**

catalyst →	$\text{Cu}(\text{H}_2\text{O})_2^{2+}$			
structure ↓	E / a.u.	E_ZPC / a.u.	H / a.u.	G / a.u.
compl. gluc.	-2478.982	-2478.729	-2478.709	-2478.777
deprot. glucose	-2478.544	-2478.307	-2478.286	-2478.356
TS2	-2478.520	-2478.287	-2478.266	-2478.337
deprot. fructose	-2478.550	-2478.314	-2478.292	-2478.365
fructofuranose	-2478.984	-2478.732	-2478.712	-2478.779

Table 32: Absolute energies for isomerization catalyzed by an $[\text{Cu}(\text{H}_2\text{O})_6]^{2+}$ complex (PBE0/6-31+G, CPCM(water)).**

catalyst →	$\text{Cu}(\text{H}_2\text{O})_6^{2+}$			
structure ↓	E / a.u.	E_ZPC / a.u.	H / a.u.	G / a.u.
compl. gluc.	-2784.474	-2784.121	-2784.088	-2784.184
glucose	-2784.465	-2784.113	-2784.081	-2784.174
TS2	-2784.412	-2784.064	-2784.033	-2784.126
deprot. fructose	-2784.426	-2784.078	-2784.046	-2784.143
fructofuranose	-2784.482	-2784.128	-2784.097	-2784.188

Table 33: Absolute energies for isomerization catalyzed by an $[\text{Cu}(\text{H}_2\text{O})\text{Cl}]^+$ complex (PBE0/6-31+G, CPCM(water)).**

catalyst →	$\text{Cu}(\text{H}_2\text{O})\text{Cl}^+$			
structure ↓	E / a.u.	E_ZPC / a.u.	H / a.u.	G / a.u.
compl. gluc.	-2862.870	-2862.642	-2862.622	-2862.690
glucose	-2862.848	-2862.622	-2862.602	-2862.671
TS2	-2862.791	-2862.570	-2862.550	-2862.621
deprot. fructose	-2862.803	-2862.579	-2862.558	-2862.631
fructofuranose	-2862.869	-2862.641	-2862.622	-2862.689

Table 34: Absolute energies for isomerization catalyzed by an CuCl_2 complex (PBE0/6-31+G, CPCM(water)).**

catalyst →	CuCl_2			
structure ↓	E / a.u.	E_ZPC / a.u.	H / a.u.	G / a.u.
compl. gluc.	-3246.747	-3246.544	-3246.525	-3246.593
glucose	-3246.723	-3246.523	-3246.503	-3246.573
TS2	-3246.669	-3246.473	-3246.453	-3246.525
deprot. fructose	-3246.678	-3246.480	-3246.459	-3246.532
fructose	-3246.733	-3246.534	-3246.513	-3246.586
fructofuranose	-3246.744	-3246.542	-3246.523	-3246.592

Table 35: Absolute energies for isomerization catalyzed by an $[\text{Fe}(\text{H}_2\text{O})_6]^{3+}$ complex (PBE0/6-31+G, CPCM(water)).**

catalyst →	$\text{Fe}(\text{H}_2\text{O})_6^{3+}$			
structure ↓	E / a.u.	E_ZPC / a.u.	H / a.u.	G / a.u.
compl. gluc.	-2407.620	-2407.268	-2407.237	-2407.329
glucop. O5 prot.	-2407.608	-2407.254	-2407.223	-2407.315
glucose	-2407.589	-2407.237	-2407.205	-2407.299
TS2	-2407.573	-2407.226	-2407.195	-2407.289
deprot. fructose	-2407.599	-2407.249	-2407.217	-2407.311
fructose	-2407.606	-2407.256	-2407.224	-2407.319
TS3	-2407.597	-2407.250	-2407.219	-2407.311
fructofuranose O5 prot.	-2407.606	-2407.254	-2407.223	-2407.314
fructofuranose	-2407.632	-2407.280	-2407.250	-2407.340

Table 36: Absolute energies for isomerization catalyzed by an $[\text{Fe}(\text{H}_2\text{O})_3\text{OH}]^{2+}$ complex (PBE0/6-31+G, CPCM(water)).**

catalyst →	$\text{Fe}(\text{H}_2\text{O})_3\text{OH}^{2+}$			
structure ↓	E / a.u.	E_ZPC / a.u.	H / a.u.	G / a.u.
compl. gluc.	-2254.467	-2254.177	-2254.152	-2254.232
glucop. O5 prot.	-2254.447	-2254.156	-2254.131	-2254.210
glucose	-2254.448	-2254.159	-2254.134	-2254.212
TS2	-2254.412	-2254.128	-2254.103	-2254.183
deprot. fructose	-2254.444	-2254.159	-2254.133	-2254.214
fructose	-2254.453	-2254.165	-2254.140	-2254.220
fructofuranose O5 prot.	-2254.453	-2254.164	-2254.139	-2254.218
fructofuranose	-2254.484	-2254.195	-2254.170	-2254.248

Table 37: Absolute energies for isomerization catalyzed by an $[\text{Fe}(\text{H}_2\text{O})_2(\text{OH})_2]^+$ complex (PBE0/6-31+G, CPCM(water)).**

catalyst →	$\text{Fe}(\text{H}_2\text{O})_2(\text{OH})_2^+$			
structure ↓	E / a.u.	E_ZPC / a.u.	H / a.u.	G / a.u.
compl. gluc.	-2254.042	-2253.766	-2253.740	-2253.820
glucose	-2254.034	-2253.758	-2253.733	-2253.812
TS2	-2253.983	-2253.713	-2253.687	-2253.769
deprot. fructose	-2254.005	-2253.733	-2253.707	-2253.789
fructofuranose	-2254.051	-2253.774	-2253.750	-2253.827

Table 38: Absolute energies for isomerization catalyzed by an $[\text{Fe}(\text{H}_2\text{O})_4]^{3+}$ complex (PBE0/6-31+G, CPCM(water)).**

catalyst →	$\text{Fe}(\text{H}_2\text{O})_4^{3+}$			
structure ↓	E / a.u.	E_ZPC / a.u.	H / a.u.	G / a.u.
compl. gluc.	-2254.861	-2254.558	-2254.532	-2254.610
glucop. O5 prot.	-2254.859	-2254.556	-2254.531	-2254.610
glucose	-2254.856	-2254.554	-2254.529	-2254.606
deprot. glucose	-2254.466	-2254.178	-2254.152	-2254.232
TS2	-2254.434	-2254.149	-2254.124	-2254.202
deprot. fructose	-2254.471	-2254.184	-2254.157	-2254.239
fructose	-2254.866	-2254.566	-2254.540	-2254.620
TS3	-2254.855	-2254.554	-2254.529	-2254.607
fructofuranose O5 prot.	-2254.859	-2254.532	-2254.531	-2254.611
fructofuranose	-2254.887	-2254.586	-2254.561	-2254.639

Table 39: Absolute energies for isomerization catalyzed by an $[\text{Fe}_2(\text{H}_2\text{O})_8(\text{OH})_2]^{4+}$ complex (PBE0/6-31+G, CPCM(water)).**

catalyst →	$\text{Fe}_2(\text{H}_2\text{O})_8(\text{OH})_2^{4+}$			
structure ↓	E / a.u.	E_ZPC / a.u.	H / a.u.	G / a.u.
compl. gluc.	-2254.861	-2254.558	-2254.532	-2254.610
deprot. glucose	-3822.411	-3822.026	-3821.992	-3822.089
TS2	-3822.389	-3822.011	-3821.975	-3822.076
deprot. fructose	-3822.436	-3822.054	-3822.018	-3822.121

Table 40: Absolute energies for isomerization catalyzed by an $[\text{Fe}(\text{H}_2\text{O})_3\text{Cl}]^{2+}$ complex (PBE0/6-31+G, CPCM(water)).**

catalyst →	$\text{Fe}(\text{H}_2\text{O})_3\text{Cl}^{2+}$			
structure ↓	E / a.u.	E_ZPC / a.u.	H / a.u.	G / a.u.
compl. gluc.	-2638.768	-2638.489	-2638.464	-2638.544
glucop. O5 prot.	-2638.752	-2638.473	-2638.448	-2638.526
glucose	-2638.756	-2638.479	-2638.454	-2638.532
TS2	-2638.713	-2638.441	-2638.416	-2638.496
deprot. fructose	-2638.731	-2638.455	-2638.430	-2638.510
fructose	-2638.767	-2638.491	-2638.466	-2638.547
fructofuranose O5 prot.	-2638.760	-2638.482	-2638.457	-2638.534
fructofuranose	-2638.788	-2638.510	-2638.485	-2638.561

Table 41: Absolute energies for isomerization catalyzed by an $[\text{Fe}(\text{H}_2\text{O})_2(\text{OH})\text{Cl}]^+$ complex (PBE0/6-31+G, CPCM(water)).**

catalyst →	$\text{Fe}(\text{H}_2\text{O})_2(\text{OH})\text{Cl}^+$			
structure ↓	E / a.u.	E_ZPC / a.u.	H / a.u.	G / a.u.
compl. gluc.	-2638.353	-2638.087	-2638.062	-2638.142
glucose	-2638.340	-2638.075	-2638.051	-2638.129
TS2	-2638.294	-2638.036	-2638.010	-2638.092
deprot. fructose	-2638.316	-2638.057	-2638.031	-2638.114
fructofuranose	-2638.363	-2638.097	-2638.073	-2638.150

Table 42: Absolute energies for isomerization catalyzed by an $[\text{Fe}(\text{H}_2\text{O})_2\text{Cl}_2]^+$ complex (PBE0/6-31+G, CPCM(water)).**

catalyst →	$\text{Fe}(\text{H}_2\text{O})_2\text{Cl}_2^+$			
structure ↓	E / a.u.	E_ZPC / a.u.	H / a.u.	G / a.u.
compl. gluc.	-3022.659	-3022.405	-3022.380	-3022.458
glucop. O5 prot.	-3022.634	-3022.379	-3022.355	-3022.432
glucose	-3022.642	-3022.390	-3022.365	-3022.444
TS2	-3022.590	-3022.344	-3022.318	-3022.402
deprot. fructose	-3022.630	-3022.382	-3022.356	-3022.440
fructose	-3022.636	-3022.385	-3022.359	-3022.442
fructofuranose O5 prot.	-3022.638	-3022.385	-3022.361	-3022.439
fructofuranose	-3022.667	-3022.413	-3022.389	-3022.466

Table 43: Absolute energies for isomerization catalyzed by an $\text{Fe}(\text{H}_2\text{O})(\text{OH})\text{Cl}_2$ complex (PBE0/6-31+G, CPCM(water)).**

catalyst →	$\text{Fe}(\text{H}_2\text{O})(\text{OH})\text{Cl}_2$			
structure ↓	E / a.u.	E_ZPC / a.u.	H / a.u.	G / a.u.
compl. gluc.	-3022.225	-3021.985	-3021.960	-3022.038
glucose	-3022.210	-3021.971	-3021.947	-3022.026
TS2	-3022.167	-3021.933	-3021.909	-3021.988
deprot. fructose	-3022.188	-3021.952	-3021.927	-3022.008
fructofuranose	-3022.228	-3021.987	-3021.963	-3022.041

Table 44: Absolute energies for isomerization catalyzed by an $[\text{Fe}(\text{OH})\text{Cl}_3]^-$ complex (PBE0/6-31+G, CPCM(water)).**

catalyst →	$\text{Fe}(\text{OH})\text{Cl}_3^-$			
structure ↓	E / a.u.	E_ZPC / a.u.	H / a.u.	G / a.u.
TS2	-3406.025	-3405.816	-3405.792	-3405.872

Table 45: Absolute energies for isomerization catalyzed by an $\text{Fe}(\text{H}_2\text{O})\text{Cl}_3$ complex (PBE0/6-31+G, CPCM(water)).**

catalyst →	$\text{Fe}(\text{H}_2\text{O})\text{Cl}_3$			
structure ↓	E / a.u.	E_ZPC / a.u.	H / a.u.	G / a.u.
compl. gluc.	-3406.529	-3406.300	-3406.276	-3406.354
glucose	-3406.516	-3406.289	-3406.265	-3406.344
TS2	-3406.468	-3406.246	-3406.222	-3406.303
deprot. fructose	-3406.499	-3406.274	-3406.250	-3406.330
fructofuranose	-3406.527	-3406.299	-3406.275	-3406.354

Table 46: Absolute energies for isomerization catalyzed by an $[\text{Cr}(\text{H}_2\text{O})_4]^{3+}$ complex (PBE0/6-31+G, CPCM(water)).**

catalyst →	$\text{Cr}(\text{H}_2\text{O})_4^{3+}$			
structure ↓	E / a.u.	E_ZPC / a.u.	H / a.u.	G / a.u.
compl. gluc.	-2035.731	-2035.424	-2035.400	-2035.475
glucop. O5 prot.	-2035.724	-2035.418	-2035.394	-2035.469
glucose	-2035.73	-2035.424	-2035.400	-2035.475
deprot. glucose	-2035.329	-2035.038	-2035.014	-2035.090
TS2	-2035.305	-2035.017	-2034.993	-2035.068
deprot. fructose	-2035.335	-2035.045	-2035.020	-2035.097
fructose	-2035.736	-2035.432	-2035.408	-2035.484
TS3	-2035.724	-2035.420	-2035.396	-2035.472
fructofuranose O5 prot.	-2035.735	-2035.430	-2035.406	-2035.481
fructofuranose	-2035.758	-2035.453	-2035.430	-2035.503

Table 47: Absolute energies for isomerization catalyzed by an $[\text{r}_2(\text{H}_2\text{O})_8(\text{OH})_2]^{4+}$ complex (PBE0/6-31+G, CPCM(water)).**

catalyst →	$\text{Cr}_2(\text{H}_2\text{O})_8(\text{OH})_2^{4+}$			
structure ↓	E / a.u.	E_ZPC / a.u.	H / a.u.	G / a.u.
deprot. glucose	-3384.127	-3383.740	-3383.706	-3383.800
TS2	-3384.117	-3383.733	-3383.700	-3383.794
deprot. fructose	-3384.168	-3383.781	-3383.747	-3383.842

Table 48: Absolute energies for isomerization catalyzed by an $\text{Cr}(\text{H}_2\text{O})_6^{3+}$ complex (PBE0/6-31+G, CPCM(water)).**

catalyst →	$\text{Cr}(\text{H}_2\text{O})_6^{3+}$			
structure ↓	E / a.u.	E_ZPC / a.u.	H / a.u.	G / a.u.
compl. gluc.	-2188.492	-2188.135	-2188.106	-2188.192
glucop. O5 prot.	-2188.474	-2188.089	-2188.088	-2188.176
TS1	-2188.469	-2188.117	-2188.088	-2188.173
glucose	-2188.484	-2188.130	-2188.100	-2188.189
TS2	-2188.440	-2188.090	-2188.060	-2188.149
deprot. fructose	-2188.466	-2188.112	-2188.083	-2188.170
fructose	-2188.479	-2188.123	-2188.094	-2188.181
TS3	-2188.473	-2188.118	-2188.090	-2188.174
fructofuranose O5 prot.	-2188.473	-2188.118	-2188.090	-2188.174
fructofuranose	-2188.504	-2188.148	-2188.119	-2188.203

Table 49: Absolute energies for isomerization catalyzed by an $[\text{Cr}(\text{H}_2\text{O})_3\text{OH}]^{2+}$ complex (PBE0/6-31+G, CPCM(water)).**

catalyst →	$\text{Cr}(\text{H}_2\text{O})_3\text{OH}^{2+}$			
structure ↓	E / a.u.	E_ZPC / a.u.	H / a.u.	G / a.u.
compl. gluc.	-2035.329	-2035.036	-2035.011	-2035.087
glucop. O5 prot.	-2035.306	-2035.013	-2034.989	-2035.064
glucose	-2035.325	-2035.035	-2035.010	-2035.086
TS2	-2035.274	-2034.990	-2034.965	-2035.042
deprot. fructose	-2035.297	-2035.009	-2034.984	-2035.064
fructose	-2035.317	-2035.028	-2035.002	-2035.084
TS3	-2035.311	-2035.020	-2034.996	-2035.071
fructofuranose O5 prot.	-2035.313	-2035.022	-2034.998	-2035.074
fructofuranose	-2035.346	-2035.054	-2035.031	-2035.104

Table 50: Absolute energies for isomerization catalyzed by an $[\text{Cr}(\text{H}_2\text{O})_3\text{Cl}]^{2+}$ complex (PBE0/6-31+G, CPCM(water)).**

catalyst →	$\text{Cr}(\text{H}_2\text{O})_3\text{Cl}^{2+}$			
structure ↓	E / a.u.	E_ZPC / a.u.	H / a.u.	G / a.u.
compl. gluc.	-2419.628	-2419.347	-2419.323	-2419.398
glucop. O5 prot.	-2419.609	-2419.328	-2419.304	-2419.378
glucose	-2419.617	-2419.338	-2419.314	-2419.390
TS2	-2419.576	-2419.304	-2419.279	-2419.357
deprot. fructose	-2419.601	-2419.325	-2419.299	-2419.379
fructose	-2419.628	-2419.350	-2419.325	-2419.402
TS3	-2419.614	-2419.335	-2419.311	-2419.387
fructofuranose O5 prot.	-2419.622	-2419.341	-2419.318	-2419.392
fructofuranose	-2419.650	-2419.370	-2419.347	-2419.420

Table 51: Absolute energies for isomerization catalyzed by an $[\text{Cr}(\text{H}_2\text{O})_2\text{Cl}_2]^+$ complex (PBE0/6-31+G, CPCM(water)).**

catalyst →	$\text{Cr}(\text{H}_2\text{O})_2\text{Cl}_2^+$			
structure ↓	E / a.u.	E_ZPC / a.u.	H / a.u.	G / a.u.
compl. gluc.	-2803.514	-2803.258	-2803.234	-2803.310
glucop. O5 prot.	-2803.488	-2803.232	-2803.209	-2803.284
glucose	-2803.497	-2803.244	-2803.220	-2803.298
TS2	-2803.450	-2803.204	-2803.180	-2803.258
deprot. fructose	-2803.473	-2803.222	-2803.198	-2803.276
fructose	-2803.505	-2803.252	-2803.228	-2803.304
fructofuranose O5 prot.	-2803.495	-2803.240	-2803.217	-2803.292
fructofuranose	-2803.529	-2803.273	-2803.250	-2803.322

Table 52: Absolute energies for isomerization catalyzed by an $\text{Cr}(\text{H}_2\text{O})\text{Cl}_3$ complex (PBE0/6-31+G, CPCM(water)).**

catalyst →	$\text{Cr}(\text{H}_2\text{O})\text{Cl}_3$			
structure ↓	E / a.u.	E_ZPC / a.u.	H / a.u.	G / a.u.
compl. gluc.	-3187.382	-3187.151	-3187.128	-3187.203
glucose	-3187.372	-3187.143	-3187.120	-3187.197
TS2	-3187.321	-3187.099	-3187.076	-3187.152
deprot. fructose	-3187.336	-3187.110	-3187.086	-3187.164
fructofuranose	-3187.389	-3187.159	-3187.137	-3187.210

Table 53: Absolute energies for isomerization catalyzed by an $[\text{Al}(\text{H}_2\text{O})_6]^{3+}$ complex (PBE0/6-31+G, CPCM(water)).**

catalyst →	$[\text{Al}(\text{H}_2\text{O})_6]^{3+}$			
structure ↓	E / a.u.	E_ZPC / a.u.	H / a.u.	G / a.u.
compl. gluc.	-1386.685	-1386.327	-1386.298	-1386.384
glucop. O5 prot.	-1386.664	-1386.307	-1386.277	-1386.363
TS1	-1386.660	-1386.308	-1386.278	-1386.363
glucose	-1386.677	-1386.320	-1386.291	-1386.376
TS2	-1386.630	-1386.279	-1386.249	-1386.337
deprot. fructose	-1386.653	-1386.298	-1386.269	-1386.354
fructose	-1386.669	-1386.315	-1386.284	-1386.372
TS3	-1386.659	-1386.307	-1386.278	-1386.362
fructofuranose O5 prot.	-1386.663	-1386.306	-1386.277	-1386.361
fructofuranose	-1386.688	-1386.332	-1386.303	-1386.389

Table 54: Absolute energies for isomerization catalyzed by an $[\text{Al}(\text{H}_2\text{O})_3\text{OH}]^{2+}$ complex (PBE0/6-31+G, CPCM(water)).**

catalyst →	$\text{Al}(\text{H}_2\text{O})_3\text{OH}^{2+}$			
structure ↓	E / a.u.	E_ZPC / a.u.	H / a.u.	G / a.u.
compl. gluc.	-1233.512	-1233.218	-1233.194	-1233.267
glucop. O5 prot.	-1233.491	-1233.196	-1233.173	-1233.245
glucose	-1233.499	-1233.209	-1233.185	-1233.258
TS2	-1233.458	-1233.173	-1233.149	-1233.223
deprot. fructose	-1233.482	-1233.192	-1233.167	-1233.242
fructose	-1233.514	-1233.223	-1233.198	-1233.273
TS3	-1233.502	-1233.211	-1233.187	-1233.260
fructofuranose O5 prot.	-1233.507	-1233.214	-1233.190	-1233.262
fructofuranose	-1233.535	-1233.241	-1233.218	-1233.289

Table 55: Absolute energies for isomerization catalyzed by an $[\text{Al}(\text{H}_2\text{O})_3\text{Cl}]^{2+}$ complex (PBE0/6-31+G, CPCM(water)).**

catalyst →	$\text{Al}(\text{H}_2\text{O})_3\text{Cl}^{2+}$			
structure ↓	E / a.u.	E_ZPC / a.u.	H / a.u.	G / a.u.
compl. gluc.	-1617.809	-1617.526	-1617.503	-1617.575
glucop. O5 prot.	-1617.794	-1617.512	-1617.488	-1617.561
glucose	-1617.800	-1617.521	-1617.497	-1617.571
TS2	-1617.761	-1617.488	-1617.464	-1617.539
deprot. fructose	-1617.787	-1617.510	-1617.486	-1617.562
fructose	-1617.800	-1617.522	-1617.497	-1617.574
TS3	-1617.794	-1617.514	-1617.490	-1617.564
fructofuranose O5 prot.	-1617.800	-1617.518	-1617.495	-1617.568
fructofuranose	-1617.828	-1617.546	-1617.524	-1617.594

Table 56: Absolute energies for isomerization catalyzed by an $[\text{Al}(\text{H}_2\text{O})_4]^{3+}$ complex (PBE0/6-31+G, CPCM(water)).**

catalyst →	$\text{Al}(\text{H}_2\text{O})_4^{3+}$			
structure ↓	E / a.u.	E_ZPC / a.u.	H / a.u.	G / a.u.
compl. gluc.	-1233.920	-1233.614	-1233.589	-1233.664
glucop. O5 prot.	-1233.907	-1233.601	-1233.576	-1233.650
glucose	-1233.913	-1233.608	-1233.584	-1233.656
deprot. glucose	-1233.515	-1233.223	-1233.199	-1233.272
TS2	-1233.520	-1233.202	-1233.179	-1233.252
deprot. fructose	-1233.520	-1233.228	-1233.204	-1233.278
fructose	-1233.924	-1233.620	-1233.595	-1233.670
TS3	-1233.914	-1233.584	-1233.584	-1233.656
fructofuranose O5 prot.	-1233.923	-1233.617	-1233.593	-1233.666
fructofuranose	-1233.948	-1233.642	-1233.619	-1233.690

Table 57: Absolute energies for isomerization catalyzed by an $[\text{Al}_2(\text{H}_2\text{O})_8(\text{OH})_2]^{4+}$ complex (PBE0/6-31+G, CPCM(water)).**

catalyst →	$\text{Al}_2(\text{H}_2\text{O})_8(\text{OH})_2^{4+}$			
structure ↓	E / a.u.	E_ZPC / a.u.	H / a.u.	G / a.u.
compl. gluc.	-1233.920	-1233.614	-1233.589	-1233.664
deprot. glucose	-1780.508	-1780.119	-1780.086	-1780.177
TS2	-1780.499	-1780.113	-1780.080	-1780.170
deprot. fructose	-1780.548	-1780.159	-1780.125	-1780.218

References

- [1] G. Yang, E. A. Pidko, E. J. M. Hensen, *J. Catal.* **2012**, *295*, 122-132.
- [2] A. V. Marenich, C. J. Cramer, D. G. Truhlar, *J. Phys. Chem. B* **2009**, *113*, 4538-4543.
- [3] a) D. M. Camaioni, C. A. Schwerdtfeger, *J. Phys. Chem. A* **2005**, *109*, 10795-10797; b) C. P. Kelly, C. J. Cramer, D. G. Truhlar, *J. Phys. Chem. B* **2006**, *110*, 16066-16081.
- [4] M. D. Liptak, G. C. Shields, *J. Am. Chem. Soc.* **2001**, *123*, 7314-7319.
- [5] a) N. Wiberg, *Holleman-Wiberg, Lehrbuch der Anorganischen Chemie*, Walter de Gruyter, Berlin, New York, **1995**; b) W. Grzybowski, *Polish J. of Environ. Stud.* **2006**, *15*, 655-663; c) G. Ottonello, M. V. Zuccolini, *Geochim. Cosmochim. Ac.* **2009**, *73*, 6447-6469; d) G. Ottonello and M. V. Zuccolini, *Geochim. Cosmochim. Ac.* **2005**, *69*, 851-874.
- [6] a) K. S. Alongi, G. C. Shields in *Theoretical Calculations of Acid Dissociation Constants, Vol. 6* Elsevier, **2010**, pp. 113-138; b) J. Ho, M. L. Coote, *Theor. Chem. Acc.* **2009**, *125*, 3-21.
- [7] R. B. Martin, *J. Inorg. Biochem.* **1991**, *44*, 141-147.
- [8] K. Geetha, M. S. S. Raghavan, S. K. Kulshreshtha, R. Sasikala, C. P. Rao, *Carbohydr. Res.* **1995**, *271*, 163-175.
- [9] L. Nagy, H. Ohtaki, T. Yamaguchi, M. Nomura, *Inorg. Chim. Acta* **1989**, *159*, 201-207.
- [10] J. Briggs, P. Finch, M. C. Matulewicz, H. Weigel, *Carbohydr. Res.* **1981**, *97*, 181-188.
- [11] E. A. Pidko, V. Degirmenci, E. J. M. Hensen, *ChemCatChem* **2012**, *4*, 1263-1271.
- [12] K. N. Allen, A. Lavie, G. K. Farber, A. Glasfeld, G. A. Petsko, D. Ringe, *Biochemistry* **1994**, *33*, 1481-1487.
- [13] J. Guan, Q. Cao, X. Guo, X. Mu, *Compu. Theor. Chem.* **2011**, *963*, 453-462.
- [14] E. A. Pidko, V. Degirmenci, R. A. van Santen, E. J. M. Hensen, *Angew. Chem. Int. Edit.* **2010**, *49*, 2530-2534.
- [15] G. Yang, E. A. Pidko, E. J. M. Hensen, *ChemSusChem* **2013**, *6*, 1688-1696.

